Variational Calculations of Positronium Scattering with Hydrogen

Denton Woods

Dissertation Prepared for the Degree of
DOCTOR OF PHILOSOPHY

UNIVERSITY OF NORTH TEXAS
August 2015

APPROVED:

Sandra J. Quintanilla (Ward),
Major Professor
Peter Van Reeth, Minor Professor
Duncan Weathers, Committee Member
David Shiner, Committee Member
Carlos Ordonez, Committee Member
David Schultz, Chair of the Department of Physics
Mark Wardell, Dean of the Toulouse Graduate School

Abstract

Positronium-hydrogen (Ps-H) scattering is of interest, as it is a fundamental four-body Coulomb problem. We have investigated low-energy Ps-H scattering below the Ps(n=2) excitation threshold using the Kohn variational method and variants of the method with a trial wavefunction that includes highly correlated Hylleraas-type short-range terms. We give an elegant formalism that combines all Kohn-type variational methods into a single form. Along with this, we have also developed a general formalism for Kohn-type matrix elements that allows us to evaluate arbitrary partial waves with a single codebase. Computational strategies we have developed and use in this work are also discussed.

With these methods, we have computed phase shifts for the first six partial waves for both the singlet and triplet states. The ^{1,3}S and ^{1,3}P phase shifts are highly accurate results and could potentially be viewed as benchmark results. Resonance positions and widths for the ^{1}S-, ^{1}P-, ^{1}D-, and ^{1}F-waves have been calculated.

We present elastic integrated, elastic differential, and momentum transfer cross sections using all six partial waves and note interesting features of each. We use multiple effective range theories, including several that explicitly take into account the long-range van der Waals interaction, to investigate scattering lengths and effective ranges.

Acknowledgements

Many people helped me through this project. Special thanks goes to Ryan Bosca, who helped me at times and let me bounce ideas off of him. Keri Ward, Cassie Whitmire, Robert Whitmire, and Lauren Murphy have been part of a great support network that helped me survive this process, along with all of my friends in the physics department.

Great thanks goes to my advisor, Dr. S. J. Ward and to our collaborator, Dr. Peter Van Reeth, who helped immensely with this project through discussions, plenty of notes, and codes. I also appreciate discussions with Drs. Y. K. Ho, J. W. Humberston, K. Pachucki, Z.-C. Yan, Edward Armour, James Cooper, Martin Plummer, and Gillian Peach during the course of this project.

I received several travel grants to help me go to and present at conferences, including from DAMOP, UNT's Student Government Association, and UNT's College of Arts and Sciences. Dr. Ward received a grant from the National Science Foundation under grant no. PHYS-0968638 and another from UNT through the UNT faculty research grant GA9150, both of which supported my research.

Computational resources were provided by UNT's High Performance Computing Services, a project of Academic Computing and User Services division of the University Information Technology with additional support from UNT Office of Research and Economic Development.

Contents

List of Tables

List of Figures

List of Abbreviations

short-short	short-range–short-range
long-short	long-range–short-range
long-long	long-range–long-range
BO	Born-Oppenheimer
CC	close coupling
CI	configuration interaction
CVM	confined variational method
DMC	diffusion Monte Carlo
Ps	positronium
PsH	positronium hydride
SVM	stochastic variational method
SE	static-exchange
vdW	van der Waals

1 Introduction

1.1 Positronium

Positronium (Ps) is an exotic atom formed from the bound state of a positron (antielectron, e^+) and an electron (e^-). Stjepan Mohorovičić theorized the existence of Ps in 1934 [10], but it was not created until 1951 by Martin Deutsch [11]. This atom is similar in some ways to hydrogen (H) but also differs in some key aspects. Namely that Ps annihilates, emitting two or three γ rays, depending on the spin [12]. In the singlet state, also known as parapositronium (p-Ps), the lifetime is 125 ps [13]. The triplet state, or orthopositronium (o-Ps), lasts approximately 1000 times longer with a lifetime of 142 ns [14]. Due to the short lifetime of p-Ps, the majority of experimental data of Ps-atom and Ps-molecule scattering comes from o-Ps.

Working in atomic units (see Section 1.7), the ground state wavefunctions of H and that of Ps are

$$\Phi_{\mathrm{H}}(r_3) = \frac{1}{\sqrt{\pi}} \mathrm{e}^{-r_3} \tag{1.1}$$

and

$$\Phi_{\mathrm{Ps}}(r_{12}) = \frac{1}{\sqrt{8\pi}} \mathrm{e}^{-r_{12}/2} \,. \tag{1.2}$$

When the Schrödinger equation is solved for the hydrogen atom, the energy is seen to be (neglecting higher-order effects)

$$E_{n,\mathrm{H}} = -\frac{R_\infty}{n^2}. \tag{1.3}$$

In Hartree atomic units, $R_\infty = \frac{1}{2}$, giving a ground state energy of

$$E_{\mathrm{H}} = -\frac{1}{2}. \tag{1.4}$$

Due to the reduced mass of half that of hydrogen, the ground state energy of Ps is

$$E_{\mathrm{Ps}} = -\frac{1}{4}. \tag{1.5}$$

1.2 Motivation

Ps formation is important in the galactic core [15], and Ps-atom scattering is of interest in the study of solar processes [16]. As well as the basic interest of Ps-atom scattering in atomic physics, Ps is also important in material science. As Ps is neutral, it penetrates deeper into material than a charged particle, such as a positron. Ps scattering also has applications in other areas of physics such as biophysics and astrophysics [17]. A brief overview of the state of the art in antimatter atomic physics is Ref. [18], and a more in-depth review of Ps collisions is Ref. [17].

With the increased interest in antihydrogen ($\bar{H}$) production at CERN [19], there have been investigations by groups exploring alternate mechanisms other than dumping antiprotons ($\bar{p}$) into a cloud of e^+ and relying on the reaction of $\bar{p} + e^+ + e^+ \rightarrow \bar{H} + e^+$. Refs. [20, 21] explore the inelastic low-energy reaction of $\bar{p} + Ps \rightarrow \bar{H} + e^-$, where the Ps is in its ground state. A recent paper [22] (also mentioned in the popular science press [23]) found that if the target Ps is in an excited state ($1 < n \leq 3$), the $\bar{H}$ production rate is improved by several orders of magnitude.

The original motivation for this research was a proposed experiment to measure low-energy Ps scattering from alkali metals by Jason Engbrecht of the Positron Research Group at St. Olaf College. There has not been much theoretical work on these systems so far. Unfortunately, it appears that this project is put on hold indefinitely, and the group's website [24] no longer exists. We started investigating Ps-H scattering and plan to extend this work into Ps scattering from the alkali metals.

However, there is still interesting ongoing experimental work on Ps scattering, though with different targets. The University College London (UCL) Positron Group [25] has developed energy-tunable o-Ps beams [26, 27, 28, 29, 30] over the course of many years. This group has been able to study Ps scattering from He, Ne, Ar, Kr, and Xe [29, 30, 31, 32, 33, 34, 35, 36] and the H_2, N_2, O_2, CO_2, H_2O, and SF_6 molecules [29, 31, 33, 34, 36, 37, 38].

A recent development in the field is the surprising discovery that Ps scattering is electron-like [36, 39], which was also reported in the popular science literature [40]. If the cross sections are plotted with respect to the velocity of the incoming projectile, not momentum like typical, e^- and Ps scattering look similar when the target is the same. This is despite the Ps projectile having twice the mass of e^- and being electrically neutral versus negatively charged. It can be seen in Figure 1.1 that e^+ scattering looks different when compared to these two. Fabrikant and Gribakin [41, 42] compare low-energy e^- and Ps scattering from Kr and Ar targets, also finding that the cross sections are similar for e^- and Ps projectiles. The tentative conclusion is that the e^+ plays a much smaller role in the scattering process than the e^- in Ps-atom and Ps-molecule scattering. This shows that there is still plenty of work to do to understand Ps scattering more fully, but it does suggest that for certain cases, a decent first approximation to Ps scattering can be made by using e^- scattering data.

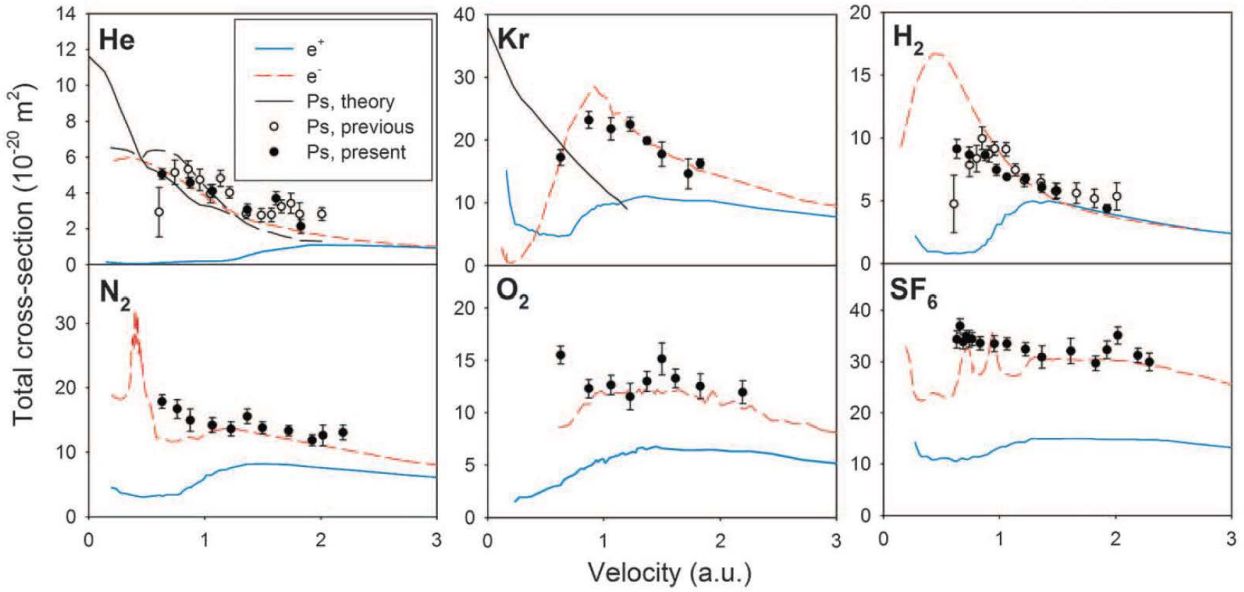

Figure 1.1: Comparisons of e^-, e^+, and Ps scattering from different atomic and molecular targets from Ref. [36]. Reprinted with permission from AAAS.

1.3 Partial Waves and Kohn-Type Variational Methods

The most common way of approaching scattering problems is to use the complete set of Legendre polynomials to expand the scattering wavefunction. For a central potential, this can be written as [43]

$$\Psi(k,r,\theta) = \sum_{\ell=0}^{\infty} R_\ell(k,r) P_\ell(\cos\theta). \tag{1.6}$$

The method of partial waves evaluates each term in this summation separately, with each referred to as a partial wave, and each has a different angular momentum. The typical naming of each partial wave starting from $\ell = 0$ is the S-, P-, D-, F-, G-, H-wave, etc., which is similar to the usual spectroscopic notation. For low energies, usually only a few terms in this expansion are required, and for very low energies, the S-wave ($\ell = 0$) is typically the only significant contribution.

The Kohn variational method [44] and its variants, derived and described in Chapter 3, have been used successfully in many scattering problems, such as e^--H [45], e^--methane [46], H-$\bar{\text{H}}$ [47], e^+-H_2 [48], e^--Ps [49], e^+-He [50], and nucleon-nucleon scattering [51, 52]. The Kohn variational method and its variants suffer from well-known spurious singularities (see Section 3.5), so they are often used in conjunction with each other to identify these. To avoid cumbersome wording in this document, the Kohn variational method and variants of the method are simply referred to as "Kohn-type methods". Complex Kohn methods that use spherical Hankel functions instead of the spherical Bessel and Neumann functions are often used due to a smaller, but nonzero, chance of the Schwartz singulari-

ties [46, 53, 54]. This work uses the Kohn, inverse Kohn, generalized Kohn [55], S-matrix complex Kohn, and T-matrix complex Kohn variational methods.

1.4 Ps-H Scattering

For this work [5, 6, 7, 8, 9, 56], we have computed phase shifts for the first six partial waves of Ps-H scattering and resonance parameters for ^{1}S through ^{1}F (Chapters 5 to 7 and 9). We also calculate scattering lengths and effective ranges for ^{1,3}S (Section 11.1), scattering lengths for ^{1,3}P (Section 11.2), and multiple cross sections (Chapter 10). Each of these is compared to previously published research where possible.

This work is an extension of the earlier work on Ps-H collisions using the Kohn and inverse Kohn variational methods by Van Reeth and Humberston [57, 58]. In these papers, they calculated ^{1,3}S and ^{1,3}P phase shifts and obtained resonance parameters, scattering lengths and effective ranges from these. The most important difference from this earlier work is that we have increased the number of partial waves examined from two to six, requiring developing a general formalism and code that works for arbitrary partial waves. This allows us to calculate elastic integrated, elastic differential, and momentum transfer cross sections (Chapter 10), which would not be possible with only the ^{1,3}S- and ^{1,3}P-waves. We also develop a very general form (Chapter 3) of the scattering wavefunction and codes that allows us to calculate phase shifts with not only the Kohn and inverse Kohn variational methods but also with the generalized Kohn, S-matrix complex Kohn, T-matrix complex Kohn, generalized S-matrix complex Kohn, and generalized T-matrix complex Kohn variational methods. Over the previous work, we also perform a thorough analysis of the van der Waals contribution to the ^{1,3}S scattering lengths and effective ranges and investigate the ^{1,3}P scattering lengths (Section 11.1).

We have increased the number of short-range terms (Equation (3.9)) used over prior work [57, 58]. This is enabled by several changes. The largest improvement has been the introduction of the Todd method (Section 4.1.3), which selects the "best" set of short-range terms from the full set determined by ω in Equation (3.1). Some short-range terms contribute more to linear dependence than others, and this method removes those in a systematic manner. This is often an improvement over the restriction in powers that Van Reeth and Humberston [57] did, though we still use that restricted basis set for the ^{1,3}F-wave (Section 9.4). We also implement the asymptotic expansion [59, 60] for the short-range–short-range integrals instead of only doing a direction summation (Section 4.1.1.1). This gives much more accurate short-range–short-range integrals, allowing us to use more short-range terms and solve larger matrices in Equation (3.56). We specifically noted a threefold increase in the number of terms we could use for the ^{3}S state when the asymptotic expansion was included. We use approximately seven times as many integration points as this previous work (Appendix C.4.3). For $\ell \geq 1$ especially, an increase in the number of integration points for the long-range–long-range and long-range–short-range integrals (Section 4.2) lead to more stable results and the ability to use more short-range terms. For $\ell \geq 2$ (not investigated by the prior work), we also introduced extra expo-

nentials in several coordinates to the Gauss-Laguerre quadratures (Section 4.2.4) that are subsequently removed, increasing the convergence rate of the long-range–short-range integrals.

The Ps-H collision problem has been treated by multiple groups with different methods over the years. Our paper [56] also has discussion of the different methods used for low-energy Ps-H scattering. Various properties of this system have been calculated using the first Born approximation [61, 62], diffusion Monte Carlo (DMC) [63], the SVM [64, 65], CC [66, 67, 68, 69, 70, 71, 72], static exchange [73, 74, 75], Kohn variational [57, 58, 76], and inverse Kohn variational [57, 58] methods.

The CC method has been used in multiple papers for Ps-H scattering by the Belfast group. Campbell et al. [67] used 22 pseudostates and eigenstates of Ps with the ground state of H in an approximation they denote as 22Ps1H for singlet and triplet Ps-H scattering. Blackwood et al. [71] later included the e^+-H^- channel, using a 22Ps1H + H^- approximation, finding that it improved the convergence of the binding energy and allowed them to calculate resonance parameters for the ^{1}F-wave and ^{1}G-wave. In another paper by Blackwood [70], they use a 14Ps14H approximation with 14 Ps and 14 H pseudostates and eigenstates to compute ^{1,3}S phase shifts and a 9Ps9H approximation to compute ^{1,3}P and ^{1,3}D phase shifts, finding that this performed better than the earlier 22Ps1H calculation [67]. Walters et al. [72] also included the e^+-H^- channel in a 14Ps14H + H^- approximation for the ^{1}S-wave phase shifts and a 9Ps9H + H^- approximation for the ^{1}S-, ^{1}P, and ^{1}D-wave phase shifts and resonances through the ^{1}F-wave.

Page [76] calculated ^{1,3}S Ps-H scattering lengths using the Kohn variational method with 35 short-range terms. The Kohn/inverse Kohn variational methods [57, 58] have been used to calculate ^{1,3}S phase shifts, scattering lengths, and effective ranges, along with ^{1}S resonance parameters. The Kohn/inverse Kohn variational methods [58] have also been used to calculate ^{1,3}P phase shifts and parameters for the first ^{1}P resonance. The Kohn-type variational methods give empirical bounds on the phase shifts, and adding short-range terms to the wavefunction allows us to improve the phase shift convergence in a rigorous way. The Kohn-type methods can generate very accurate phase shifts, but the choice of trial wavefunction can make computation very difficult. Then there are the spurious Schwartz singularities, but these can often be mitigated by using complex Kohn methods.

1.5 Positronium Hydride

Positronium hydride (PsH) is a bound state comprised of a hydrogen atom and a positronium atom. After Wheeler [77] showed that positrons could be part of what he called a polyelectronic compound, Ore shortly thereafter predicted PsH in 1951 [78]. PsH was not experimentally verified until 1992 by Schrader [79] using the reaction $e^+ + CH_4 \rightarrow CH_3^+ +$ PsH.

We first investigated the bound state of PsH instead of Ps-H scattering, as it is a simpler problem and has been studied extensively in the literature (see Table 2.4 on page 15). The

purpose of first studying PsH was not to try to contribute more accurate results but to develop the experience with the short-range Hylleraas-type correlation terms that we used in both the ^{1}S PsH and ^{1}S Ps-H scattering problems. The full discussion of our work on PsH is found in Chapter 2. There are dozens of calculations of the ground state or binding energy of PsH given in Table 2.4. The binding energy of 1.066 406 eV compares well with the most accurate value from Ref. [80] of 1.066 598 eV, which gives confidence in the short-range part of the scattering wavefunction in Section 3.1.

1.6 Positronium Hydride Structure

There has been some discussion in the literature about whether PsH is more like an atomic structure or more like a molecule with Ps and H. We did not attempt an analysis of this problem, since the PsH system is not the goal of this work. Bressanini and Morosi [81] give a good overview of the lack of consensus on this problem.

Frolov and Smith [82] note that they expect PsH to be a cluster consisting of a Ps atom and an H atom. Then from their calculations, they conclude that it acts as some kind of sum of H^- with Ps^-.

Saito [83] attempted to answer this question using Ho's [84] Hylleraas basis set by plotting e^+ and e^- densities. Saito's conclusion was that PsH has an atomic structure but also has a diatomic molecular structure, or Ps with H. Bromley and Mitroy [85] also state that PsH has a molecular structure, comparing it "to a light isotope of the H_2 molecule."

Biswas and Darewych [86] find that the difference between the S(1) resonance and the binding energy (Section 2.3.1) for various calculations of differing accuracy is roughly constant. They suggest that this means that PsH is less like e^+ orbiting H^- and more like a diatomic molecule.

Bressanini and Morosi [81] perform calculations on PsH with a highly optimized one term wavefunction to determine the structure and conclude that PsH cannot be viewed as Ps+H or e^+ orbiting around H^-. They state, "Keeping in mind the quantum nature of the leptons and so the impossibility of defining a structure, we suggest to look at PsH as a hydrogen negative ion with the positron that, staying more distant from the nucleus than the electrons, correlates its motion with those of both the electrons. Its attraction on the electrons squeezes them nearer to each other and nearer to the nucleus."

Heyrovska [87] treats PsH as a molecule and calculates bond lengths to try to gain a better understanding of its structure. However, this preprint does not settle the debate.

1.7 Final Notes

Unless otherwise stated, values throughout are given in atomic units, i.e. $\hbar = m_e = e = 4\pi\epsilon_0 = 1$ [88]. Energies are given in hartrees, with $1\,E_h = 27.211\,385\,05(60)$ eV [89, 90]. Momentum is given as units of a_0^{-1}, where a_0 is the Bohr radius. Cross sections are given

in units of πa_0^2, and differential cross sections are given in units of a_0^2/sr, unless otherwise noted.

Some of the figures in this document are adapted from our paper submitted to Physical Review A [56]. Some figures are available as interactive plots on the plotly page at `http://plot.ly/~Denton`. Additional notes for derivations are available at `http://figshare.com/authors/Denton_Woods/581638`, and codes discussed are available at `https://github.com/DentonW/Ps-H-Scattering`. These notes and codes are also linked at `http://www.dentonwoods.com` and on the Research Wiki [4].

2

Positronium Hydride and Short-Range Terms

As discussed in Section 1.5, PsH consists of one atom of both Ps and of H. Figure 2.1 shows the PsH coordinate system. There are 6 interparticle coordinates, given by r_1, r_2, r_3, r_{12}, r_{13}, and r_{23}. The proton is considered infinitely heavy in this treatment. Armour et al. [91] point out that positronium antihydride is an equivalent system, assuming CPT symmetry. Another related system is e^+PsH, which is stable and can be thought of as e^+ orbiting around PsH [91].

2.1 PsH Wavefunction

The wavefunction we use for the bound state has a Hylleraas-style [57, 92] set of terms, given by

$$\Psi^{\pm} = \sum_{i=1}^{N(\omega)} c_i \bar{\phi}_i^{\pm} \tag{2.1a}$$

$$\bar{\phi}_i^{\pm} = (1 \pm P_{23})\phi_i \tag{2.1b}$$

$$\phi_i = e^{-(\alpha r_1 + \beta r_2 + \gamma r_3)} r_1^{k_i} r_2^{l_i} r_{12}^{m_i} r_3^{n_i} r_{13}^{p_i} r_{23}^{q_i}, \tag{2.1c}$$

where the plus sign indicates the spatially symmetric singlet case, and the minus sign indicates the spatially antisymmetric triplet case. The permutation operator P_{23} is needed, as the two electrons are indistinguishable. The $\frac{1}{\sqrt{2}}$ needed to normalize $\Psi^{\pm}$ (to cancel out the 2 in Equation (2.14)) is absorbed into the c_i constant in Equation (2.1a). The constant $Y_0^0(\theta, \phi) = \frac{1}{\sqrt{4\pi}}$ is also absorbed into c_i. The Hylleraas-type basis set satisfies the Kato cusp condition [93] well [55].

The variable ω is an integer ≥ 0 that determines the number of terms in the basis set. For a chosen value of ω, the integer powers of r_i and r_{ij} are constructed in such a way that [57]

$$k_i + l_i + m_i + n_i + p_i + q_i \leq \omega, \tag{2.2}$$

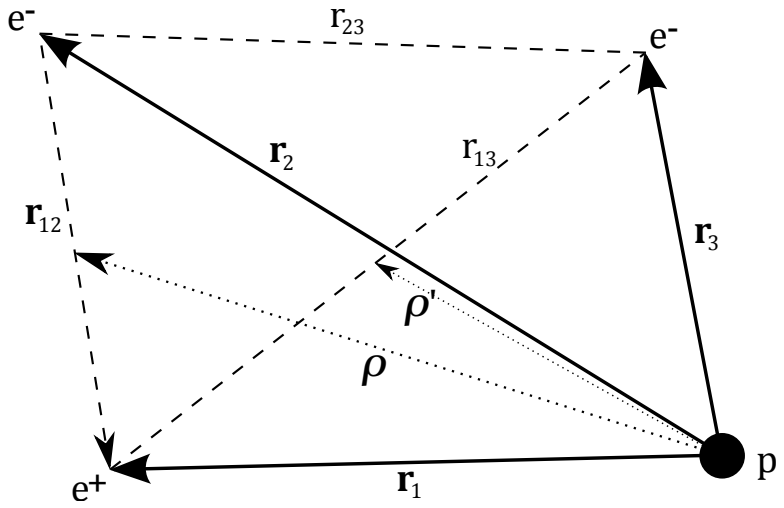

Figure 2.1: Positronium hydride coordinate system

with all k_i, l_i, m_i, n_i, q_i and $p_i \geq 0$. Using combination with repetition, an explicit formula for $N(\omega)$ is given as

$$N(\omega) = \binom{\omega + 6}{6}, \tag{2.3}$$

where the 6 comes from the 6 coordinates of r_i and r_{ij}. A plot of $N(\omega)$ versus ω is given in Figure 2.2.

2.2 Rayleigh-Ritz Variational Method

The Rayleigh-Ritz variational method is given as the functional [43]

$$E[\Psi] = \frac{\langle \Psi \,|\, H \,|\, \Psi \rangle}{\langle \Psi \,|\, \Psi \rangle}. \tag{2.4}$$

This provides an upper bound to the ground-state energy, E_0. In other words,

$$E_0 \leq E[\Psi]. \tag{2.5}$$

Equation (2.4) can be rewritten in matrix notation as a generalized eigenvalue problem [94]

$$\mathbf{Hc} = E\mathbf{Sc}, \tag{2.6}$$

where

$$H_{ij} = \langle \bar{\phi}_i \,|H|\, \bar{\phi}_j \rangle,\ S_{ij} = \langle \bar{\phi}_i \,|\, \bar{\phi}_j \rangle, \tag{2.7}$$

and $\mathbf{c}$ is the vector of coefficients for the wavefunction Ψ. The normalization here is unimportant due to the division in Equation (2.4) and the form of Equation (2.6).

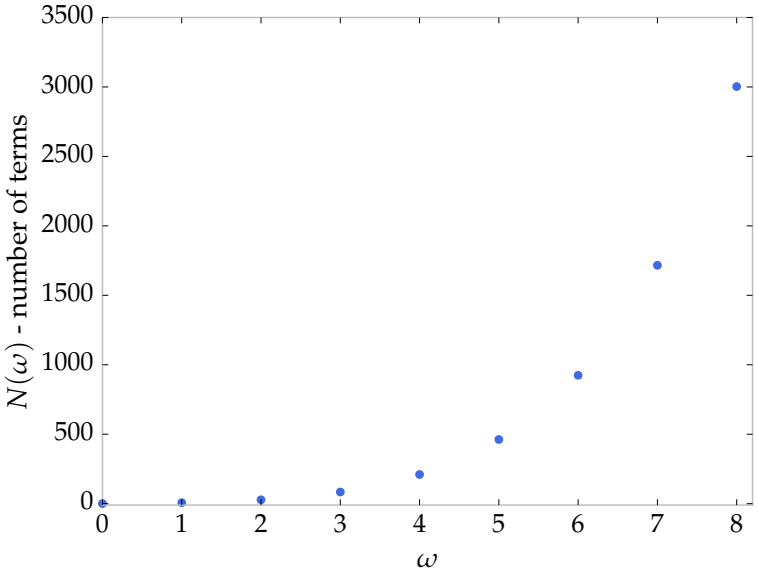

Figure 2.2: $N(\omega)$ versus ω

For PsH, the non-relativistic Hamiltonian is

$$H = -\frac{1}{2}\nabla_{r_1}^2 - \frac{1}{2}\nabla_{r_2}^2 - \frac{1}{2}\nabla_{r_3}^2 + \frac{1}{r_1} - \frac{1}{r_2} - \frac{1}{r_3} - \frac{1}{r_{12}} - \frac{1}{r_{13}} + \frac{1}{r_{23}}. \tag{2.8}$$

The Laplacians in Equation (2.8) are complicated when applied to the ϕ_j function. We exploit the short-range nature of ϕ_i and ϕ_j by using integration by parts, similar to equation (3.21) of Armour and Humberston [55].

$$-\int \phi_i \left(\nabla_{r_1}^2 + \nabla_{r_2}^2 + \nabla_{r_3}^2\right) \phi_j \, d\tau = \int \sum_{l=1}^{3} \boldsymbol{\nabla}_{\boldsymbol{r}_l} \phi_i \cdot \boldsymbol{\nabla}_{\boldsymbol{r}_l} \phi_j \, d\tau \tag{2.9}$$

The differential $d\tau$ represents the 9-dimensional configuration space given by r_1, r_2, and r_3 (see Appendix A). This expression is simpler than applying the Laplacian operators directly to ϕ_j, and the summation is given by the following expression (a full derivation is given on the research Wiki [4]):

$$\begin{aligned}
\sum_{l=1}^{3} \boldsymbol{\nabla}_{\mathbf{r}_l} \phi_i \cdot \boldsymbol{\nabla}_{\mathbf{r}_l} \phi_j = \phi_i \phi_j \Bigg\{ & (\alpha^2 + \beta^2 + \gamma^2) - \frac{\alpha}{r_1}(k_i + k_j) - \frac{\beta}{r_2}(l_i + l_j) + \frac{\gamma}{r_3}(n_i + n_j) \\
& + \frac{k_i k_j}{r_1^2} + \frac{l_i l_j}{r_2^2} + \frac{n_i n_j}{r_3^2} + \frac{2m_i m_j}{r_{12}^2} + \frac{2p_i p_j}{r_{13}^2} + \frac{2q_i q_j}{r_{23}^2} \\
& + \frac{r_1^2 + r_{12}^2 - r_2^2}{2r_1^2 r_{12}^2} \left[-\alpha r_1 (m_i + m_j) + (k_i m_j + k_j m_i)\right] \\
& + \frac{r_1^2 + r_{13}^2 - r_3^2}{2r_1^2 r_{13}^2} \left[-\alpha r_1 (p_i + p_j) + (k_i p_j + k_j p_i)\right]
\end{aligned}$$

$$
\begin{aligned}
&+ \frac{r_{12}^2 + r_{13}^2 - r_{23}^2}{2r_{12}^2 r_{13}^2} \left[m_i p_j + m_j p_i \right] \\
&+ \frac{r_2^2 + r_{12}^2 - r_1^2}{2r_2^2 r_{12}^2} \left[-\beta r_2 (m_i + m_j) + (m_i l_j + m_j l_i) \right] \\
&+ \frac{r_2^2 + r_{23}^2 - r_3^2}{2r_2^2 r_{23}^2} \left[-\beta r_2 (q_i + q_j) + (l_i q_j + l_j q_i) \right] \\
&+ \frac{r_{12}^2 + r_{23}^2 - r_{13}^2}{2r_{12}^2 r_{23}^2} \left[m_i q_j + m_j q_i \right] \\
&+ \frac{r_3^2 + r_{13}^2 - r_1^2}{2r_3^2 r_{13}^2} \left[-\gamma r_3 (p_i + p_j) + (n_i p_j + n_j p_i) \right] \\
&+ \frac{r_3^2 + r_{23}^2 - r_2^2}{2r_3^2 r_{23}^2} \left[-\gamma r_3 (q_i + q_j) + (n_i q_j + n_j q_i) \right] \\
&+ \frac{r_{13}^2 + r_{23}^2 - r_{12}^2}{2r_{13}^2 r_{23}^2} \left[p_i q_j + p_j q_i \right] \Bigg\}. \qquad (2.10)
\end{aligned}
$$

This is similar to the forms given in Refs. [55, 95]. The S-wave code also has an alternate formalism using the Laplacian, as given in Ref. [60].

The full expression for H_{ij} from Equation (2.7) for real-valued ϕ after using Equations (2.8) and (2.9) is then

$$
\left\langle \bar{\phi}_i \left| H \right| \bar{\phi}_j \right\rangle = \int \left[\frac{1}{2} \sum_{l=1}^{3} \boldsymbol{\nabla}_{\mathbf{r}_l} \bar{\phi}_i \cdot \boldsymbol{\nabla}_{\mathbf{r}_l} \bar{\phi}_j + \left(\frac{1}{r_1} - \frac{1}{r_2} - \frac{1}{r_3} - \frac{1}{r_{12}} - \frac{1}{r_{13}} + \frac{1}{r_{23}} \right) \bar{\phi}_i \bar{\phi}_j \right] d\tau. \qquad (2.11)
$$

To reduce the number of integrations needed by half, we use a property of the permutation operator. Since

$$
\left\langle \phi_i \left| H \right| \phi_j \right\rangle = \left\langle P_{23} \phi_i \left| H \right| P_{23} \phi_j \right\rangle \qquad (2.12)
$$

and

$$
\left\langle \phi_i \left| H \right| P_{23} \phi_j \right\rangle = \left\langle P_{23} \phi_i \left| H \right| \phi_j \right\rangle, \qquad (2.13)
$$

Equation (2.11) becomes

$$
\begin{aligned}
\left\langle (1 \pm P_{23}) \phi_i \left| H \right| (1 \pm P_{23}) \phi_j \right\rangle =& \left\langle \phi_i \left| H \right| \phi_j \right\rangle \pm \left\langle P_{23} \phi_i \left| H \right| \phi_j \right\rangle \\
& \pm \left\langle \phi_i \left| H \right| P_{23} \phi_j \right\rangle + \left\langle P_{23} \phi_i \left| H \right| P_{23} \phi_j \right\rangle \qquad (2.14a) \\
=& 2 \left[\left\langle \phi_i \left| H \right| \phi_j \right\rangle \pm \left\langle P_{23} \phi_i \left| H \right| \phi_j \right\rangle \right] \qquad (2.14b) \\
=& 2 \left[\left\langle \phi_i \left| H \right| \phi_j \right\rangle \pm \left\langle \phi_i \left| H \right| P_{23} \phi_j \right\rangle \right]. \qquad (2.14c)
\end{aligned}
$$

ω	Terms	α	β	γ	Total Energy (a.u.)	Binding Energy (eV)	ΔE (a.u.)
0	1	0.60	0.60	1.00	−0.541 492 378 889	—	—
1	7	0.60	0.60	1.00	−0.744 334 244 165	—	0·202841865276
2	28	0.60	0.60	1.00	−0.778 357 106 972	0.771 636 156 726	0·034022862807
3	84	0.60	0.60	1.00	−0.786 807 448 395	1.001 581 651 009	0·008450341423
4	210	0.60	0.60	1.00	−0.788 685 563 109	1.052 687 753 648	0·001878114714
5	462	0.60	0.60	1.00	−0.789 082 645 582	1.063 492 917 716	0·000397082473
6	916	0.60	0.60	1.00	−0.789 169 509 836	1.065 856 614 384	0·000086864254
7	1585	0.60	0.60	1.00	−0.789 189 568 390	1.066 402 435 425	0·000020058554
8	1925	0.60	0.60	1.00	−0.789 194 559 324	1.066 538 245 640	0·000004990934
9	2166	0.60	0.60	1.00	−0.789 195 830 870	1.066 572 846 182	0·000001271546
10	2205	0.60	0.60	1.00	−0.789 196 323 586	1.066 586 253 647	0·000000492716
11	1674	0.58	0.60	1.00	−0.789 196 284 600	1.066 585 192 793	−0·000000038986

Table 2.1: Ground state energy of PsH

2.3 Results

The binding energy (also known as the dissociation energy) is given by Ref. [96] as

$$E_d = -E_1 - \frac{3}{4} \text{ a.u.} \tag{2.15}$$

The $-\frac{3}{4}$ comes from adding the ground state energies of Ps and H. If the PsH system has a lower energy than $-\frac{3}{4}$, the system is bound. Using the accurate Bubin and Adamowicz energy in Table 2.4, this gives that ^{1}S PsH is stable against dissociation into Ps and H by 0.039 196 765 251 au or 1.066 598 271 959 eV.

2.3.1 Bound State: Singlet

The original double precision PsH code was run for a simple choice of the nonlinear parameters α, β and γ. During these initial runs, LAPACK returned valid energies through $\omega = 5$. With the $\omega = 6$ runs, it had trouble using the full 924 terms, with `dsygv` giving an error. Using Todd's algorithm (Section 4.1.3), this code returned a usable 916 terms for $\omega = 6$, as given in Table 2.1. The original code worked well through $\omega = 10$, but going from $\omega = 9$ to $\omega = 10$ only added an additional 39 terms. The run for $\omega = 11$ was obviously a problem, since it gave less terms than $\omega = 10$ and a higher energy, even when changing the α parameter slightly.

ω	Terms	α	β	γ	Total Energy (a.u.)	Binding Energy (eV)	ΔE (a.u.)
0	1	0.586	0.580	1.093	-0.558 977 058 051	—	—
1	7	0.586	0.580	1.093	-0.744 698 936 920	—	0.185 721 878 869
2	28	0.586	0.580	1.093	-0.778 246 602 473	0.768 629 176 247	0.033 547 665 553
3	84	0.586	0.580	1.093	-0.786 743 703 126	0.999 847 053 924	0.008 497 100 653
4	210	0.586	0.580	1.093	-0.788 672 801 036	1.052 340 479 962	0.001 929 097 910
5	462	0.586	0.580	1.093	-0.789 082 645 582	1.063 460 197 197	0.000 409 844 546
6	924	0.586	0.580	1.093	-0.789 169 509 836	1.065 861 354 038	0.000 086 864 254
7	1716	0.586	0.580	1.093	-0.789 189 730 694	1.066 406 851 931	0.000 020 220 858

Table 2.2: Ground state energy of ^{1}S PsH with full set of terms and original ordering

ω	Terms	α	β	γ	Total Energy (a.u.)	Binding Energy (eV)	ΔE (a.u.)
0	1	0.586	0.580	1.093	-0.558 977 058 051	—	—
1	5	0.586	0.580	1.093	-0.718 445 865 883	—	0.159 468 807 832
2	25	0.586	0.580	1.093	-0.776 355 701 568	0.717 175 143 631	0.057 909 835 685
3	77	0.586	0.580	1.093	-0.786 645 720 870	0.997 180 821 018	0.010 290 019 302
4	199	0.586	0.580	1.093	-0.788 665 304 510	1.052 136 489 091	0.002 019 583 640
5	436	0.586	0.580	1.093	-0.789 080 739 334	1.063 441 046 057	0.000 415 434 824
6	856	0.586	0.580	1.093	-0.789 169 644 174	1.065 860 269 913	0.000 088 904 841
7	1505	0.586	0.580	1.093	-0.789 189 725 050	1.066 406 698 333	0.000 020 080 875

Table 2.3: Ground state energy of ^{1}S PsH with Todd set of terms and original ordering

The next and current version of the code uses quadruple precision and is able to do full runs through $\omega = 8$ without omitting terms (not shown in Table 2.2). Linear dependence is also decreased when the nonlinear parameters are different (Appendix C.1 for parameter optimization). The Ps-H scattering problem (Chapter 5) is more difficult, so a run with $\omega = 7$ is all that is needed. Table 2.2 shows the PsH energies through $\omega = 7$ for the full set of terms described by Equation (2.2).

As described later in Section 4.3, we cannot use the full 1716 terms for the Ps-H scattering problem. Table 2.3 gives the ground state energies using the restricted set of terms using Todd's method with the original ordering. The cutoffs in ω are easily seen using the ViewOmegaCutoffs.py script (Appendix D).

Group / Method	Terms	Total Energy (au)	Binding Energy (eV)
Current work / Variational Hylleraas ($\omega = 7$)	1505	-0.789 189 725	1.066 406 705
Frolov (2010) [97] / Semi-exponential	84	-0.788 516 419⋆	1.048 085 11
Bubin (2006) [80] / ECGs variational	5000	-0.789 196 765 251⋆	1.066 598 271 959
Bubin (2006) [80] / ECGs variational[a]	5000	-0.788 870 710 444⋆	1.057 725 869 06
Mitroy (2006) [98] / ECGs with SVM	1800	-0.789 196 740⋆	1.066 597 58
Chiesa (2004) [99] / Quantum Monte Carlo	—	-0.784 620⋆	0.942 058
Bubin (2004) [100] / ECGs[a]	3200	-0.788 870 706 6⋆	1.057 725 764
Van Reeth (2003) [57] / Variational Hylleraas ($\omega = 6$)	721	-0.789 156	1.065 5⋆
Bressanini (2003) [81] / Variational Monte Carlo	1	-0.786 073⋆	0.981 596
Saito (2003) [101] / CI	13230	-0.786 793⋆	1.001 19
Bromley (2001) [85] / CI	95324	-0.786 776 1⋆	1.000 729
Saito (2000) [83] / Hylleraas	396	-0.788 951⋆	1.059 91
Bromley (2000) [102] / CI	—	-0.784 301 8⋆	0.933 399 5
Yan (1999) [92] / Variational Hylleraas ($\omega = 12$)	5741	-0.789 196 705 1⋆	1.066 596 635
Yan (1999) [92] / Variational Hylleraas ($\omega \to \infty$)	—	-0.789 196 714 7⋆	1.066 596 896
Yan (1999) [103] / Variational Hylleraas[a]	4705	-0.788 853 107⋆	1.057 246 85
Ryzhikh (1999) [104] / ECGs	750	-0.789 196 0⋆	1.066 577
Adhikari (1999) [68] / Five-state CC	—	-0.788 6	1.05⋆
Mella (1999) [105] / DMC	—	-0.789 15⋆	1.065 3
Ryzhikh (1998) [106] / ECGs with SVM	500	-0.789 194 4⋆	1.066 534
Strasburger (1998) [107] / ECGs	332	-0.789 185⋆	1.066 278
Bressanini (1998) [108] / DMC	—	-0.789 175⋆	1.066 01
Jiang (1998) [109] / DMC	—	-0.789 18⋆	1.066 1
Jiang (1998) [109] / Variational Monte Carlo	1	-0.777 4⋆	0.745 6
Le Sech (1998) [110] / Variational Monte Carlo	1	-0.772 3⋆	0.606 8
Usukura (1998) [111] / ECGs with SVM	1600	-0.789 196 553 6⋆	1.066 592 513
Frolov (1997) [112] / James-Coolidge variational	924	-0.789 136 9⋆	1.064 969
Frolov (1997) [112] / James-Coolidge variational	—	-0.789 181 8⋆	1.066 191
Frolov (1997) [82] / Kolesnikov-Tarasov variational	—	-0.789 179 4⋆	1.066 126
Frolov (1997) [82] / Kolesnikov-Tarasov variational[a]	—	-0.788 853 4⋆	1.057 254
Ryzhikh (1997) [113] / SVM	400	-0.789 183⋆	1.066 22
Yoshida (1996) [114] / DMC	—	-0.789 1⋆	1.06⋆

Continued on next page

Table 2.4: Positronium hydride energy values. Starred values are the reported values. Unstarred values are obtained by using the conversion factor given in Section 1.7. Results marked by [a] take into account the finite mass correction.

Group / Method	Terms	Dissociation Energy (au)	Binding Energy (eV)
Saito (1995) [115] / Hylleraas	—	-0.774 71⋆	0.672 39
Saito (1995) [116] / Restricted Hartree-Fock	—	-0.776	0.70⋆
Strasburger (1995) [117] / CI	—	-0.763 7⋆	0.372 8
Strasburger (1995) [117] / SCF	—	-0.666 9⋆	-2.261
Schrader (1992) [79] / Experiment	—	-0.790	1.1 ± 0.2
Ho (1986) [84] / Variational with Hylleraas	396	-0.788 945⋆	1.059 75
Maruyama (1985) [101, 118] / Hylleraas	—	-0.788 211⋆	1.039 77
Ho (1978) [119] / Variational with Hylleraas	210	-0.787 525⋆	1.021 12⋆
Clary (1976) [120] / Variational	67	-0.784 161⋆	0.929 568
Page (1974) [96] / Variational	70	-0.786 79⋆	1.00 11
Navin (1974) [121] / Variational	17	-0.779 2⋆	0.794 6
Houston (1973) [122] / Variational	56	-0.774 7⋆	0.672 5
Lebeda (1969) [123] / Variational	12	-0.774 2⋆	0.658 5
Ludwig (1966) [124] / Configuration interaction	9	-0.759 0⋆	0.244 9
Goldanskii (1964) [120, 125] / —	—	-0.667 7⋆	-2.2395
Neamtan (1962) [126] / Variational exponential	2	-0.758 4⋆	0.228 6
Ore (1951) [78] / Variational exponential	2	-0.752 51⋆	0.068 301
Walters (2004) [72] / CC 14Ps14H + H^-	—	-0.787 9	1.03⋆
Walters (2004) [72] / CC 9Ps9H + H^-	—	-0.787 5	1.02⋆
Blackwood (2002) [70] / CC 14Ps14H	—	-0.786 5	0.994⋆
Blackwood (2002) [70] / CC 9Ps9H	—	-0.785 4	0.963⋆
Blackwood (2002) [71] / CC 22Ps1H + H^-	—	-0.781 2	0.850⋆
Campbell (1998) [67] / CC 22Ps1H	—	-0.773 3	0.634⋆

Table 2.4: Continued from previous page. Positronium hydride energy values. Starred values are the reported values. Unstarred values are obtained by using the conversion factor given in Section 1.7. Results marked by ^{a} take into account the finite mass correction.

There have been a large number of calculations of the PsH binding energy over the years, starting with Ore's prediction in 1951 that PsH could exist [78]. As computing power increased, using a Hylleraas-type basis set with hundreds or even thousands of terms became possible [57, 84, 92, 119]. The Hylleraas-type results were the most accurate until very accurate ECG results from Mitroy [98] and Bubin and Adamowicz [80, 100]. The ECGs do not satisfy the Kato cusp condition [93], but good optimization of the basis set can give good results [127].

Another paper by Frolov [97] is more of an introduction of a modified basis set to this problem, showing how only 84 terms gives a better energy than a much larger Hylleraas set. Yan and Ho [92] use a Hylleraas basis set with 5 sectors that each have different nonlinear parameters. Frolov's work essentially uses the same basis set but gives each term its own set of nonlinear parameters, optimizing all of them simultaneously.

The last six entries of this table give the CC results of the Belfast group. These are grouped together to show how different states and pseudostates in the CC calculations can give better approximations to the binding energy. It is particularly clear that adding the H^- channel vastly improves the accuracy.

The Hylleraas binding energy from our work in the first line of the table compares well with the accurate energies of Refs. [80, 92, 98], but it is not as accurate of a calculation. The purpose of doing the PsH calculation was not to get the best result but to test how well the short- range terms for Ps-H scattering represent the short-range interactions. Based on Table 2.4, the short-range interactions are described well. This also gave experience working with the Hylleraas basis set, and finding the PsH energy is a simpler problem than Ps-H scattering.

2.3.2 Triplet Energy Eigenvalues

Our code does not predict a triplet bound state. Mitroy and Bromley have published a paper [128] claiming a stable triplet bound state, but our code does not have the appropriate type of wavefunction to see this, since it is for a H($2p$) + Ps($2p$) state. They also use a very large configuration interaction basis, and this bound state is very shallow.

Despite not predicting a bound state, we run the energy eigenvalue code for the triplet so that we can use this for the short-range terms for the scattering programs. The triplet case was more sensitive to the accuracy of the matrix elements. Changing the energy eigenvalue code to quadruple precision let us use more short-range terms in our calculations.

Similar to the singlet, we cannot use the full 1716 terms for the Ps-H scattering problem. Table 2.6 gives the energy eigenvalues using the restricted set of terms using Todd's method with original ordering.

2.4 Stabilization

Hazi and Taylor [129] introduced the concept of stabilization plots to PsH bound state calculations. Specifically, they plotted the four lowest eigenvalues with respect to N and looked for avoided crossings. A resonance only exists if there is an avoided crossing between eigenvalues. The avoided crossing that they found at 0.428 985 a u (or 5.8366 eV as shown in Table 5.3) corresponds roughly with the first ^{1}S resonance. Van Reeth and Humberston [58] also did an analysis of stabilized eigenvalues but with the same type of

ω	Terms	α	β	γ	Total Energy (a.u.)	ΔE (a.u.)
0	1	0.323	0.334	0.975	-0.500 031 146 247	—
1	7	0.323	0.334	0.975	-0.623 725 636 031	0.123 694 489 784
2	28	0.323	0.334	0.975	-0.679 176 805 541	0.055 451 169 510
3	84	0.323	0.334	0.975	-0.710 407 818 871	0.031 231 013 330
4	210	0.323	0.334	0.975	-0.727 102 619 903	0.016 694 801 032
5	462	0.323	0.334	0.975	-0.735 860 693 040	0.008 758 073 137
6	924	0.323	0.334	0.975	-0.740 622 381 908	0.004 761 688 868
7	1716	0.323	0.334	0.975	-0.743 386 825 704	0.002 764 443 796

Table 2.5: Eigenvalues of ^{3}S with full set of terms and original ordering

ω	Terms	α	β	γ	Total Energy (a.u.)	ΔE (a.u.)
0	1	0.323	0.334	0.975	-0.500 031 146 247	—
1	7	0.323	0.334	0.975	-0.623 725 636 031	0.123 694 489 784
2	27	0.323	0.334	0.975	-0.679 173 632 477	0.055 447 996 446
3	81	0.323	0.334	0.975	-0.710 405 860 558	0.031 232 228 081
4	201	0.323	0.334	0.975	-0.727 100 988 826	0.016 695 128 267
5	432	0.323	0.334	0.975	-0.735 860 470 972	0.008 759 482 146
6	854	0.323	0.334	0.975	-0.740 622 201 811	0.004 761 730 840
7	1633	0.323	0.334	0.975	-0.743 386 893 723	0.002 764 691 911

Table 2.6: Eigenvalues of ^{3}S with Todd set of terms and original ordering

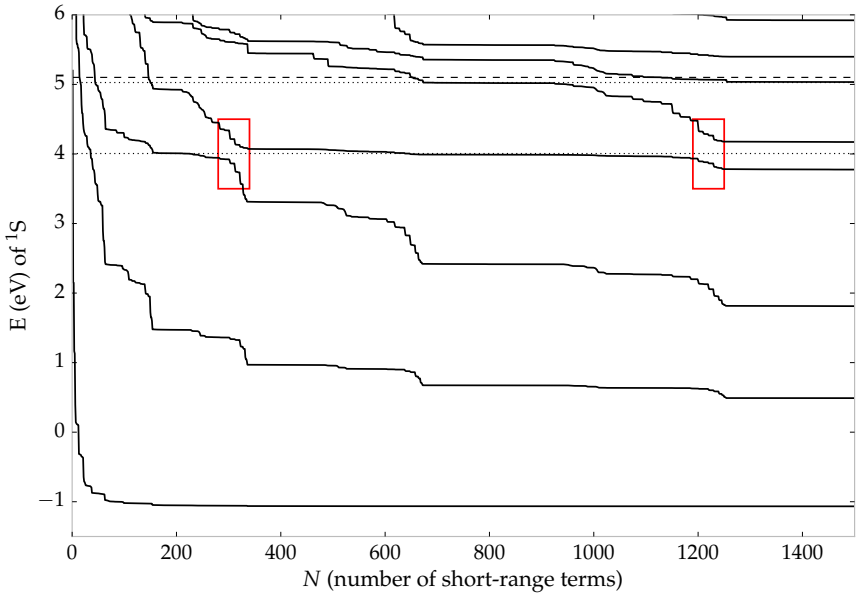

Figure 2.3: ^{1}S eigenvalues. The dashed line represents the Ps(n=2) threshold. Dotted lines represent complex Kohn ^{1}S resonance positions. The red rectangles are potential avoided crossings.

basis set that we use.

Plotting the first 10 eigenvalues with respect to N for ^{1}S gives Figure 2.3. As noted, the dashed line represents the Ps(n=2) inelastic threshold at 5.102 eV. The dotted lines correspond to the first two complex Kohn ^{1}S resonance positions given in Table 5.3. The wavefunction we use is not optimized for this type of analysis, but there is evidence of avoided crossings given by the red rectangles in Figure 2.3. The position of the plateau in between these rectangles corresponds relatively well with the first resonance position, ^1E_R, we find in Table 5.3 from the full scattering calculations in Chapter 5. The line for the second resonance lines up with the 5th eigenvalue from roughly 700 to 900 terms and with the 6th eigenvalue starting at about 1250 terms. The estimates of the two resonance positions are 3.99 eV and 5.03 eV.

Van Reeth and Humberston [58] had difficulty doing the same type of stabilization with these Hylleraas-type terms. Other wavefunctions or stabilization methods may work better for this system. For instance, Yan and Ho [130] vary a scaling factor and plot the eigenvalue energies with respect to this.

Figure 2.4 shows the same type of stabilization plot for ^{3}S. It is clear that below the Ps(n=2) threshold, there are no avoided crossings, meaning that there are no resonances in the S-wave triplet for this energy range.

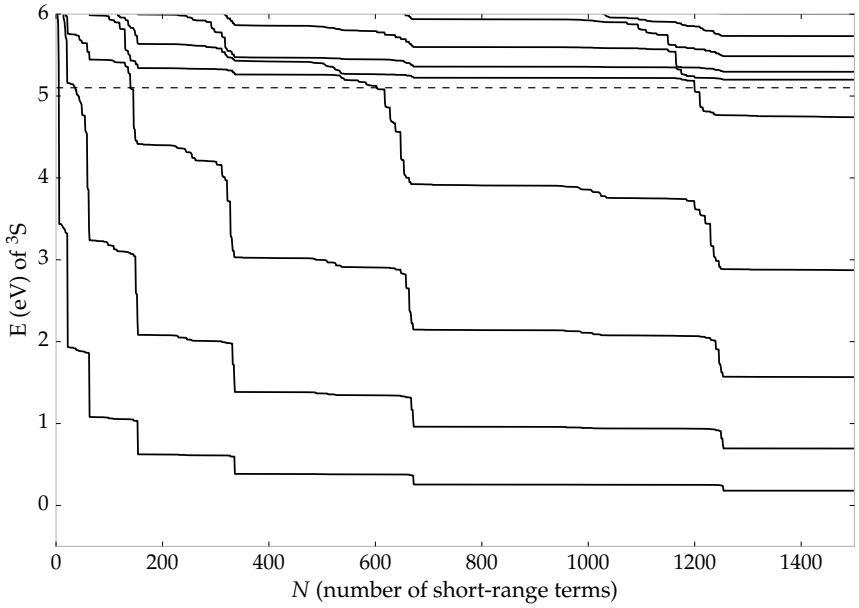

Figure 2.4: ^{3}S eigenvalues. The dashed line represents the Ps(n=2) threshold.

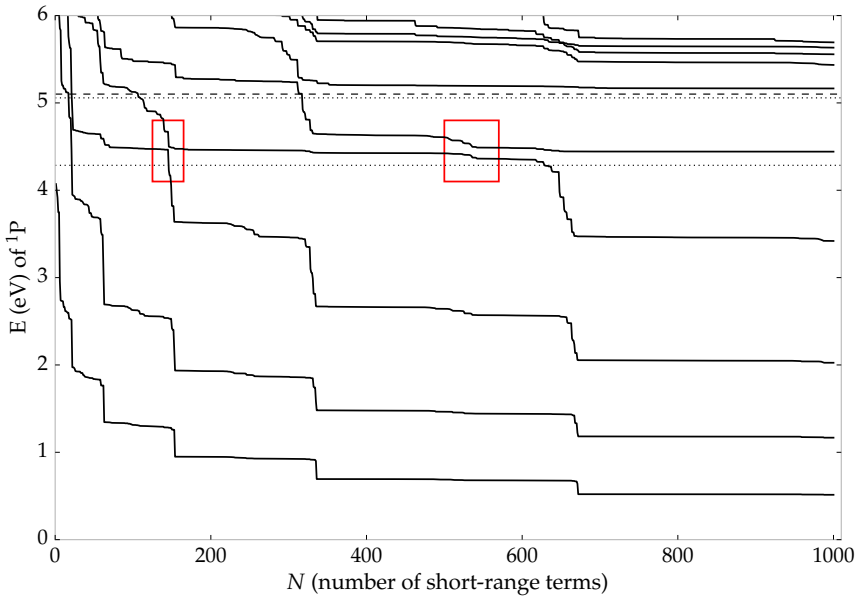

Figure 2.5: ^{1}P eigenvalues for first symmetry only. The dashed line represents the Ps(n=2) threshold. Dotted lines represent complex Kohn ^{1}P resonance positions.

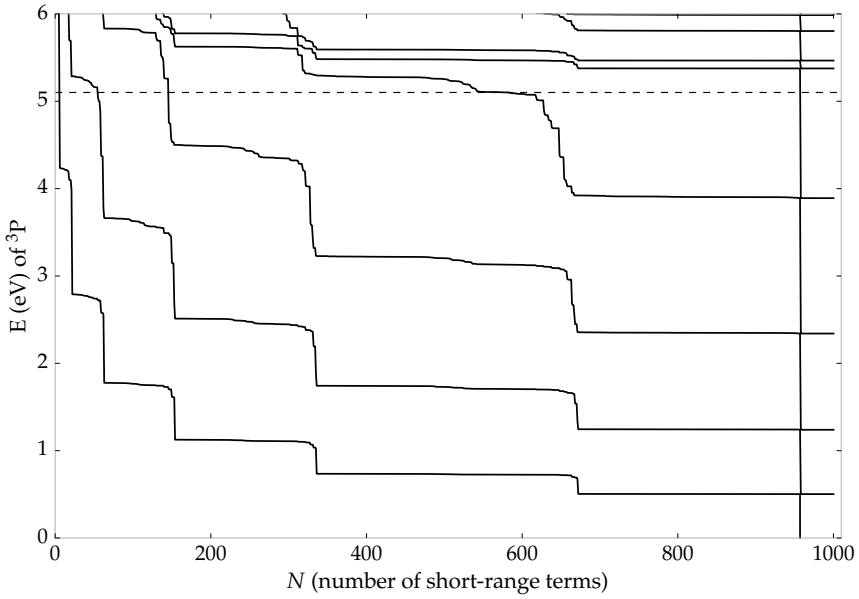

Figure 2.6: ^{3}P eigenvalues for first symmetry only. The dashed line represents the Ps(n=2) threshold.

Figures 2.5 and 2.6 show the stabilization plots for the P-wave eigenvalues when only the first symmetry (see Section 6.1) is evaluated. In Figure 2.6, linear dependence becomes a problem at 957 terms; hence there is an extra eigenvalue below zero, which is not actually indicative of a bound state.

In Figure 2.5, there is evidence of avoided crossings for the first resonance marked by the red rectangles. The second avoided crossing is barely noticeable. Taking the fifth eigenvalue at 800 terms gives 4.44 eV, which is not very much in line with the accurate calculations shown in Table 6.3, including the complex Kohn. The second resonance is above the Ps(n=2) threshold here, making it physically different from the actual resonance.

Figures 2.7 and 2.8 are also for the P-wave, but they use both the first and second symmetries paired. So each term number given on the x-axis is actually two terms, i.e. $N = 200$ is a total of 400 short-range terms, 200 of the first symmetry and 200 of the second symmetry.

In Figure 2.7, the first resonance position lines up relatively well with the full scattering calculations. The second resonance is a narrow resonance, and there is an avoided crossing enclosed in the dashed blue rectangle. The approximate position of the resonances are taken as the fifth and sixth eigenvalues at 1000 terms, which are tabulated in Table 2.7 and

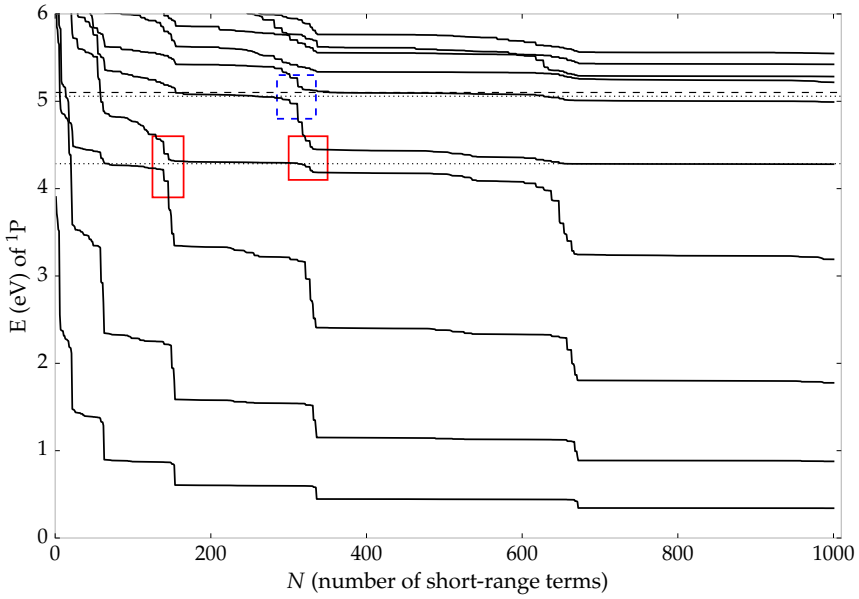

Figure 2.7: ^{1}P eigenvalues for both symmetries. The dashed line represents the Ps(n=2) threshold. Dotted horizontal lines represent complex Kohn ^{1}P resonance positions. The approximate avoided crossings are denoted by rectangles.

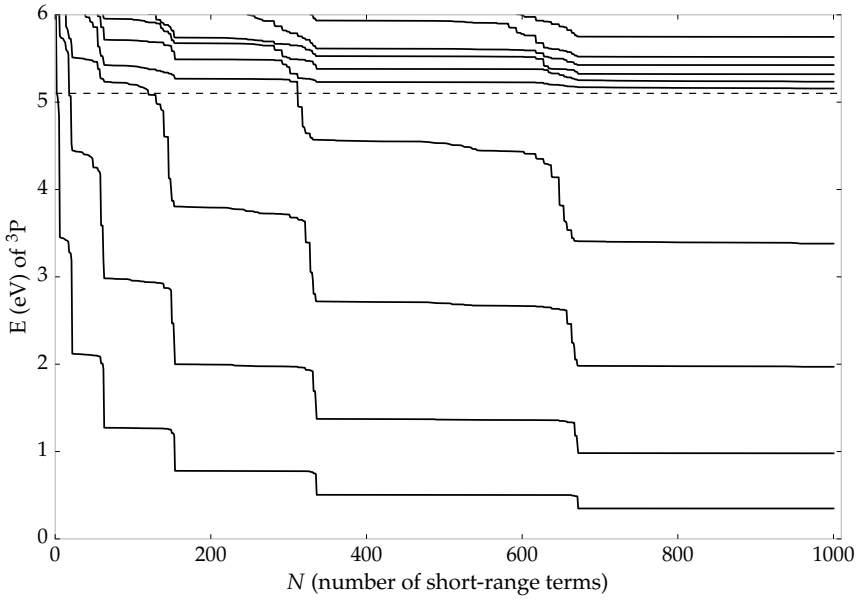

Figure 2.8: ^{3}P eigenvalues for both symmetries. The dashed line represents the Ps(n=2) threshold.

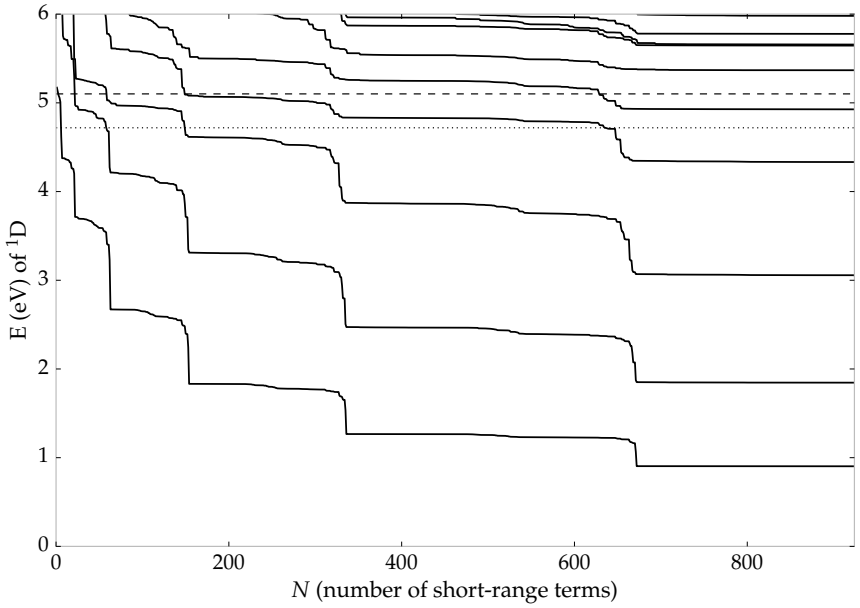

Figure 2.9: ^{1}D eigenvalues for first symmetry only. The dashed line represents the Ps(n=2) threshold. The dotted line represents the complex Kohn ^{1}D resonance position.

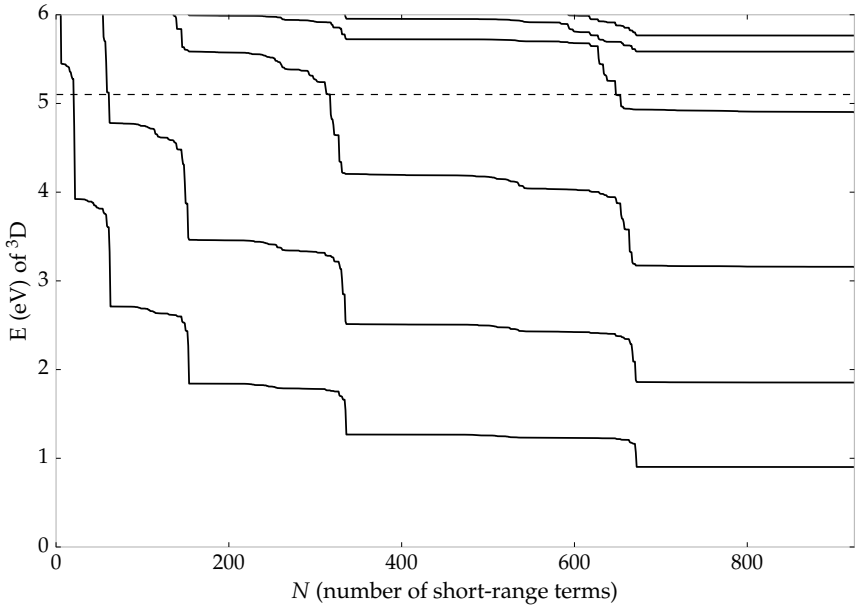

Figure 2.10: ^{3}D eigenvalues for first symmetry only. The dashed line represents the Ps(n=2) threshold.

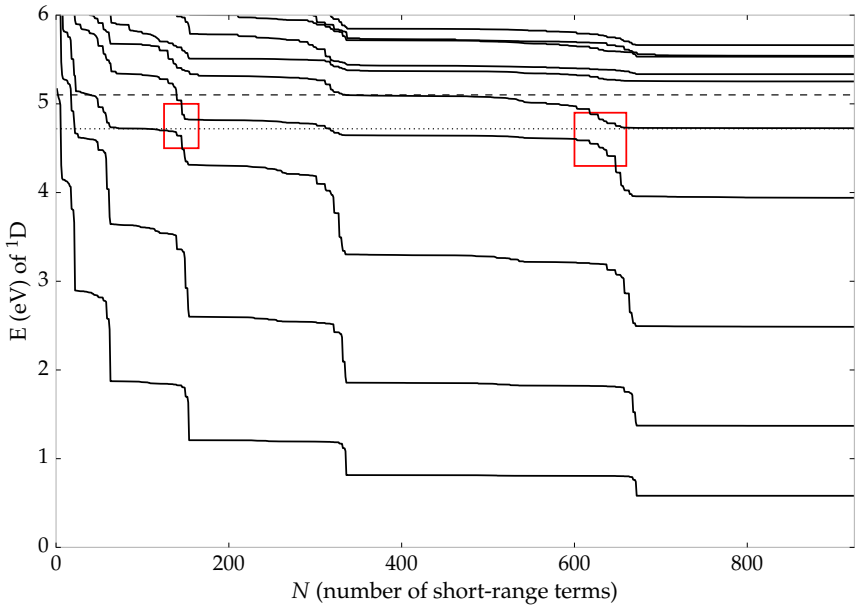

Figure 2.11: ^{1}D eigenvalues for both symmetries. The dashed line represents the Ps(n=2) threshold. The dotted line represents the complex Kohn ^{1}D resonance position.

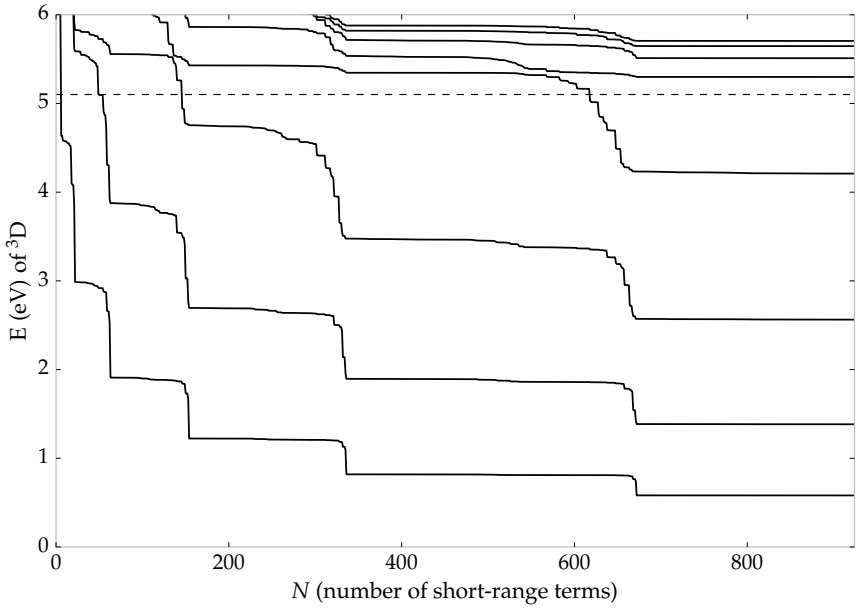

Figure 2.12: ^{3}D eigenvalues for both symmetries. The dashed line represents the Ps(n=2) threshold.

Partial wave	${}^1E_R$	${}^2E_R$
^{1}S	3.99	5.03
^{1}P	4.28	4.99
^{1}D	4.73	—

Table 2.7: Approximate resonance positions found using stabilization method

can be compared to the full complex Kohn calculation in Table 6.3.

To complete the discussion for resonances below the inelastic threshold, the D-wave stabilization plots for the first symmetry only are in Figures 2.9 and 2.10. Compared to Figures 2.11 and 2.12, the first symmetry obviously is not enough to adequately describe the system. There is only one resonance before the threshold, and the fifth eigenvalue is taken at 924 paired terms in Table 2.7.

Table 2.7 gives the resonance positions found using the stabilization method. Despite the fact that this stabilization method does not give very accurate resonance positions in this work, we can learn some things from these. First, we can determine the number of resonances before the Ps(n=2) threshold and where to look for them in the full complex Kohn calculations. Secondly, the triplet states do not have resonances before this threshold for any of these partial waves. Lastly, for $\ell > 0$, both the first and second symmetries are needed to accurately describe the system. The first symmetry alone cannot adequately describe the P-wave and D-wave.

3 Scattering Theory

As mentioned in the introduction, the Kohn variational method and its variants have been used for many types of systems. This chapter discusses the trial wavefunction used, derives the Kohn-type variational methods, and applies them to this system.

3.1 General Wavefunction

The applications of the Kohn, inverse Kohn, complex Kohn for the S-matrix and T-matrix, generalized Kohn, and generalized complex Kohn for the S-matrix and T-matrix to the trial wavefunctions for each of the partial waves through the H-wave are all very similar in form. The trial wavefunctions for the partial waves (Equations (5.1), (6.1) and (7.1)) can be written in a general form as

$$\Psi_\ell^{\pm,t} = \widetilde{S}_\ell + L_\ell^{\pm,t}\,\widetilde{C}_\ell + \sum_{i=1}^{N(\omega)} c_i \bar{\phi}_i. \tag{3.1}$$

We only consider the Ps(1s)+H(1s) system for energies up to the excitation threshold of Ps(n=2)+H(1s), which is at an energy of $\frac{3}{16}$ a.u. (5.102 eV) [56]. The coordinate system used is the same as in Figure 2.1.

To avoid confusion with $L_\ell^{\pm,t}$ here and $\mathcal{L}$ in Equation (3.16), since the orbital angular momentum ℓ of the incoming Ps is the same as the total angular momentum L, we use ℓ to indicate the partial wave.

The short-range $\bar{\phi}_i$ terms can represent terms of different symmetries, such as the $\bar{\phi}_{1i}$ and $\bar{\phi}_{2j}$ of the P-wave in Equation (6.1). The only requirement in this derivation is that these are Hylleraas-type short-range terms. In addition to letting the $\widetilde{S}_\ell$ and $\widetilde{C}_\ell$ represent the $\bar{S}_\ell$ and $\bar{C}_\ell$ for the different partial waves, we can define them in such a way as to use multiple Kohn methods (Kohn, inverse Kohn, etc.). We begin by defining a matrix $\mathbf{u}$ which satisfies

$$\begin{bmatrix} \widetilde{S}_\ell \\ \widetilde{C}_\ell \end{bmatrix} = \mathbf{u} \begin{bmatrix} \bar{S}_\ell \\ \bar{C}_\ell \end{bmatrix} = \begin{bmatrix} u_{00} & u_{01} \\ u_{10} & u_{11} \end{bmatrix} \begin{bmatrix} \bar{S}_\ell \\ \bar{C}_\ell \end{bmatrix}. \tag{3.2}$$

This notation is similar to that of Lucchese [53] and Cooper et al. [54]. From this, it can easily be seen that

$$\widetilde{S}_\ell = u_{00}\bar{S}_\ell + u_{01}\bar{C}_\ell \tag{3.3a}$$

$$\widetilde{C}_\ell = u_{10}\bar{S}_\ell + u_{11}\bar{C}_\ell. \tag{3.3b}$$

We define

$$\bar{S}_\ell = \frac{1}{\sqrt{2}}(S_\ell \pm S'_\ell) \text{ and } \bar{C}_\ell = \frac{1}{\sqrt{2}}(C_\ell \pm C'_\ell), \tag{3.4}$$

where

$$S'_\ell = P_{23}S_\ell \text{ and } C'_\ell = P_{23}C_\ell. \tag{3.5}$$

The general form for the long-range terms S_ℓ and C_ℓ is

$$S_\ell = Y_\ell^0(\theta_\rho, \varphi_\rho)\, \Phi_{Ps}(r_{12})\, \Phi_H(r_3)\, \sqrt{2\kappa}\, j_\ell(\kappa\rho) \tag{3.6a}$$

$$C_\ell = -Y_\ell^0(\theta_\rho, \varphi_\rho)\, \Phi_{Ps}(r_{12})\, \Phi_H(r_3)\, \sqrt{2\kappa}\, n_\ell(\kappa\rho)\, f_\ell(\rho). \tag{3.6b}$$

The $Y_\ell^0(\theta_\rho, \varphi_\rho)$ are the spherical harmonics, $j_\ell(\kappa\rho)$ are the spherical Bessel functions, and $n_\ell(\kappa\rho)$ are the spherical Neumann functions. These are all given in Appendix B.1 through $\ell = 5$. $\Phi_{\mathrm{Ps}}(r_{12})$ and $\Phi_{\mathrm{H}}(r_3)$ are the Ps and H ground state wavefunctions given in Equations (1.1) and (1.2).

The shielding function, f_ℓ, removes the singularity at the origin due to the spherical Neumann function, n_ℓ. The form that we have chosen for this is

$$f_\ell(\rho) = \left[1 - \mathrm{e}^{-\mu\rho}\left(1 + \frac{\mu}{2}\rho\right)\right]^{m_\ell}. \tag{3.7}$$

At a minimum, m_ℓ is chosen so that C_ℓ behaves like S_ℓ as $\rho \to 0$. For more discussion of this, see Appendix B.6. The values used for the different partial waves are given in Table C.13. Prior work [57] used a slightly simpler shielding function for the S-wave of

$$f(\rho) = (1 - \mathrm{e}^{-\lambda\rho})^3. \tag{3.8}$$

Note that their paper is missing the negative sign in the exponential.

The Hylleraas-type short-range terms are similar to that used in Equation (2.1), again with $k_i + l_i + m_i + n_i + p_i + q_i \leq \omega$ (Equation (2.2)). These are chosen to have two symmetries, one with a prefactor of r_1^ℓ and the other with a prefactor of r_2^ℓ. The prefactors are included so that the correct asymptotic form of $\Psi_\ell^{\pm,t} \sim r_k^\ell$ at the origin follows [131, p.87]. The first and second symmetries are given respectively by

$$\bar{\phi}_{1i} = (1 \pm P_{23})\, Y_\ell^0(\theta_1, \varphi_1)\, \mathrm{e}^{-(\alpha r_1 + \beta r_2 + \gamma r_3)} r_1^\ell r_1^{k_i} r_2^{l_i} r_{12}^{m_i} r_3^{n_i} r_{13}^{p_i} r_{23}^{q_i} \tag{3.9a}$$

$$\bar{\phi}_{2j} = (1 \pm P_{23})\, Y_\ell^0(\theta_2, \varphi_2)\, \mathrm{e}^{-(\alpha r_1 + \beta r_2 + \gamma r_3)} r_2^\ell r_1^{k_j} r_2^{l_j} r_{12}^{m_j} r_3^{n_j} r_{13}^{p_j} r_{23}^{q_j}. \tag{3.9b}$$

From Refs. [95, 132], the D-wave and higher can have additional symmetries where the angular momentum is shared between the Ps and H. From these references, we see

that there are a possible $\ell + 1$ sets of short-range terms for each partial wave. We do not consider these mixed terms in this work (see Section 7.5).

The S-wave has only a single symmetry, so $\bar{\phi}_i$ is a single set of terms. Similar to Section 2.1, the $\frac{1}{\sqrt{2}}$ is absorbed into c_{i0}. The full S-wave trial wavefunction can be written as

$$\Psi_0^{\pm,t} = \widetilde{S}_0 + L_0^{\pm,t}\,\widetilde{C}_0 + \sum_{i=1}^{N(\omega)} c_{i0}\bar{\phi}_{i1}. \tag{3.10}$$

For the P-wave and higher ($\ell > 0$),

$$\Psi_\ell^{\pm,t} = \widetilde{S}_\ell + L_\ell^{\pm,t}\,\widetilde{C}_\ell + \sum_{i=1}^{N(\omega)} c_{i\ell}\bar{\phi}_{i1} + \sum_{i=N(\omega)+1}^{2N(\omega)} d_{i\ell}\bar{\phi}_{i2}. \tag{3.11}$$

The symbols ρ and ρ' are defined as (refer to Figure 2.1 and Appendix B.2)

$$\boldsymbol{\rho} = \frac{1}{2}\left(\boldsymbol{r}_1 + \boldsymbol{r}_2\right) \tag{3.12a}$$

$$\boldsymbol{\rho}' = \frac{1}{2}\left(\boldsymbol{r}_1 + \boldsymbol{r}_3\right). \tag{3.12b}$$

3.2 General Kohn Principle Derivation

Much of this derivation is similar to that in Peter Van Reeth's thesis [95] but is for single channel scattering and also generalized to a variety of Kohn-type variational methods. His thesis covers the Kohn and inverse Kohn methods for two channel e^+-He scattering. For this derivation, I will use Equation (3.1) but drop the short-range $\bar{\phi}_i^t$ terms. The derivation follows through the same with these terms, but it is clearer to ignore them here. Likewise, we only consider the direct terms here, unless otherwise specified. The final result of this section applies equally well to both the direct and exchanged terms.

The kinetic energy for Ps is

$$E_{\boldsymbol{\kappa}} = \frac{\hbar^2\kappa^2}{2m} = \frac{\kappa^2}{2m} = \frac{1}{4}\kappa^2, \tag{3.13}$$

where κ is the momentum of the Ps atom. Including this in the total energy with the ground-state energies of H and Ps, E_H and E_{Ps}, gives

$$E = E_H + E_{Ps} + E_{\boldsymbol{\kappa}} = -\frac{1}{2} - \frac{1}{4} + \frac{1}{4}\kappa^2 = -\frac{3}{4} + \frac{1}{4}\kappa^2. \tag{3.14}$$

The functional I_ℓ is defined as [133]

$$I[\Psi_\ell^t] \equiv \left\langle \Psi_\ell^{t\star} | \mathcal{L} | \Psi_\ell^t \right\rangle = \left(\Psi_\ell^t, \mathcal{L}\Psi_\ell^t\right) = \int \Psi_\ell^t \mathcal{L} \Psi_\ell^t \, d\tau, \tag{3.15}$$

where the operator $\mathcal{L}$ is given by

$$\mathcal{L} = 2(H - E). \tag{3.16}$$

Note that the exact wavefunction Ψ_ℓ solves the Schrödinger equation, giving

$$I[\Psi_\ell] = 0. \tag{3.17}$$

Normally, the bra in bra-ket notation is conjugated, but as noted by Refs. [53, 54, 134], the bra is not conjugated for the Kohn-type variational methods.

The trial wavefunction is related to the exact solution by

$$\Psi_\ell^t = \Psi_\ell + \delta\Psi_\ell. \tag{3.18}$$

The variation of I_ℓ is

$$\begin{aligned}
\delta I_\ell &= I_\ell[\Psi_\ell^t] - I_\ell[\Psi_\ell] \\
&= I_\ell[\Psi_\ell + \delta\Psi_\ell] - I_\ell[\Psi_\ell] \\
&= (\Psi_\ell, \mathcal{L}\Psi_\ell) + (\Psi_\ell, \mathcal{L}\,\delta\Psi_\ell) + (\delta\Psi_\ell, \mathcal{L}\Psi_\ell) + (\delta\Psi_\ell, \mathcal{L}\,\delta\Psi_\ell) - (\Psi_\ell, \mathcal{L}\Psi_\ell).
\end{aligned} \tag{3.19}$$

The first and last terms are equal to 0, by virtue of Equation (3.17).

We define $\delta I_\ell'$ as

$$\delta I_\ell' = \delta I_\ell - (\delta\Psi_\ell, \mathcal{L}\,\delta\Psi_\ell). \tag{3.20}$$

Since $\mathcal{L}\Psi_\ell = 0$,

$$(\delta\Psi_\ell, \mathcal{L}\Psi_\ell) = -(\delta\Psi_\ell, \mathcal{L}\Psi_\ell), \tag{3.21}$$

which combined with the definition of $\mathcal{L}$ from Equation (3.16), allows us to write the above equation as

$$\delta I_\ell' = 2\,(\Psi_\ell, (H-E)\delta\Psi_\ell) - 2\,(\delta\Psi_\ell, (H-E)\Psi_\ell)\,. \tag{3.22}$$

The Hamiltonian for the fundamental Coulombic system is

$$H = -\frac{1}{2}\nabla_{\boldsymbol{r}_1}^2 - \frac{1}{2}\nabla_{\boldsymbol{r}_2}^2 - \frac{1}{2}\nabla_{\boldsymbol{r}_3}^2 + \frac{1}{r_1} - \frac{1}{r_2} - \frac{1}{r_3} - \frac{1}{r_{12}} - \frac{1}{r_{13}} + \frac{1}{r_{23}}. \tag{3.23}$$

The Hamiltonian can also be expressed in terms of other variables in Jacobi coordinates as

$$H = -\frac{1}{4}\nabla_{\boldsymbol{\rho}}^2 - \frac{1}{2}\nabla_{\boldsymbol{r}_3}^2 - \nabla_{\boldsymbol{r}_{12}}^2 + \frac{1}{r_1} - \frac{1}{r_2} - \frac{1}{r_3} - \frac{1}{r_{12}} - \frac{1}{r_{13}} + \frac{1}{r_{23}} \tag{3.24}$$

and for the permuted version,

$$H = -\frac{1}{4}\nabla_{\boldsymbol{\rho}'}^2 - \frac{1}{2}\nabla_{\boldsymbol{r}_2}^2 - \nabla_{\boldsymbol{r}_{13}}^2 + \frac{1}{r_1} - \frac{1}{r_2} - \frac{1}{r_3} - \frac{1}{r_{12}} - \frac{1}{r_{13}} + \frac{1}{r_{23}}. \tag{3.25}$$

Substituting the second form of H in Equation (3.22) and using the total energy from Equation (3.14) gives

$$\begin{aligned}\delta I'_\ell = 2\int_{V_{12}}\int_{V_3}\int_{V_\rho}\Psi_\ell\Bigg[&-\frac{1}{4}\nabla^2_{\boldsymbol{\rho}}-\frac{1}{2}\nabla^2_{\boldsymbol{r}_3}-\nabla^2_{\boldsymbol{r}_{12}}+\frac{1}{r_1}-\frac{1}{r_2}-\frac{1}{r_3}\\&-\frac{1}{r_{12}}-\frac{1}{r_{13}}+\frac{1}{r_{23}}-E_H-E_{Ps}-\frac{1}{4}\kappa^2\Bigg]\delta\Psi_\ell\, d\tau_\rho d\tau_{r_3} d\tau_{r_{12}}\\ -2\int_{V_{12}}\int_{V_3}\int_{V_\rho}\delta\Psi_\ell\Bigg[&-\frac{1}{4}\nabla^2_{\boldsymbol{\rho}}-\frac{1}{2}\nabla^2_{\boldsymbol{r}_3}-\nabla^2_{\boldsymbol{r}_{12}}+\frac{1}{r_1}-\frac{1}{r_2}-\frac{1}{r_3}\\&-\frac{1}{r_{12}}-\frac{1}{r_{13}}+\frac{1}{r_{23}}-E_H-E_{Ps}-\frac{1}{4}\kappa^2\Bigg]\Psi_\ell\, d\tau_\rho d\tau_{r_3} d\tau_{r_{12}}.\end{aligned}\tag{3.26}$$

The H and Ps equations are respectively (for large values of ρ)

$$\left(-\frac{1}{2}\nabla^2_{\boldsymbol{r}_3}-\frac{1}{r_3}\right)\Phi_H(r_3)=E_H\Phi_H(r_3)\tag{3.27a}$$

$$\left(-\nabla^2_{\boldsymbol{r}_{12}}-\frac{1}{r_{12}}\right)\Phi_{Ps}(r_{12})=E_{Ps}\Phi_{Ps}(r_{12}).\tag{3.27b}$$

Realizing then that the Hamiltonians for H and Ps are given by

$$H_H=-\frac{1}{2}\nabla^2_{\boldsymbol{r}_3}-\frac{1}{r_3}\tag{3.28a}$$

$$H_{Ps}=-\nabla^2_{\boldsymbol{r}_{12}}-\frac{1}{r_{12}},\tag{3.28b}$$

and rearranging terms, Equation (3.26) becomes

$$\begin{aligned}\delta I'_\ell = -\frac{1}{2}\int_{V_{12}}\int_{V_3}\int_{V_\rho}&\left[\Psi_\ell\nabla^2_{\boldsymbol{\rho}}\,\delta\Psi_\ell-\delta\Psi_\ell\nabla^2_{\boldsymbol{\rho}}\Psi_\ell\right]d\tau_\rho d\tau_{r_3} d\tau_{r_{12}}\\ +2\int_{V_{12}}\int_{V_3}\int_{V_\rho}&\Psi_\ell\left[H_H+H_{Ps}+\frac{1}{r_1}-\frac{1}{r_2}-\frac{1}{r_{13}}+\frac{1}{r_{23}}-E_H-E_{Ps}-\frac{1}{4}\kappa^2\right]\delta\Psi_\ell\, d\tau_\rho d\tau_{r_3} d\tau_{r_{12}}\\ -2\int_{V_{12}}\int_{V_3}\int_{V_\rho}&\delta\Psi_\ell\left[H_H+H_{Ps}+\frac{1}{r_1}-\frac{1}{r_2}-\frac{1}{r_{13}}+\frac{1}{r_{23}}-E_H-E_{Ps}-\frac{1}{4}\kappa^2\right]\Psi_\ell\, d\tau_\rho d\tau_{r_3} d\tau_{r_{12}}.\end{aligned}\tag{3.29}$$

From Green's theorem,

$$\left\langle\Psi^\star_\ell\,\middle|\,\nabla^2_{\boldsymbol{\rho}}\,\middle|\,\delta\Psi_\ell\right\rangle-\left\langle\delta\Psi^\star_\ell\,\middle|\,\nabla^2_{\boldsymbol{\rho}}\,\middle|\,\Psi_\ell\right\rangle=\int_{V_3}\int_{V_{12}}\int_{V_\rho}\left[\Psi_\ell\nabla^2_{\boldsymbol{\rho}}\,\delta\Psi_\ell-\delta\Psi_\ell\nabla^2_{\boldsymbol{\rho}}\Psi_\ell\right]d\tau_\rho\, d\tau_{12} d\tau_3$$

$$= \int_{V_3}\int_{V_{12}}\int_{S_\rho} \left[\Psi_\ell \boldsymbol{\nabla}_\rho \delta\Psi - \delta\Psi_\ell \boldsymbol{\nabla}_\rho \Psi_\ell\right] \cdot d\boldsymbol{\sigma}_\rho d\tau_{12} d\tau_3. \tag{3.30}$$

S_ρ is the surface at $\rho \to \infty$. Due to the exponential form of $\Phi_{Ps}(r_{12})$ and $\Phi_H(r_3)$ given in Equations (1.1) and (1.2), the last two lines of Equation (3.29) cancel each other.

Since we are only considering the direct terms in Equation (3.1) so far, let us define a direct term only version of Equation (3.3) with

$$\widetilde{S}_d = u_{00} S_\ell + u_{01} C_\ell \tag{3.31a}$$

$$\widetilde{C}_d = u_{10} S_\ell + u_{11} C_\ell. \tag{3.31b}$$

From Equation (3.18) and Equation (3.1),

$$\delta\Psi = \Psi_\ell^t - \Psi_\ell = (\widetilde{S}_d + L_\ell^t \widetilde{C}_d) - (\widetilde{S}_d + L_\ell \widetilde{C}_d) = (L_\ell^t - L_\ell)\widetilde{C}_d \,. \tag{3.32}$$

Substituting this into Equation (3.29) with Equation (3.30),

$$\delta I'_\ell = -\frac{1}{2}(L_\ell^t - L_\ell) \int_{V_{12}}\int_{V_3}\int_{S_\rho} \left[(\widetilde{S}_d + L_\ell \widetilde{C}_d)\boldsymbol{\nabla}_\rho \widetilde{C}_d - \widetilde{C}_d \boldsymbol{\nabla}_\rho (\widetilde{S}_d + L_\ell \widetilde{C}_d)\right] \cdot d\boldsymbol{\sigma}_\rho d\tau_{12} d\tau_3 \,. \tag{3.33}$$

From Equations (3.6) and (B.23a), to first order, the gradient acting on $\widetilde{S}_d$ and $\widetilde{C}_d$ in Equation (3.3) gives

$$\boldsymbol{\nabla}_\rho \widetilde{S}_d \sim \kappa \left[u_{00} C_\ell - u_{01} S_\ell\right] \hat{\boldsymbol{\rho}} \tag{3.34a}$$

$$\boldsymbol{\nabla}_\rho \widetilde{C}_d \sim \kappa \left[u_{10} C_\ell - u_{11} S_\ell\right] \hat{\boldsymbol{\rho}} \,. \tag{3.34b}$$

Substituting this into Equation (3.33) and dropping the dot product, since the surface elements are in the same direction as $\hat{\boldsymbol{\rho}}$, this becomes

$$\begin{aligned}\delta I'_\ell \sim -\frac{1}{2}(L_\ell^t - L_\ell) \int_{V_{12}}\int_{V_3}\int_{S_\rho} \Big\{ &(\widetilde{S}_d + L_\ell \widetilde{C}_d)\kappa(u_{10} C_\ell - u_{11} S_\ell) \\ &- \widetilde{C}_d \kappa \left[(u_{00} C_\ell - u_{01} S_\ell) + L_\ell (u_{10} C_\ell - u_{11} S_\ell)\right] \Big\} d\sigma_\rho d\tau_{12} d\tau_3.\end{aligned} \tag{3.35}$$

Omitting terms quadratic in L_ℓ or L_ℓ^t, including $L_\ell^t L_\ell$,

$$\begin{aligned}\delta I'_\ell &\sim -\frac{1}{2}\kappa(L_\ell^t - L_\ell) \int_{V_{12}}\int_{V_3}\int_{S_\rho} \left[\widetilde{S}_d (u_{10} C_\ell - u_{11} S_\ell) - \widetilde{C}_d (u_{00} C_\ell - u_{01} S_\ell)\right] d\sigma_\rho d\tau_{12} d\tau_3 \\ &= -\frac{1}{2}\kappa(L_\ell^t - L_\ell) \int_{V_{12}}\int_{V_3}\int_{S_\rho} \left[\widetilde{S}_d u_{10} C_\ell - \widetilde{S}_d u_{11} S_\ell - \widetilde{C}_d u_{00} C_\ell + \widetilde{C}_d u_{01} S_\ell\right] d\sigma_\rho d\tau_{12} d\tau_3\end{aligned}$$

$$= -\frac{1}{2}\kappa(L_\ell^t - L_\ell) \int_{V_{12}} \int_{V_3} \int_{S_\rho} \Big[u_{00}u_{10}S_\ell C_\ell + u_{01}u_{10}C_\ell^2 - u_{00}u_{11}S_\ell^2 - u_{01}u_{11}C_\ell S_\ell$$
$$- u_{10}u_{00}S_\ell C_\ell - u_{11}u_{00}C_\ell^2 + u_{10}u_{01}S_\ell^2 + u_{11}u_{01}C_\ell S_\ell \Big] \, d\sigma_\rho d\tau_{12} d\tau_3$$
$$= -\frac{1}{2}\kappa(L_\ell^t - L_\ell) \int_{V_{12}} \int_{V_3} \int_{S_\rho} (u_{10}u_{01} - u_{00}u_{11}) \left(S_\ell^2 + C_\ell^2 \right) d\sigma_\rho d\tau_{12} d\tau_3$$
$$= \frac{1}{2}\kappa(L_\ell^t - L_\ell) \det \mathbf{u} \int_{V_{12}} \int_{V_3} \int_{S_\rho} \left(S_\ell^2 + C_\ell^2 \right) d\sigma_\rho d\tau_{12} d\tau_3. \tag{3.36}$$

The rest of this derivation considers only the direct terms. The final result applies as well when the exchanged terms are included. Since we are considering the surface as $\rho \to \infty$, $f_\ell(\rho)$ in Equation (3.6b) becomes 1. Then from Equation (3.6),

$$S_\ell^2 + C_\ell^2 = Y_\ell^0(\theta_\rho, \varphi_\rho)^2 \, \Phi_{Ps}(r_{12})^2 \, \Phi_H(r_3)^2 \, (2\kappa) \left[j_\ell(\kappa\rho)^2 + n_\ell(\kappa\rho)^2 \right]. \tag{3.37}$$

The asymptotic forms of j_ℓ and n_ℓ as $\rho \to \infty$ are given by [135, p.729]

$$j_\ell(\kappa\rho) \sim \frac{1}{\kappa\rho} \sin\left(\kappa\rho - \frac{n\pi}{2} \right) \tag{3.38a}$$
$$n_\ell(\kappa\rho) \sim \frac{1}{\kappa\rho} \cos\left(\kappa\rho - \frac{n\pi}{2} \right). \tag{3.38b}$$

As $\rho \to \infty$,

$$S_\ell^2 + C_\ell^2 \sim Y_\ell^0(\theta_\rho, \varphi_\rho)^2 \, \Phi_{Ps}(r_{12})^2 \, \Phi_H(r_3)^2 \, (2\kappa) \frac{1}{\kappa^2\rho^2}. \tag{3.39}$$

Substituting this in Equation (3.36) and expanding the $d\sigma_\rho$ volume element,

$$\delta I'_\ell \sim \kappa(L_\ell^t - L_\ell) \det \mathbf{u} \int_{V_{12}} \int_{V_3} \int_{S_\rho} Y_\ell^0(\theta_\rho, \varphi_\rho)^2 \, \Phi_{Ps}(r_{12})^2 \, \Phi_H(r_3)^2 \, \frac{1}{\kappa\rho^2} \rho^2 \sin\theta_\rho d\theta_\rho d\varphi_\rho d\tau_{12} d\tau_3$$
$$= (L_\ell^t - L_\ell) \det \mathbf{u} \int_{V_{12}} \int_{V_3} \int_{S_\rho} Y_\ell^0(\theta_\rho, \varphi_\rho)^2 \, \Phi_{Ps}(r_{12})^2 \, \Phi_H(r_3)^2 \sin\theta_\rho d\theta_\rho d\varphi_\rho d\tau_{12} d\tau_3. \tag{3.40}$$

Since the Ps and H eigenfunctions are normalized, i.e.

$$\int_{V_3} |\Phi_H(r_3)|^2 \, d\tau_3 = 1 \text{ and } \int_{V_{12}} |\Phi_{Ps}(r_{12})|^2 \, d\tau_{12} = 1, \tag{3.41}$$

we now have

$$\delta I'_\ell = (L_\ell^t - L_\ell) \det \mathbf{u} \int_{S_\rho} Y_\ell^0(\theta_\rho, \varphi_\rho)^2 \sin\theta_\rho d\theta_\rho d\varphi_\rho. \tag{3.42}$$

The spherical harmonics are normalized so that [135, p.788]

$$\int_{S_\rho} \left| Y_\ell^0(\theta_\rho, \varphi_\rho) \right|^2 d\Omega = 1. \tag{3.43}$$

This gives that

$$\delta I'_\ell = (L_\ell^t - L_\ell) \det \mathbf{u}. \tag{3.44}$$

From Equations (3.20) and (3.44),

$$\delta I'_\ell = (L_\ell^t - L_\ell) \det \mathbf{u} + (\delta\Psi_\ell, \mathcal{L}\, \delta\Psi_\ell). \tag{3.45}$$

This is the Kato identity [136]. For the Kohn-type variational methods, the last term is neglected, since it is second order in $\delta\Psi_\ell$. Using the approximation $\delta I'_\ell \approx \delta I_\ell$, we have

$$\delta I_\ell = I_\ell[\Psi_\ell^t] - I_\ell[\Psi_\ell] \approx (L_\ell^t - L_\ell) \det \mathbf{u}. \tag{3.46}$$

Replacing the exact L_ℓ by the variational L_ℓ^v and rearranging, we finally get the general Kohn variational method of

$$L_\ell^v = L_\ell^t - I_\ell[\Psi_\ell^t] / \det \mathbf{u}, \tag{3.47}$$

which is correct to second-order. This was only derived using the direct terms, but the exchange terms follow the same steps with ρ' instead of ρ. This was also only shown for the long-range terms, but it applies equally as well to the full wavefunction with the short-range terms.

3.3 Application of the Kohn-Type Variational Methods

We use the general Kohn variational method (Equation (3.47)) with the full trial wavefunction to get

$$L_\ell^v = L_\ell^t - \tfrac{1}{\det \mathbf{u}} \Big((\widetilde{S}_\ell + L_\ell^t \widetilde{C}_\ell + \sum_i c_i \bar{\phi}_i^t), \mathcal{L}(\widetilde{S}_\ell + L_\ell^t \widetilde{C}_\ell + \sum_j c_j \bar{\phi}_j^t) \Big). \tag{3.48}$$

The property of the Kohn functional that it is stationary with respect to variations in the linear parameters [137] can be written in this case as

$$\frac{\partial L_\ell^v}{\partial L_\ell^t} = 0 \text{ and } \frac{\partial L_\ell^v}{\partial c_i} = 0, \text{ where } i = 1, \ldots, N. \tag{3.49}$$

Performing the first variation gives

$$0 = \frac{\partial L_\ell^v}{\partial L_\ell^t}$$

$$= \det \mathbf{u} - \left[(\widetilde{S}_\ell, \mathcal{L}\widetilde{C}_\ell) + (\widetilde{C}_\ell, \mathcal{L}\widetilde{S}_\ell) + \frac{\partial}{\partial L_\ell^t}(L_\ell^t \widetilde{C}_\ell, \mathcal{L} L_\ell^t \widetilde{C}_\ell) + (\widetilde{C}_\ell, \mathcal{L}\sum_i c_i \bar{\phi}_i) + (\sum_i c_i \bar{\phi}_i, \mathcal{L}\widetilde{C}_\ell) \right]. \tag{3.50}$$

The third term in brackets becomes

$$\frac{\partial}{\partial L_\ell^t}(L_\ell^t \widetilde{C}_\ell, \mathcal{L} L_\ell^t \widetilde{C}_\ell) = (\widetilde{C}_\ell, \mathcal{L}\widetilde{C}_\ell) \frac{\partial}{\partial L_\ell^t} {L_\ell^t}^2 = 2(\widetilde{C}_\ell, \mathcal{L}\widetilde{C}_\ell) L_\ell^t. \tag{3.51}$$

The last two terms of Equation (3.50) are equal to each other, and we can use Equation (3.97) to rewrite this as

$$0 = -2(\widetilde{C}_\ell, \mathcal{L}\widetilde{S}_\ell) - 2L_\ell^t(\widetilde{C}_\ell, \mathcal{L}\widetilde{C}_\ell) - 2\sum_i c_i (\widetilde{C}_\ell, \mathcal{L}\bar{\phi}_i). \tag{3.52}$$

Rearranging gives

$$-(\widetilde{C}_\ell, \mathcal{L}\widetilde{S}_\ell) = L_\ell^t(\widetilde{C}_\ell, \mathcal{L}\widetilde{C}_\ell) + \sum_i c_i (\widetilde{C}_\ell, \mathcal{L}\bar{\phi}_i). \tag{3.53}$$

Now we perform the variation with respect to a general c_k as in Equation (3.49).

$$0 = \frac{\partial \mathcal{L}_v}{\partial c_k} = -\left[(\widetilde{S}_\ell, \mathcal{L}\bar{\phi}_k) + L_\ell^t(\widetilde{C}_\ell, \mathcal{L}\bar{\phi}_k) + (\bar{\phi}_k, \mathcal{L}\widetilde{S}_\ell) + L_\ell^t(\bar{\phi}_k, \mathcal{L}\widetilde{C}_\ell) + \frac{\partial}{\partial c_k}(\sum_i c_i \bar{\phi}_i, \mathcal{L}\sum_j c_j \bar{\phi}_j) \right] \tag{3.54}$$

Rearranging gives

$$-\left(\bar{\phi}_k, \mathcal{L}\widetilde{S}_\ell\right) = L_\ell^t \left(\bar{\phi}_k, \mathcal{L}\widetilde{C}_\ell\right) + \sum_i (\bar{\phi}_k, \mathcal{L} c_i \bar{\phi}_i). \tag{3.55}$$

The set of linear equations in Equations (3.53) and (3.55) can be written in matrix form as

$$\begin{bmatrix} (\widetilde{C}_\ell, \mathcal{L}\widetilde{C}_\ell) & (\widetilde{C}_\ell, \mathcal{L}\bar{\phi}_1) & \cdots & (\widetilde{C}_\ell, \mathcal{L}\bar{\phi}_j) & \cdots \\ (\bar{\phi}_1, \mathcal{L}\widetilde{C}_\ell) & (\bar{\phi}_1, \mathcal{L}\bar{\phi}_1) & \cdots & (\bar{\phi}_1, \mathcal{L}\bar{\phi}_j) & \cdots \\ \vdots & \vdots & \ddots & \vdots & \\ (\bar{\phi}_i, \mathcal{L}\widetilde{C}_\ell) & (\bar{\phi}_i, \mathcal{L}\bar{\phi}_1) & \cdots & (\bar{\phi}_i, \mathcal{L}\bar{\phi}_j) & \cdots \\ \vdots & \vdots & & \vdots & \end{bmatrix} \begin{bmatrix} L_\ell^t \\ c_1 \\ \vdots \\ c_i \\ \vdots \end{bmatrix} = - \begin{bmatrix} (\widetilde{C}_\ell, \mathcal{L}\widetilde{S}_\ell) \\ (\bar{\phi}_1, \mathcal{L}\widetilde{S}_\ell) \\ \vdots \\ (\bar{\phi}_i, \mathcal{L}\widetilde{S}_\ell) \\ \vdots \end{bmatrix}. \tag{3.56}$$

This matrix equation can be rewritten as

$$\boldsymbol{A}\boldsymbol{X} = -\boldsymbol{B}. \tag{3.57}$$

Solving this for $\boldsymbol{X}$ gives

$$\boldsymbol{X} = -\boldsymbol{A}^{-1}\boldsymbol{B}. \tag{3.58}$$

To obtain L_ℓ^v from this matrix equation, we must next expand Equation (3.48).

$$L_\ell^v = L_\ell^t - \tfrac{1}{\det \mathbf{u}} \Bigg[(\widetilde{S}_\ell, \mathcal{L}\widetilde{S}_\ell) + L_\ell^t(\widetilde{S}_\ell, \mathcal{L}\widetilde{C}_\ell) + \sum_i c_i(\widetilde{S}_\ell, \mathcal{L}\bar{\phi}_i) + L_\ell^t(\widetilde{C}_\ell, \mathcal{L}\widetilde{S}_\ell) + {L_\ell^t}^2(\widetilde{C}_\ell, \mathcal{L}\widetilde{C}_\ell) + L_\ell^t \sum_i c_i(\widetilde{C}_\ell, \mathcal{L}\bar{\phi}_i) + \sum_i c_i(\bar{\phi}_i, \mathcal{L}\widetilde{S}_\ell) + L_\ell^t \sum_i c_i(\bar{\phi}_i, \mathcal{L}\widetilde{C}_\ell) + \sum_i \sum_j c_i c_j(\bar{\phi}_i, \mathcal{L}\bar{\phi}_j) \Bigg] \tag{3.59}$$

By substituting Equation (3.97) in for $(\widetilde{S}_\ell, \mathcal{L}\widetilde{C}_\ell)$, the first L_ℓ^t above is canceled, leaving

$$L_\ell^v = -\tfrac{1}{\det \mathbf{u}} \Bigg[(\widetilde{S}_\ell, \mathcal{L}\widetilde{S}_\ell) + L_\ell^t(\widetilde{C}_\ell, \mathcal{L}\widetilde{S}_\ell) + \sum_i c_i(\widetilde{S}_\ell, \mathcal{L}\bar{\phi}_i) + L_\ell^t(\widetilde{C}_\ell, \mathcal{L}\widetilde{S}_\ell) + {L_\ell^t}^2(\widetilde{C}_\ell, \mathcal{L}\widetilde{C}_\ell) + L_\ell^t \sum_i c_i(\widetilde{C}_\ell, \mathcal{L}\bar{\phi}_i) + \sum_i c_i(\bar{\phi}_i, \mathcal{L}\widetilde{S}_\ell) + L_\ell^t \sum_i c_i(\bar{\phi}_i, \mathcal{L}\widetilde{C}_\ell) + \sum_i \sum_j c_i c_j(\bar{\phi}_i, \mathcal{L}\bar{\phi}_j) \Bigg]. \tag{3.60}$$

Using the following definitions of

$$D = \begin{bmatrix} L_\ell^t & c_1 & \cdots & c_N & 1 \end{bmatrix} \text{ and} \tag{3.61}$$

$$F = \begin{bmatrix} (\widetilde{\boldsymbol{C}}_{\boldsymbol{\ell}}, \boldsymbol{\mathcal{L}}\widetilde{\boldsymbol{C}}_{\boldsymbol{\ell}}) & (\widetilde{\boldsymbol{C}}_{\boldsymbol{\ell}}, \boldsymbol{\mathcal{L}}\bar{\phi}) & (\widetilde{\boldsymbol{C}}_{\boldsymbol{\ell}}, \boldsymbol{\mathcal{L}}\widetilde{\boldsymbol{S}}_{\boldsymbol{\ell}}) \\ (\bar{\phi}, \boldsymbol{\mathcal{L}}\widetilde{\boldsymbol{C}}_{\boldsymbol{\ell}}) & (\bar{\phi}, \boldsymbol{\mathcal{L}}\bar{\phi}) & (\bar{\phi}, \boldsymbol{\mathcal{L}}\widetilde{\boldsymbol{S}}_{\boldsymbol{\ell}}) \\ (\widetilde{\boldsymbol{C}}_{\boldsymbol{\ell}}, \boldsymbol{\mathcal{L}}\widetilde{\boldsymbol{S}}_{\boldsymbol{\ell}}) & (\widetilde{\boldsymbol{S}}_{\boldsymbol{\ell}}, \boldsymbol{\mathcal{L}}\bar{\phi}) & (\widetilde{\boldsymbol{S}}_{\boldsymbol{\ell}}, \boldsymbol{\mathcal{L}}\widetilde{\boldsymbol{S}}_{\boldsymbol{\ell}}) \end{bmatrix}, \tag{3.62}$$

Equation (3.60) can be rewritten as the following matrix equation:

$$L_\ell^v = -\tfrac{1}{\det \mathbf{u}} DFD^T. \tag{3.63}$$

Using Equation (3.57) in Equation (3.63) and expanding gives

$$\begin{aligned} \det \mathbf{u}\, L_\ell^v &= -\begin{bmatrix} \boldsymbol{X^T} & 1 \end{bmatrix} \begin{bmatrix} \boldsymbol{A} & \boldsymbol{B} \\ \boldsymbol{B^T} & (\widetilde{\boldsymbol{S}}_{\boldsymbol{\ell}}, \boldsymbol{\mathcal{L}}\widetilde{\boldsymbol{S}}_{\boldsymbol{\ell}}) \end{bmatrix} \begin{bmatrix} \boldsymbol{X} \\ 1 \end{bmatrix} = -\begin{bmatrix} \boldsymbol{X^T} & 1 \end{bmatrix} \begin{bmatrix} 0 \\ \boldsymbol{B^T X} + (\widetilde{S}_\ell, \mathcal{L}\widetilde{S}_\ell) \end{bmatrix} \\ &= -\boldsymbol{B^T X} - (\widetilde{S}_\ell, \mathcal{L}\widetilde{S}_\ell), \end{aligned} \tag{3.64}$$

where

$$\boldsymbol{B^T X} = L_\ell^t(\widetilde{C}_\ell, \mathcal{L}\widetilde{S}_\ell) + \sum_i c_i(\bar{\phi}_i, \mathcal{L}\widetilde{S}_\ell). \tag{3.65}$$

A more compact way of writing Equation (3.64) is by

$$L_\ell^v = -\tfrac{1}{\det \mathbf{u}} \left(\Psi^{t,0}, \mathcal{L}\widetilde{S}_\ell \right), \tag{3.66}$$

where $\Psi^{t,0}$ is the full general wavefunction in Equation (3.1) with its nonlinear parameters optimized. Finally, to obtain the phase shifts, we use the relation given by Ref. [53] as

$$K_\ell = \tan\delta_\ell = (u_{01} + u_{11}L_\ell)(u_{00} + u_{10}L_\ell)^{-1}. \tag{3.67}$$

The $\mathbf{u}$ and $L_\ell^{\pm,t}$ for the various Kohn methods are described now. Note that for each of these, $\det\mathbf{u} = 1$, except for the ones describing the S-matrix complex Kohn and generalized S-matrix complex Kohn. When we create the matrix in Equation (3.56), we only calculate the matrix elements for the Kohn, along with $(\bar{S}_\ell, \mathcal{L}\bar{S}_\ell)$ and $(\bar{S}_\ell, \mathcal{L}\bar{C}_\ell)$. Then from the definitions in Equation (3.3), this matrix can be changed to any of the other Kohn methods without recomputing any of the integrals.

Kohn

$$\mathbf{u} = \begin{bmatrix} 1 & 0 \\ 0 & 1 \end{bmatrix} \tag{3.68}$$

$$L_\ell^{\pm,t} = \lambda_t = K_t \tag{3.69}$$

Inverse Kohn

$$\mathbf{u} = \begin{bmatrix} 0 & 1 \\ -1 & 0 \end{bmatrix} \tag{3.70}$$

$$L_\ell^{\pm,t} = -\mu_t = -K_t^{-1} = -\bar{K}_t \tag{3.71}$$

Generalized Kohn

$$\mathbf{u} = \begin{bmatrix} \cos\tau & \sin\tau \\ -\sin\tau & \cos\tau \end{bmatrix} \tag{3.72}$$

The generalized Kohn method is described by Cooper et al. [54, 138]. When $\tau = 0$ is substituted in Equation (3.72) , the $\mathbf{u}$-matrix for the Kohn method is generated (Equation (3.68)). Similarly, when $\tau = \frac{\pi}{2}$, the $\mathbf{u}$-matrix for the inverse Kohn method is generated (Equation (3.70)).

***T*-matrix Complex Kohn**

$$\mathbf{u} = \begin{bmatrix} 1 & 0 \\ \mathrm{i} & 1 \end{bmatrix} \tag{3.73}$$

$$L_\ell^{\pm,t} = T_\ell \tag{3.74}$$

Lucchese [53] denotes this as $\mathcal{L}_\ell = -\pi T$, but we use the definition of the T-matrix from Bransden [139]:

$$K_\ell = \frac{T_\ell}{1 + \mathrm{i} T_\ell} \tag{3.75}$$

S-matrix Complex Kohn

$$\mathbf{u} = \begin{bmatrix} -\mathrm{i} & 1 \\ \mathrm{i} & 1 \end{bmatrix} \tag{3.76}$$

$$L_\ell^{\pm,t} = -S_\ell \tag{3.77}$$

The Lucchese [53] version of $\mathbf{u}$ differs from this, since he uses a different definition for the S-matrix. The form of the S-matrix we are using is related to the K-matrix by [43]

$$K_\ell = \frac{\mathrm{i}(1 - S_\ell)}{1 + S_\ell}, \tag{3.78}$$

which is satisfied by the above $\mathbf{u}$-matrix. Also of note is that $\det \mathbf{u} = -2\mathrm{i}$ instead of 1 like most of the other Kohn methods presented here. Cooper et al. [54] use the T-matrix but also provide a relation between the two.

Generalized T-matrix Complex Kohn

$$\mathbf{u} = \begin{bmatrix} \cos\tau & \sin\tau \\ -\sin\tau + \mathrm{i}\cos\tau & \cos\tau + \mathrm{i}\sin\tau \end{bmatrix} \tag{3.79}$$

This is a generalized form of the T-matrix complex Kohn, similar to how the generalized Kohn works. When $\tau = 0$, this reduces to the T-matrix complex Kohn. This is also a slightly different form than that of Cooper et al. [54], who have the real and imaginary parts of $\widetilde{C}_\ell$ swapped.

Generalized S-matrix Complex Kohn

$$\mathbf{u} = \begin{bmatrix} -\mathrm{i}\cos\tau - \sin\tau & -\mathrm{i}\sin\tau + \cos\tau \\ \mathrm{i}\cos\tau - \sin\tau & \mathrm{i}\sin\tau + \cos\tau \end{bmatrix} \tag{3.80}$$

This is a generalized form of the S-matrix complex Kohn. When $\tau = 0$, this reduces to the S-matrix complex Kohn.

3.4 Matrix Elements

In this section, we examine the matrix elements of Equation (3.56). The three types of matrix elements are short-range–short-range (short-short), short-range–long-range (short-long) and long-range–long-range (long-long). The short-long and long-long matrix elements have a similar analysis. For these, the effect of the $\mathcal{L} = 2(H - E)$ operator on the long-range terms must be considered, and then integrations over the external angles (see Appendix A) are performed. The remaining 6-dimensional integral is then numerically integrated as described in Sections 4.2.1 and 4.2.2.

For all of these matrix elements, looking at the barred terms, we have 4 integrations to perform. Using a property of the P_{23} permutation operator, for a general f and g,

$$(f, \mathcal{L}g) = (f', \mathcal{L}g') \text{ and } (f, \mathcal{L}g') = (f', \mathcal{L}g). \tag{3.81}$$

The functions f and g are any of $\widetilde{S}_\ell$, $\widetilde{C}_\ell$ and $\bar{\phi}_i$. This relation allows us to reduce the number of integrations needed by half by doing [95]

$$(\bar{f}, \mathcal{L}\bar{g}) = (f, \mathcal{L}g) \pm (f, \mathcal{L}g') \pm (f', \mathcal{L}g) + (f', \mathcal{L}g') = 2\left[(f, \mathcal{L}g) \pm (f, \mathcal{L}g')\right]. \tag{3.82}$$

3.4.1 Matrix Element Symmetries

Not all matrix elements in Equation (3.56) have to be calculated as presented. Some matrix elements are identical to other matrix elements, such as $(\widetilde{C}_\ell, \mathcal{L}\bar{\phi}_i) = (\bar{\phi}_i, \mathcal{L}\widetilde{C}_\ell)$. In this particular case, it is much easier to calculate $(\bar{\phi}_i, \mathcal{L}\widetilde{C}_\ell)$ instead of $(\widetilde{C}_\ell, \mathcal{L}\bar{\phi}_i)$, due to the complexity of operating $\mathcal{L}$ on $\bar{\phi}_i$ (see Equation (2.10)). We prove these claims in this section.

These arguments follow that of Appendix A of Van Reeth's thesis [95]. We start with the functional

$$F \equiv (g, \mathcal{L}f) - (f, \mathcal{L}g)\ , \tag{3.83}$$

with $\mathcal{L}$ given by Equation (3.16). Using the Hamiltonian given by Equation (3.23), only the first three terms of the above functional have to be evaluated, as the other terms go to 0 with the subtraction.

$$\begin{aligned} F &= \left(-g, \frac{1}{2}\nabla_{\boldsymbol{r}_1}^2 f\right) + \left(f, \frac{1}{2}\nabla_{\boldsymbol{r}_1}^2 g\right) + \left(-g, \frac{1}{2}\nabla_{\boldsymbol{r}_2}^2 f\right) + \left(f, \frac{1}{2}\nabla_{\boldsymbol{r}_2}^2 g\right) \\ &\quad + \left(-g, \frac{1}{2}\nabla_{\boldsymbol{r}_3}^2 f\right) + \left(f, \frac{1}{2}\nabla_{\boldsymbol{r}_3}^2 g\right) \\ &= \int_{V_3}\int_{V_2}\int_{V_1} \left[-g\nabla_{\boldsymbol{r}_1}^2 f + f\nabla_{\boldsymbol{r}_1}^2 g - g\nabla_{\boldsymbol{r}_2}^2 f + f\nabla_{\boldsymbol{r}_2}^2 g - g\nabla_{\boldsymbol{r}_3}^2 f + f\nabla_{\boldsymbol{r}_3}^2 g\right] d\tau_1 d\tau_2 d\tau_3 \end{aligned} \tag{3.84}$$

Using Green's theorem on each pair of terms,

$$F = \int_{V_3}\int_{V_2}\int_{S_1} [-g\boldsymbol{\nabla}_{r_1} f + f\boldsymbol{\nabla}_{r_1} g] \cdot d\boldsymbol{\sigma}_1 d\tau_2 d\tau_3 + \int_{V_3}\int_{V_1}\int_{S_2} [-g\boldsymbol{\nabla}_{r_2} f + f\boldsymbol{\nabla}_{r_2} g] \cdot d\boldsymbol{\sigma}_2 d\tau_1 d\tau_3 + \int_{V_1}\int_{V_2}\int_{S_3} [-g\boldsymbol{\nabla}_{r_3} f + f\boldsymbol{\nabla}_{r_3} g] \cdot d\boldsymbol{\sigma}_3 d\tau_2 d\tau_1 \,. \tag{3.85}$$

For the first pair of terms, the differential surface element contains r_1^2. The surface we are integrating over is at $r_1 \to \infty$, so if the integrand falls off faster than r_1^{-2}, the integral vanishes, the same as the argument in Equation (3.29). The same argument applies for r_2^2 and r_3^2 in the second and third pairs of terms, respectively. The short-range Hylleraas-type terms in Equation (3.9) fulfill this requirement for r_1, r_2, and r_3, so if the matrix elements contain $\bar{\phi}_i$, the right hand side is equal to 0. From Equation (3.83), this gives that matrix elements with short-range terms are symmetric, or that

$$(\bar{\phi}_i, \mathcal{L}\bar{\phi}_j) = (\bar{\phi}_j, \mathcal{L}\bar{\phi}_i) \tag{3.86a}$$

$$\left(\bar{\phi}_i, \mathcal{L}\widetilde{S}_\ell\right) = \left(\widetilde{S}_\ell, \mathcal{L}\bar{\phi}_i\right) \tag{3.86b}$$

$$\left(\bar{\phi}_i, \mathcal{L}\widetilde{C}_\ell\right) = \left(\widetilde{C}_\ell, \mathcal{L}\bar{\phi}_i\right). \tag{3.86c}$$

From Equations (2.10), (2.11) and (3.16), the form of $\mathcal{L}\phi_i$ is very complicated, but Equations (3.86b) and (3.86c) allow us to avoid having to operate $\mathcal{L}$ on the $\bar{\phi}_i$ terms.

Now if we let $g = \bar{S}_\ell$ and $f = \bar{C}_\ell$ in Equation (3.83),

$$\begin{aligned} F &= \left(\frac{1}{\sqrt{2}}\left[S_\ell \pm S'_\ell\right], \mathcal{L}\frac{1}{\sqrt{2}}\left[C_\ell \pm C'_\ell\right]\right) - \left(\frac{1}{\sqrt{2}}\left[C_\ell \pm C'_\ell\right], \mathcal{L}\frac{1}{\sqrt{2}}\left[S_\ell \pm S'_\ell\right]\right) \\ &= \frac{1}{2}\left[(S_\ell, \mathcal{L}C_\ell) \pm (S_\ell, \mathcal{L}C'_\ell) \pm (S'_\ell, \mathcal{L}C_\ell) + (S'_\ell, \mathcal{L}C'_\ell)\right. \\ &\qquad \left. - (C_\ell, \mathcal{L}S_\ell) \mp (C_\ell, \mathcal{L}S'_\ell) \mp (C'_\ell, \mathcal{L}S_\ell) - (C'_\ell, \mathcal{L}S'_\ell)\right] \end{aligned} \tag{3.87}$$

From the property of the permutation operators, $(S_\ell, \mathcal{L}C_\ell) = (S'_\ell, \mathcal{L}C'_\ell)$, $(S'_\ell, \mathcal{L}C_\ell) = (S_\ell, \mathcal{L}C'_\ell)$, $(C_\ell, \mathcal{L}S_\ell) = (S'_\ell, \mathcal{L}C'_\ell)$ and $(C'_\ell, \mathcal{L}S_\ell) = (C_\ell, \mathcal{L}S'_\ell)$, causing the above to reduce to

$$\begin{aligned} F &= \left[(S_\ell, \mathcal{L}C_\ell) - (C_\ell, \mathcal{L}S_\ell)\right] \pm \left[(S_\ell, \mathcal{L}C'_\ell) - (C'_\ell, \mathcal{L}S_\ell)\right] \\ &\equiv G \pm G'. \end{aligned} \tag{3.88}$$

Using Equation (3.24) and Green's theorem,

$$\begin{aligned} G = \frac{1}{2}&\int_{V_3}\int_{V_{12}}\int_{S_\rho} \left[S_\ell \boldsymbol{\nabla}_\rho C_\ell - C_\ell \boldsymbol{\nabla}_\rho S_\ell\right] \cdot d\boldsymbol{\sigma}_\rho d\tau_{12} d\tau_3 \\ &+ \int_{V_\rho}\int_{V_{12}}\int_{S_3} [S_\ell \boldsymbol{\nabla}_{r_3} C_\ell - C_\ell \boldsymbol{\nabla}_{r_3} S_\ell] \cdot d\boldsymbol{\sigma}_3 d\tau_{12} d\tau_\rho \end{aligned}$$

$$+2\int_{V_\rho}\int_{V_{13}}\int_{S_{12}}\left[S_\ell \boldsymbol{\nabla}_{r_{12}} C_\ell - C_\ell \boldsymbol{\nabla}_{r_{12}} S_\ell\right]\cdot d\boldsymbol{\sigma}_{12} d\tau_{13} d\tau_\rho \tag{3.89}$$

As before, the Ps and H functions have an exponential dependence on r_3 and r_{12}, respectively, so the second and third terms go to 0. The surface elements under consideration at $\rho \to \infty$ are normal to $\hat{\rho}$, so we can ignore the angular dependence in $\boldsymbol{\nabla}_\rho$. Then Equation (3.89) becomes

$$G = \frac{1}{2}\int_{V_3}\int_{V_{12}}\left[\int_{S_\rho}\left(S_\ell \frac{\partial C_\ell}{\partial \rho} - C_\ell \frac{\partial S}{\partial \rho}\right)\rho^2 \sin\theta_\rho d\theta_\rho d\varphi_\rho\right] d\tau_{12} d\tau_3. \tag{3.90}$$

Using Equation (3.6) and realizing that $f_\ell \to 1$ as $\rho \to \infty$, from the *Mathematica* notebook "SLC - CLS Proof.nb" [4], we have

$$\left(S_\ell \frac{\partial C_\ell}{\partial \rho} - C_\ell \frac{\partial S_\ell}{\partial \rho}\right) = \frac{2}{\rho^2} Y_\ell^0\left(\theta_\rho, \varphi_\rho\right)^2 \Phi_{Ps}\left(r_{12}\right)^2 \Phi_H\left(r_3\right)^2. \tag{3.91}$$

Substituting Equation (3.91) into Equation (3.90) yields

$$\begin{aligned} G &= \frac{\cancel{1}}{\cancel{2}}\int_{V_3}\int_{V_{12}}\left[\int_{S_\rho}\frac{\cancel{2}}{\cancel{\rho^2}} Y_\ell^0\left(\theta_\rho, \varphi_\rho\right)^2 \Phi_{Ps}\left(r_{12}\right)^2 \Phi_H\left(r_3\right)^2 \cancel{\rho^2} \sin\theta_\rho d\theta_\rho d\varphi_\rho\right] d\tau_{12} d\tau_3 \\ &= \int_{V_3}\int_{V_{12}} \Phi_{Ps}(r_{12})^2 \Phi_H(r_3)^2 \left[\int_{S_\rho} Y_\ell^0\left(\theta_\rho, \varphi_\rho\right)^2 \sin\theta_\rho d\theta_\rho d\varphi_\rho\right] d\tau_{12} d\tau_3 \\ &= \int_{V_3}\int_{V_{12}} \Phi_{Ps}(r_{12})^2 \Phi_H(r_3)^2 d\tau_{12} d\tau_3 = 1, \end{aligned} \tag{3.92}$$

which follows from the orthonormality of the spherical harmonics and the normalization of the Ps and H wavefunctions. These, when combined in Equation (3.88), give that

$$(S_\ell, \mathcal{L} C_\ell) = (C_\ell, \mathcal{L} S_\ell) + 1. \tag{3.93}$$

As this also applies to the permuted versions, writing this in terms of $\bar{S}_\ell$ and $\bar{C}_\ell$ gives the final relation of

$$(\bar{S}_\ell, \mathcal{L}\bar{C}_\ell) = (\bar{C}_\ell, \mathcal{L}\bar{S}_\ell) + 1. \tag{3.94}$$

This can also be shown more generally for the $(\widetilde{S}_\ell, \mathcal{L}\widetilde{C}_\ell)$ and $(\widetilde{C}_\ell, \mathcal{L}\widetilde{S}_\ell)$ matrix elements. From the definitions of $\widetilde{S}_\ell$ and $\widetilde{C}_\ell$ in Equation (3.3),

$$(\widetilde{S}_\ell, \mathcal{L}\widetilde{C}_\ell) = ((u_{00}\bar{S}_\ell + u_{01}\bar{C}_\ell), \mathcal{L}(u_{10}\bar{S}_\ell + u_{11}\bar{C}_\ell))$$

$$= u_{00}u_{10}(\bar{S}_\ell, \mathcal{L}\bar{S}_\ell) + u_{00}u_{11}(\bar{S}_\ell, \mathcal{L}\bar{C}_\ell) + u_{01}u_{10}(\bar{C}_\ell, \mathcal{L}\bar{S}_\ell) + u_{01}u_{11}(\bar{C}_\ell, \mathcal{L}\bar{C}_\ell). \tag{3.95}$$

Likewise,

$$\begin{aligned}(\widetilde{C}_\ell, \mathcal{L}\widetilde{S}_\ell) &= ((u_{10}\bar{S}_\ell + u_{11}\bar{C}_\ell), \mathcal{L}(u_{00}\bar{S}_\ell + u_{01}\bar{C}_\ell)) \\ &= u_{10}u_{00}(\bar{S}_\ell, \mathcal{L}\bar{S}_\ell) + u_{10}u_{01}(\bar{S}_\ell, \mathcal{L}\bar{C}_\ell) + u_{11}u_{00}(\bar{C}_\ell, \mathcal{L}\bar{S}_\ell) + u_{11}u_{01}(\bar{C}_\ell, \mathcal{L}\bar{C}_\ell).\end{aligned} \tag{3.96}$$

Combining Equations (3.95) and (3.96) gives

$$\begin{aligned}(\widetilde{S}_\ell, \mathcal{L}\widetilde{C}_\ell) - (\widetilde{C}_\ell, \mathcal{L}\widetilde{S}_\ell) &= [u_{00}u_{10} - u_{10}u_{00}](\bar{S}_\ell, \mathcal{L}\bar{S}_\ell) + [u_{00}u_{11} - u_{10}u_{01}](\bar{S}_\ell, \mathcal{L}\bar{C}_\ell) \\ &\quad + [u_{01}u_{10} - u_{11}u_{00}](\bar{C}_\ell, \mathcal{L}\bar{S}_\ell) + [u_{01}u_{11} - u_{11}u_{01}](\bar{C}_\ell, \mathcal{L}\bar{C}_\ell) \\ &= [u_{00}u_{11} - u_{10}u_{01}][(\bar{S}_\ell, \mathcal{L}\bar{C}_\ell) - (\bar{C}_\ell, \mathcal{L}\bar{S}_\ell)] \\ &= \det \mathbf{u}[(\bar{S}_\ell, \mathcal{L}\bar{C}_\ell) - (\bar{C}_\ell, \mathcal{L}\bar{S}_\ell)]\end{aligned}$$

This is finally written as the general form of Equation (3.94), giving

$$(\widetilde{S}_\ell, \mathcal{L}\widetilde{C}_\ell) = (\widetilde{C}_\ell, \mathcal{L}\widetilde{S}_\ell) + \det \mathbf{u}. \tag{3.97}$$

This relation can let us obtain the $(\widetilde{S}_\ell, \mathcal{L}\widetilde{C}_\ell)$ matrix element from $(\widetilde{C}_\ell, \mathcal{L}\widetilde{S}_\ell)$, but it also gives us a nice numerical check. I calculate these two matrix elements separately in the long-long code and calculate their difference for the Kohn variational method. If it is close to 1, this gives us confidence that the long-long integrations are accurate. This also allows us to check that the difficult formulation of $\mathcal{L}C_\ell$ is correct.

3.4.2 Matrix Elements Involving Long-Range Terms

The short-long and long-long matrix elements have a similar analysis. For all of these, the effect of the $\mathcal{L} = 2(H - E)$ operator on the long-range terms must be considered, and then integrations over the external angles (see Appendix A) are performed. The remaining 6-dimensional integral is then numerically integrated as described in Sections 4.2.1 and 4.2.2.

3.4.2.1 $\mathcal{L}\bar{S}_\ell$ Terms

The matrix elements in Equation (3.56) require us to first determine $\mathcal{L}\bar{S}_\ell$. We start with examining $\mathcal{L}S_\ell$ first. Using Equations (3.6a) and (3.16),

$$\begin{aligned}\mathcal{L}S_\ell = &\left(-\frac{1}{2}\nabla^2_{\boldsymbol{\rho}} - \nabla^2_{\boldsymbol{r}_3} - 2\nabla^2_{\boldsymbol{r}_{12}} + \frac{2}{r_1} - \frac{2}{r_2} - \frac{2}{r_3} - \frac{2}{r_{12}} - \frac{2}{r_{13}} + \frac{2}{r_{23}} - 2E_H - 2E_{Ps} - \frac{1}{2}\kappa^2\right) \\ &\times Y^0_\ell(\theta_\rho, \varphi_\rho)\, \Phi_{Ps}(r_{12})\, \Phi_H(r_3)\, \sqrt{2\kappa}\, j_\ell(\kappa\rho)\,.\end{aligned} \tag{3.98}$$

Since S_ℓ is independent of r_3 and r_{12} except for the Φ_H and Φ_{Ps} functions, respectively, using Equations (3.27) and (3.28) simplifies this to

$$\mathcal{L}S_\ell = \left(-\frac{1}{2}\nabla^2_{\boldsymbol{\rho}} + \frac{2}{r_1} - \frac{2}{r_2} - \frac{2}{r_{13}} + \frac{2}{r_{23}} - \frac{1}{2}\kappa^2\right) Y^0_\ell(\theta_\rho, \varphi_\rho)\, \Phi_{Ps}(r_{12})\, \Phi_H(r_3)\, \sqrt{2\kappa}\, j_\ell(\kappa\rho)\,. \tag{3.99}$$

From Appendix B.4.2, we find that $Y^0_\ell(\theta_\rho, \varphi_\rho)\, j_\ell(\kappa\rho)$ is an eigenfunction of $\nabla^2_{\boldsymbol{\rho}}$ with eigenvalue $-\kappa^2$:

$$\nabla^2_{\boldsymbol{\rho}}\left[Y^0_\ell(\theta_\rho, \varphi_\rho)\, j_\ell(\kappa\rho)\right] = \frac{(-\kappa^2\rho^2)P_\ell(\cos\theta)}{\rho^2 P_\ell(\cos\theta)} = -\kappa^2\, Y^0_\ell(\theta_\rho, \varphi_\rho)\, j_\ell(\kappa\rho). \tag{3.100}$$

Then Equation (3.99) reduces down to

$$\mathcal{L}S_\ell = \left(\frac{2}{r_1} - \frac{2}{r_2} - \frac{2}{r_{13}} + \frac{2}{r_{23}}\right) Y^0_\ell(\theta_\rho, \varphi_\rho)\, \Phi_{Ps}(r_{12})\, \Phi_H(r_3)\, \sqrt{2\kappa}\, j_\ell(\kappa\rho) \tag{3.101}$$

or

$$\mathcal{L}S_\ell = \left(\frac{2}{r_1} - \frac{2}{r_2} - \frac{2}{r_{13}} + \frac{2}{r_{23}}\right) S_\ell. \tag{3.102}$$

$\mathcal{L}S'_\ell$ is simply the same as Equation (3.102) but with $2 \leftrightarrow 3$ due to the permutation operator, or

$$\mathcal{L}S'_\ell = \left(\frac{2}{r_1} - \frac{2}{r_3} - \frac{2}{r_{12}} + \frac{2}{r_{23}}\right) S'_\ell. \tag{3.103}$$

3.4.2.2 $\mathcal{L}\bar{C}_\ell$ Terms

To calculate the matrix elements in Equation (3.56) that include $\bar{C}_\ell$ in the ket, we start by writing a general form of $\mathcal{L}C_\ell$ using Equations (3.6b) and (3.16):

$$\begin{aligned}\mathcal{L}C_\ell = -\left(-\frac{1}{2}\nabla^2_{\boldsymbol{\rho}} - \nabla^2_{\boldsymbol{r}_3} - 2\nabla^2_{\boldsymbol{r}_{12}} + \frac{2}{r_1} - \frac{2}{r_2} - \frac{2}{r_3} - \frac{2}{r_{12}} - \frac{2}{r_{13}} + \frac{2}{r_{23}} - 2E_H - 2E_{Ps} - \frac{1}{2}\kappa^2\right) \\ \times Y^0_\ell(\theta_\rho, \varphi_\rho)\, \Phi_{Ps}(r_{12})\, \Phi_H(r_3)\, \sqrt{2\kappa}\, n_\ell(\kappa\rho)\, f_\ell(\rho)\end{aligned} \tag{3.104}$$

Similar to Equation (3.99), using Equations (3.27) and (3.28) reduces this to

$$\begin{aligned}\mathcal{L}C_\ell = -\left(-\frac{1}{2}\nabla^2_{\boldsymbol{\rho}} + \frac{2}{r_1} - \frac{2}{r_2} - \frac{2}{r_{13}} + \frac{2}{r_{23}} - 2E_H - 2E_{Ps} - \frac{1}{2}\kappa^2\right) \\ \times Y^0_\ell(\theta_\rho, \varphi_\rho)\, \Phi_{Ps}(r_{12})\, \Phi_H(r_3)\, \sqrt{2\kappa}\, n_\ell(\kappa\rho)\, f_\ell(\rho).\end{aligned} \tag{3.105}$$

Unlike with $\mathcal{L}S_\ell$ in Section 3.4.2.1, there is not a direct cancellation with the $\nabla^2_{\boldsymbol{\rho}}$ and κ^2 terms, as these also operate on the shielding function f_ℓ. The combination of these terms was calculated in the "First Partial Waves LC.nb" *Mathematica* notebook [1, 4] using the code given in Figure 3.1. This is for the F-wave, and replacing the ℓ-value of 3

```
Simplify[Laplacian[FunctionExpand[SphericalBesselY[3, κ ρ]] SphericalHarmonicY[3, 0, θ, ϕ] f[ρ],
    {ρ, θ, ϕ}, "Spherical"] + κ^2 (FunctionExpand[SphericalBesselY[3, κ ρ]] SphericalHarmonicY[3, 0, θ, ϕ] f[ρ])];
Simplify[1/2 %/SphericalHarmonicY[3, 0, θ, ϕ]]
```

Figure 3.1: Listing of *Mathematica* code in "First Partial Waves LC.nb" to calculate part of $\mathcal{L}C_\ell$ for the F-wave

in `SphericalBesselY` allows this to be used for any partial wave. The results of these derivations are given in each partial wave chapter through the D-wave. The full $\mathcal{L}C_\ell$ for the S-wave is shown on page 67 by substituting the $\frac{1}{2}\left(\nabla_{\boldsymbol{\rho}}^2+\kappa^2\right) Y_\ell^0(\theta_\rho,\varphi_\rho)\, n_\ell(\kappa\rho) f_\ell(\rho)$ in Equation (3.105).
Matrix elements involving $\mathcal{L}C_\ell'$ look similar but have the 2 and 3 coordinates swapped. In other words, $\rho \leftrightarrow \rho'$.

From Equation (3.7), the general shielding function for $\widetilde{C}_\ell$ to keep it regular at the origin is given by

$$f_\ell(\rho) = \left[1 - \mathrm{e}^{-\mu\rho}\left(1+\frac{\mu}{2}\rho\right)\right]^{m_\ell}. \tag{3.106}$$

In Figure 3.1, the derivatives $f_\ell'(\rho)$ and $f_\ell''(\rho)$ are needed. In the *Mathematica* notebook "Shielding Factor.nb" [1, 4], I found out that the derivatives can be written generally as

$$f_\ell'(\rho) = -\frac{\mu m_\ell(\mu\rho+1)\left[1-\frac{1}{2}e^{-\mu\rho}(\mu\rho+2)\right]^{m_\ell}}{\mu\rho-2e^{\mu\rho}+2} \tag{3.107}$$

and

$$f_\ell''(\rho) = \frac{\mu^2 m_\ell\left[-2\mu\rho e^{\mu\rho}+m_\ell(\mu\rho+1)^2-1\right]\left[1-\frac{1}{2}e^{-\mu\rho}(\mu\rho+2)\right]^{m_\ell}}{(\mu\rho-2e^{\mu\rho}+2)^2}. \tag{3.108}$$

3.4.2.3 $(\bar{S}_\ell, \mathcal{L}\bar{S}_\ell)$ and $(\bar{C}_\ell, \mathcal{L}\bar{S}_\ell)$ Matrix Elements

From Equation (3.3), we see that, in general, any matrix element in Equation (3.56) containing only long-range terms will contain both $(\bar{S}_\ell, \mathcal{L}\bar{S}_\ell)$ and $(\bar{C}_\ell, \mathcal{L}\bar{S}_\ell)$, along with the other two combinations given in Section 3.4.2.2. When $(\bar{S}_\ell, \mathcal{L}\bar{S}_\ell)$ is expanded,

$$(\bar{S}_\ell, \mathcal{L}\bar{S}_\ell) = \frac{1}{2}\left[(S_\ell, \mathcal{L}S_\ell) \pm (S_\ell', \mathcal{L}S_\ell) \pm (S_\ell, \mathcal{L}S_\ell') \pm (S_\ell', \mathcal{L}S_\ell')\right]. \tag{3.109}$$

The properties of the permutation operator give that

$$(S_\ell, \mathcal{L}S_\ell) = (S_\ell', \mathcal{L}S_\ell') \text{ and } (S_\ell', \mathcal{L}S_\ell) = (S_\ell, \mathcal{L}S_\ell'), \tag{3.110}$$

so this becomes

$$(\bar{S}_\ell, \mathcal{L}\bar{S}_\ell) = (S_\ell, \mathcal{L}S_\ell) \pm (S_\ell', \mathcal{L}S_\ell). \tag{3.111}$$

From Equations (3.102) and (3.103), the Laplacian on S_ℓ and S'_ℓ leaves only some of the potential terms. The potential terms in Equation (3.102) are antisymmetric upon the $1 \leftrightarrow 2$ swap, and the terms in Equation (3.103) are antisymmetric upon the $1 \leftrightarrow 3$ swap. S_ℓ and S'_ℓ are symmetric with the $1 \leftrightarrow 2$ and $1 \leftrightarrow 3$ swaps, respectively. When these are integrated over these coordinates, the combination of symmetric with antisymmetric functions causes the integral to be 0:

$$(S_\ell, \mathcal{L}S_\ell) = (S'_\ell, \mathcal{L}S'_\ell) = 0. \tag{3.112}$$

Therefore, using Equations (3.102) and (3.103),

$$(\bar{S}_\ell, \mathcal{L}\bar{S}_\ell) = \pm(S'_\ell, \mathcal{L}S_\ell) = \pm\left(S'_\ell, \left[\frac{2}{r_1} - \frac{2}{r_2} - \frac{2}{r_{13}} + \frac{2}{r_{23}}\right] S_\ell\right) \tag{3.113a}$$

$$= \pm(S_\ell, \mathcal{L}S'_\ell) = \pm\left(S_\ell, \left[\frac{2}{r_1} - \frac{2}{r_3} - \frac{2}{r_{12}} + \frac{2}{r_{23}}\right] S'_\ell\right). \tag{3.113b}$$

Either form can be used to calculate $(\bar{S}_\ell, \mathcal{L}\bar{S}_\ell)$ in the long-range code.

Since C_ℓ and C'_ℓ are also symmetric with their respective swaps, the $(\bar{C}_\ell, \mathcal{L}\bar{S}_\ell)$ matrix element is a similar form given by

$$(\bar{C}_\ell, \mathcal{L}\bar{S}_\ell) = \pm(C'_\ell, \mathcal{L}S_\ell) = \pm\left(C'_\ell, \left[\frac{2}{r_1} - \frac{2}{r_2} - \frac{2}{r_{13}} + \frac{2}{r_{23}}\right] S_\ell\right) \tag{3.114a}$$

$$= \pm(C_\ell, \mathcal{L}S'_\ell) = \pm\left(C_\ell, \left[\frac{2}{r_1} - \frac{2}{r_3} - \frac{2}{r_{12}} + \frac{2}{r_{23}}\right] S'_\ell\right). \tag{3.114b}$$

3.4.2.4 $(\bar{\phi}_i, \mathcal{L}\bar{S}_\ell)$ and $(\bar{\phi}_i, \mathcal{L}\bar{C}_\ell)$ Matrix Elements

The $(\bar{\phi}_i, \mathcal{L}\widetilde{S}_\ell)$ and $(\bar{\phi}_i, \mathcal{L}\widetilde{C}_\ell)$ in Equation (3.56) have combinations of $(\bar{\phi}_i, \mathcal{L}\bar{S})$ and $(\bar{\phi}_i, \mathcal{L}\bar{C})$, as seen in Equation (3.3).

Let us investigate $(\bar{\phi}_i, \mathcal{L}\bar{S}_\ell)$ first.

$$(\bar{\phi}_i, \mathcal{L}\bar{S}_\ell) = \left((\phi_i \pm \phi'_i), \mathcal{L}\frac{(S_\ell \pm S'_\ell)}{\sqrt{2}}\right) = \frac{1}{\sqrt{2}}\left[(\phi_i, \mathcal{L}S_\ell) \pm (\phi_i, \mathcal{L}S'_\ell) \pm (\phi'_i, \mathcal{L}S_\ell) + (\phi'_i, \mathcal{L}S'_\ell)\right] \tag{3.115}$$

Again, from the properties of the P_{23} permutation operator,

$$(\phi_i, \mathcal{L}S_\ell) = (\phi'_i, \mathcal{L}S'_\ell) \text{ and } (\phi_i, \mathcal{L}S'_\ell) = (\phi'_i, \mathcal{L}S_\ell). \tag{3.116}$$

Equation (3.115) becomes

$$(\bar{\phi}_i, \mathcal{L}\bar{S}_\ell) = \frac{1}{\sqrt{2}}\left[2(\phi_i, \mathcal{L}S_\ell) \pm 2(\phi'_i, \mathcal{L}S_\ell)\right] = \frac{2}{\sqrt{2}}\left[(\phi_i, \mathcal{L}S_\ell) \pm (\phi'_i, \mathcal{L}S_\ell)\right] \tag{3.117a}$$

$$= \frac{2}{\sqrt{2}}\left[(\phi_i, \mathcal{L}S_\ell) \pm (\phi_i, \mathcal{L}S'_\ell)\right] \tag{3.117b}$$

Notice that Equations (3.117a) and (3.117b)) are equivalent ways of writing this expression. Either could be used, depending on the form desired for the computation. From Equations (3.102) and (3.103),

$$(\bar{\phi}_i, \mathcal{L}\bar{S}_\ell) = \frac{2}{\sqrt{2}}\left[\left(\phi_i\left(\frac{2}{r_1} - \frac{2}{r_2} - \frac{2}{r_{13}} + \frac{2}{r_{23}}\right)S_\ell\right) \pm \left(\phi_i'\left(\frac{2}{r_1} - \frac{2}{r_2} - \frac{2}{r_{13}} + \frac{2}{r_{23}}\right)S_\ell\right)\right] \tag{3.118}$$

$$= \frac{2}{\sqrt{2}}\left[\left(\phi_i\left(\frac{2}{r_1} - \frac{2}{r_2} - \frac{2}{r_{13}} + \frac{2}{r_{23}}\right)S_\ell\right) \pm \left(\phi_i\left(\frac{2}{r_1} - \frac{2}{r_3} - \frac{2}{r_{12}} + \frac{2}{r_{23}}\right)S_\ell'\right)\right] \tag{3.119}$$

Unlike the long-long matrix elements in Section 3.4.2.3, ϕ_i is neither symmetric nor antisymmetric in the $1 \leftrightarrow 2$ swap, so the direct-direct and exchange-exchange terms are nonzero.

3.4.3 Matrix Elements Involving Only Short-Range Terms

Using the short-range terms given by Equation (3.9) in Equation (2.11) with Equation (3.16) and realizing that the bra is not conjugated in the Kohn-type variational methods [53, 54], the short-short integrals are of the form

$$(\bar{\phi}_i, \mathcal{L}\bar{\phi}_j) = \int\left[\sum_{l=1}^{3}\boldsymbol{\nabla}_{\mathbf{r}_l}\bar{\phi}_i \cdot \boldsymbol{\nabla}_{\mathbf{r}_l}\bar{\phi}_j + \left(\frac{2}{r_1} - \frac{2}{r_2} - \frac{2}{r_3} - \frac{2}{r_{12}} - \frac{2}{r_{13}} + \frac{2}{r_{23}} - 2E\right)\bar{\phi}_i\bar{\phi}_j\right] d\tau. \tag{3.120}$$

Again, the $\bar{\phi}$ represents any of the short-range terms given in Equation (3.9) and could also represent any other Hylleraas-type terms, such as the mixed symmetry terms (see Section 7.5) or the second formalism of the P-wave (see Section 6.3). These matrix elements are numerically integrated using the methods described in Section 4.1.1.

3.5 Schwartz Singularities

A disadvantage of the Kohn-type variational methods is the presence of spurious singularities in the phase shifts. Looking at Equation (3.56), if $\boldsymbol{A}$ becomes near-singular (i.e. $\det \boldsymbol{A} \approx 0$), solving this matrix equation will yield incorrect phase shifts. These "Schwartz singularities" were described first by Schwartz [45] and analyzed by others [140, 141]. These singularities do not make the Kohn-type variational methods unusable, however. These singularities are often easily noticeable, because they do not follow the pattern of other phase shifts, and they do not agree with the results of the other Kohn-type variational methods.

As an example, refer to Figure 3.2(a). This shows an example of Schwartz singularities for the generalized Kohn method with $\tau = 1.4$. A clear Schwartz singularity exists at

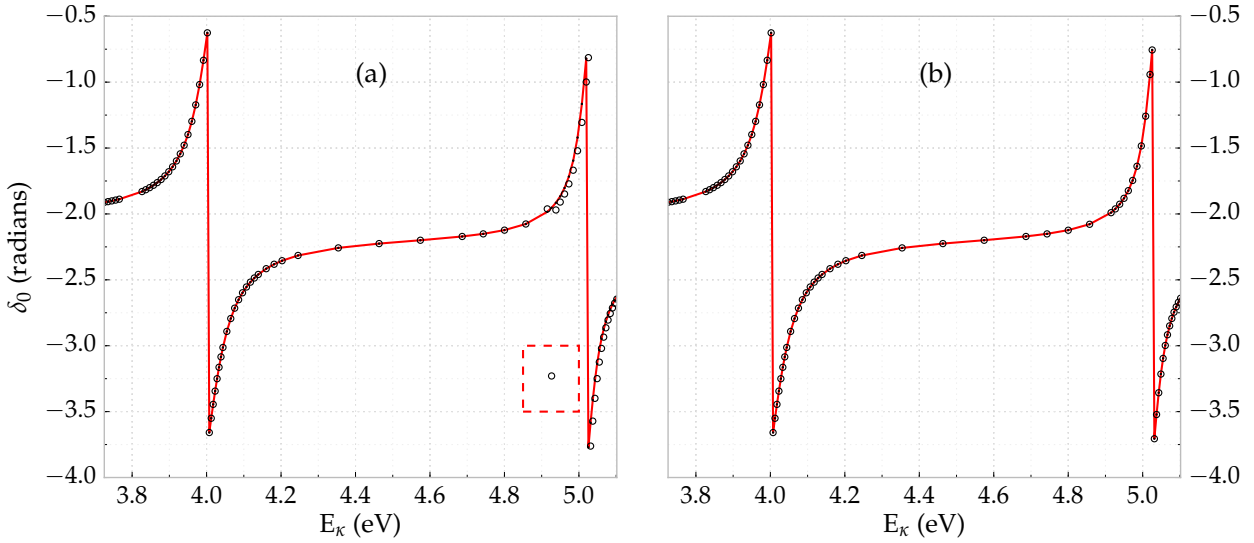

Figure 3.2: Example of Schwartz singularity for ^{1}S at $\omega = 7$. The generalized Kohn method with $\tau = 1.4$ is shown in (a), and the dashed rectangle is surrounding the Schwartz singularity. The corresponding S-matrix complex Kohn phase shifts are shown in (b), and no Schwartz singularities are present.

$\kappa = 0.851$ or $E = 4.927$ eV, which can be seen as a point on the graph that is far away from the red fitting curve. There is also a Schwartz singularity at $\kappa = 0.85$ or $E = 4.915$ eV, seen as a slight deviation from the fitting curve.

The same calculation as in Figure 3.2(a) is performed using the S-matrix complex Kohn in Figure 3.2(b), but no Schwartz singularities are evident. Normally, if one Kohn-type method described in the previous section (Section 3.3) has a Schwartz singularity, other Kohn-type methods will not. This gives us a strategy of simply rejecting Kohn methods that have obvious Schwartz singularities.

Additionally, the complex Kohn methods in Equations (3.73), (3.76), (3.79) and (3.80) are far less likely to suffer from these singularities. A complex-valued Kohn variational method was first proposed by Miller et al. [142] and used the same year by McCurdy et al. [143]. Subsequent work by Lucchese [53] showed that the complex Kohn methods can indeed have Schwartz singularities, but they are not likely to show up in practice. Cooper et al. [54] also showed that the phase shifts obtained using the complex Kohn variational method can be obtained exactly from the real-valued generalized Kohn method in Equation (3.72), but we do not use this method.

There is also much less variability in the results of the different complex Kohn-type variational methods, and even for different values of τ in Equations (3.79) and (3.80), the phase shifts generally agree to great precision (greater than the accuracy that we quote for the phase shifts). Due to the stability and agreement of the complex Kohn variational methods, the results quoted throughout this paper are for the S-matrix complex Kohn unless noted otherwise.

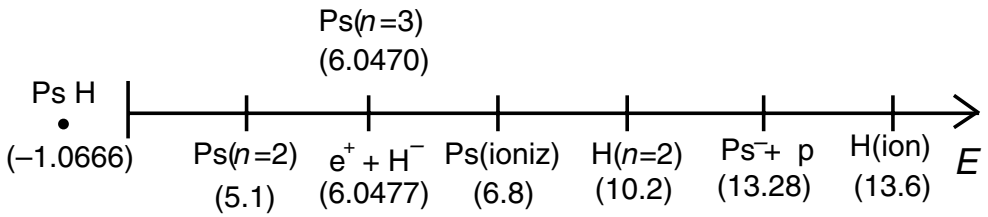

Figure 3.3: Event line for singlet Ps-H scattering from Ref. [72]. Reprinted with permission from Elsevier Limited.

3.6 Resonances

Resonances are where the phase shifts rapidly change by π. We find that there are resonances in each singlet partial wave for Ps-H scattering. Some papers refer to these resonances as Breit-Wigner resonances [144, 145], but according to Bransden and Joachain [43, p.596], Breit-Wigner resonances are a special case of Fano resonances.

The resonance positions and widths can be calculated to high accuracy by fitting the phase shift data to the following curve [58]:

$$\delta(E) = A + BE + CE^2 + \arctan\left[\frac{{}^1\Gamma}{2\left({}^1E_R - E\right)}\right] + \arctan\left[\frac{{}^2\Gamma}{2\left({}^2E_R - E\right)}\right]. \qquad (3.121)$$

The polynomial part of the above equation corresponds to hard sphere scattering. The arctangent parts correspond to the first and second Fano resonances [146, 147, 148], with ${}^1E_R$ and ${}^2E_R$ as the positions of the resonances and ${}^1\Gamma$ and ${}^2\Gamma$ as the widths of the respective resonances. The ^{1}S and ^{1}P partial waves use this fitting, and the ^{1}D and ^{1}F partial waves omit the second term, since we consider only a single resonance. See Sections 5.3.2, 6.4.2, 7.6.2 and 9.4.2 for further discussion of the resonances for each partial wave.

As Blackwood et al. [70] mention, there are an infinite number of Rydberg resonances in each partial wave converging on the e^++H^- threshold at 6.05 eV. Walters et al. [72] gives this as a a more accurate value of 6.0477 eV, as shown in Figure 3.3 from their paper. They also note that the Ps(n=3) threshold is at 6.0470 eV, making these two thresholds nearly the same energy. This work only considers the single channel problem up to the Ps(n=2) threshold at 5.102 eV.

For Ps-H scattering, Drachman predicted that these resonances correspond to the metastable state of e^+ with the H^- ion [149]. A set of close coupling papers [70, 71, 72] confirms that the H^- channel is important for the resonances, indicating that Drachman's prediction was correct. Biswas [150] also showed that H^- formation is important for describing this system.

The first ^{1}S resonance is associated with the $2s$ state [151] and was first calculated by Hazi and Taylor using a stabilization method [129]. The first ^{1}P Rydberg resonance is associated with the $3p$ state, not the $2p$ state [151], while the ^{1}D resonance corresponds

with the 3*d* state [152]. No such analysis exists in the current literature for higher partial waves or resonances for the S-, P- and D-waves other than the first resonance of each.

4 Computation

THIS chapter covers some of the major computational details of this work. For additional details, such as resonance fittings, determination of nonlinear parameters and the use of Gaussian quadratures, refer to Appendix C.

4.1 Short-Range Terms

Matrix elements in Equation (3.56) involving only short-range terms are handled differently than those that involve long-range terms (short-long and long-long). The integrals resulting from using Equations (2.10) and (2.11) in Equation (3.56) are handled in this section.

The bound state problem is a generalized eigenvalue problem (see Equation (2.6)), but to simplify the following discussion, I will refer to the set of matrices **H** and **S** as a single matrix. The diagrams in this section show a single matrix, but it is in actuality a pair of matrices forming the generalized eigenvalue problem.

4.1.1 Short-Range – Short-Range Integrations

The short-range–short-range (short-short) matrix elements make up the bulk of the $\boldsymbol{A}$ matrix (Equation (3.57)). The PsH bound state problem in Chapter 2 consists of only these types of matrix elements (see Equation (2.1)). The form of these short-range integrals is

$$I = \int e^{-(\bar{\alpha}r_1+\bar{\beta}r_2+\bar{\gamma}r_3)} r_1^{k_i} r_2^{l_i} r_{12}^{m_i} r_3^{n_i} r_{13}^{p_i} r_{23}^{q_i} d\mathbf{r}_1 d\mathbf{r}_2 d\mathbf{r}_3, \tag{4.1}$$

with real-valued $\bar{\alpha}, \bar{\beta}, \bar{\gamma} > 0$. The $\bar{\alpha}$ is related to α through Equation (3.56), as are the relations of the other nonlinear parameters $\bar{\beta}$, β, $\bar{\gamma}$, and γ.

This class of integrals, the Hylleraas three-electron or four-body integrals, has been studied extensively. See Refs. [59, 153, 154, 155, 156] for just some of the papers detailing strategies on how to compute these integrals. Refs. [59, 153, 154] use the same infinite

summation to numerically solve this integral but use different techniques to accelerate the convergence, as the summation converges slowly for some arguments. The paper by Pachucki et al. [156] uses a very different approach with recursion relations, described in Section 4.1.1.2.

Each of these methods has some restriction on how singular these integrals can be. For Drake and Yan's asymptotic expansion [59, 60], $k_i, l_i, n_i \geq -2$ and $m_i, p_i, q_i \geq -1$. Yan extends these to $k_i, l_i, m_i, n_i, p_i, q_i \geq -3$ in an additional paper [157]. For the recursion relations of Pachucki et al. [156], $k_i, l_i, m_i, n_i, p_i, q_i \geq -1$. Pachucki and Puchalski have two other papers, one extending this to $k_i, l_i, m_i, n_i, p_i, q_i \geq -2$ [158] and another even extending these to $k_i, l_i, m_i, n_i, p_i, q_i \geq -3$ [159]. Our work for the D-wave has some terms with k_i, l_i, or $n_i = -2$, restricting what methods we can use. The biggest need for integrals more singular than r_i^{-1} or r_{ij}^{-1} in most work (such as lithium energies [160, 161]) is for relativistic or quantum electrodynamics effects [60, 159, 161].

Öhrn and Nordling [162] were the first to give a method to solve this type of integral by splitting it into summations over W functions. To deal with odd powers of r_{ij}, these terms are usually expanded in a Laplace expansion using Perkins's expression [163]. A related expression is given by Sack [164]. Porras and King [165] also use another expansion with Gegenbauer polynomials.

From Drake and Yan's paper [59], splitting into W functions gives

$$\begin{aligned}
I = (4\pi)^3 \sum_{q=0}^{\infty} \sum_{k_{12}=0}^{L_{12}} \sum_{k_{12}=0}^{L_{23}} \sum_{k_{12}=0}^{L_{13}} & \frac{1}{(2q+1)^2} C_{j_{12}qk_{12}} C_{j_{23}qk_{23}} C_{j_{13}qk_{13}} \\
\times [& W(\tilde{k}_i + 2q + 2k_{12} + 2k_{13}, \tilde{l}_i + m_i - 2k_{12} + 2k_{23}, \tilde{n}_i + q_i - 2q - 2k_{23} + p_i - 2k_{13}; \alpha, \beta, \gamma) \\
& + W(\tilde{k}_i + 2q + 2k_{12} + 2k_{13}, \tilde{n}_i + p_i - 2k_{13} + 2k_{23}, \tilde{l}_i + m_i - 2q - 2k_{23} + q_i - 2k_{13}; \alpha, \gamma, \beta) \\
& + W(\tilde{l}_i + 2q + 2k_{12} + 2k_{23}, \tilde{k}_i + m_i - 2k_{12} + 2k_{13}, \tilde{n}_i + q_i - 2q - 2k_{23} + p_i - 2k_{13}; \beta, \alpha, \gamma) \\
& + W(\tilde{l}_i + 2q + 2k_{12} + 2k_{23}, \tilde{n}_i + q_i - 2k_{23} + 2k_{13}, \tilde{k}_i + m_i - 2q - 2k_{23} + p_i - 2k_{13}; \beta, \gamma, \alpha) \\
& + W(\tilde{n}_i + 2q + 2k_{23} + 2k_{13}, \tilde{k}_i + p_i - 2k_{13} + 2k_{12}, \tilde{l}_i + m_i - 2q - 2k_{23} + q_i - 2k_{13}; \gamma, \alpha, \beta) \\
& + W(\tilde{n}_i + 2q + 2k_{23} + 2k_{13}, \tilde{l}_i + q_i - 2k_{23} + 2k_{12}, \tilde{k}_i + m_i - 2q - 2k_{23} + p_i - 2k_{13}; \gamma, \beta, \alpha)].
\end{aligned} \tag{4.2}$$

The C_{jqk} coefficients are given by Perkins [163] as

$$C_{jqk} = \frac{2q+1}{j+2} \binom{j+2}{2k+1} \prod_{t=0}^{\min(q-1), \frac{1}{2}(j+1)} \frac{2k+2t-j}{2k+2q-2t+1}. \tag{4.3}$$

The W functions are expressed as an infinite summation of the ${}_2F_1$ hypergeometric functions [59]:

$$W(l, m, n; \alpha, \beta, \gamma) = \frac{l!}{(\alpha+\beta+\gamma)^{l+m+n+3}} \sum_{p=0}^{\infty} \frac{(l+m+n+p+2)!}{(l+1+p)!(l+m+2+p)} \left(\frac{\alpha}{\alpha+\beta+\gamma}\right)^p$$

$$\times {}_2F_1\left(1, l+m+n+p+3; l+m+p+3; \frac{\alpha+\beta}{\alpha+\beta+\gamma}\right). \tag{4.4}$$

To reduce computation time, we also use the recursion relation in their paper of

$${}_2F_1(1, a; c; z) = 1 + \left(\frac{a}{c}\right) z \; {}_2F_1(1, a+1; c+1; z). \tag{4.5}$$

A derivation of this is given in Appendix B.5.

The k_{ij} summations in Equation (4.2) are all finite. If all powers of r_{ij} are odd, the q summation is infinite, and if any of r_{ij} is even, the q summation becomes finite. For the finite q sums, these direct sums are solved very accurately, but for the infinite sums, some integrals converge slowly. Particularly when all three r_{ij} powers are odd and at least one is -1, the integrals converge the slowest. It is possible to restrict the basis set described by Equation (2.2) so that at least one of the r_{ij} powers is even, making solving the integrals easier. However, this leads to slow convergence in the energy [59].

As Frolov and Bailey [153] note, these four-body integrals only work for systems with one infinitely heavy particle, such as PsH or Ps-H scattering. For systems with arbitrary masses, such as Ps_2 or Ps-Ps scattering, this has to be generalized to

$$I = \int e^{-(\bar{\alpha}r_1 + \bar{\beta}r_2 + \bar{\gamma}r_3 + a_{12}r_{12} + a_{13}r_{13} + a_{23}r_{23})} r_1^{k_i} r_2^{l_i} r_{12}^{m_i} r_3^{n_i} r_{13}^{p_i} r_{23}^{q_i} d\mathbf{r}_1 d\mathbf{r}_2 d\mathbf{r}_3. \tag{4.6}$$

Fromm and Hill give an analytic solution to this [166], but it is extremely difficult to work with. Harris more recently solved this problem analytically using recursion relations [167], using a similar method to the recursion relations of Pachucki et al. [156]. Both of these solutions restrict the powers of r_i and r_{ij} to $k_i, l_i, m_i, n_i, p_i, q_i \geq -1$. We have also looked at a subset of these integrals. As another extension of the Hylleraas basis set, some four-electron integrals can be reduced down to the three-electron integrals [168, 169].

4.1.1.1 Asymptotic Expansion

For cases of Equation (4.2) with all odd powers of r_{ij}, the q summation is infinite, and the summation converges slowly. The convergence accelerator approach of Pelzl and King [154, 169] is one way to deal with this. I did limited testing with this approach but chose to instead use the asymptotic expansion method of Drake and Yan [59]. In my testing, it was more numerically stable, and it has been generalized to arbitrary angular momenta [60].

As an example in Drake and Yan's paper [59], direct calculation of the q summation for $I(0,0,0,-1,-1,-1;1,1,1)$ only reaches an accuracy of $1.5x10^{-13}$ after 6860 terms. With their asymptotic expansion method, the integral has converged to approximately $2.2x10^{-16}$ after only 21 terms. The summation converges monotonically and asymptotically. Drake and Yan use this knowledge to speed up the convergence of the integration. Details of this method can be found in their paper [59].

I use this asymptotic expansion method in all calculations of the short–short integrals through the H-wave, and it performed very well. In fact, my quadruple precision code

N	$S_d(N)$	$\Delta S_d(N)$	$S_a(N)$
17	684.106 432 091		684.113 411 842 629 912 374 349
18	684.107 475 306	0.001 043 214	684.113 411 842 629 911 836 645
19	684.108 320 637	0.000 845 331	684.113 411 842 629 911 829 661
20	684.109 012 851	0.000 692 213	684.113 411 842 629 911 835 071
21	684.109 585 093	0.000 572 241	684.113 411 842 629 911 836 095
22	684.110 062 261	0.000 477 167	684.113 411 842 629 911 836 195
23	684.110 463 302	0.000 401 041	684.113 411 842 629 911 836 186
24	684.110 802 809	0.000 339 506	684.113 411 842 629 911 836 178
25	684.111 092 142	0.000 289 333	684.113 411 842 629 911 836 174
26	684.111 340 236	0.000 248 094	684.113 411 842 629 911 836 173
27	684.111 554 183	0.000 213 946	684.113 411 842 629 911 836 172
28	684.111 739 660	0.000 185 477	684.113 411 842 629 911 836 172
29	684.111 901 249	0.000 161 588	684.113 411 842 629 911 836 172
30	684.112 042 674	0.000 141 425	684.113 411 842 629 911 836 172

Table 4.1: Convergence of direct sum, $S_d(N)$, against the asymptotic expansion, $S_a(N)$. This is an extension of Table I in Drake and Yan's work [59] and uses $\Lambda = 15$. $\Delta S_d(N)$ gives the difference between successive direct sums.

often calculates matrix elements to better than 1 part in 10^{20} for the S-wave. Table 4.1 gives an example of the convergence of a single integral by only calculating the direct sum of Equation (4.2) in the $S_d(N)$ column and with the asymptotic expansion in the $S_a(N)$ column. These four-body integrals are relatively quick to calculate, and most of the runs to compute them for $\ell \leq 2$ complete in a matter of hours on a typical desktop computer.

4.1.1.2 Recursion Relations

After the S-wave calculations were completed, we learned of an analytic, instead of numerical, solution to these three-electron integrals, derived by Pachucki et al. [156]. They were not the first to derive an analytic solution to the three-electron integrals, but the first by Fromm and Hill [166] is not very practical to use, considering its very complicated form. Each set of r_i and r_{ij} powers requires a new rederivation from the Fromm and Hill result. The recursion relations from Pachucki et al. are complicated but also general.

Like many other types of recursion relations, these recursion relations may not be stable for higher ω values, depending on the calculated precision. I have tested through $\omega = 8$, and this method produced stable results under quadruple precision. In some of their work on Li and Be^+, their group uses sextuple precision, as quadruple precision

ω	Used Terms	Total Terms	Percentage Used
1	115	20,000	0.575%
2	921	27,040	3.41%
3	1,939	34,992	5.54%
4	3,140	43,904	7.15%
5	4,573	53,824	8.49%
6	6,246	64,800	9.64%
7	8,147	76,880	10.6%

Table 4.2: S-wave W function terms used

becomes insufficient near $\omega = 10$ [170], which is much higher than we can use in the Ps-H scattering calculations.

These are used as a check on the accuracy of the asymptotic expansion method in Section 4.1.1.1 for the S-wave and P-wave. The D-wave short-range integrals cannot be evaluated using the recursion relations in Ref. [156] due to the r_i^{-2} terms that appear. Solving these using the recursion relations would require implementing the extended method in Ref. [158]. However, the asymptotic expansion method has proven to be stable and accurate so far.

4.1.1.3 W Functions

While evaluating the integrals in the PsH short-range code, we noticed that the W functions in Equation (4.2) could be called more than once by multiple integrals. For the S-wave, there are 34 terms in Equation (2.10), and each matrix element in $\mathbf{H}$ in Equation (2.6) requires these 34 integrals to be evaluated. The overall powers of r_1, r_2, r_{12}, etc. in Equation (4.1) can be the same for a set of ϕ_i with ϕ_j. Also for a set of integrals without the overall powers the same, there is the possibility of two different integrals calling the same W function.

To speed up the partial wave specific programs for the short-short S-, P-, and D-wave matrix elements significantly, we precompute the W functions and store the results in a look up table stored in a 4-dimensional matrix. Even though there is a possibility for the W function arguments to be anywhere in this space, not all of the W matrix elements will be used.

The current S-, P-, and D-wave short-range codes first do a dummy run where the integrals are not actually calculated, but any W matrix elements that need to be computed are marked. Only these are computed, and then the code runs through again using this W matrix look up table. Table 4.2 shows that only 10.6% of the W matrix elements are actually needed for the S-wave at a relatively high value of ω. Similarly for the D-wave,

ω	Used Terms	Total Terms	Percentage Used
0	150	196,290	0.0764%
1	1,670	259,932	0.642%
2	14,076	332,262	4.24%
3	23,384	413,520	5.65%
4	36,418	503,946	7.23%
5	51,420	603,780	8.52%
6	68,438	713,262	9.60%
7	87,520	832,632	10.5%

Table 4.3: D-wave W function terms used

Table 4.3 shows that only 10.5% are needed.

Another more sophisticated method that we have started using is looking instead at the overall integrations instead of the W function arguments using prime factorization to avoid calculating integrals more than once [171].

4.1.2 Linear Dependence in the Bound State Calculation

With infinite precision in calculations, all terms from the basis set could be used. However, due to the limited precision inherent in computer calculations, when using large basis sets, near linear dependences will exist in the matrices. The goal is to identify and eliminate terms that exhibit near linear dependence with other terms. These terms are not exactly linearly dependent, if infinite precision was possible, but they are linearly dependent to computer precision.

To calculate the eigenvalues of the generalized eigenproblem, the LAPACK routine `dsygv` is used [172]. For the basis set consisting of terms from $\omega = 5$, LAPACK computes the eigenvalues without errors. Adding in terms corresponding to $\omega = 6$ for some sets of nonlinear parameters causes `dsygv` to fail with an error set in the last parameter, info. This error is always an integer greater than the number of terms, indicating from the library documentation that "the leading minor of order i of B is not positive definite" [172]. Lüchow and Kleindienst [173] also encountered a similar problem using other libraries.

This error does suggest that one approach to identifying problematic terms is to check for positive definiteness of the overlap matrix $\langle \phi_i | \phi_j \rangle$. This is one method that Yan and Ho [92] use to isolate problematic terms. They test the eigenvalues of the overlap matrix to see if any are small or negative, though there is no mention in their paper of what value of "small" is used. We attempted to use this fact to remove problematic terms, but too many terms were removed, leading to an energy that converged too slowly. In several papers by Yan and others [59, 92, 160, 174, 175], terms with $j1 > j2$ are omitted if $l_1 = l_2$ and $\bar{\alpha} \approx \bar{\beta}$,

along with $j_1 = j_2$ if $j_{23} > j_{31}$.

Another technique Yan and Ho [92] used was to partition the basis set into five sectors, each with a different set of nonlinear parameters and maximum ω. The sectors also have restrictions on the interparticle r_{ij} terms, mainly limiting the power of r_{23} and r_{31}, which are the electron-positron coordinates in their paper (corresponding to r_{12} and r_{13} in our work). These techniques used for restricting the set of terms are not used in our work.

4.1.3 Todd's Method

In trying to determine the energy eigenvalues, we noticed that the ordering of the terms could determine whether there was linear dependence in the matrices. Todd's method [176, 177] was attractive, because it reorders the matrices to obtain the best possible energy, and it is a purely computational approach. We have not seen any physical reason why certain terms should introduce a near linear dependence. Todd's method is very similar to the algorithm in Ref. [178] that we also considered, but it did not work as well. A description of his algorithm as implemented in this work follows.

The total number of terms to look at is $N = N(\omega)$ (see Equation (2.3)). N matrices of size 1x1 are created for each term. This is done for the overlap and the $\langle \phi_i \mid H \mid \phi_j \rangle$ matrices together. The LAPACK `dsygv` routine is used to determine the lowest eigenvalue for each of these N sets. These energy eigenvalues are compared against one another, and the term with the lowest energy is chosen. In the next step, the first basis function from the previous step is combined with each unused term to create N-1 matrices of size 2x2. Again, the energy eigenvalues for each of the N-1 matrices are compared against each other, and the term yielding the lowest energy is chosen as the second basis function. This is done again with 3x3 matrices for each of the N-2 remaining terms combined with the basis functions chosen in the first two steps. This procedure is repeated until all terms have been used or the remaining terms are problematic.

In his original algorithm, Todd looked at the eigenvalues computed from the upper and lower triangular matrices. Normally, the overlap and H matrices are symmetric, but this is not true to machine precision due to truncation and rounding. If the energy eigenvalues from the upper and lower triangles differ by more than 10^{-6} (in atomic units), the last added term is considered problematic and discarded.

In our testing for $\omega = 6$ for the S-wave, no terms were omitted due to the reordering. As noted earlier, before implementing this algorithm, LAPACK would fail when trying to calculate the eigenvalues, so the ordering is important for getting the best possible energy. For $\omega = 7$, 116 terms were omitted, out of a total of 1716 terms. The criteria that the eigenvalues for the upper and lower matrices differs by no more than a certain amount was not needed in this case. The info parameter of the LAPACK `dsygv` function is checked for both the upper and lower matrix eigenvalue calculations, and the last added term is discarded if it causes an error due to linear dependence. When only the 116 problematic terms were left, every one of them caused LAPACK to error. If a term was problematic at any stage, it continued to be problematic in all further stages, so computation time can be decreased by immediately discarding it.

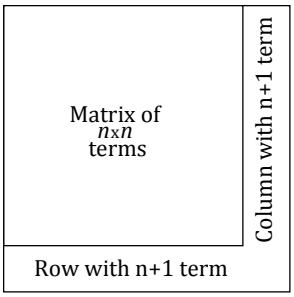

Figure 4.1: Diagram of Todd's procedure

For larger basis sets, this algorithm becomes extremely slow, as determining the eigenvalues is an $O(N^3)$ operation. It can easily be parallelized, since we are computing the eigenvalues for a large number of matrices. Our program has been parallelized using OpenMP [179] for intranode communications and MPI [180] for internode communications. Todd's algorithm provides the best converged energy for a set of terms, albeit at a cost of computational speed.

4.1.4 Restricted Set

Van Reeth and Humberston [57] found that restricting the power of the r_3 coordinate could significantly improve their numerics, allowing them to use more short-range terms. Specifically, we restrict the r_3 power (see Equation (3.9)) so that $n_i \leq 2$ if $\omega \geq 3$, and we refer to this as the restricted set.

We normally use Todd's method applied to the scattering problem, described in Section 4.3, or we use the full unrestricted set when possible. For the cases of ^{1}F and ^{3}F for low κ, described in Section 9.4, we use the restricted set. This allowed us to keep the convergence ratios less than 1 for these cases.

4.2 Long-Range Terms

To minimize verbosity, the long-long and long-short integrations are collectively referred to as the long-range integrations. Each of the long-range integrations are performed using Gaussian quadratures, which are described fully in Appendix C.4.

4.2.1 Long-Range – Long-Range

The scattering program calculates only the short-long and long-long matrix elements. The volume element in Equation (A.8) has an internal angle of φ_{23} to integrate over. When a term has a negative power of r_{23} due to the Hamiltonian in Equations (3.23) to (3.25), a large number of integration points must be used for reasonable accuracy. Instead, we split

the integration such that one part is missing the r_{23}^{-1} term and the other contains only the r_{23}^{-1} term [95, 171].

The first integration excluding the r_{23}^{-1} term has negative powers of r_i and r_{ij} canceled by the corresponding terms in the volume element given by Equation (A.8). For the integration over the r_{23}^{-1} term, we use an alternative volume element, namely that given by equation Equation (A.10). The r_{23}^{-1} is then canceled by the r_{23} in this volume element.

4.2.1.1 Integration without the r_{23}^{-1} term

The simplest long-long matrix element to evaluate is $(\bar{S}_\ell, \mathcal{L}\bar{S}_\ell)$. From Equation (3.113), not including its r_{23}^{-1} term, this is

$$(\bar{S}_\ell, \mathcal{L}\bar{S}_\ell)_A = \pm \left(S'_\ell, \mathcal{L}S_\ell\right)_A = \pm \left(S'_\ell, \left[\frac{2}{r_1} - \frac{2}{r_2} - \frac{2}{r_{13}}\right] S_\ell\right). \tag{4.7}$$

For this type of integration, we use perimetric coordinates as described in Appendix B.3.

$$(\bar{S}_\ell, \mathcal{L}\bar{S}_\ell)_A = \pm 2\pi^2 \int_0^\infty \int_0^\infty \int_0^\infty \int_0^\infty \int_{|r_1-r_3|}^{|r_1+r_3|} \int_0^{2\pi} S'_\ell S_\ell \left[\frac{2}{r_1} - \frac{2}{r_2} - \frac{2}{r_{13}}\right] \tag{4.8}$$

$$\times\, r_2 r_3 r_{12} r_{13}\, d\varphi_{23}\, dr_{13}\, dr_3\, dz\, dy\, dx \tag{4.9}$$

The φ_{23} integration is done analytically. Since S_ℓ and S'_ℓ have no r_{23} dependence and there is no r_{23} term in the brackets, the integration over φ_{23} is simply 2π. The r_{13} integration uses the Gauss-Laguerre quadrature from Appendix C.4. The x, y and z integrations use Gauss-Laguerre quadrature, since they are semi-infinite.

The r_3 integration could also be performed using just the Gauss-Laguerre quadrature. However, the integrand for the r_3 integration has a discontinuity in its slope at $r_3 = r_1$, creating a cusp (see Section 4.2.3), so the accuracy is improved greatly if we split the integration interval into two parts and employ different quadratures for each. The integration is split to use Gauss-Legendre on the interval $(0, r_1)$ and Gauss-Laguerre on the interval (r_1, ∞).

4.2.1.2 Integration over the r_{23}^{-1} term

The other part of the $(\bar{S}_\ell, \mathcal{L}\bar{S}_\ell)$ integral contains the r_{23}^{-1} term.

$$(\bar{S}_\ell, \mathcal{L}\bar{S}_\ell)_B = \pm \left(S'_\ell, \left[\frac{2}{r_{23}}\right] S_\ell\right) \tag{4.10}$$

The volume element for this integral is $d\tau$ from Equation (A.10). The integration also does not need to be converted to perimetric coordinates, so its form is

$$(\bar{S}_\ell, \mathcal{L}\bar{S}_\ell)_B = \pm 8\pi^2 \int_0^\infty \int_0^\infty \int_0^\infty \int_{|r_1-r_3|}^{|r_1+r_3|} \int_{|r_2-r_3|}^{|r_2+r_3|} \int_0^{2\pi} S'_\ell S_\ell \frac{2}{r_{23}} r_1 r_2 r_{13} r_{23}$$

$$\times d\varphi_{12}\, dr_{23}\, dr_{13}\, dr_2\, dr_3\, dr_1. \tag{4.11}$$

The r_{13} and r_{23} integrals have finite limits, so here we use Gauss- Legendre quadrature. Again, for the internal angular integration, this time over φ_{12}, we use Chebyshev-Gauss quadrature. The cusp in the r_3 integration is at $r_3 = r_1$, and the cusp in the r_2 integration is at $r_2 = r_3$. Similar to before, we split up these integrations by using Gauss- Legendre before the cusp and Gauss-Laguerre after the cusp.

The $(\bar{C}_\ell, \mathcal{L}\bar{S}_\ell)$ and $(\bar{C}_\ell, \mathcal{L}\bar{C}_\ell)$ terms are integrated in the same manner as the $(\bar{S}_\ell, \mathcal{L}\bar{S}_\ell)$ integral just described. With all four matrix elements calculated, as mentioned on 41, if the difference of $(\bar{S}_\ell, \mathcal{L}\bar{C}_\ell)$ and $(\bar{C}_\ell, \mathcal{L}\bar{S}_\ell)$ is close to 1, we can have reasonable confidence in the long-long integrations. Another check is that if we explicitly calculate $(S_\ell, \mathcal{L}S_\ell)$, we should get 0 (Equation (3.112)). We find that the choice of innermost integration, over φ_{12} or φ_{13}, can cause this to be nonzero, so this gives us another check on the accuracy of the long-long integrations.

4.2.2 Short-Range – Long-Range

We will consider only the integrations for $(\bar{\phi}_i, \mathcal{L}\bar{S}_\ell)$ here, as the integrations for $(\bar{\phi}_i, \mathcal{L}\bar{C}_\ell)$ are evaluated in the same manner. As in the case of long-long integrations in Section 4.2.1, we split up the integration into two parts – one containing the r_{23}^{-1} term and another containing the rest of the terms. The short-range terms have the added benefit of the possibility of the polynomial $r_{23}^{q_i}$ being present, which cancels the r_{23}^{-1} term or gives it an overall positive power.

From Equations (3.102), (3.103) and (3.117b),

$$\begin{aligned}(\bar{\phi}_i, \mathcal{L}\bar{S}_\ell) &= \frac{2}{\sqrt{2}}\,(\phi_i, \mathcal{L}\bar{S}_\ell) \\ &= \frac{2}{\sqrt{2}} \int \phi_i \left[\left(\frac{2}{r_1} - \frac{2}{r_2} - \frac{2}{r_{13}} + \frac{2}{r_{23}} \right) S_\ell \pm \left(\frac{2}{r_1} - \frac{2}{r_3} - \frac{2}{r_{12}} + \frac{2}{r_{23}} \right) S'_\ell \right] d\tau. \end{aligned} \tag{4.12}$$

4.2.2.1 Case I: $q_i > 0$

When $q_i > 0$ in ϕ_i (Equation (3.9)), the power of r_{23} is equal to or greater than 0. Gaussian quadratures can safely integrate this type of term, so we integrate the full expression in Equation (4.12).

$$\begin{aligned}(\bar{\phi}_i, \mathcal{L}\bar{S}_\ell) = \frac{2}{\sqrt{2}} \cdot 8\pi^2 \int_0^\infty \int_0^\infty \int_0^\infty \int_{|r_1 - r_2|}^{|r_1 + r_2|} \int_{|r_1 - r_3|}^{|r_1 + r_3|} \int_0^{2\pi} \phi_i \\ \times \left[\left(\frac{2}{r_1} - \frac{2}{r_2} - \frac{2}{r_{13}} + \frac{2}{r_{23}} \right) S_\ell \pm \left(\frac{2}{r_1} - \frac{2}{r_3} - \frac{2}{r_{12}} + \frac{2}{r_{23}} \right) S'_\ell \right] \qquad (4.13) \\ \times r_2 r_3 r_{12} r_{13}\, d\varphi_{23}\, dr_{13}\, dr_{12}\, dr_3\, dr_2\, dr_1 \qquad (4.14)\end{aligned}$$

Similar to the long-long integrations from Section 4.2.1, the r_1 integration is performed using the Gauss-Laguerre quadrature. The r_2 integral is broken into two parts at the cusp

of $r_2 = r_1$, with the Gauss-Legendre quadrature before the cusp and the Gauss-Laguerre quadrature after the cusp. In the r_3 coordinate, there is a cusp at $r_3 = r_2$, so the integration is also split up into Gauss-Legendre before the cusp and Gauss-Laguerre after the cusp. The finite intervals for r_{12} and r_{13} ensure that we can use Gauss-Legendre quadratures for these coordinates. The φ_{23} integration uses the Chebyshev-Gauss quadrature.

4.2.2.2 Case II: $q_i = 0$

When $q_i = 0$, the overall power of the r_{23} term is -1, so we cannot use the Gaussian quadratures in the form of Equation (4.13). Similar to the long-long integrations, the r_{23}^{-1} term is integrated separately, using the same type of integrations as Equation (4.13). Refer to the previous section for the description of the quadratures used.

$$\begin{aligned}(\bar{\phi}_i, \mathcal{L}\bar{S}_\ell)_A &= \frac{2}{\sqrt{2}} \int \phi_i \left[\left(\frac{2}{r_1} - \frac{2}{r_2} - \frac{2}{r_{13}} \right) S_\ell \pm \left(\frac{2}{r_1} - \frac{2}{r_3} - \frac{2}{r_{12}} \right) S'_\ell \right] d\tau \\ &= \frac{2}{\sqrt{2}} \cdot 8\pi^2 \int_0^\infty \int_0^\infty \int_0^\infty \int_{|r_1 - r_2|}^{|r_1 + r_2|} \int_{|r_1 - r_3|}^{|r_1 + r_3|} \int_0^{2\pi} \phi_i r_2 r_3 r_{12} r_{13} \\ &\quad \times \left[\left(\frac{2}{r_1} - \frac{2}{r_2} - \frac{2}{r_{13}} \right) S_\ell \pm \left(\frac{2}{r_1} - \frac{2}{r_3} - \frac{2}{r_{12}} \right) S'_\ell \right] d\varphi_{23}\, dr_{13}\, dr_{12}\, dr_3\, dr_2\, dr_1\end{aligned} \tag{4.15}$$

The integration over the r_{23}^{-1} term is done the same way as the second integration of the long-long matrix elements in Section 4.2.1. The r_{23} in the $d\tau$ volume element cancels the r_{23}^{-1} term. Refer to Section 4.2.1.2 for a description of the quadratures used here.

$$\begin{aligned}(\bar{\phi}_i, \mathcal{L}\bar{S}_\ell)_B &= \frac{2}{\sqrt{2}} \int \phi_i \left[\frac{2}{r_{23}} \left(S_\ell \pm S'_\ell \right) \right] d\tau' \\ &= \frac{2}{\sqrt{2}} \cdot 8\pi^2 \int_0^\infty \int_0^\infty \int_0^\infty \int_{|r_1 - r_3|}^{|r_1 + r_3|} \int_{|r_2 - r_3|}^{|r_2 + r_3|} \int_0^{2\pi} \phi_i \left[\frac{2}{r_{23}} \left(S_\ell \pm S'_\ell \right) \right] \\ &\quad \times r_1 r_2 r_{13} r_{23}\, d\varphi_{12}\, dr_{23}\, dr_{13}\, dr_2\, dr_3\, dr_1\end{aligned} \tag{4.16}$$

For a discussion on the final quadrature points used, refer to Appendix C.4.4.

4.2.3 Cusp Behavior

The short-long and long-long matrix element integrals have cusps in the integrands that must be dealt with [55, 95]. As an example, consider$(\bar{\phi}_i, L\bar{C}_0)$ from the S-wave. Using the notation of Section 4.2.1.2, where we are only computing the r_{23}^{-1} terms (given fully later in Equation (5.5) on 67),

$$(\bar{\phi}_i, L\bar{C}_0)_B = 8\pi^2 \int_0^\infty \int_0^\infty \int_0^\infty \int_{|r_1 - r_2|}^{|r_1 + r_2|} \int_{|r_2 - r_3|}^{|r_2 + r_3|} \int_0^{2\pi} \bar{\phi}_i (\mathcal{L}\bar{C})_B$$

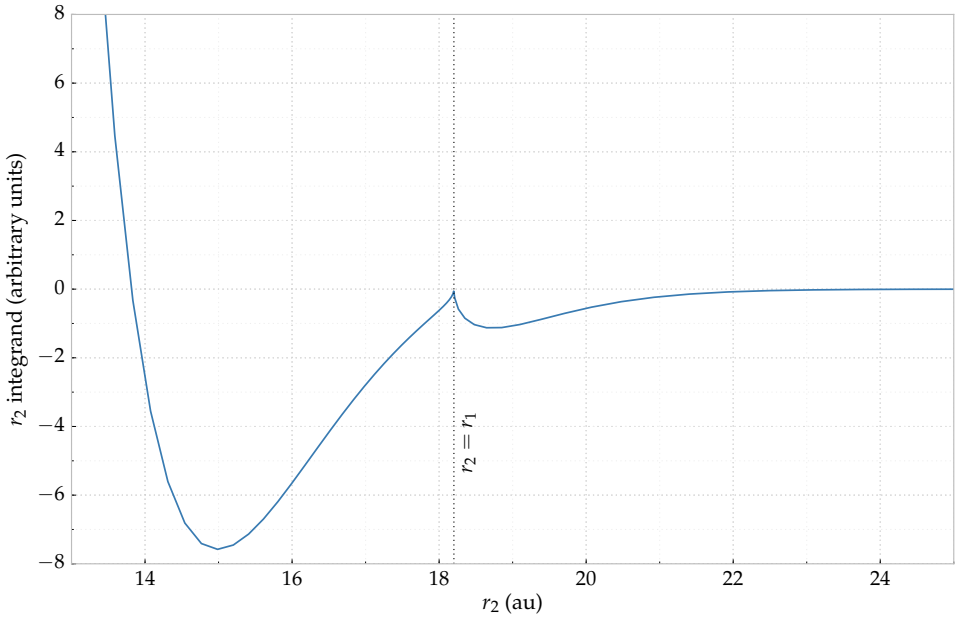

Figure 4.2: Example of cusp in S-wave short-long integration for $1/r_{23}$ term of $(\bar{\phi}_3, \mathcal{L}\bar{C}_0)$ with $r_1 = 18.201$

$$\times\, r_1 r_3 r_{13} r_{23}\, d\varphi_{13}\, dr_{23}\, dr_{12}\, dr_3\, dr_2\, dr_1. \tag{4.17}$$

Due to the integration limits of the r_{13} and r_{23} integrations, the r_2 integrand has a cusp at $r_2 = r_1$, and the r_3 integrand has a cusp at $r_3 = r_2$.

Figure 4.2 shows one such example of this cusp behavior for the r_2 integrand. All inner integrations (φ_{13}, r_{23}, r_{12}, and r_3) are performed with a full set of integration points as described in Table C.17.

The r_2 integration could be performed using just the Gauss-Laguerre quadrature, since we are integrating over $[0, \infty)$. However, the cusp makes this integration slowly convergent. We instead split the integration interval into two parts and employ different quadratures for each. The integration is split to use Gauss-Legendre on the interval $[0, r_1]$ and Gauss-Laguerre (Appendix C.4) on the interval $[r_1, \infty)$. Likewise, the r_3 integration is split into the intervals $[0, r_2]$ and $[r_2, \infty)$.

Doing this splitting requires many more function evaluations, so we use an approximation whenever r_1 is large enough. Specifically when r_1 is greater than a chosen distance, we use Gauss-Laguerre over the entire $[0, \infty)$ range. In the example given in Figure 4.2, at $r_2 = 100$, the r_2 integrand is approximately 10^{-57}, while at $r_2 = 25$, the integrand is approximately 10^{-9}.

For all partial waves, runs were performed with the cusp parameters set at $r_1 = 100$. When $r_1 > 100$, the r_2 and r_3 integrations are done using only Gauss-Laguerre, since the cusp is considered unimportant at that distance. When $r_1 \leq 100$, we use Gauss-Legendre before the cusp and Gauss-Laguerre after the cusp, as described in Sec-

tions 4.2.1.1 and 4.2.1.2.

4.2.4 Extra Exponential

To further improve the convergence of the short-long matrix elements in equation Equation (3.56), we investigated the integrands [171]. The biggest source of difficulty in converging these results comes through the Gauss-Laguerre quadratures in the r_1, r_2 and r_3 integrations. Specifically, the region near the origin is not adequately represented. The integrands fall off quickly due to the exponential falloffs in r_1, r_2 and r_3, so it is not as important to have abscissae far away from the origin. We are using approximately 7 times as many integration points total as the earlier Kohn and inverse Kohn work [57, 58] (see Appendix C.4.4), but this brute force approach of adding quadrature points can increase the computational time greatly. We took another approach to further increase the accuracy. For each of the Gauss- Laguerre quadratures, we introduce an extra $e^{-\lambda r_i}$ and remove it with $e^{\lambda r_i}$ after the quadrature, bringing the abscissae closer to the origin without increasing the number of integration points.

The basic form of the Gauss-Laguerre quadrature is given in Equation (C.2) as

$$\int_0^\infty e^{-x} f(x) dx \approx \sum_{i=1}^{n} w_i f(x_i). \tag{4.18}$$

Introducing an extra $e^{-\lambda x}$ and removing it with $e^{\lambda x}$, we can bring the abscissae closer in by

$$\int_0^\infty e^{-x} f(x) dx \approx \sum_{i=1}^{n} \frac{w_i}{\lambda} f\left(\frac{x_i}{\lambda}\right) \mathrm{e}^{\lambda x_i}. \tag{4.19}$$

As an example, the full expression for the r_2 Gauss-Laguerre quadrature is given by

$$\int_a^\infty e^{-\beta r_2} f(r_2) dr_2 \approx \frac{e^{-\beta a}}{\beta} \sum_{i=1}^{n} w_i f\left(\frac{y_i}{\beta} + a\right), \tag{4.20}$$

where $y_i = \beta x_i$, and a is an arbitrary lower limit starting at the cusp described in Section 4.2.3. With the exponential in λ, this becomes

$$\int_a^\infty e^{-\beta r_2} f(r_2) dr_2 \approx \frac{e^{-a(\beta+\lambda)}}{\beta+\lambda} \sum_{i=1}^{n} w_i f\left(\frac{r_2 + a(\beta+\lambda)}{\beta+\lambda}\right) \mathrm{e}^{\lambda r_2}. \tag{4.21}$$

Figure 4.3 shows the effect of introducing this λ into the r_1 exponential. We use 50 quadrature points for each curve, meaning that there are points represented past the cutoff of 18 au in the graph. For the black curve with $\lambda = 0$, the curve is very jagged around the peak of approximately 4 au. With $\lambda = 1.0$, the curve is much smoother, and as λ is increased to 2.0, the peak is represented even better. If λ is too large, the area near the origin may be overrepresented and the area farther out may be underrepresented. We

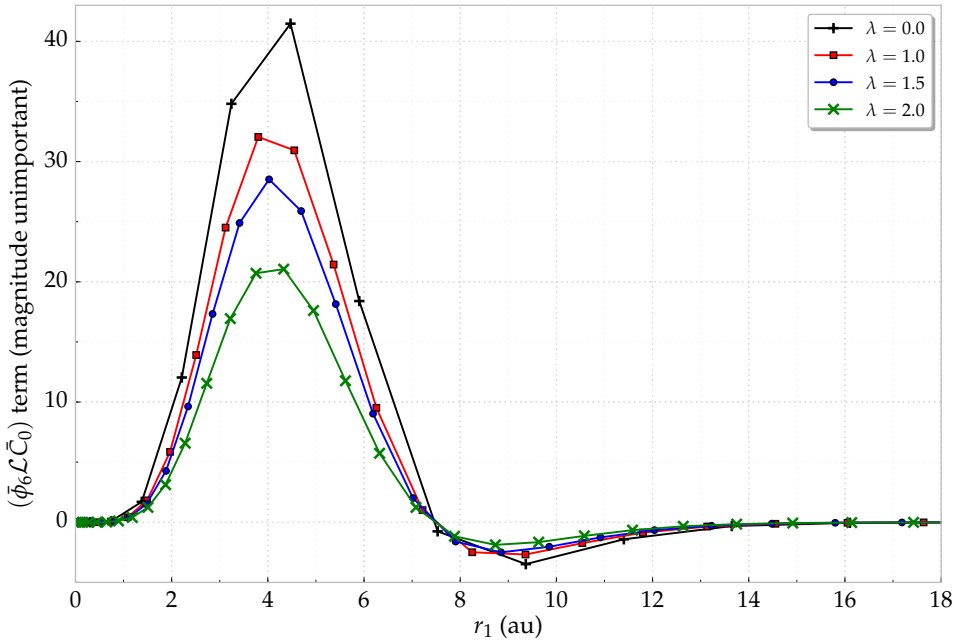

Figure 4.3: Effect of introducing λ in r_1 exponential

have chosen $\lambda = 1.0$ for all of our runs for the r_1, r_2 and r_3 coordinates, which gives better representation near the origin but does not run the risk of neglecting the small contribution of the curve for large r_i values. Our D-wave and general long-range codes could use different λ for each of the r_1, r_2 and r_3 integrations, but we set them equal here. The matrix elements converge better for $\lambda = 1.0$ than for $\lambda = 0$.

4.3 Phase Shifts

We solve for the phase shifts by solving Equation (3.56) for $\boldsymbol{X}$ and then using Equations (3.64) and (3.67). Note that as mentioned in Section 3.3, we only have to calculate one set of integrals for the Kohn variational method, and the other Kohn-type methods are used by rearrangement of these integrals in the matrix equation. The different Kohn-type variational methods typically agree well when linear dependence in the matrix equation does not occur. We use this fact to determine how many short-range terms we are able to use in our final calculations. If we plot the ^{1}S phase shifts with respect to the number of terms, as in Figure 4.4, it is clear that around 1530 terms, the phase shifts from the different generalized Kohn methods begin to diverge. In this particular example, we chose the cutoff as a more conservative 1505 terms–before the "jump" that precedes the clear divergence. No Schwartz singularities (Section 3.5) are evident here, but if any are present, we discard the generalized Kohn variational methods that contain spurious singularities.

Using the short-range terms chosen by Todd's method (Section 4.1.3) normally allows

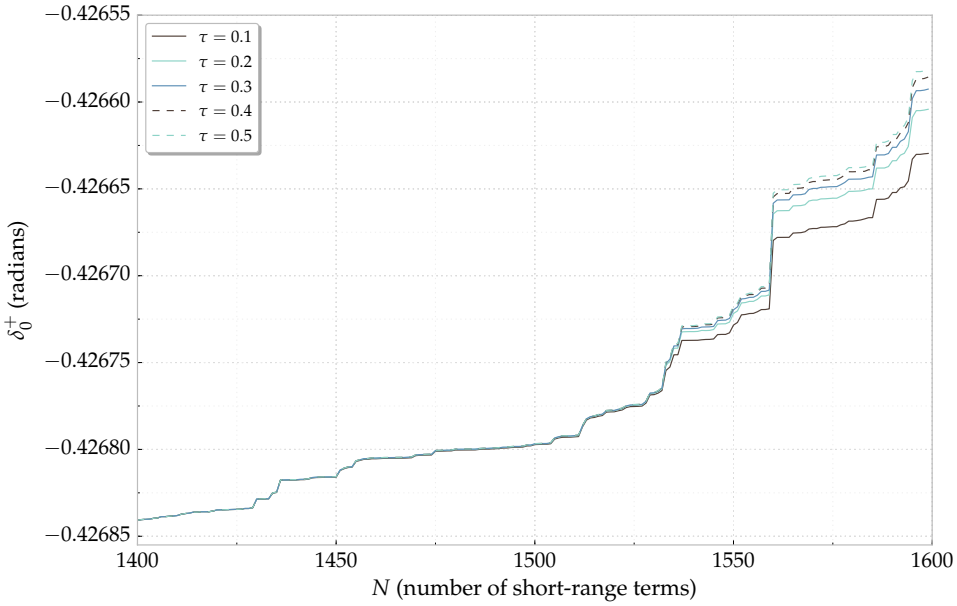

Figure 4.4: Breakdown in convergence of the ^1S phase shifts with respect to number of short-range terms for different τ values for the generalized Kohn variational method

us to increase the number of terms used over using the terms chosen just by Equation (2.2) for the Ps-H scattering problem. Since Todd's method chooses an ordering with the most "important" terms at the beginning, we obtain well-converged phase shifts using this method with the above-mentioned cutoffs for the first two partial waves (which do not have omitted symmetries). So we perform one truncation of the basis set by using Todd's method for just the short-range terms and then an additional truncation by using plots as in Figure 4.4 to reduce linear dependence.

The number of terms used for each partial wave are given in Appendix C.2, denoted as $N'(\omega)$. For $\ell \geq 3$, we either use the full set of terms described by Equation (2.2) or the restricted set described in Section 4.1.4.

The phase shifts presented in this work are found using the S-matrix complex Kohn, unless otherwise indicated. We normally only use the Kohn, inverse Kohn, and generalized Kohn variational method results to determine the number of short-range terms to use as described in this section. Then the phase shifts for this set of terms with the S-matrix complex Kohn method are determined.

4.4 Convergence and Extrapolations

For comparing quantities such as the convergence of the matrix elements or the convergence of the differential cross sections, we use the percent difference:

$$\% \text{ Diff} = \left| \frac{a-b}{(a+b)/2} \right| \times 100\%, \tag{4.22}$$

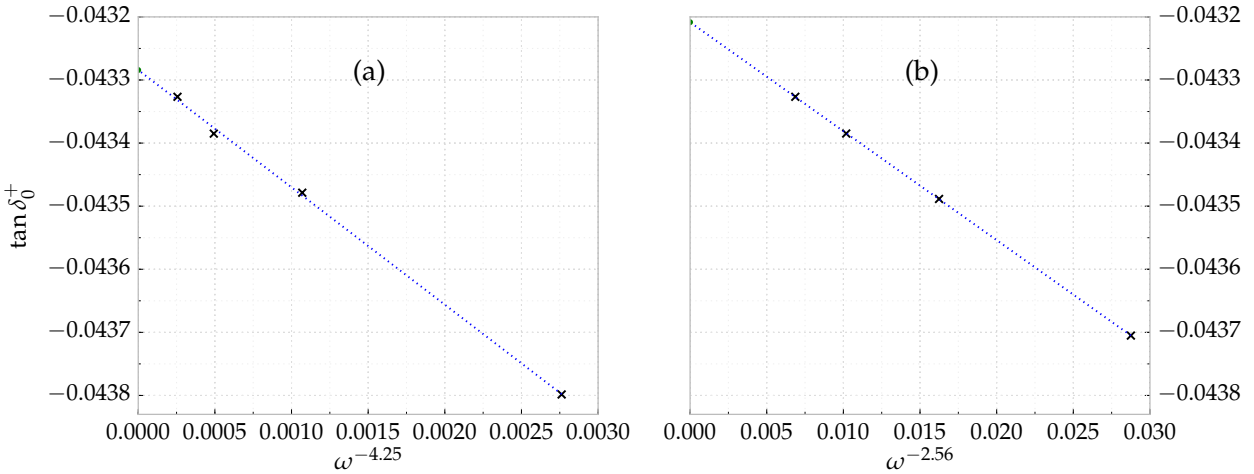

Figure 4.5: Extrapolation for ^{1}S at $\kappa = 0.01$. The extrapolation without resorting the short-range terms into increasing ω is given in (a), and the resorted version is in (b).

where a and b can represent any of these quantities. When we can compare convergence with respect to ω, we define a convergence ratio as

$$R'(\omega) = \frac{\delta_\ell^\pm(\omega) - \delta_\ell^\pm(\omega-1)}{\delta_\ell^\pm(\omega-1) - \delta_\ell^\pm(\omega-2)}. \tag{4.23}$$

This is similar to the inverse of the ratio for the energy eigenvalues given in Ref. [92]. If $R'(\omega) \geq 1$, there is no convergence pattern. A ratio of less than 1 shows convergence but does not guarantee a reliable extrapolation. We find that $R'(\omega) \lesssim 0.5$ is needed to properly extrapolate phase shifts. We also find that when $\delta_\ell \lesssim 10^{-4}$, the convergence often becomes poor (see Section 7.6.1).

The tangent of the phase shifts is fitted to the function

$$\tan\delta_\ell^\pm(\omega) = \tan\delta_\ell^\pm(\omega\to\infty) + \frac{c}{\omega^p}. \tag{4.24}$$

The c and p in this equation are fitting parameters and depend on each extrapolation. When plotted with respect to ω^{-p}, the tangents of the phase shifts form nearly a straight line, with the y-intercept being the tangent of the extrapolated value of the phase shift, $\tan\delta^\pm(\omega\to\infty)$.

Van Reeth and Humberston [57] do the extrapolation using $\omega = 3$ through $\omega = 6$. We have completed the extrapolation using the sets $\omega = 3-6$, $\omega = 3-7$ and $\omega = 4-7$. The smallest residuals are normally found with the set $\omega = 4-7$. The values of the extrapolated phase shifts using this method are in Table 5.1.

As described in Section 4.1.3, we omit certain terms using Todd's method. The output of this method from the bound state program described in Section 4.1.3 is not ordered in

terms of increasing ω. This leads to difficulties when attempting to do the extrapolation in Equation (4.24). The tangent of the phase shifts cannot be fitted to a straight line in this order, as seen in Figure 4.5(a). If we reorder the short-range terms back into their original order while still omitting terms, the tangent of the phase shifts can now be fitted to this straight line, as can be seen in Figure 4.5(b). The reordering does not affect the phase shifts in any case that we tested, since more terms are normally omitted in the scattering problem than just the bound state problem.

We also extrapolate scattering lengths as shown in Equation (11.3). There is no clear convergence pattern for the effective ranges, which are described in Section 11.1.

5 S-Wave

THE S-wave is the simplest of the partial waves to consider, since the spherical harmonic $Y_0^0(\theta_\rho, \varphi_\rho)$ is constant. The form of the Kohn matrix elements was derived in Chapter 3 for general ℓ, but when we started this project, we went through the S-wave derivation first and wrote code to compute this partial wave only. This chapter shows the matrix elements specifically for the S-wave, which can be shown from the general results in Chapter 3. The code described in Chapter 8 works for any partial wave but is slower than the S-wave specific code (Appendix D).

Van Reeth and Humberston [57] previously performed ^{1,3}S-wave Ps-H calculations using the Kohn and inverse Kohn. We extend their work here and used Van Reeth's notes and code [171] for guidance, though we rederived everything, and I wrote my own codes.

5.1 Wavefunction

The general wavefunction for any ℓ is given in Equation (3.1), and the S-wave version is

$$\Psi_0^{\pm,t} = \widetilde{S}_0 + L_0^{\pm,t}\,\widetilde{C}_0 + \sum_{i=1}^{N'(\omega)} c_i \bar{\phi}_i. \tag{5.1}$$

The S-wave has only one set of short-range terms. $\widetilde{S}_0$, $\widetilde{C}_0$, and $\bar{\phi}_i$ are given by Equations (3.3) and (3.9). The forms of the short-range terms in Equation (3.9) are equivalent for the S-wave ($\ell = 0$). There is one notable difference about what we did here for the S-wave versus the general code, namely that we absorb the spherical harmonic on the short-range terms into the c_i coefficients, similar to what we did with the $\frac{1}{\sqrt{2}}$.

5.2 Matrix Elements with $\mathcal{L}\bar{C}_0$

These can be calculated using the results in Section 3.4.2.2, but the S-wave code was written using these derivations. The analysis for $\mathcal{L}C_0$ is more difficult than that of $\mathcal{L}S_0$

in Equation (3.102) and Equation (3.103). The shielding factor, $f_0(\rho)$, complicates the derivatives slightly.

$$\mathcal{L}C_0 = \left(-\frac{1}{2}\nabla^2_{\boldsymbol{\rho}} - \nabla^2_{\mathbf{r}_3} - 2\nabla^2_{\mathbf{r}_{12}} + \frac{2}{r_1} - \frac{2}{r_2} - \frac{2}{r_3} - \frac{2}{r_{12}} - \frac{2}{r_{13}} + \frac{2}{r_{23}} - 2E_H - 2E_{Ps} - \frac{1}{2}\kappa^2\right) \times \Phi_{Ps}(r_{12})\Phi_H(r_3)\frac{\cos(\kappa\rho)}{\kappa\rho}\sqrt{\frac{2\kappa}{4\pi}}\left[1 + e^{-\mu\rho}\left(1 + \frac{\mu}{2}\rho\right)\right] \tag{5.2}$$

Again, we use Equations (3.27a) and (3.27b)) to simplify this expression.

$$\mathcal{L}C_0 = \left(-\frac{1}{2}\nabla^2_{\boldsymbol{\rho}} + \frac{2}{r_1} - \frac{2}{r_2} - \frac{2}{r_{13}} + \frac{2}{r_{23}} - \frac{1}{2}\kappa^2\right) \times \Phi_{Ps}(r_{12})\Phi_H(r_3)\frac{\cos(\kappa\rho)}{\kappa\rho}\sqrt{\frac{2\kappa}{4\pi}}\left[1 + e^{-\mu\rho}\left(1 + \frac{\mu}{2}\rho\right)\right] \tag{5.3}$$

Similar to Appendix B.4.2, $n_0(\kappa\rho)$ is an eigenfunction of $\nabla^2_{\boldsymbol{\rho}}$ with eigenvalue $-\kappa^2$. To properly take into account the shielding function, we use the code in Figure 3.1 for the S-wave, yielding

$$\frac{1}{2}\left(\nabla^2_{\boldsymbol{\rho}} + \kappa^2\right) Y_0^0(\theta_\rho, \varphi_\rho)\, n_0(\kappa\rho) f_0(\rho) = \frac{2\kappa f'(\rho)\sin(\kappa\rho) - f''(\rho)\cos(\kappa\rho)}{2\kappa\rho}. \tag{5.4}$$

The $f'(\rho)$ and $f''(\rho)$ are given in Equation (3.107). Combining Equations (5.3) and (5.4) and the permuted versions gives

$$\begin{aligned}
\mathcal{L}\bar{C}_0 &= \frac{1}{\sqrt{2}}\mathcal{L}(C_0 \pm C_0') = \frac{1}{\sqrt{2}}(\mathcal{L}C_0 \pm \mathcal{L}C_0') \\
&= \frac{1}{\sqrt{8\pi}}\Phi_{Ps}(r_{12})\Phi_H(r_3)\sqrt{2\kappa} \\
&\quad \times \left\{\frac{\kappa\mu}{2}e^{-\mu\rho}(1+\mu\rho)\frac{\sin(\kappa\rho)}{\kappa\rho} + \frac{\mu^3\rho}{4}e^{-\mu\rho}\frac{\cos(\kappa\rho)}{\kappa\rho}\right. \\
&\quad \left. + \left(\frac{2}{r_1} - \frac{2}{r_2} - \frac{2}{r_{13}} + \frac{2}{r_{23}}\right)\frac{\cos(\kappa\rho)}{\kappa\rho}\left[1 - e^{-\mu\rho}\left(1 + \frac{\mu}{2}\rho\right)\right]\right\} \\
&\pm \frac{1}{\sqrt{8\pi}}\Phi_{Ps}(r_{13})\Phi_H(r_2)\sqrt{2\kappa} \\
&\quad \times \left\{\frac{\kappa\mu}{2}e^{-\mu\rho'}(1+\mu\rho')\frac{\sin(\kappa\rho')}{\kappa\rho'} + \frac{\mu^3\rho'}{4}e^{-\mu\rho'}\frac{\cos(\kappa\rho')}{\kappa\rho'}\right. \\
&\quad \left. + \left(\frac{2}{r_1} - \frac{2}{r_3} - \frac{2}{r_{12}} + \frac{2}{r_{23}}\right)\frac{\cos(\kappa\rho')}{\kappa\rho'}\left[1 - e^{-\mu\rho'}\left(1 + \frac{\mu}{2}\rho'\right)\right]\right\}.
\end{aligned} \tag{5.5}$$

5.2.1 $(\bar{C}_0, \mathcal{L}\bar{C}_0)$ Matrix Element

Using Equations (3.4) and (3.82),

$$(\bar{C}_0, \mathcal{L}\bar{C}_0) = \frac{1}{2}\left[2(C_0, \mathcal{L}C_0) \pm 2(C_0', \mathcal{L}C_0)\right] = (C_0, \mathcal{L}C_0) \pm (C_0', \mathcal{L}C_0). \tag{5.6}$$

Substitute Equations (3.6b) and (5.5) in Equation (5.6) and simplify to get

$$\begin{aligned}(\bar{C}_0, \mathcal{L}\bar{C}_0) =& \frac{\kappa\mu}{2}\left((C_0 \pm C_0')e^{-\mu\rho}(1+\mu\rho)S_0\right) \\ &+ \sqrt{\frac{2\kappa}{4\pi}}\frac{\mu^3}{4}\left((C_0 \pm C_0')e^{-\mu\rho}\frac{\cos(\kappa\rho)}{\kappa\rho}\Phi_{Ps}(r_{12})\Phi_H(r_3)\right) \\ &+ \left((C_0 \pm C_0')\left(\frac{2}{r_1} - \frac{2}{r_3} - \frac{2}{r_{12}} + \frac{2}{r_{23}}\right)C_0\right).\end{aligned} \tag{5.7}$$

Looking at just the last term:

$$\begin{aligned}&\left((C_0 \pm C_0')\left(\frac{2}{r_1} - \frac{2}{r_3} - \frac{2}{r_{12}} + \frac{2}{r_{23}}\right)C_0\right) \\ &\quad= \left(\left(\frac{2}{r_1} - \frac{2}{r_3} - \frac{2}{r_{12}} + \frac{2}{r_{23}}\right)C_0^2\right) \pm \left(\left(\frac{2}{r_1} - \frac{2}{r_3} - \frac{2}{r_{12}} + \frac{2}{r_{23}}\right)C_0'C_0\right).\end{aligned} \tag{5.8}$$

The first set of parentheses has the same form as Equation (3.113). These terms in parentheses are antisymmetric with respect to the $1 \leftrightarrow 2$ permutation. Also, C_0 is symmetric with respect to this permutation. So the first set of parentheses is 0. Thus,

$$\left((C_0 \pm C_0')\left(\frac{2}{r_1} - \frac{2}{r_3} - \frac{2}{r_{12}} + \frac{2}{r_{23}}\right)C_0\right) = \pm\left(C_0'\left(\frac{2}{r_1} - \frac{2}{r_3} - \frac{2}{r_{12}} + \frac{2}{r_{23}}\right)C_0\right) \tag{5.9}$$

We finally have that

$$\begin{aligned}(\bar{C}_0, \mathcal{L}\bar{C}_0) =& \frac{\kappa\mu}{2}\left((C_0 \pm C_0')e^{-\mu\rho}(1+\mu\rho)S_0\right) \\ &+ \sqrt{\frac{2\kappa}{4\pi}}\frac{\mu^3}{4}\left((C_0 \pm C_0')e^{-\mu\rho}\frac{\cos(\kappa\rho)}{\kappa\rho}\Phi_{Ps}(r_{12})\Phi_H(r_3)\right) \\ &\pm \left(C_0'\left(\frac{2}{r_1} - \frac{2}{r_3} - \frac{2}{r_{12}} + \frac{2}{r_{23}}\right)C_0\right).\end{aligned} \tag{5.10}$$

This is the form that is used in the S-wave long-range code (Appendix D).

5.2.2 $(\bar{\phi}_i, \mathcal{L}\bar{C}_0)$ Matrix Elements

For the S-wave, following the work of Van Reeth [95], we chose to absorb both the $\frac{1}{\sqrt{2}}$ and $Y_0^0(\theta_\rho, \varphi_\rho) = \frac{1}{\sqrt{4\pi}}$ into the c_i constants of the short-range terms in Equation (3.9).

From Equation (3.82),

$$(\bar{\phi}_i, \mathcal{L}\bar{C}_0) = \frac{2}{\sqrt{2}}\left[(\phi_i, \mathcal{L}C_0) \pm (\phi_i', \mathcal{L}C_0)\right] \tag{5.11a}$$

$$= \frac{2}{\sqrt{2}}\left[(\phi_i, \mathcal{L}C_0) \pm (\phi_i, \mathcal{L}C_0')\right]. \tag{5.11b}$$

Using Equation (5.5) in the above gives the results for $(\bar{\phi}_i, \mathcal{L}\bar{C}_0)$.

$$\begin{aligned}(\bar{\phi}_i, \mathcal{L}\bar{C}_0) =& \sqrt{\frac{\kappa}{\pi}}\left((\phi_i \pm \phi_i')\Phi_{Ps}(r_{12})\Phi_H(r_3)\left\{\left(\frac{2}{r_1} - \frac{2}{r_2} - \frac{2}{r_{13}} + \frac{2}{r_{23}}\right)\frac{\cos(\kappa\rho)}{\kappa\rho}\right.\right. \\ & \left.\left. \times\left[1 - e^{-\mu\rho}\left(1 + \frac{\mu}{2}\rho\right)\right] + \frac{e^{-\mu\rho}\mu^3\rho}{4}\frac{\cos(\kappa\rho)}{\kappa\rho} + \frac{e^{-\mu\rho}}{2}\kappa\mu(1+\mu\rho)\frac{\sin(\kappa\rho)}{\kappa\rho}\right\}\right)\end{aligned} \tag{5.12a}$$

$$\begin{aligned}=& \sqrt{\frac{\kappa}{\pi}}\left(\phi_i\Phi_{Ps}(r_{12})\Phi_H(r_3)\left\{\left(\frac{2}{r_1} - \frac{2}{r_2} - \frac{2}{r_{13}} + \frac{2}{r_{23}}\right)\frac{\cos(\kappa\rho)}{\kappa\rho}\left[1 - e^{-\mu\rho}\left(1 + \frac{\mu}{2}\rho\right)\right]\right.\right. \\ & \left.\left. + \frac{e^{-\mu\rho}\mu^3\rho}{4}\frac{\cos(\kappa\rho)}{\kappa\rho} + \frac{e^{-\mu\rho}}{2}\kappa\mu(1+\mu\rho)\frac{\sin(\kappa\rho)}{\kappa\rho}\right\}\right) \\ & \pm\sqrt{\frac{\kappa}{\pi}}\left(\phi_i\Phi_{Ps}(r_{12})\Phi_H(r_3)\left\{\left(\frac{2}{r_1} - \frac{2}{r_3} - \frac{2}{r_{12}} + \frac{2}{r_{23}}\right)\frac{\cos(\kappa\rho')}{\kappa\rho'}\left[1 - e^{-\mu\rho'}\left(1 + \frac{\mu}{2}\rho'\right)\right]\right.\right. \\ & \left.\left. + \frac{e^{-\mu\rho}\mu^3\rho'}{4}\frac{\cos(\kappa\rho')}{\kappa\rho'} + \frac{e^{-\mu\rho'}}{2}\kappa\mu(1+\mu\rho')\frac{\sin(\kappa\rho')}{\kappa\rho'}\right\}\right)\end{aligned} \tag{5.12b}$$

Either of these forms can be used. We use the second form, since this only has ϕ_i, not ϕ_i and ϕ_i'.

5.3 Results

5.3.1 Phase Shifts

All runs here were performed using the set of integration points described in Appendix C.4.4. The number of terms used for ^{1}S was determined using the procedure in Appendix C.3, and for ^{3}S, the method in Section 4.3. The phase shifts are calculated with the programs described in Appendix D. Table 5.1 shows the ^{1,3}S phase shifts calculated using the S-matrix complex Kohn at regular intervals of κ, which we compare to the results from other groups in Table 5.2. The extrapolations in the fourth and fifth columns are performed using the technique described in Section 4.4. The last two columns show the percent difference given by Equation (4.22).

Table 5.2 gives comparisons between the complex Kohn phase shifts and phase shifts calculated elsewhere in the literature. The $\omega = 7$ phase shifts from this table are the same

κ	$\delta^+(\omega = 7)$	$\delta^-(\omega = 7)$	$\delta^+(\omega \to \infty)$	$\delta^-(\omega \to \infty)$	% Diff$^+$	% Diff$^-$
0.1	-0.427	-0.215	-0.426	-0.214	0.223%	0.120%
0.2	-0.820	-0.431	-0.819	-0.431	0.010%	0.063%
0.3	-1.161	-0.645	-1.161	-0.645	0.040%	0.094%
0.4	-1.446	-0.850	-1.446	-0.849	0.022%	0.130%
0.5	-1.678	-1.041	-1.677	-1.040	0.031%	0.166%
0.6	-1.858	-1.217	-1.857	-1.214	0.040%	0.273%
0.7	-1.964	-1.375	-1.963	-1.372	0.045%	0.250%

Table 5.1: ^{1,3}S phase shifts using the S-matrix complex Kohn. % Diff$^+$ and % Diff$^-$ are the percent differences between the current complex Kohn $\omega = 7$ and $\omega \to \infty$ results.

as Van Reeth and Humberston's results for $\omega = 6$ [57], with some exceptions in the last digit. This indicates that the prior Kohn variational method S-wave phase shifts were well converged, despite only using 721 short-range terms. We use a larger basis set here, which brings the phase shifts up slightly, but the larger set of integration points for the long-range terms (see Appendix C.4.3) tended to bring the phase shifts down slightly. Figure 5.1 has the more complete set of phase shifts plotted with respect to the incoming Ps energy, $E_{\boldsymbol{\kappa}}$. This compares the complex Kohn phase shifts to that of the ^{1}S CC [72] and the ^{3}S CC [70], along with the ^{1,3}S CVM [181].

As seen in Table 5.2 and Figure 5.1, the ^{1}S CC phase shifts are slightly below the complex Kohn phase shifts, with a larger difference at higher κ. The complex Kohn ^{3}S results are almost exactly the same as the prior Kohn [57], and Van Reeth and Humberston noted then that the CC ^{3}S phase shifts were higher. For scattering problems, there is no rigorous bound, but the phase shifts are typically empirically bound. In the inset in Figure 5.1 however, we see that the recent CVM results line up well with the complex Kohn results for both ^{1}S and ^{3}S, potentially indicating that complex Kohn phase shifts are more accurate than the CC.

Figure 5.2 shows comparisons of the complex Kohn phase shifts to that of other groups for calculations of ^{1}S and ^{3}S. The different Kohn-type methods agree to the accuracy given after methods with Schwartz singularities are removed. The current S-matrix complex Kohn results are extremely close to Van Reeth and Humberston's results [57], so they follow along the solid line as well. Several groups have results that cluster very closely to the current S-matrix complex Kohn phase shifts, namely Blackwood et al. [70], Walters et al. [72], Chiesa et al. [63] and Ivanov et al. [65]. Ivanov et al. [65] discuss that the higher phase shifts of Adhikari and Biswas [68] are likely to be in error. Likewise, the further ^{1}S calculations by Biswas et al. [183] are near that of Adhikari and Biswas [68]. The Biswas et al. [150] phase shifts agree relatively well with the current complex Kohn and that of

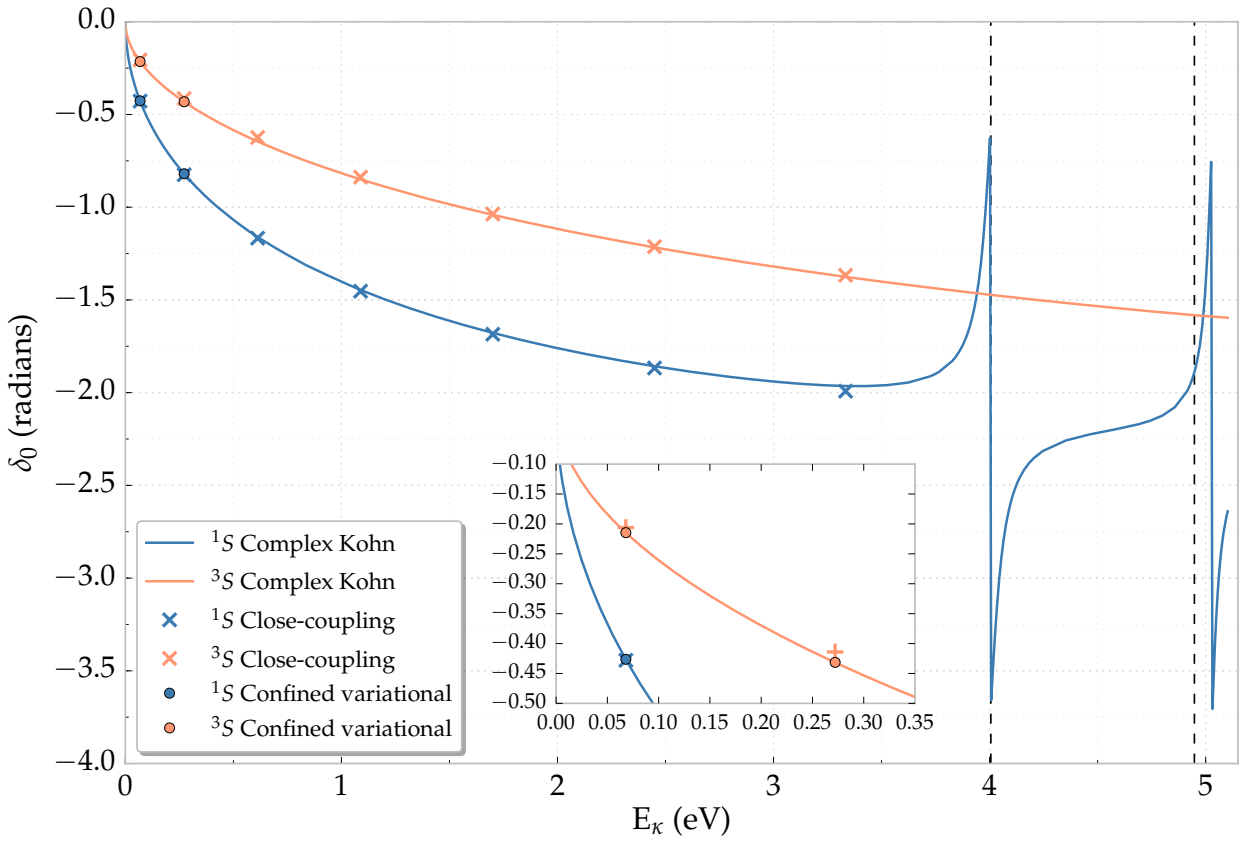

Figure 5.1: ^{1,3}S complex Kohn phase shifts. The ^1S CC phase shifts [72] are given by $\times$, and the ^3S CC phase shifts [70] are given by $+$. The CVM ^1S and ^3S phase shifts [181] are blue and red circles, respectively. Vertical dashed lines denote the complex rotation resonance positions [92, 175, 182]. An interactive version of this figure is available online [3] at `https://plot.ly/~Denton/3/s-wave-ps-h-scattering/`.

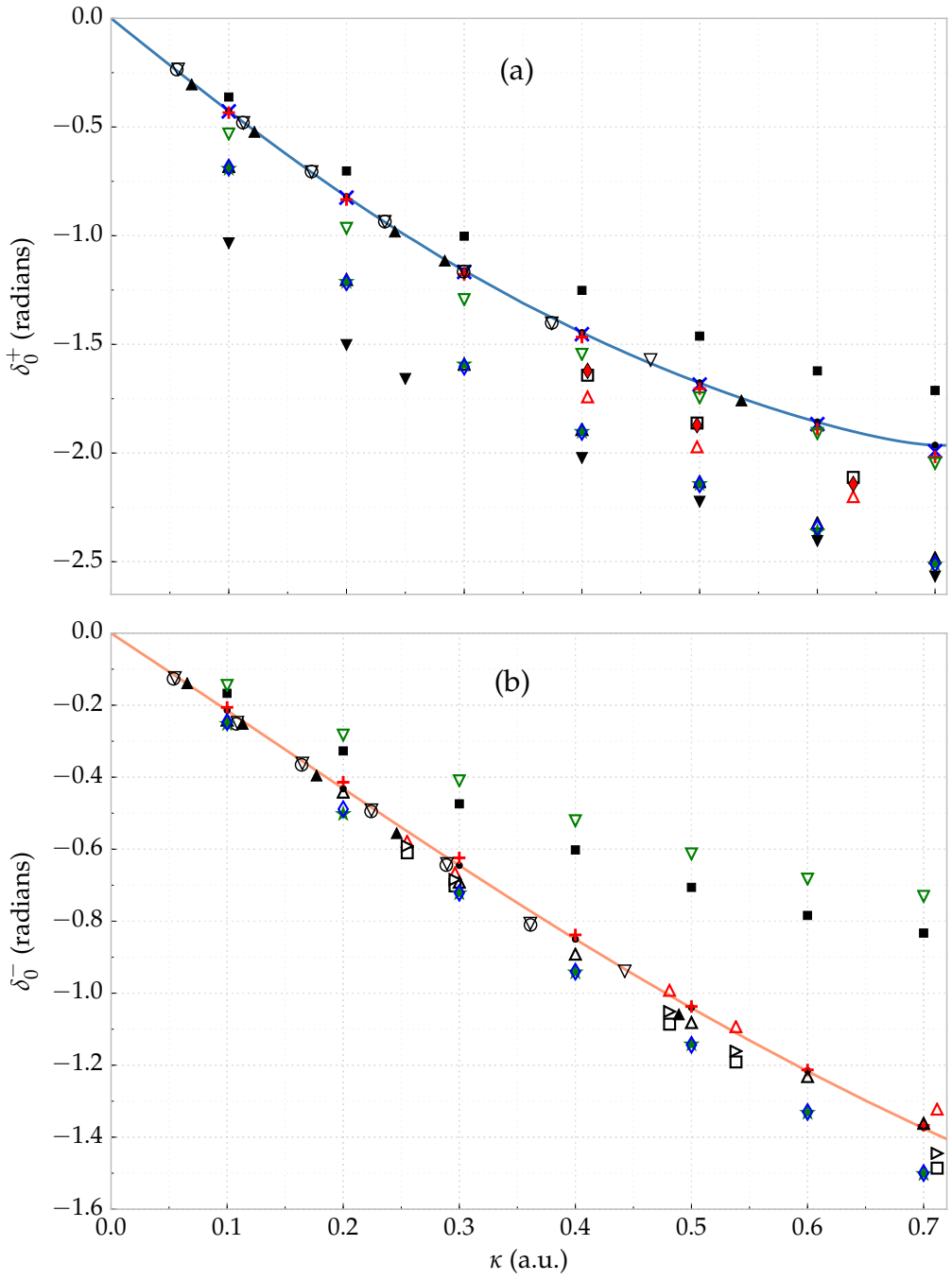

Figure 5.2: Comparison of ^1S (a) and ^3S (b) phase shifts with results from other groups. Results are ordered according to year of publication. Solid curves – this work; × – CC [72]; ● – Kohn [57]; + – CC [70]; ▲ – DMC [63]; ▽ – SVM 2002 [65]; ▲ – T-matrix [183]; ○ – SVM 2001 [64]; ▽ – 2 channel / static exchange with model exchange [150]; △ – 6-state CC [69]; ■ – 5-state CC [68]; □ – Coupled-pseudostate [67]; △ – 3-state CC [66]; ★ – Static-exchange [75]; ▷ – Stabilization [184]; ♦ – Stabilization [185]; ◊ – Static-exchange [73]; ▼ – Static-exchange [186].

Method	0.1	0.2	0.3	0.4	0.5	0.6	0.7
This work $\omega = 7$ δ_0^+	−0.427	−0.820	−1.161	−1.446	−1.678	−1.858	−1.964
This work $\omega \to \infty$ δ_0^+	−0.426	−0.819	−1.161	−1.446	−1.677	−1.857	−1.963
Kohn $\omega = 6$ [57] δ_0^+	−0.427	−0.820	−1.161	−1.446	−1.677	−1.857	−1.964
Kohn $\omega \to \infty$ [57] δ_0^+	−0.425	−0.817	−1.158	−1.443	−1.674	−1.852	−1.959
CVM [181] δ_0^+	−0.42636	−0.81973	—	—	—	—	—
CC 14Ps14H+H^- [72] δ_0^+	−0.428	−0.825	−1.167	−1.453	−1.685	−1.867	−1.992
CC 14Ps14H [70] δ_0^+	−0.434	−0.834	−1.178	−1.467	−1.704	−1.890	−2.018
T-matrix [183] δ_0^+	−0.38269	−0.73419	−1.03799	−1.2924	−1.5014	−1.6667	—
2 channel ME [150] δ_0^+	−0.532	−0.966	−1.294	−1.546	−1.746	−1.910	−2.048
3-state CC [66] δ_0^+	−0.68	−1.20	−1.59	−1.89	−2.13	−2.32	−2.48
SE [75] δ_0^+	−0.692	−1.212	−1.592	−1.902	−2.142	−2.362	−2.512
5-state CC [68] δ_0^+	−0.362	−0.702	−1.002	−1.252	−1.462	−1.622	−1.712
SE [73] δ_0^+	−0.68649	−1.2147	−1.6029	−1.9026	−2.144	−2.344	−2.511
This work $\omega = 7$ δ_0^-	−0.215	−0.431	−0.645	−0.850	−1.041	−1.217	−1.375
This work $\omega \to \infty$ δ_0^-	−0.214	−0.431	−0.645	−0.849	−1.040	−1.214	−1.372
Kohn $\omega = 6$ [57] δ_0^-	−0.215	−0.432	−0.645	−0.850	−1.040	−1.215	−1.373
Kohn $\omega \to \infty$ [57] δ_0^-	−0.214	−0.431	−0.645	−0.849	−1.038	−1.211	−1.366
CVM [181] δ_0^-	−0.21464	−0.43159	—	—	—	—	—
CC 14Ps14H [70] δ_0^-	−0.206	−0.414	−0.624	−0.838	−1.037	−1.213	−1.367
SE ME [150] δ_0^-	−0.145	−0.283	−0.410	−0.521	−0.613	−0.683	−0.731
3-state CC [66] δ_0^+	−0.24	−0.44	−0.69	−0.89	−1.08	−1.23	−1.362
SE [75] δ_0^-	−0.252	−0.502	−0.722	−0.942	−1.142	−1.332	−1.502
5-state CC [68] δ_0^-	−0.167	−0.327	−0.474	−0.602	−0.706	−0.784	−0.833
SE [73] δ_0^-	−0.2469	−0.4888	−0.7211	−0.9402	−1.1435	−1.3300	−1.4996

Table 5.2: Comparison of ^{1,3}S phase shifts between complex Kohn results and those from other groups. Values in the header are κ in a.u.

the accurate Refs. [57, 70, 72] for ^{1}S but seem to overestimate the ^{3}S phase shifts.

An extensive comparison of the S-wave phase shifts with calculations from other groups is also shown in Table 5.2. Fewer groups have attempted this problem than the PsH bound state problem in Table 2.4. We see that the accurate complex Kohn results are very similar to the prior Kohn [57] and agree extremely well with the CVM results [181]. The CC phase shifts [70, 72] also agree relatively well, with closer agreement for ^{1}S than ^{3}S.

Method	${}^1E_R$ (eV)	${}^1\Gamma$ (eV)	${}^2E_R$ (eV)	${}^2\Gamma$ (eV)
Current work:				
Average $\pm$ standard deviation	4.0065 ± 0.0001	0.0955 ± 0.0001	5.0272 ± 0.0029	0.0608 ± 0.0007
Current work:				
S-matrix complex Kohn	4.0065	0.0955	5.0278	0.0608
CC (9Ps9H + H^-) [72]	4.149	0.103	4.877	0.0164
Kohn variational [58]	4.0072 ± 0.0020	0.0956 ± 0.010	5.0267 ± 0.0020	0.0597 ± 0.0010
Stabilization [130]	4.007	0.0969	4.953	0.0574
CC (22Ps1H + H^-) [71]	4.141	0.071	4.963	0.033
CC (9Ps9H) [70]	4.37	0.10	—	—
Optical potential [151]	4.021	0.0259	—	—
T-matrix [183]	4.06	—	—	—
CC [86]	4.04	—	—	—
Five-state CC [187]	4.01	0.15	—	—
Complex rotation [92]	4.0058 ± 0.0005	0.0952 ± 0.0011	4.9479 ± 0.0014	0.0585 ± 0.0027
Coupled-pseudostate [67]	4.55	0.084	—	—
Complex rotation [119]	4.013 ± 0.014	0.075 ± 0.027	—	—
Complex rotation [185]	4.455 ± 0.010	0.062 ± 0.015	—	—
Stabilization [129]	5.8366	0.2693	—	—

Table 5.3: S-wave resonance parameters

5.3.2 Resonance Parameters

Before the Ps(n=2) threshold at 5.102 eV, there are two very clear resonances for ^{1}S scattering, which can be seen in Figure 5.1. The trial wavefunction we use cannot be extended past this threshold without modifications to take into account the Ps(n=2) channel. We use the numerical methods described in Appendix C.5 to accurately determine the resonance parameters.

The current complex Kohn resonance parameters in Table 5.3 are very similar to that of the previous Kohn calculations [58], but the first resonance position matches better with the complex rotation of Yan and Ho [92]. The complex rotation can be considered one of the best calculations for these resonances, and the stabilization method in Ref. [130] from the same authors agrees well with the complex rotation. Both the complex Kohn and prior Kohn calculations give a second resonance position that is at a higher energy than the complex rotation, but the current results agree relatively well with the complex rotation for most parameters.

The CC calculations of Ref. [72] tabulate resonance parameters through the F-wave singlet. Their resonance parameters are close to the complex Kohn and CC results, but there is a significant difference in the second resonance width, which is much smaller than

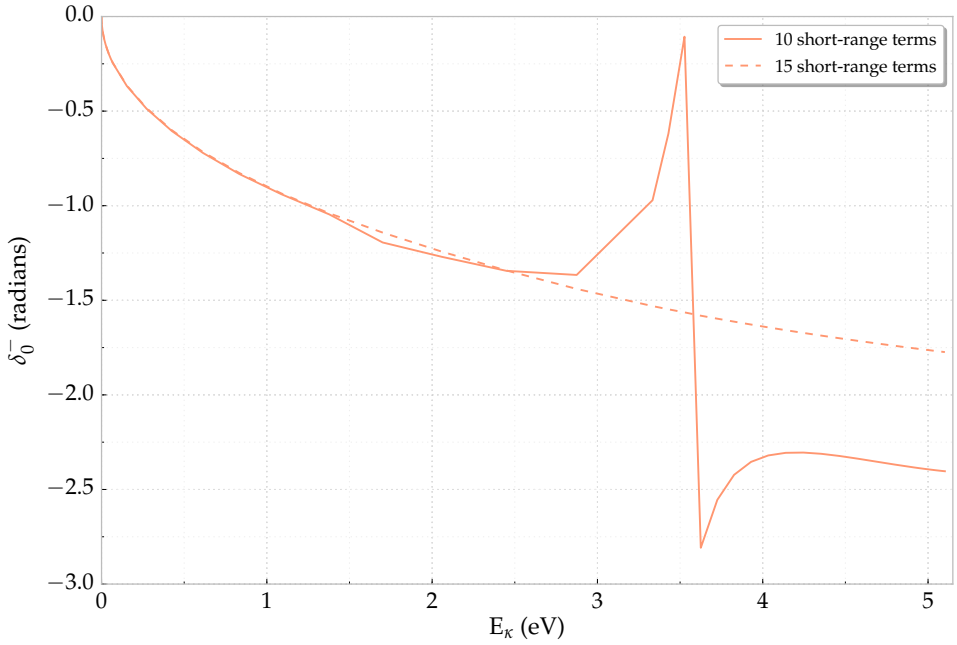

Figure 5.3: ^{3}S plot showing Schwartz singularity at low N

the other calculations. Other calculations shown in this table agree approximately on the position and width of the resonances, with the exception of the much earlier stabilization by Hazi and Taylor [129].

Ray [188] reports a ^{3}S resonance in a 3-state CC approximation. This has not been reported by any other groups, and it appears that this may not be a true resonance. The Belfast group notes this in Ref. [67], stating that "Since H^- is in a spin singlet state, the resonances must have total electronic spin zero. Accordingly, we find no resonances in our triplet partial waves." Figure 5.3 shows that for a small number of terms, we get a Schwartz singularity in the triplet. As the number of terms increases, this singularity disappears, which can illustrate how critical it is to have basis sets with a large number of terms for Ps-H scattering.

5.4 Summary

The Kohn-type variational methods have provided highly accurate phase shifts and reliable resonance parameters for the ^{1,3}S-wave. The S-matrix complex Kohn phase shifts and resonance parameters compare well with those of accurate calculations from other groups [70, 72, 181].

6 P-Wave

LIKE the S-wave in Chapter 5, the general formalism in Chapter 3 was developed much later than the P-wave derivations and code were developed. So though the analysis in Chapter 3 will work properly for the P-wave, it is worthwhile to show the exact formulas that are used in the P-wave long-range code. Similar to the S-wave (Chapter 5), we used Van Reeth's [171] P-wave notes and code for guidance in performing our derivations and writing code.

6.1 Wavefunction

We include both short-range symmetries for the P-wave, so that Equation (3.1) becomes

$$\Psi_1^{\pm,t} = \widetilde{S}_1 + L_1^{\pm,t}\,\widetilde{C}_1 + \sum_{i=1}^{N'(\omega)} c_i \bar{\phi}_{1i} + \sum_{j=1}^{N'(\omega)} d_j \bar{\phi}_{2j}. \tag{6.1}$$

The forms of the long-range terms $\widetilde{S}_1$ and $\widetilde{C}_1$ are found in Section 3.1. Like for the S-wave and as mentioned in Section 3.3, we compute only matrix elements with the barred $\bar{S}_1$ and $\bar{C}_1$ for the Kohn, then use these to construct the matrices (Equation (3.56)) to compute the other Kohn-type variational methods.

The short-range terms are given by Equation (3.9), rewritten as

$$\bar{\phi}_{1i} = (1 \pm P_{23})\, Y_{10}(\theta_1) r_1 \phi_i \tag{6.2a}$$
$$\bar{\phi}_{2j} = (1 \pm P_{23})\, Y_{10}(\theta_2) r_2 \phi_j, \tag{6.2b}$$

where ϕ_i and ϕ_j are given by Equation (2.1c). We also use the shortcuts

$$\phi_{1i} = r_1 \phi_i \text{ and } \phi_{2j} = r_2 \phi_j. \tag{6.3}$$

We refer to the short-range Hylleraas-type terms ϕ_{1i} and ϕ_{2j} as the first and second symmetries, respectively.

To derive the form of the matrix elements involving $\widetilde{C}_1$, we used the *Mathematica* code in Figure 3.1 to find that

$$\begin{aligned}
&\frac{1}{2}\left(\nabla_\rho^2+\kappa^2\right)Y_1^0(\theta_\rho,\varphi_\rho)\,n_1(\kappa\rho)f_1(\rho)\\
&\quad=-\frac{\rho f''(\rho)\left[\kappa\rho\sin(\kappa\rho)+\cos(\kappa\rho)\right]+2f'(\rho)\left[\left(\kappa^2\rho^2-1\right)\cos(\kappa\rho)-\kappa\rho\sin(\kappa\rho)\right]}{2\kappa^2\rho^3}.
\end{aligned}\tag{6.4}$$

Derivations are not given in the following sections – just the final results for each matrix element. The notes on derivations are available on my figshare page [2].

6.2 First Formalism

We used two different formalisms for the P-wave. The first places the orbital angular momentum mainly on the positron ($\boldsymbol{r}_1$) and the electron of Ps ($\boldsymbol{r}_2$, and $\boldsymbol{r}_3$ with exchange). Section 6.3 covers the second formalism that we tried.

6.2.1 Matrix Equation

Since the P-wave trial wavefunction has two sets of short-range terms, the matrix equation can be seen from Equation (3.56) to be

$$\begin{bmatrix}
(\widetilde{C},\mathcal{L}\widetilde{C}) & (\widetilde{C},\mathcal{L}\bar{\phi}_{11}) & \cdots & (\widetilde{C},\mathcal{L}\bar{\phi}_{1N}) & (\widetilde{C},\mathcal{L}\bar{\phi}_{21}) & \cdots & (\widetilde{C},\mathcal{L}\bar{\phi}_{2N})\\
(\bar{\phi}_{11},\mathcal{L}\widetilde{C}) & (\bar{\phi}_{11},\mathcal{L}\bar{\phi}_{11}) & \cdots & (\bar{\phi}_{11},\mathcal{L}\bar{\phi}_{1N}) & (\bar{\phi}_{11},\mathcal{L}\bar{\phi}_{21}) & \cdots & (\bar{\phi}_{11},\mathcal{L}\bar{\phi}_{2N})\\
\vdots & \vdots & \ddots & \vdots & \vdots & \ddots & \vdots\\
(\bar{\phi}_{1N},\mathcal{L}\widetilde{C}) & (\bar{\phi}_{1N},\mathcal{L}\bar{\phi}_{11}) & \cdots & (\bar{\phi}_{1N},\mathcal{L}\bar{\phi}_{1N}) & (\bar{\phi}_{1N},\mathcal{L}\bar{\phi}_{21}) & \cdots & (\bar{\phi}_{1N},\mathcal{L}\bar{\phi}_{2N})\\
(\bar{\phi}_{21},\mathcal{L}\widetilde{C}) & (\bar{\phi}_{21},\mathcal{L}\bar{\phi}_{11}) & \cdots & (\bar{\phi}_{21},\mathcal{L}\bar{\phi}_{1N}) & (\bar{\phi}_{21},\mathcal{L}\bar{\phi}_{21}) & \cdots & (\bar{\phi}_{21},\mathcal{L}\bar{\phi}_{2N})\\
\vdots & \vdots & \ddots & \vdots & \vdots & \ddots & \vdots\\
(\bar{\phi}_{2N},\mathcal{L}\widetilde{C}) & (\bar{\phi}_{2N},\mathcal{L}\bar{\phi}_{11}) & \cdots & (\bar{\phi}_{2N},\mathcal{L}\bar{\phi}_{1N}) & (\bar{\phi}_{2N},\mathcal{L}\bar{\phi}_{21}) & \cdots & (\bar{\phi}_{2N},\mathcal{L}\bar{\phi}_{2N})
\end{bmatrix}
\begin{bmatrix} L_\ell^t\\ c_1\\ \vdots\\ c_N\\ d_1\\ \vdots\\ d_N \end{bmatrix}
=-\begin{bmatrix} (\widetilde{C},\mathcal{L}\widetilde{S})\\ (\bar{\phi}_{11},\mathcal{L}\widetilde{S})\\ \vdots\\ (\bar{\phi}_{1N},\mathcal{L}\widetilde{S})\\ (\bar{\phi}_{21},\mathcal{L}\widetilde{S})\\ \vdots\\ (\bar{\phi}_{2N},\mathcal{L}\widetilde{S}) \end{bmatrix}.
\tag{6.5}$$

The analysis in Section 3.3 applies directly to the P-wave.

6.2.2 Short-Range – Short-Range Matrix Elements

Due to the angular dependence of the $Y_1^0(\theta,\phi)$ spherical harmonic, the P-wave short-short integrals are more complicated than the S-wave. Using the results in Appendix A, these integrals with both symmetries can be written as shown in Equations (6.6) to (6.9). Each of these equations has re-expressed the Laplacian as the gradient-gradient, allowing us to use Equation (2.10). Full derivations are available from the Research Wiki [4] and on figshare at `http://figshare.com/s/82e47cbe0d9b11e58ed806ec4b8d1f61`.

The short-short matrix elements involving all four combinations of the two symmetries are given below:

$$
\begin{aligned}
(\bar{\phi}_{1i}, \mathcal{L}\bar{\phi}_{1j}) =& 2 \cdot 2\pi \int \Bigg\{ \sum_{k=1}^{3} \left[\boldsymbol{\nabla}_{\mathbf{r}_k} \phi_{1i} \cdot \boldsymbol{\nabla}_{\mathbf{r}_k} \phi_{1j} \pm \boldsymbol{\nabla}_{\mathbf{r}_k} \phi_{1i} \cdot \boldsymbol{\nabla}_{\mathbf{r}_k} \phi'_{1j} \right] \\
&+ \left[\frac{2}{r_1} - \frac{2}{r_2} - \frac{2}{r_3} - \frac{2}{r_{12}} - \frac{2}{r_{13}} + \frac{2}{r_{23}} - 2E_H - 2E_{Ps} - \frac{1}{2}\kappa^2 + \frac{2}{r_1^2} \right] \\
&\times \left(\phi_{1i}\phi_{1j} \pm \phi_{1i}\phi'_{1j} \right) \Bigg\} d\tau_{int}
\end{aligned} \tag{6.6}
$$

$$
\begin{aligned}
(\bar{\phi}_{2i}, \mathcal{L}\bar{\phi}_{2j}) =& \, 2 \cdot 2\pi \int \Bigg\{ \sum_{k=1}^{3} \left[\boldsymbol{\nabla}_{\mathbf{r}_k} \phi_{2i} \cdot \boldsymbol{\nabla}_{\mathbf{r}_k} \phi_{2j} \pm \cos\theta_{23} \boldsymbol{\nabla}_{\mathbf{r}_k} \phi_{2i} \cdot \boldsymbol{\nabla}_{\mathbf{r}_k} \phi'_{2j} \right] + \frac{2}{r_2^2} \phi_{2i}\phi_{2j} \\
&\mp \phi_{2i}\phi'_{2j} \left[p_i \frac{r_1}{r_3 r_{13}^2} (\cos\theta_{12} - \cos\theta_{23}\cos\theta_{13}) + m'_j \frac{r_1}{r_2 r_{12}^2} (\cos\theta_{13} \right. \\
&\left. - \cos\theta_{23}\cos\theta_{12}) + \sin^2\theta_{23} \left(q_i \frac{r_2}{r_3 r_{23}^2} + q'_j \frac{r_3}{r_2 r_{23}^2} \right) \right] \\
&+ \left[\frac{2}{r_1} - \frac{2}{r_2} - \frac{2}{r_3} - \frac{2}{r_{12}} - \frac{2}{r_{13}} + \frac{2}{r_{23}} - 2E_H - 2E_{Ps} - \frac{1}{2}\kappa^2 \right] \\
&\times \left(\phi_{2i}\phi_{2j} \pm \cos\theta_{23}\phi_{2i}\phi'_{2j} \right) \Bigg\} d\tau_{int}
\end{aligned} \tag{6.7}
$$

$$
\begin{aligned}
(\bar{\phi}_{1i}, \mathcal{L}\bar{\phi}_{2j}) =& \, 2 \cdot 2\pi \int \Bigg\{ \sum_{k=1}^{3} \left[\cos\theta_{12} \boldsymbol{\nabla}_{\mathbf{r}_k} \phi_{1i} \cdot \boldsymbol{\nabla}_{\mathbf{r}_k} \phi_{2j} \pm \cos\theta_{13} \boldsymbol{\nabla}_{\mathbf{r}_k} \phi_{1i} \cdot \boldsymbol{\nabla}_{\mathbf{r}_k} \phi'_{2j} \right] \\
&\mp \phi_{1i}\phi_{2j} \left[q_i \frac{r_3}{r_2 r_{23}^2} (\cos\theta_{13} - \cos\theta_{12}\cos\theta_{23}) + p_j \frac{r_3}{r_1 r_{13}^2} (\cos\theta_{23} \right. \\
&\left. - \cos\theta_{12}\cos\theta_{13}) + \sin^2\theta_{12} \left(m_i \frac{r_1}{r_2 r_{12}^2} + m_j \frac{r_2}{r_1 r_{12}^2} \right) \right] \\
&\mp \phi_{1i}\phi'_{2j} \left[q_i \frac{r_2}{r_3 r_{23}^2} (\cos\theta_{12} - \cos\theta_{13}\cos\theta_{23}) + m'_j \frac{r_2}{r_1 r_{12}^2} (\cos\theta_{23} \right. \\
&\left. - \cos\theta_{12}\cos\theta_{13}) + \sin^2\theta_{13} \left(p_i \frac{r_1}{r_3 r_{13}^2} + p'_j \frac{r_3}{r_1 r_{13}^2} \right) \right] \\
&+ \left[\frac{2}{r_1} - \frac{2}{r_2} - \frac{2}{r_3} - \frac{2}{r_{12}} - \frac{2}{r_{13}} + \frac{2}{r_{23}} - 2E_H - 2E_{Ps} - \frac{1}{2}\kappa^2 \right]
\end{aligned}
$$

$$\times \left(\cos\theta_{12}\phi_{1i}\phi_{2j} \pm \cos\theta_{13}\phi_{1i}\phi'_{2j}\right) \Bigg\} d\tau_{int} \tag{6.8}$$

$$\begin{aligned}
(\bar{\phi}_{2i}, \mathcal{L}\bar{\phi}_{1j}) = 2\cdot 2\pi \int \Bigg\{ & \sum_{k=1}^{3} \cos\theta_{12} \left[\boldsymbol{\nabla}_{\mathbf{r}_k}\phi_{2i}\cdot\boldsymbol{\nabla}_{\mathbf{r}_k}\phi_{1j} \pm \boldsymbol{\nabla}_{\mathbf{r}_k}\phi_{2i}\cdot\boldsymbol{\nabla}_{\mathbf{r}_k}\phi'_{1j}\right] \\
& \mp \phi_{2i}\phi_{1j}\left[p_i\frac{r_3}{r_1{r_{13}}^2}(\cos\theta_{23}-\cos\theta_{12}\cos\theta_{13}) + q_j\frac{r_3}{r_2{r_{23}}^2}(\cos\theta_{13}\right. \\
& \left. -\cos\theta_{12}\cos\theta_{23}) + \sin^2\theta_{12}\left(m_i\frac{r_2}{r_1{r_{12}}^2} + m_j\frac{r_1}{r_2{r_{12}}^2}\right)\right] \\
& \mp \phi_{2i}\phi'_{1j}\left[p_i\frac{r_3}{r_1 r_{13}^2}(\cos\theta_{23}-\cos\theta_{12}\cos\theta_{13}) + q'_j\frac{r_3}{r_2{r_{23}}^2}(\cos\theta_{13}\right. \\
& \left. -\cos\theta_{12}\cos\theta_{23}) + \sin^2\theta_{12}\left(m_i\frac{r_2}{r_1{r_{12}}^2} + m'_j\frac{r_1}{r_2{r_{12}}^2}\right)\right] \\
& + \left[\frac{2}{r_1}-\frac{2}{r_2}-\frac{2}{r_3}-\frac{2}{r_{12}}-\frac{2}{r_{13}}+\frac{2}{r_{23}}-2E_H-2E_{Ps}-\frac{1}{2}\kappa^2\right] \\
& \times \cos\theta_{12}\left(\phi_{2i}\phi_{12j} \pm \phi_{2i}\phi'_{1j}\right) \Bigg\} d\tau_{int}
\end{aligned} \tag{6.9}$$

The $\cos\theta_{ij}$ that are present in these equations have to be rewritten in terms of r_i and r_{ij} using Equation (B.44) so that the short-short code in Section 4.1 can be used with these. I wrote a *Mathematica* notebook (see Appendix D) that transforms these equations into a form that allows us to copy and paste them directly into Fortran code.

6.2.3 Short-Range – Long-Range Matrix Elements

Like the S-wave in Section 5.2, we derived these and wrote code using these results based on Van Reeth's [171] notes and codes before we developed a general formalism described in Chapter 3. They can easily be shown to be equivalent, but it is easier to compare these forms to the P-wave long-range code.

$$\begin{aligned}
(\bar{\phi}_{1i}, \mathcal{L}\bar{S}_1) = \sqrt{2}\pi \int \phi_{1i} \Bigg[& \frac{r_1 + r_2\cos\theta_{12}}{\rho}\left(\frac{2}{r_1}-\frac{2}{r_2}-\frac{2}{r_{13}}+\frac{2}{r_{23}}\right) S_{22} \\
& \pm \frac{r_1 + r_3\cos\theta_{13}}{\rho'}\left(\frac{2}{r_1}-\frac{2}{r_3}-\frac{2}{r_{12}}+\frac{2}{r_{23}}\right) S_{23}\Bigg] d\tau_{int}
\end{aligned} \tag{6.10}$$

$$(\bar{\phi}_{1i}, \mathcal{L}\bar{C}_1) = -2\pi\sqrt{\kappa}\int \phi_{1i}$$

$$\times \left\{ \frac{r_1 + r_2\cos\theta_{12}}{\rho}\Phi_{Ps}(r_{12})\Phi_H(r_3)\left[\left(\frac{2}{r_1}-\frac{2}{r_2}-\frac{2}{r_{13}}+\frac{2}{r_{23}}\right)n_1(\kappa\rho)f_1(\rho)\right.\right.$$
$$\left.+\left[f_1'(\rho)\frac{1}{\rho}\left(n_1(\kappa\rho)+\cos(\kappa\rho)\right)-\frac{1}{2}f_1''(\rho)n_1(\kappa\rho)\right]\right] \pm \frac{r_1 + r_3\cos\theta_{13}}{\rho'}\Phi_{Ps}(r_{13})\Phi_H(r_2)$$
$$\times\left[\left(\frac{2}{r_1}-\frac{2}{r_3}-\frac{2}{r_{12}}+\frac{2}{r_{23}}\right)n_1(\kappa\rho')f_1(\rho')\right.$$
$$\left.\left.+\left[f_1'(\rho')\frac{1}{\rho'}\left(n_1(\kappa\rho')+\cos(\kappa\rho')\right)-\frac{1}{2}f_1''(\rho')n_1(\kappa\rho')\right]\right]\right\} d\tau_{int} \tag{6.11}$$

$$\left(\bar{\phi}_{2j},\mathcal{L}\bar{S}_1\right) = \sqrt{2}\pi\int\phi_{2j}\left[\frac{1}{\rho}\left(r_2+r_1\cos\theta_{12}\right)\left(\frac{2}{r_1}-\frac{2}{r_2}-\frac{2}{r_{13}}+\frac{2}{r_{23}}\right)S_{22}\right.$$
$$\left.\pm\frac{1}{\rho'}\left(r_1\cos\theta_{12}+r_3\cos\theta_{23}\right)\left(\frac{2}{r_1}-\frac{2}{r_3}-\frac{2}{r_{12}}+\frac{2}{r_{23}}\right)S_{23}\right]d\tau_{int} \tag{6.12}$$

$$\left(\bar{\phi}_{2j},\mathcal{L}\bar{C}_1\right) = -2\pi\sqrt{\kappa}\int\phi_{2j}$$
$$\times\left\{\frac{r_2+r_1\cos\theta_{12}}{\rho}\Phi_{Ps}(r_{12})\Phi_H(r_3)\left[\left(\frac{2}{r_1}-\frac{2}{r_2}-\frac{2}{r_{13}}+\frac{2}{r_{23}}\right)n_1(\kappa\rho)f_1(\rho)\right.\right. \tag{6.13}$$
$$\left.+\left[f_1'(\rho)\frac{1}{\rho}\left(n_1(\kappa\rho)+\cos(\kappa\rho)\right)-\frac{1}{2}f_1''(\rho)n_1(\kappa\rho)\right]\right]$$
$$\pm\frac{r_1\cos\theta_{12}+r_3\cos\theta_{23}}{\rho'}\Phi_{Ps}(r_{13})\Phi_H(r_2)$$
$$\times\left[\left(\frac{2}{r_1}-\frac{2}{r_3}-\frac{2}{r_{12}}+\frac{2}{r_{23}}\right)n_1(\kappa\rho')f_1(\rho')\right. \tag{6.14}$$
$$\left.\left.+\left[f_1'(\rho')\frac{1}{\rho'}\left(n_1(\kappa\rho')+\cos(\kappa\rho')\right)-\frac{1}{2}f_1''(\rho')n_1(\kappa\rho')\right]\right]\right\}$$

6.2.4 Long-Range – Long-Range Matrix Elements

The long-long matrix elements are a straightforward application of the $\mathcal{L}$ operator on S_1 and C_1. The resulting integrals after external angular integration (see Appendix A) are given below:

$$\left(\bar{S}_1,\mathcal{L}\bar{S}_1\right) = \pm\frac{\pi}{2}\int\frac{1}{\rho\rho'}\left[S_1'S_1\left(\frac{2}{r_1}-\frac{2}{r_2}-\frac{2}{r_{13}}+\frac{2}{r_{23}}\right)\right.$$
$$\left.\times\left(r_1^2+r_1r_2\cos\theta_{12}+r_1r_3\cos\theta_{13}+r_2r_3\cos\theta_{23}\right)\right]d\tau_{int} \tag{6.15}$$

$$\left(\bar{C}_1,\mathcal{L}\bar{S}_1\right) = \pm\frac{\pi}{2}\int\frac{1}{\rho\rho'}\left[C_1'S_1\left(\frac{2}{r_1}-\frac{2}{r_2}-\frac{2}{r_{13}}+\frac{2}{r_{23}}\right)\right.$$

$$\times \left(r_1^2 + r_1 r_2 \cos\theta_{12} + r_1 r_3 \cos\theta_{13} + r_2 r_3 \cos\theta_{23} \right) \Big] \, d\tau_{int} \qquad (6.16)$$

$$\begin{aligned}
(\bar{C}_1, \mathcal{L}\bar{C}_1) = 2\pi\kappa \int \Phi_{Ps}(r_{12})\Phi_H(r_3) \Big\{ & 2\Phi_{Ps}(r_{12})\Phi_H(r_3) n_1(\kappa\rho) f_1(\rho) \\
& \times \left(\frac{1}{\rho} f_1'(\rho) \left(n_1(\kappa\rho) + \cos(\kappa\rho) \right) - \frac{1}{2} f_1''(\rho) n_1(\kappa\rho) \right) \\
& \pm \frac{1}{2\rho\rho'} (r_1^2 + r_1 r_2 \cos\theta_{12} + r_1 r_3 \cos\theta_{13} + r_2 r_3 \cos\theta_{23}) \\
& \times \Phi_{Ps}(r_{13})\Phi_H(r_2) n_1(\kappa\rho') f_1(\rho') \\
& \times \Big[n_1(\kappa\rho) f_1(\kappa\rho) \left(\frac{2}{r_1} - \frac{2}{r_2} - \frac{2}{r_{13}} + \frac{2}{r_{23}} \right) \\
& + \left(\frac{1}{\rho} f_1'(\rho) \left(n_1(\kappa\rho) + \cos(\kappa\rho) \right) - \frac{1}{2} f_1''(\rho) n_1(\kappa\rho) \right) \Big] \Big\} d\tau_{int}
\end{aligned} \qquad (6.17)$$

6.3 Second Formalism

Van Reeth and Humberston [58] had difficulty with convergence of the ^{3}P phase shifts. They specifically state:

> "The present triplet p-wave phase shifts are not yet fully converged; at very low energies we estimate them to be $\approx 20\%$ below the fully converged values and $\approx 3\%$ in the higher energy range. This relatively poor convergence is due to the fact that we have not yet included in the wavefunction a set of terms for which the unit of angular momentum is on the electron in the H atom."

Due to this, we looked at a second formalism that includes these short-range terms instead of what we call the first formalism in Section 6.1. This second formalism places the orbital angular momentum mainly on the Ps ($\boldsymbol{\rho}$) and the electron of H ($\boldsymbol{r}_3$, and $\boldsymbol{r}_2$ with exchange).

6.3.1 Wavefunction

The trial wavefunction that we use for the second formalism is similar to the first formalism in Section 6.1.

$$\Psi_1^{\pm,t} = \widetilde{S}_1 + L_1^{\pm,t} \widetilde{C}_1 + \sum_{i=1}^{N'(\omega)} c_i \bar{\phi}_{\rho i} + \sum_{j=1}^{N'(\omega)} d_j \bar{\phi}_{3j} \qquad (6.18)$$

The new short-range terms are given by

$$\bar{\phi}_{\rho i} = (1 \pm P_{23}) \, Y_1^0(\theta_\rho, \varphi_\rho) \, \rho \, \phi_i \qquad (6.19a)$$

$$\bar{\phi}_{3j} = (1 \pm P_{23})\, Y_1^0(\theta_3, \varphi_3)\, r_3 \phi_j. \tag{6.19b}$$

These place the angular momentum on the Ps and on the electron of H, instead of on the positron and the electron in the Ps. In the first formalism, some amount of the angular momentum is placed on the second electron through the P_{23} permutation operator.

The short-long terms can be directly computed by changing the short-range terms in the code, but the integration routines (see Section 4.1.1) for the short-short terms cannot handle the ρ factor of $\bar{\phi}_{\rho 1}$ directly. The following relations are used:

$$\rho Y_1^0(\theta_\rho, \varphi_\rho) = \frac{1}{2}\left[r_1 Y_1^0(\theta_1, \varphi_1) + r_2 Y_1^0(\theta_2, \varphi_2)\right] \tag{6.20a}$$

$$\rho' Y_1^0\left(\theta_{\rho'}, \varphi_{\rho'}\right) = \frac{1}{2}\left[r_1 Y_1^0(\theta_1, \varphi_1) + r_3 Y_1^0(\theta_3, \varphi_3)\right]. \tag{6.20b}$$

The first of these is obtained by substituting

$$\cos\theta_\rho = \frac{r_1 \cos\theta_1 + r_2 \cos\theta_2}{2\rho} \tag{6.21}$$

in the $Y_1^0(\theta_\rho, \varphi_\rho)$ spherical harmonic. The second is found by using the P_{23} permutation of this.

6.3.2 Short-Short Matrix Elements

The $(\bar{\phi}_{\rho i}, \mathcal{L}\bar{\phi}_{\rho j})$ matrix elements of the second formalism can easily be rewritten in terms of the first formalism by using Equation (6.20). In terms of the first formalism (denoted by $1st$ subscripts),

$$(\bar{\phi}_{\rho i}, \mathcal{L}\bar{\phi}_{\rho j}) = \frac{1}{4}\left[(\bar{\phi}_{1i}, \mathcal{L}\bar{\phi}_{1j})_{1st} + (\bar{\phi}_{1i}, \mathcal{L}\bar{\phi}_{2j})_{1st} + (\bar{\phi}_{2i}, \mathcal{L}\bar{\phi}_{1j})_{1st} + (\bar{\phi}_{2i}, \mathcal{L}\bar{\phi}_{2j})_{1st}\right]. \tag{6.22}$$

The other types of terms cannot be expressed as combinations of the first formalism results, but these calculations are similar to the first formalism.

$$\begin{aligned}(\bar{\phi}_{\rho i}, \mathcal{L}\bar{\phi}_{3j}) =& (Y_{10}(\theta_1) r_1 \phi_i, \mathcal{L} Y_{10}(\theta_3) r_3 \phi_j) + (Y_{10}(\theta_2) r_2 \phi_i, \mathcal{L} Y_{10}(\theta_3) r_3 \phi_j) \\ &\pm (Y_{10}(\theta_1) r_1 \phi_i, \mathcal{L} Y_{10}(\theta_2) r_2 \phi'_j) \pm (Y_{10}(\theta_2) r_2 \phi_i, \mathcal{L} Y_{10}(\theta_2) r_2 \phi'_j)\end{aligned} \tag{6.23}$$

$$\begin{aligned}(\bar{\phi}_{\rho i}, \mathcal{L}\bar{\phi}_{3j}) =& \pm (Y_{10}(\theta_2) r_2 \phi'_i, \mathcal{L} Y_{10}(\theta_1) r_1 \phi_j) \pm (Y_{10}(\theta_2) r_2 \phi'_i, \mathcal{L} Y_{10}(\theta_2) r_2 \phi_j) \\ &+ (Y_{10}(\theta_2) r_2 \phi'_i, \mathcal{L} Y_{10}(\theta_1) r_1 \phi'_j) + (Y_{10}(\theta_2) r_2 \phi'_i, \mathcal{L} Y_{10}(\theta_3) r_3 \phi'_j)\end{aligned} \tag{6.24}$$

$$(\bar{\phi}_{\rho i}, \mathcal{L}\bar{\phi}_{3j}) = 2\left[\pm (Y_{10}(\theta_2) r_2 \phi_i, \mathcal{L} Y_{10}(\theta_3) r_3 \phi_j) + (Y_{10}(\theta_2) r_2 \phi'_i, \mathcal{L} Y_{10}(\theta_2) r_2 \phi'_j)\right]$$

Derivations for all four of these are found on figshare [2].

	δ_1^+		δ_1^-	
κ	1^{st} Formalism	2^{nd} Formalism	1^{st} Formalism	2^{nd} Formalism
0.1	2.26^{-2}	2.27^{-2}	-1.79^{-3}	-1.80^{-3}
0.2	1.91^{-1}	1.91^{-1}	-1.68^{-2}	-1.67^{-2}
0.3	6.08^{-1}	6.08^{-1}	-5.54^{-2}	-5.52^{-2}
0.4	9.93^{-1}	9.93^{-1}	-1.15^{-1}	-1.15^{-1}
0.5	1.14	1.14	-1.84^{-1}	-1.84^{-1}
0.6	1.16	1.16	-2.49^{-1}	-2.48^{-3}
0.7	1.15	1.15	-2.93^{-1}	-2.93^{-1}

Table 6.1: Comparison of ^{1,3}P phase shifts for the first and second formalisms ($\omega = 6$). The 2^{nd} formalism for δ_1^- uses 889 terms, while the others use 924 terms.

6.3.3 Short-Long Matrix Elements

The short-long second formalism matrix elements are easily written as combinations of matrix elements from the first formalism. In terms of the first formalism (denoted by $1st$ subscripts),

$$\left(\bar{\phi}_{\rho i}, \mathcal{L}\bar{S}_1\right) = \frac{1}{2}\left[\left(\bar{\phi}_{1i}, \mathcal{L}\bar{S}_1\right)_{1st} + \left(\bar{\phi}_{2i}, \mathcal{L}\bar{S}_1\right)_{1st}\right] \tag{6.25a}$$

$$\left(\bar{\phi}_{\rho i}, \mathcal{L}\bar{C}_1\right) = \frac{1}{2}\left[\left(\bar{\phi}_{1i}, \mathcal{L}\bar{C}_1\right)_{1st} + \left(\bar{\phi}_{2i}, \mathcal{L}\bar{C}_1\right)_{1st}\right]. \tag{6.25b}$$

Since these are both linear combinations of the first formalism results, the code is a straightforward adaptation of the first formalism code.

6.3.4 Phase Shifts

The phase shifts for ^{1}P and ^{3}P in Table 6.1 were not improved in general by using the second formalism and were even lower in the $\kappa = 0.1$ triplet case. One exception is $\kappa = 0.3$ for ^{3}P, where the second formalism phase shift is slightly higher. We note that this is the same result as the $\omega = 7$ case with 1000 terms as presented in Table 6.2. The difficulty with the second formalism is that linear dependence becomes more of an issue, forcing us to only use 889 terms for $\omega = 6$ and unable to do an $\omega = 7$ run. I tried an $\omega = 7$ run with the Todd energy program, but it could only select 767 terms, leading to worse phase shifts than the $\omega = 6$ runs.

The energy eigenvalues in Tables C.5 and C.6 were also lower for the first formalism, so we did not pursue using the second formalism any further. The convergence of the phase shifts for the first formalism, even for ^{3}P, appears to be good. The second formalism

was not tried for the D-wave due to its difficulty and because it did not generally improve the results for the P-wave.

6.4 Results

Results in this section were computed using the nonlinear parameters α, β, and γ described in Appendix C.1.3, which has discussion on how these were chosen.

6.4.1 Phase Shifts

Table 6.2 compares the current S-matrix complex Kohn phase shifts for the first P-wave formalism with that of other groups. We use $\omega = 4 - 7$ phase shifts to do the extrapolations for $\omega \to \infty$. The % Diff entries comparing the $\omega = 7$ and $\omega \to \infty$ extrapolated phases shifts give an estimate of the error for the complex Kohn results. The singlet results are converged very well. The triplet results are also converged well, but there is more possible error at $\kappa = 0.1$ and $\kappa = 0.7$. Even with these slightly larger percentages, the ^{3}P phase shifts appear to be well converged.

The different Kohn-type variational methods generate phase shifts that agree with the S-matrix complex Kohn results presented in Table 6.2 when methods with Schwartz singularities are removed. The previous Kohn / inverse Kohn ^{1}P phase shifts [58], published only in graph form in their paper, agree well with the current S-matrix complex Kohn phase shifts though generally are slightly higher.

Table 6.2 and Figure 6.1 give good comparisons with the CC results of the Belfast group [70, 72]. The complex Kohn phase shifts are higher for ^{1}P, but they are slightly lower for much of the range for ^{3}P. We note that this was also the case for the S-wave (see Table 5.2 on 73), but the CVM results seem to confirm the complex Kohn ^{3}S phase shifts. Both the S-matrix complex Kohn and the CC phase shifts of the Belfast group appear to give the most accurate sets of phase shifts, with the current complex Kohn giving highly accurate results.

Figure 6.2 gives a detailed comparison to phase shifts from many other groups, similar to the S-wave comparisons in Figure 5.2. The 5-state CC method of Adhikari and Biswas [68] again gives phase shifts that do not agree well with other methods, and Ivanov et al. [65] has a detailed discussion of this. The SVM results of Ivanov et al. [65] follow along well with the current complex Kohn and the CC [70, 72] but are below throughout the energy range. The SE [73, 75] and smaller CC calculations [66] do not match the complex Kohn phase shifts well.

Method	0.1	0.2	0.3	0.4	0.5	0.6	0.7
This work ($\omega = 7$) δ_1^+	0.226^{-1}	0.191	0.609	0.994	1.140	1.162	1.152
This work ($\omega \to \infty$) δ_1^+	0.227^{-1}	0.192	0.611	0.996	1.142	1.163	1.154
% Diff$^+$	0.465%	0.306%	0.314%	0.205%	0.140%	0.137%	0.181%
Kohn ($\omega = 6$) [171] δ_1^+	0.226^{-1}	0.192	0.612	0.997	1.143	1.165	1.155
CC 9Ps9H+H$^-$ [72] δ_1^+	0.221^{-1}	0.183	0.580	0.956	1.106	1.134	1.133
CC 9Ps9H [70] δ_1^+	0.213^{-1}	0.175	0.545	0.908	1.068	1.103	1.099
3-state CC [66] δ_1^+	8.14^{-3}	6.27^{-2}	0.190	0.358	0.489	0.551	0.556
SE [75] δ_1^+	0.798^{-2}	0.614^{-1}	0.186	0.349	0.477	0.536	0.538
5-state CC [68] δ_1^+	0.477^{-2}	0.370^{-1}	0.116	0.239	0.372	0.478	0.541
SE [73] δ_1^+	0.79^{-2}	0.611^{-1}	0.1853	0.3487	0.4772	0.5361	0.5388
This work ($\omega = 7$) δ_1^-	-0.178^{-2}	-0.167^{-1}	-0.552^{-1}	-0.115	-0.183	-0.248	-0.292
This work ($\omega \to \infty$) δ_1^-	-0.172^{-2}	-0.165^{-1}	-0.540^{-1}	-0.114	-0.182	-0.246	-0.288
% Diff$^-$	3.176%	0.993%	0.749%	0.698%	0.749%	0.896%	1.237%
CC 9Ps9H [70] δ_1^-	-0.953^{-3}	-0.122^{-1}	-0.456^{-1}	-0.104	-0.178	-0.247	-0.295
3-state CC [66] δ_1^-	-4.43^{-3}	-3.08^{-2}	-8.51^{-2}	-0.159	-0.236	-0.302	-0.332
SE [75] δ_1^-	-0.503^{-2}	-0.352^{-1}	-0.980^{-1}	-0.186	-0.287	-0.390	-0.488
5-state CC [68] δ_1^-	-0.233^{-2}	-0.167^{-1}	-0.476^{-1}	-0.918^{-1}	-0.142	-0.190	-0.228
SE [73] δ_1^-	-0.50^{-2}	-0.350^{-1}	-0.978^{-1}	-0.1860	-0.2872	-0.3906	-0.4882

Table 6.2: Comparison of the S-matrix complex Kohn ^{1,3}P phase shifts with results from other groups. % Diff$^{\pm}$ is the percent difference between the current complex Kohn $\omega = 7$ and $\omega \to \infty$ results. Values in the header are κ in au. Exponents denote powers of 10.

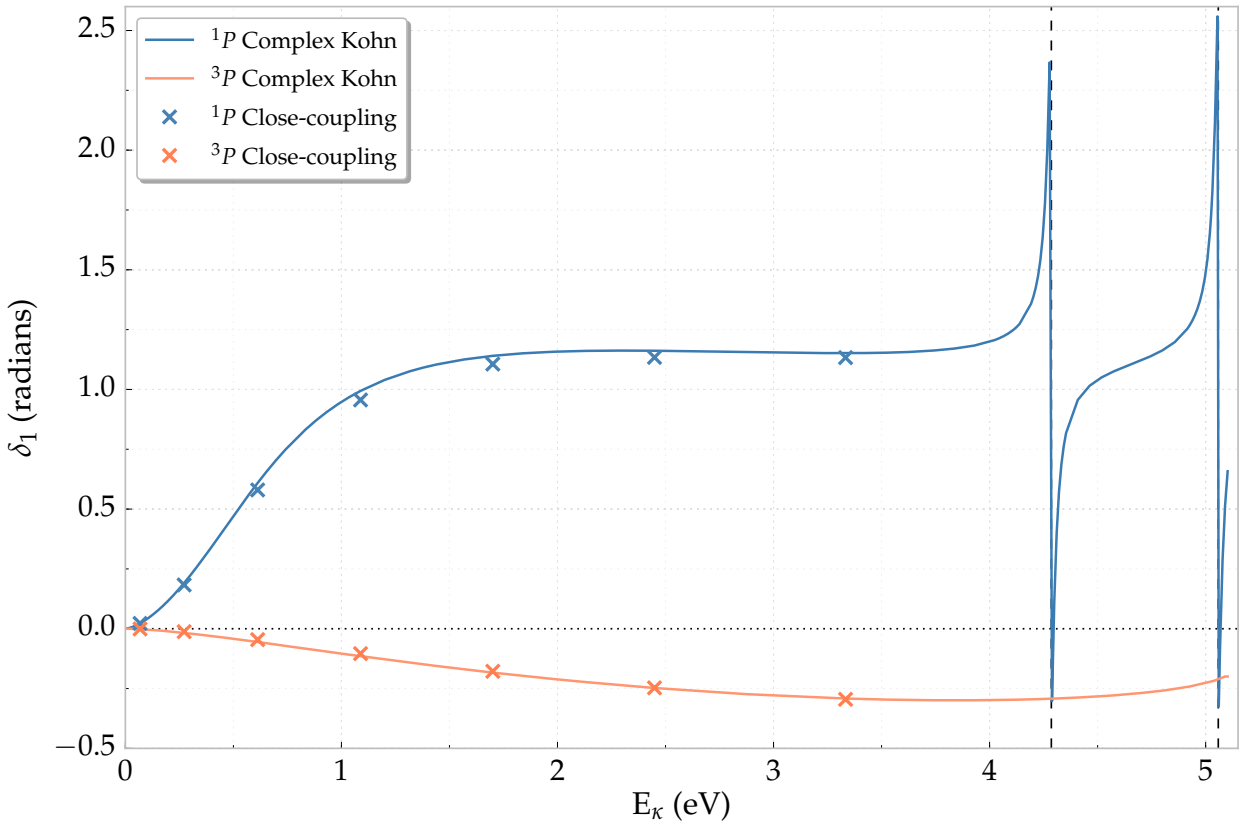

Figure 6.1: ^{1,3}P complex Kohn phase shifts. The ^{1}P CC phase shifts [72] are given by $\times$, and the ^{3}P CC phase shifts [70] are given by $+$. Vertical dashed lines denote the complex rotation resonance positions [92]. An interactive version of this figure is available online [3] at `https://plot.ly/~Denton/4/p-wave-ps-h-scattering/`.

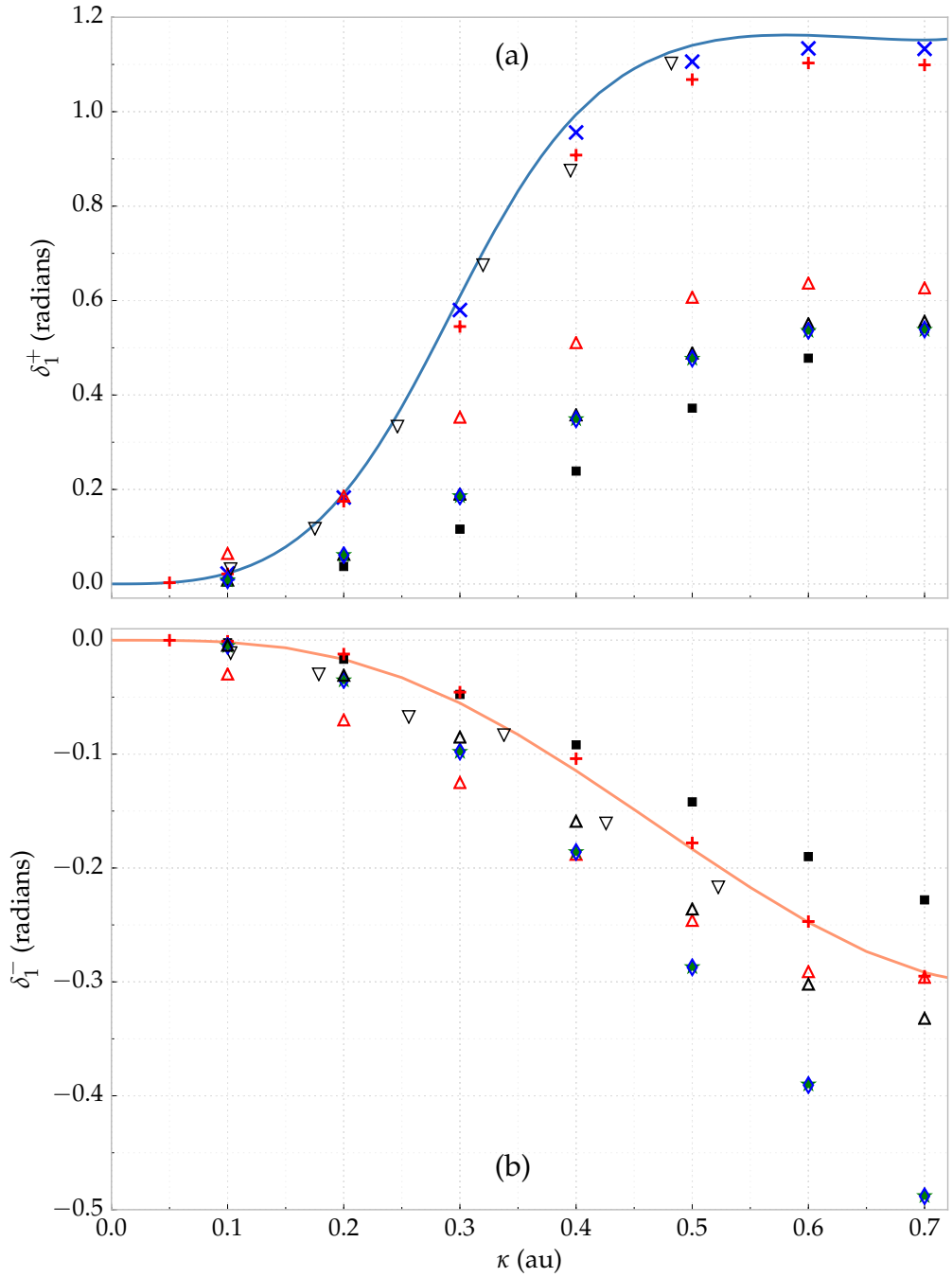

Figure 6.2: Comparison of ^{1}P (a) and ^{3}P (b) phase shifts with results from other groups. Results are ordered according to year of publication. Solid curves – this work; × – CC [72]; ● – Kohn [57]; + – CC [70];▽ – SVM 2002 [65]; △ – 6-state CC [69]; ■ – 5-state CC [68]; △ – 3-state CC [66]; ★ – CC [75]; ◊ – Static-exchange [73].

Method	${}^1E_R$ (eV)	${}^1\Gamma$ (eV)	${}^2E_R$ (eV)	${}^2\Gamma$ (eV)
Current work:				
Average $\pm$ standard deviation	4.2856 ± 0.0001	0.0445 ± 0.0001	5.0577 ± 0.0004	0.0459 ± 0.0005
Current work:				
S-matrix complex Kohn	4.2856	0.0445	5.0579	0.0459
Kohn variational [58]	4.29 ± 0.01	0.042 ± 0.005	—	—
CC (9Ps9H + H^-) [72]	4.475	0.0827	4.905	0.0043
Stabilization [130]	4.287	0.0446	5.062	0.0563
CC (22Ps1H + H^-) [71]	4.401	0.029	5.108	0.017
Optical potential [151]	4.472	0.082	—	—
Five-state CC [187]	5.08	0.004	—	—
CC (9Ps9H) [70]	4.66	0.084	—	—
Complex rotation [92]	4.2850 ± 0.0014	0.0435 ± 0.0027	5.0540 ± 0.0027	0.0585 ± 0.0054
Coupled-pseudostate [67]	4.88	0.058	—	—

Table 6.3: ^{1}P-wave resonance parameters

6.4.2 Resonance Parameters

The P-wave has two resonances before the inelastic threshold, as seen in Figure 6.1. These resonances are shifted to higher energies than the S-wave, and we use the numerical fittings described in Appendix C.5 to determine the resonance parameters given in Table 6.3.

Table 6.3 has the ^{1}P-wave resonances calculated in this work and compared to that of calculations from other groups. The complex rotation result of Yan and Ho [92] is one of the most accurate calculations of these resonance parameters. The positions of the first and resonances using the complex Kohn agree very well with the complex rotation, as does the width of the first resonance. We find a width for the second resonance about half that of the complex rotation. A more recent result of Yan and Ho uses a stabilization method [130], which has a result for the second resonance closer to the complex Kohn result.

The CC results of the Belfast group [70, 71, 72] show again that the H^- channel is important for the resonances. The ${}^1E_R$ that they calculate is still higher than this work and that of Yan and Ho [92, 130], but it is roughly comparable. The ${}^2E_R$ they calculate is lower than the complex Kohn, stabilization and complex rotation, although it is also close. The complex Kohn and complex rotation second resonance widths are much larger than the CC.

6.5 Summary

We have investigated the P-wave by using two different formalisms but found little difference in the resulting phase shifts between them. Using the first formalism S-matrix

results, we have obtained accurate ^{1,3}P-wave phase shifts that converge well and compare against the results from multiple groups. We also obtain reliable ^{1}P resonance parameters that compare well with those of other groups.

7 D-Wave

VAN Reeth [171] had D-wave notes that I used as guidance for the D-wave derivations. He also had code for the ^{1}D-wave that we used to compare our independent code against after it was written. His D-wave work was unpublished, unlike that of the S-wave [57, 58] and P-wave [58].

7.1 Wavefunction

Similar to the discussions for the S-wave (Chapter 5) and the P-wave (Chapter 6), here we present the D-wave wavefunction for multiple Kohn-type variational methods in Equation (7.1), but throughout this chapter, we only consider the Kohn variational method. The wavefunction for each of the variants of the Kohn can be easily constructed from this by using the general formalism in Sections 3.1 and 3.3. The general D-wave wavefunction is given by

$$\Psi_t^{\pm} = \widetilde{S}_2 + L_2^{\pm,t}\,\widetilde{C}_2 + \sum_{i=1}^{N'(\omega)} c_i \bar{\phi}_{1i} + \sum_{j=1}^{N'(\omega)} d_j \bar{\phi}_{2j} + \sum_{j=1}^{N'(\omega)} f_k \bar{\phi}_{12k}. \tag{7.1}$$

The long-range $\widetilde{S}_\ell$ and $\widetilde{C}_\ell$ are given by Equation (3.3). As noted in Section 3.1, the full wavefunction has $(\ell+1) = 3$ short-range symmetries. The short-range terms are given by

$$\bar{\phi}_{1i} = (1 \pm P_{23})\, Y_{20}(\theta_1) r_1^2 \phi_i \tag{7.2a}$$

$$\bar{\phi}_{2j} = (1 \pm P_{23})\, Y_{20}(\theta_2) r_2^2 \phi_j \tag{7.2b}$$

$$\bar{\phi}_{12k} = (1 \pm P_{23})\, \psi_{(1,1,2,0)}(\theta_1, \theta_2) r_1 r_2 \phi_k, \tag{7.2c}$$

where ϕ_i, ϕ_j and ϕ_k are given by Equation (2.1c). We also use the shortcuts

$$\phi_{1i} = r_1^2 \phi_i,\ \phi_{2j} = r_2^2 \phi_j, \text{ and } \phi_{12k} = r_1 r_2 \phi_k. \tag{7.3}$$

The mixed symmetry terms, given as $\bar{\phi}_{12k}$, are discussed in Section 7.5. There is also a second formalism, similar to that for the P-wave (Section 6.3), which we did not use.

Only the results of the derivations of the matrix elements are shown here, but full derivations are found on figshare [2].

7.2 Short-Range – Short-Range Matrix Elements

The D-wave short-short integrals are generally more complicated than those for the S-wave and P-wave. Equations (7.4) to (7.7) give the short-short integrals needed evaluate the matrix in Equation (3.56). Full derivations for each of these are given in separate notes available on the Wiki [4] and figshare [2].

$$\begin{aligned}\left(\bar{\phi}_{1i}, \mathcal{L}\bar{\phi}_{1j}\right) =& 2 \cdot 2\pi \int \Bigg\{ \sum_{k=1}^{3} \left[\boldsymbol{\nabla}_{\mathbf{r}_k} \phi_{1i} \cdot \boldsymbol{\nabla}_{\mathbf{r}_k} \phi_{1j} \pm \boldsymbol{\nabla}_{\mathbf{r}_k} \phi_{1i} \cdot \boldsymbol{\nabla}_{\mathbf{r}_k} \phi'_{1j} \right] \\ &+ \left[\frac{2}{r_1} - \frac{2}{r_2} - \frac{2}{r_3} - \frac{2}{r_{12}} - \frac{2}{r_{13}} + \frac{2}{r_{23}} - 2E_H - 2E_{Ps} - \frac{1}{2}\kappa^2 + \frac{6}{r_1^2} \right] \\ &\times \left(\phi_{1i}\phi_{1j} \pm \phi_{1i}\phi'_{1j} \right) \Bigg\} d\tau_{int} \end{aligned} \tag{7.4}$$

$$\begin{aligned}\left(\bar{\phi}_{2i}, \mathcal{L}\bar{\phi}_{2j}\right) =& 2 \cdot 2\pi \int \Bigg\{ \sum_{k=1}^{3} \left[\boldsymbol{\nabla}_{\mathbf{r}_k} \phi_{2i} \cdot \boldsymbol{\nabla}_{\mathbf{r}_k} \phi_{2j} \pm \left(1 - \tfrac{3}{2}\sin^2\theta_{23}\right) \boldsymbol{\nabla}_{\mathbf{r}_k} \phi_{2i} \cdot \boldsymbol{\nabla}_{\mathbf{r}_k} \phi'_{2j} \right] + \frac{6}{r_2^2}\phi_{2i}\phi_{2j} \\ &\mp 3\phi_{2i}\phi'_{2j}\cos\theta_{23} \left[p_i \frac{r_1}{r_3 r_{13}^2}(\cos\theta_{12} - \cos\theta_{23}\cos\theta_{13}) + m'_j \frac{r_1}{r_2 r_{12}^2}(\cos\theta_{13} \right. \\ &\left. - \cos\theta_{23}\cos\theta_{12}) + \sin^2\theta_{23} \left(q_i \frac{r_2}{r_3 r_{23}^2} + q'_j \frac{r_3}{r_2 r_{23}^2} \right) \right] \\ &+ \left[\frac{2}{r_1} - \frac{2}{r_2} - \frac{2}{r_3} - \frac{2}{r_{12}} - \frac{2}{r_{13}} + \frac{2}{r_{23}} - 2E_H - 2E_{Ps} - \frac{1}{2}\kappa^2 \right] \\ &\times \left[\phi_{2i}\phi_{2j} \pm \left(1 - \tfrac{3}{2}\sin^2\theta_{23}\right) \phi_{2i}\phi'_{2j} \right] \Bigg\} d\tau_{int} \end{aligned} \tag{7.5}$$

$$\begin{aligned}\left(\bar{\phi}_{1i}, \mathcal{L}\bar{\phi}_{2j}\right) =& 2 \cdot 2\pi \int \Bigg\{ \sum_{k=1}^{3} \Big[\left(1 - \tfrac{3}{2}\sin^2\theta_{12}\right) \boldsymbol{\nabla}_{\mathbf{r}_k} \phi_{1i} \cdot \boldsymbol{\nabla}_{\mathbf{r}_k} \phi_{2j} \\ &\pm \left(1 - \tfrac{3}{2}\sin^2\theta_{13}\right) \boldsymbol{\nabla}_{\mathbf{r}_k} \phi_{1i} \cdot \boldsymbol{\nabla}_{\mathbf{r}_k} \phi'_{2j} \Big] \end{aligned}$$

$$
\begin{aligned}
&\mp 3\phi_{1i}\phi_{2j}\cos\theta_{12}\left[q_i\frac{r_3}{r_2r_{23}^2}(\cos\theta_{13}-\cos\theta_{12}\cos\theta_{23})+p_j\frac{r_3}{r_1r_{13}^2}(\cos\theta_{23}\right.\\
&\quad\left.-\cos\theta_{12}\cos\theta_{13})+\sin^2\theta_{12}\left(m_i\frac{r_1}{r_2r_{12}^2}+m_j\frac{r_2}{r_1r_{12}^2}\right)\right]\\
&\mp 3\phi_{1i}\phi'_{2j}\cos\theta_{13}\left[q_i\frac{r_2}{r_3r_{23}^2}(\cos\theta_{12}-\cos\theta_{13}\cos\theta_{23})+m'_j\frac{r_2}{r_1r_{12}^2}(\cos\theta_{23}\right.\\
&\quad\left.-\cos\theta_{12}\cos\theta_{13})+\sin^2\theta_{13}\left(p_i\frac{r_1}{r_3r_{13}^2}+p'_j\frac{r_3}{r_1r_{13}^2}\right)\right]\\
&+\left[\frac{2}{r_1}-\frac{2}{r_2}-\frac{2}{r_3}-\frac{2}{r_{12}}-\frac{2}{r_{13}}+\frac{2}{r_{23}}-2E_H-2E_{Ps}-\frac{1}{2}\kappa^2\right]\\
&\quad\times\left[\left(1-\tfrac{3}{2}\sin^2\theta_{12}\right)\phi_{1i}\phi_{2j}\pm\left(1-\tfrac{3}{2}\sin^2\theta_{13}\right)\phi_{1i}\phi'_{2j}\right]\Bigg\}d\tau_{int}
\end{aligned}
\tag{7.6}
$$

$$
\begin{aligned}
(\bar{\phi}_{2i},\mathcal{L}\bar{\phi}_{1j}) = 2\cdot 2\pi\int\Bigg\{&\sum_{k=1}^{3}\left(1-\tfrac{3}{2}\sin^2\theta_{12}\right)\left[\boldsymbol{\nabla}_{\mathbf{r}_k}\phi_{2i}\cdot\boldsymbol{\nabla}_{\mathbf{r}_k}\phi_{1j}\pm\boldsymbol{\nabla}_{\mathbf{r}_k}\phi_{2i}\cdot\boldsymbol{\nabla}_{\mathbf{r}_k}\phi'_{1j}\right]\\
&\mp 3\phi_{2i}\phi_{1j}\cos\theta_{12}\left[p_i\frac{r_3}{r_1{r_{13}}^2}(\cos\theta_{23}-\cos\theta_{12}\cos\theta_{13})+q_j\frac{r_3}{r_2{r_{23}}^2}(\cos\theta_{13}\right.\\
&\quad\left.-\cos\theta_{12}\cos\theta_{23})+\sin^2\theta_{12}\left(m_i\frac{r_2}{r_1{r_{12}}^2}+m_j\frac{r_1}{r_2{r_{12}}^2}\right)\right]\\
&\mp 3\phi_{2i}\phi'_{1j}\cos\theta_{12}\left[p_i\frac{r_3}{r_1r_{13}^2}(\cos\theta_{23}-\cos\theta_{12}\cos\theta_{13})+q'_j\frac{r_3}{r_2{r_{23}}^2}(\cos\theta_{13}\right.\\
&\quad\left.-\cos\theta_{12}\cos\theta_{23})+\sin^2\theta_{12}\left(m_i\frac{r_2}{r_1{r_{12}}^2}+m'_j\frac{r_1}{r_2{r_{12}}^2}\right)\right]\\
&+\left[\frac{2}{r_1}-\frac{2}{r_2}-\frac{2}{r_3}-\frac{2}{r_{12}}-\frac{2}{r_{13}}+\frac{2}{r_{23}}-2E_H-2E_{Ps}-\frac{1}{2}\kappa^2\right]\\
&\quad\times\left(1-\tfrac{3}{2}\sin^2\theta_{12}\right)\left(\phi_{2i}\phi_{1j}\pm\phi_{2i}\phi'_{1j}\right)\Bigg\}d\tau_{int}
\end{aligned}
\tag{7.7}
$$

The $\cos\theta_{ij}$ factors in each of these must be re-expressed in terms of r_i and r_{ij} by using Equation (B.44) so that these can solved using the techniques given in Section 4.1.1. Similar to the P-wave, I wrote a *Mathematica* notebook (see Appendix D) that transforms these equations into a form that allows us to copy and paste them directly into Fortran code.

7.3 Short-Range – Long-Range Matrix Elements

To calculate $\mathcal{L}C_2$, we again use the code in Figure 3.1 to get

$$\begin{aligned}\frac{1}{2}\left(\nabla_\rho^2+\kappa^2\right)Y_2^0(\theta_\rho,\varphi_\rho)n_2(\kappa\rho)f_2(\rho) = \\ -\frac{1}{2\kappa^3\rho^4}\left\{\rho f_2''(\rho)\left[\left(3-\kappa^2\rho^2\right)\cos(\kappa\rho)+3\kappa\rho\sin(\kappa\rho)\right]\right. \\ \left.+2f_2'(\rho)\left[\kappa\rho\left(\kappa^2\rho^2-6\right)\sin(\kappa\rho)+3\left(\kappa^2\rho^2-2\right)\cos(\kappa\rho)\right]\right\}. \quad (7.8)\end{aligned}$$

To simplify these equations, define

$$\begin{aligned}\mathscr{L}S_2 =& \frac{\mathcal{L}S_2}{Y_{20}(\theta_\rho)} = \left(\frac{2}{r_1}-\frac{2}{r_2}-\frac{2}{r_{13}}+\frac{2}{r_{23}}\right)\Phi_{Ps}(r_{12})\Phi_H(r_3)\sqrt{2\kappa}\,j_2(\kappa\rho) \\ \mathscr{L}C_2 =& \frac{\mathcal{L}C_2}{Y_{20}(\theta_\rho)} = -\left(\frac{2}{r_1}-\frac{2}{r_2}-\frac{2}{r_{13}}+\frac{2}{r_{23}}\right)\Phi_{Ps}(r_{12})\Phi_H(r_3)\sqrt{2\kappa}\,n_2(\kappa\rho)f_2(\rho) \\ &-\Phi_{Ps}(r_{12})\Phi_H(r_3)\sqrt{2\kappa}\frac{1}{2\rho}\left\{\left[4n_2(\kappa\rho)-2\kappa\rho\,n_1(\kappa\rho)\right]f_2'(\rho)-\rho\,n_2(\kappa\rho)f_2''(\rho)\right\}. \quad (7.9)\end{aligned}$$

Equivalently,

$$\mathscr{L}S_2' = \frac{\mathcal{L}S'}{Y_{20}(\theta_{\rho'})} \text{ and } \mathscr{L}C_2' = \frac{\mathcal{L}C'}{Y_{20}(\theta_{\rho'})}. \quad (7.10)$$

Each of the following equations has multiple forms that can be used due to the properties of the permutation operator, but these equations show the form that we used in our code. These equations are mainly straightforward applications of the external angular integrations in Appendix A to the matrix elements of Equation (3.56).

$$(\bar{\phi}_{1i},\mathcal{L}\bar{S}_2) = \sqrt{2}\cdot 2\pi\int\phi_{1i}\left[\left(1-\frac{3r_2^2\sin^2\theta_{12}}{8\rho^2}\right)\mathscr{L}S_2 \pm \left(1-\frac{3r_3^2\sin^2\theta_{13}}{8\rho'^2}\right)\mathscr{L}S_2'\right]d\tau_{int} \quad (7.11)$$

$$(\bar{\phi}_{1i},\mathcal{L}\bar{C}_2) = \sqrt{2}\cdot 2\pi\int\phi_{1i}\left[\left(1-\frac{3r_2^2\sin^2\theta_{12}}{8\rho^2}\right)\mathscr{L}C_2 \pm \left(1-\frac{3r_3^2\sin^2\theta_{13}}{8\rho'^2}\right)\mathscr{L}C_2'\right]d\tau_{int} \quad (7.12)$$

$$\begin{aligned}(\bar{\phi}_{2j},\mathcal{L}\bar{S}_2) =& \sqrt{2}\cdot 2\pi\int\phi_{2j}\left[\left(\frac{3(r_1\cos\theta_{12}+r_2)^2}{8\rho^2}-\frac{1}{2}\right)\mathscr{L}S_2\right. \\ &\left.\pm\left(\frac{3(r_1\cos\theta_{12}+r_3\cos\theta_{23})^2}{8\rho'^2}-\frac{1}{2}\right)\mathscr{L}S_2'\right]d\tau_{int} \quad (7.13)\end{aligned}$$

$$(\bar{\phi}_{2j}, \mathcal{L}\bar{C}_2) = \sqrt{2} \cdot 2\pi \int \phi_{2j} \left[\left(\frac{3(r_1 \cos\theta_{12} + r_2)^2}{8\rho^2} - \frac{1}{2} \right) \mathscr{L} C_2 \right.$$
$$\left. \pm \left(\frac{3(r_1 \cos\theta_{12} + r_3 \cos\theta_{23})^2}{8\rho'^2} - \frac{1}{2} \right) \mathscr{L} C_2' \right] d\tau_{int} \tag{7.14}$$

7.4 Long-Range – Long-Range Matrix Elements

Similar to the short-short terms, the derivations for the long-long terms are available on the Wiki [4] and figshare [2]. After external angular integrations (see Appendix A), these matrix elements are:

$$(\bar{S}_2, \mathcal{L}\bar{S}_2) = \pm 2\pi \int \left\{ S_2 S_2' \left(\frac{2}{r_1} - \frac{2}{r_2} - \frac{2}{r_{13}} + \frac{2}{r_{23}} \right) \left[\frac{3}{8} \frac{(4\rho^2 + 4\rho'^2 - r_{23}^2)^2}{16\rho^2\rho'^2} - \frac{1}{2} \right] \right\} d\tau_{int} \tag{7.15}$$

$$(\bar{C}_2, \mathcal{L}\bar{S}_2) = \pm 2\pi \int \left\{ S_2 C_2' \left(\frac{2}{r_1} - \frac{2}{r_2} - \frac{2}{r_{13}} + \frac{2}{r_{23}} \right) \left[\frac{3}{8} \frac{(4\rho^2 + 4\rho'^2 - r_{23}^2)^2}{16\rho^2\rho'^2} - \frac{1}{2} \right] \right\} d\tau_{int} \tag{7.16}$$

$$(\bar{S}_2, \mathcal{L}\bar{C}_2) = 2\pi \int \left\{ \pm S_2' C_2 \left(\frac{2}{r_1} - \frac{2}{r_2} - \frac{2}{r_{13}} + \frac{2}{r_{23}} \right) \left[\frac{3}{8} \frac{(4\rho^2 + 4\rho'^2 - r_{23}^2)^2}{16\rho^2\rho'^2} - \frac{1}{2} \right] \right.$$
$$- \left[S_2 \pm \left(\frac{3}{8} \frac{(4\rho^2 + 4\rho'^2 - r_{23}^2)^2}{16\rho^2\rho'^2} - \frac{1}{2} \right) S_2' \right] \sqrt{2\kappa}\, \Phi_{Ps}(r_{12})\, \Phi_H(r_3)$$
$$\left. \times \frac{1}{2\rho} \left([4n_2(\kappa\rho) - 2\kappa\rho\, n_1(\kappa\rho)]\, f_2'(\rho) - \rho\, n_2(\kappa\rho) f_2''(\rho) \right) \right\} d\tau_{int} \tag{7.17}$$

$$(\bar{C}_2, \mathcal{L}\bar{C}_2) = 2\pi \int \left\{ \pm C_2' C_2 \left(\frac{2}{r_1} - \frac{2}{r_2} - \frac{2}{r_{13}} + \frac{2}{r_{23}} \right) \left[\frac{3}{8} \frac{(4\rho^2 + 4\rho'^2 - r_{23}^2)^2}{16\rho^2\rho'^2} - \frac{1}{2} \right] \right.$$
$$\left. - \left[C_2 \pm \left(\frac{3}{8} \frac{(4\rho^2 + 4\rho'^2 - r_{23}^2)^2}{16\rho^2\rho'^2} - \frac{1}{2} \right) C_2' \right] \sqrt{2\kappa}\, \Phi_{Ps}(r_{12})\, \Phi_H(r_3) \right.$$

$$\times \frac{1}{2\rho}\left([4n_2(\kappa\rho) - 2\kappa\rho\, n_1(\kappa\rho)]\, f_2'(\rho) - \rho\, n_2(\kappa\rho) f_2''(\rho)\right)\Bigg\} d\tau_{int}. \tag{7.18}$$

7.5 Mixed Symmetry Terms

According to Schwartz [132], to have a complete description, each partial wave needs $\ell + 1$ symmetries. As shown in Equations (5.1) and (6.1), we use the full sets of symmetries for the S-wave and P-wave. There is a third symmetry for the D-wave, which we refer to as the mixed symmetry terms, or mixed terms, given by

$$\begin{aligned}
\psi(\ell_1, \ell_2, L, M) = \psi_{(1,1,2,0)} &= \sum_{m=-1}^{+1} Y_{1,m}(\theta_1, \varphi_1) Y_{1,m}(\theta_2, \varphi_2)\, \langle 1, m; 1, -m, 0 | 2, 0\rangle \\
&= Y_{1,-1}(\theta_1, \varphi_1) Y_{1,+1}(\theta_2, \varphi_2)\, \langle 1, -1, 1, +1 | 2, 0\rangle \\
&\quad + Y_{1,0}(\theta_1, \varphi_1) Y_{1,0}(\theta_2, \varphi_2)\, \langle 1, 0, 1, 0 | 2, 0\rangle \\
&\quad + Y_{1,+1}(\theta_1, \varphi_1) Y_{1,-1}(\theta_2, \varphi_2)\, \langle 1, +1, 1, -1 | 2, 0\rangle\,,
\end{aligned} \tag{7.19}$$

where ℓ_1 and ℓ_2 are the angular momenta on the particles in Ps, and L and M give the angular momentum of the Ps. These three terms can be combined into a single set as

$$\psi_{(1,1,2,0)}(\theta_1, \theta_2) = \frac{3}{4\pi}\frac{1}{\sqrt{6}}\left(3\cos\theta_1 \cos\theta_2 - \cos\theta_{12}\right). \tag{7.20}$$

This avoids the issue of dealing with complex terms in the $m = -1$ and $m = 1$ cases. Refer to Appendix B.7 for the derivation of Equation (7.20) from Equation (7.19).

The short-long matrix elements that include the mixed terms are not much more difficult to deal with than the first and second symmetry terms. The evaluation of the short-short matrix elements involving the mixed terms is much more difficult than those with just the first and second symmetry terms. I spent some time trying to derive the expressions for the short-short matrix elements but ran into difficulty doing so. There has been some preliminary progress on this front.

For three-body problems, the mixed terms are substantially easier to deal with. For e^+-H, Refs. [50, 131, 189, 190, 191] used the mixed terms. Dunn et al. [192, 193] also treated e^+-He as a three-body problem, using one-electron models of He and including the mixed terms.

Prior work [50, 95] on e^+-He scattering (also a four-body problem) neglected the mixed terms. The justification they used was that for e^+-H scattering, adding the third symmetry changed the K-matrix elements less than 1.5%. The e^+-H scattering problem also has mixed terms, but these are much easier to deal with analytically, since it is a three-body problem. However, this conclusion is now believed to be in error, as described in Ref. [56]. A corrected code in a preliminary investigation by Van Reeth and Humberston [194] for

e^+-H scattering found that these mixed terms can change the K-matrix elements by about 10% near the Ps formation threshold. Since they believed that the mixed terms did not contribute much, they were neglected for e^+-He scattering and virtual Ps terms were added in to improve the convergence, getting the final results to within 1 to 2% of the corrected code from this preliminary investigation. It is clear that these virtual Ps terms are no longer needed if the mixed terms are included.

The same preliminary investigation [194] also looked at e^--H scattering. This investigation found that the mixed terms change the ^{1}D and ^{3}D phase shifts less than 1%, but the ^{1}D phase shifts are affected more by the inclusion of the mixed terms. The ^{1}D phase shifts are affected less at low κ and more at higher κ, though the contributions are still small.

Due to the difficulty we had evaluating the analytical portion (the external angular integrals) for the mixed terms, we only included the first two symmetries in the D-wave calculations in this work. The preliminary investigation [194] took place only recently, after we had attempted other methods to accelerate the convergence of the D-wave phase shifts. As we discovered in Section 7.6, this turns out to be an acceptable approximation.

7.6 Results

This section gives the results of the ^{1,3}D-wave calculations using the nonlinear parameters determined in Appendix C.1.4.

7.6.1 Phase Shifts

Table 7.1 and Figure 7.2 show the final results of the phase shifts using the S-matrix complex Kohn with the nonlinear parameters given in Appendix C.1.4 and compares to multiple other calculations by other groups. One of the most easily noticeable problems is the poor convergence for $\kappa = 0.1$ for both ^{1}D and ^{3}D. As mentioned in Section 4.4 on page 64, our code does not seem to handle very small phase shifts particularly well, and we likely would have to increase the number of integration points further. Also, the lack of mixed terms likely affects the convergence. Both of these effects likely combine to give a bad extrapolation of over 100%. However, note that the phase shifts for $\kappa = 0.1$ are not extremely far from the CC of Refs. [70, 72]. We do not show this extrapolation for ^{1}D in Ref. [56], as it is obviously not good.

For $\kappa \geq 0.2$, the extrapolations look more reasonable, and for ^{1}D, the phase shifts look relatively well converged, especially for $\kappa \geq 0.3$. We believe that with the exception of $\kappa < 0.2$, the ^{1}D phase shifts are reasonably accurate, even with the omission of the mixed terms. The ^{1}D phase shifts for $\omega = 5$ and $\omega = 6$ differ by less than 10%.

For ^{3}D, the extrapolations are worse when the phase shift curve goes from positive to negative, which happens around $\kappa = 0.35$, as can be seen in Figure 7.2(b). In Ref. [70], they note that this change in sign of the phase shifts indicates a switch from being repulsive at low κ and attractive at high κ. In the higher κ region ($\kappa \geq 0.5$), the ^{3}D phase shift

Method	0.1	0.2	0.3	0.4	0.5	0.6	0.7
This work ($\omega = 6$) δ_2^+	1.36^{-4}	2.99^{-3}	1.60^{-2}	4.98^{-2}	1.13^{-1}	2.06^{-1}	3.28^{-1}
This work ($\omega \to \infty$) δ_2^+	4.24^{-4}	3.18^{-3}	1.62^{-2}	5.05^{-2}	1.14^{-1}	2.09^{-1}	3.33^{-1}
% Diff$^+$	103.0%	6.27%	1.54%	1.33%	1.52%	1.67%	1.67%
% Diff$^+$ CC	39.1%	15.4%	7.81%	4.71%	2.62%	0.97%	1.23%
CC 9Ps9H+H$^-$ [72] δ_2^+	2.02^{-4}	3.49^{-3}	1.73^{-2}	5.22^{-2}	1.16^{-1}	2.08^{-1}	3.24^{-1}
CC 9Ps9H [70] δ_2^+	1.46^{-4}	3.15^{-3}	1.65^{-2}	4.95^{-2}	1.08^{-1}	1.94^{-1}	3.02^{-1}
3-state CC [66] δ_2^-	3.22^{-5}	9.29^{-4}	5.96^{-3}	2.01^{-2}	4.63^{-2}	8.29^{-2}	1.23^{-1}
SE [75] δ_2^+	3.18^{-5}	9.17^{-4}	5.87^{-3}	1.97^{-2}	4.54^{-2}	8.09^{-2}	1.19^{-1}
5-state CC [68] δ_2^+	1.8^{-5}	5.3^{-4}	3.5^{-3}	1.2^{-2}	2.9^{-2}	5.5^{-2}	8.8^{-2}
SE [73] δ_2^+	0.0	0.0009	0.0058	0.0195	0.0453	0.0810	0.1194
This work ($\omega = 6$) δ_2^-	5.81^{-5}	7.12^{-4}	1.07^{-3}	-2.00^{-3}	-1.12^{-2}	-2.65^{-2}	-4.45^{-2}
This work ($\omega \to \infty$) δ_2^-	3.13^{-4}	8.67^{-4}	1.41^{-3}	-1.20^{-3}	-9.34^{-2}	-2.32^{-2}	-4.02^{-2}
% Diff$^-$	137.4%	19.6%	24.4%	39.8%	13.5%	9.10%	6.28%
CC 9Ps9H [70] δ_2^-	8.48^{-5}	1.15^{-3}	2.84^{-3}	2.37^{-3}	-4.66^{-3}	-1.85^{-2}	-3.27^{-2}
3-state CC [66] δ_2^-	-2.74^{-5}	-7.77^{-4}	-4.83^{-3}	-1.55^{-2}	-3.41^{-2}	-5.83^{-2}	-8.25^{-2}
SE [75] δ_2^+	-3.00^{-5}	-8.56^{-4}	-5.37^{-3}	-1.76^{-2}	-3.95^{-2}	-7.03^{-2}	-1.06^{-1}
5-state CC [68] δ_2^+	-1.4^{-5}	-4.0^{-4}	-2.6^{-3}	-8.6^{-3}	-2.0^{-2}	-3.6^{-2}	-5.5^{-2}
SE [73] δ_2^+	0.0	-8.0^{-4}	-5.3^{-3}	-1.74^{-2}	-3.95^{-2}	-7.04^{-2}	-1.062^{-1}

Table 7.1: Comparison of ^{1,3}D phase shifts and comparisons with other groups. Values in the header are κ in au. % Diff$^\pm$ is the percent difference between the current complex Kohn $\omega = 6$ and extrapolated values. % Diff$^+$ CC is the percent difference between the complex Kohn $\omega = 6$ and CC 14Ps14H+H$^-$ [72] phase shifts. Exponents denote powers of 10.

convergence is much better, getting down to $\sim 6\%$. Due to the worse extrapolations for ^{3}D than for the ^{1,3}S, ^{1,3}P, and ^{1}D partial waves, we do not report any ^{3}D extrapolations in Ref. [56].

We see from Table 7.1 and Figure 7.2 that the CC phase shifts [70, 72] are generally above the S-matrix complex Kohn phase shifts. The exception is the $\kappa = 0.7$ phase shift for ^{1}D and the extrapolated phase shifts for $\kappa = 0.6$ and 0.7, where the complex Kohn results are slightly higher. For ^{1}D, the complex Kohn and CC [72] results overall agree very well, as seen in the fourth line of Table 7.1, with percent differences $\sim 1\%$ at higher κ.

There is much more discrepancy between the ^{3}D complex Kohn and CC phase shifts, as can be seen easily in Figure 7.2 and the inset of Figure 7.1. This discrepancy plus the poorer ^{3}D extrapolations show that the ^{3}D phase shifts are not fully converged. It should be noted however that the CC phase shifts could be overestimates, considering that the CVM [181] ^{3}S phase shifts agree extremely well with the complex Kohn phase shifts, but the CC ^{3}S phase shifts are slightly higher than both. The CC also differs from the complex Kohn at low κ for the ^{3}P-wave, where we do not have a neglected symmetry, and the phase shifts are well converged.

Unfortunately, it is not possible to know at the moment how far the complex Kohn phase shifts differ from the true phase shifts, and further investigation into the mixed terms could help resolve this discrepancy. Thankfully, the contribution to the cross sections in Chapter 10 from the ^3D is small, even in the differential cross section. The ^{1}D contribution to the cross sections is very small in the low κ region where the phase shifts are less converged. In the resonance region, where the ^{1}D resonance contributes significantly, the phase shifts are well converged.

7.6.2 Resonance Parameters

The ^{1}D-wave has a single resonance before the Ps(n=2) threshold, unlike the ^{1}S- and ^{1}P-waves, which have two. We use Equation (3.121) to fit this curve but without the second arctan term. As mentioned in the previous section, the ^{1}D phase shifts are well converged in the higher κ region, where the resonance is located.

From the discussion in Appendix C.1.4, the complex Kohn resonance parameters presented in Table 7.2 are more sensitive to the nonlinear parameters than the two lower partial waves. The complex Kohn resonance parameters agree very well with the complex rotation [182]. The 9Ps9H CC results [70] are brought closer to the complex Kohn and complex rotation results by the inclusion of the H^- channel for both the position and width. The stabilization [130] results are also similar to the complex rotation results, both of which are carried out by Yan and Ho.

This ^{1}D-wave resonance has a very important contribution to the cross sections in Chapter 10. Due to the $(2\ell + 1)$ dependence for the elastic integrated and elastic differential cross sections and the $(\ell + 1)$ dependence for the momentum transfer cross section, the

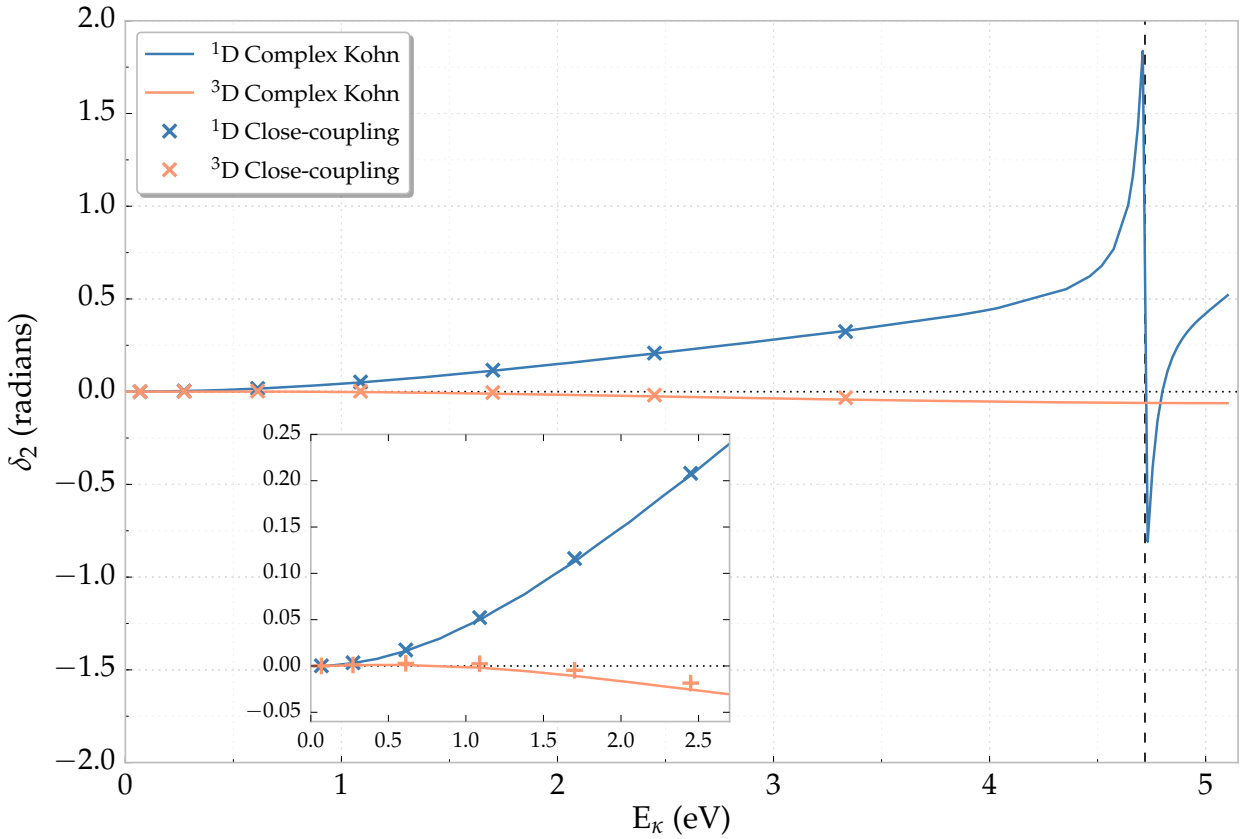

Figure 7.1: ^{1,3}D complex Kohn phase shifts. The ^{1}D CC phase shifts [72] are given by $\times$, and the ^{3}D CC phase shifts [70] are given by $+$. Vertical dashed lines denote the complex rotation resonance positions [182]. An interactive version of this figure is available online [3] at `https://plot.ly/~Denton/5/d-wave-ps-h-scattering/`.

Method	^1E_R (eV)	$^1\Gamma$ (eV)
Current work: Average $\pm$ standard deviation	4.720 ± 0.001	0.0908 ± 0.0010
Current work: S-matrix complex Kohn	4.720	0.0909
CC (9Ps9H + H^-) [72]	4.899	0.0872
Stabilization [130]	4.714	0.0969
CC (9Ps9H) [70]	5.16	0.15
CC (22Ps1H + H^-) [71]	4.814	0.065
Optical potential [152]	4.729	0.327
Complex rotation [182]	4.710 ± 0.0027	0.0925 ± 0.0054
Coupled-pseudostate [67]	5.28	0.47

Table 7.2: ^{1}D-wave resonance parameters

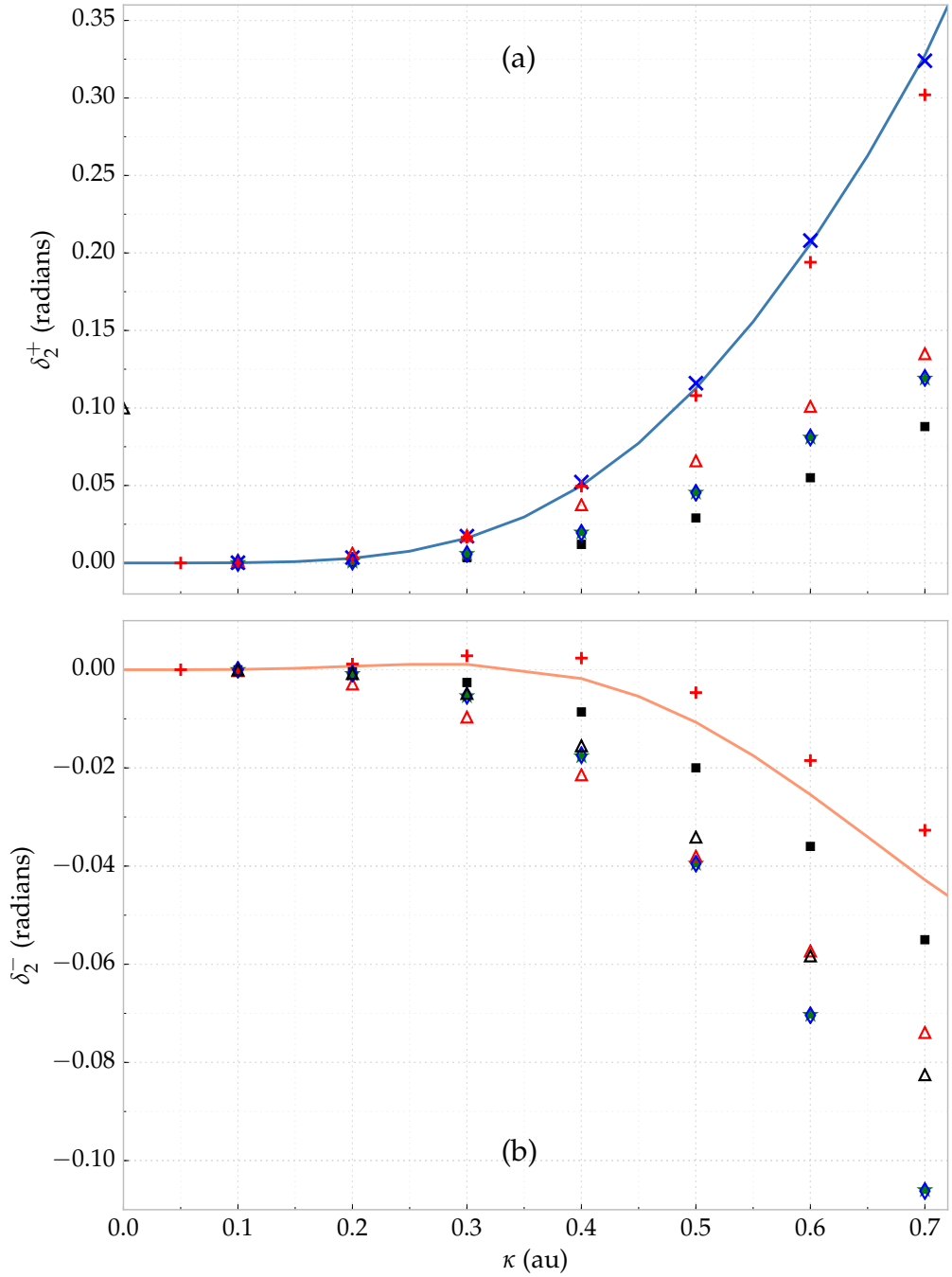

Figure 7.2: Comparison of ^{1}D (a) and ^{3}D (b) phase shifts with results from other groups. Results are ordered according to year of publication. Solid curves – this work; × – CC [72]; ● – Kohn [57]; + – CC [70]; △ – 6-state CC [69]; ■ – 5-state CC [68]; △ – 3-state CC [66]; ★ – CC [75]; ◊ – Static-exchange [73].

^{1}D resonance has a larger contribution to these cross sections than the ^{1}S- and ^{1}P-waves.

7.7 Summary

The ^{1}D-wave phase shifts obtained by the Kohn-type methods using the first two short-range symmetries are relatively well converged at higher κ but do not appear to be as well converged at low κ values. The ^{3}D-wave phase shifts are less converged than the ^{1}D phase shifts and show poor convergence at low κ. Including the mixed symmetry terms may improve the convergence, but we have not included them in this work, primarily due to the difficulty of evaluating the short-short integrations. However, we are able to reliably calculate the ^{1}D resonance, and the contribution to the cross sections from the less accurate ^{3}D phase shifts is minimal (see Chapter 10). The contribution to the cross sections from the ^{1}D low κ phase shifts is also small.

8 General Ps-H Formalism

To extend this work to higher partial waves, we could have continued as before, performing derivations and writing new code for each partial wave. This takes time and is error prone, so during the course of writing the D-wave code, I investigated creating a general formalism that works for arbitrary ℓ. The long-range code, covered in Section 8.1, is a straightforward generalization from the previous codes. The short-range code, discussed in Section 8.2, uses the Laplacian formalism instead of the gradient-gradient that we used in the S-, P-, and D-wave short-short codes, which also enabled us to compare the two different methods for the first three partial waves.

8.1 General Long-Range Matrix Elements

If the mixed symmetry terms in Section 7.5 are not included for the D-wave, the P-wave and D-wave long-range codebases are very similar. The S-wave is not much different as well, but it only has a single symmetry. We also only treat the first two symmetries for $\ell \geq 2$.

8.1.1 Long-Long Matrix Elements

One major difference for similar matrix elements is the angular integrations. As shown in Appendix A, the external angular integrations for each partial wave have different results, due to the different spherical harmonics. $\widetilde{S}_\ell$ and $\widetilde{C}_\ell$ are also of a similar form between the partial waves, as seen in Equations (3.3) and (3.4). Other than the spherical harmonics, the spherical Bessel functions are different, as is the shielding function for $\widetilde{C}_\ell$. The spherical Bessel functions are easily called through the GNU Scientific Library [195] for any ℓ-value. The power of the shielding function varies as $m_\ell \geq (2\ell + 1)$. All of this allows us to easily generalize the long-long integrations.

8.1.2 Short-Long Matrix Elements

The short-range functions are also easily generalizable. For the P-wave and D-wave, these are seen in Equations (6.2) and (7.2). The ϕ_i and ϕ_j parts for each are the same. This fact can only be easily used for the short-long calculations and not the short-short calculations, due to the action of the $\mathcal{L}$-operator on these terms. The formalism we have used for the short-long terms at every stage only operates $\mathcal{L}$ on the long-range parts. Section 8.2 covers the calculations of the short-short terms using a general formalism.

8.2 General Short-Range–Short-Range

The short-short integrals are more complicated due to the gradient-gradient operator acting on the short-range terms (see Equation (2.9)). As an example of the nature of these, refer to Section 7.2. The derivations were previously performed by rotating the coordinate system and integrating over external angles first, as described in Appendix A. This approach works, but it cannot be extended to higher partial waves without completing a full derivation for each partial wave. Drake and Yan [60] expand upon their previous work for the three-electron Hylleraas integrals to include the spherical harmonics using the Laplacian formalism instead, which still has a complicated form but works for arbitrary ℓ. It is this approach that we take here. All equations in this section have been rederived for the Ps-H system in my notes [2, 4]. The work of Harris [196] may also be directly applicable to this problem, but this has not yet been explored.

8.2.1 Hamiltonian

As we have for the bound state problem, the Hamiltonian is given compactly as in Equation (2.8) by

$$H = \sum_{i=1}^{3}\left(-\frac{1}{2}\nabla_i^2 - \frac{1}{r_i}\right) + \sum_{i>j}^{3}\frac{1}{r_{ij}}. \tag{8.1}$$

As in Ref. [60], when the Laplacians are expanded, this is given by the form

$$\begin{aligned} H = -\frac{1}{2}\Bigg[&\sum_{i=1}^{3}\left(\frac{\partial^2}{\partial r_i^2} + \frac{2}{r_i}\frac{\partial}{\partial r_i} - \frac{\ell(\ell+1)}{r_i^2}\right) + \sum_{i>j}^{3}\left(2\frac{\partial^2}{\partial r_i^2} + \frac{4}{r_{ij}}\frac{\partial}{\partial r_i}\right) + \sum_{i\neq j}^{3}\left(\frac{r_i^2 - r_j^2 + r_{12}^2}{r_i r_j}\right) \\ &+ \frac{r_{12}^2 + r_{13}^2 - r_{23}^2}{r_{12}r_{13}}\frac{\partial^2}{\partial r_{12}\partial r_{13}} + \frac{r_{12}^2 + r_{23}^2 - r_{13}^2}{r_{12}r_{23}}\frac{\partial^2}{\partial r_{12}\partial r_{23}} + \frac{r_{13}^2 + r_{23}^2 - r_{12}^2}{r_{13}r_{23}}\frac{\partial^2}{\partial r_{13}\partial r_{23}} \\ &+ \sum_{i>j}^{3}\frac{1}{r_{ij}}\frac{r_i}{r_j}\frac{\partial}{\partial r_{ij}}\left(\hat{\boldsymbol{r}}_i\cdot\hat{\nabla}_j^{Y}\right) + \sum_{i>j}^{3}\frac{1}{r_{ji}}\frac{r_j}{r_i}\frac{\partial}{\partial r_{ji}}\left(\hat{\boldsymbol{r}}_j\cdot\hat{\nabla}_i^{Y}\right)\Bigg]. \end{aligned} \tag{8.2}$$

This is the form when the mass polarization terms are unimportant (with $\mu \to 0$). As defined in Ref. [60], $\hat{\boldsymbol{r}}_j = \boldsymbol{r}_i/r_i$ and $\hat{\nabla}_i^{Y} = r_i\nabla_i^{Y}$. The terms involving ∇_i^{Y} only operate on the spherical harmonics, and they will be discussed in Section 8.2.3.

The wavefunction we use is slightly different from the form Yan and Drake [60] use. Specifically, we handle the antisymmetrization operator differently in our code, and we do not include the Ω function, given by Equation (10) in their paper. Part of the difference here is that we are working with two electrons and one positron, whereas they are working with systems that have three electrons, such as binding energy calculations of Li.

8.2.2 General Integrals

Using the notation in Ref. [60], the terms in Equation (8.2) without the spherical harmonic operator, $\hat{\nabla}_i^Y$, will be of the general form

$$\begin{aligned} I(\ell_1' m_1', \ell_2' m_2', \ell_3' m_3', \ell_1 m_1, \ell_2 m_2, \ell_3 m_3; j_1, j_2, j_3, j_{12}, j_{23}, j_{31}; \bar{\alpha}, \bar{\beta}, \bar{\gamma}) \\ = \int d\boldsymbol{r}_1 d\boldsymbol{r}_2 d\boldsymbol{r}_3 r_1^{j_1} r_2^{j_2} r_3^{j_3} r_{12}^{j_{12}} r_{23}^{j_{23}} r_{31}^{j_{31}} e^{-(\bar{\alpha} r_1 + \bar{\beta} r_2 + \bar{\gamma} r_3)} \\ \times Y^*_{\ell_1' m_1'}(\boldsymbol{r}_1) Y^*_{\ell_2' m_2'}(\boldsymbol{r}_2) Y^*_{\ell_3' m_3'}(\boldsymbol{r}_3) Y_{\ell_1 m_1}(\boldsymbol{r}_1) Y_{\ell_2 m_2}(\boldsymbol{r}_2) Y_{\ell_3 m_3}(\boldsymbol{r}_3)\,. \end{aligned} \tag{8.3}$$

As noted on page 29 for the Kohn-type variational methods, these should not be conjugated, but for this work with $m = 0$ (so excluding the mixed symmetry terms described in Section 7.5), the real-valued short-range terms will be the same with and without the conjugate. The method described here is an extension of that in Section 4.1.1. Note that α, β, and γ are not necessarily the same as those in Equation (3.9). These will be 2α, 2β, and 2γ for the direct-direct terms and 2α, $\beta+\gamma$, $\gamma+\beta$ for the direct-exchange terms. After some manipulation, this integral can be written as [60]

$$\begin{aligned} I(\ell_1' m_1', \ell_2' m_2', \ell_3' m_3', \ell_1 m_1, \ell_2 m_2, \ell_3 m_3; j_1, j_2, j_3, j_{12}, j_{23}, j_{31}; \bar{\alpha}, \bar{\beta}, \bar{\gamma}) \\ = \sum_{q_{12}=0}^{M_{12}} \sum_{q_{23}=0}^{M_{23}} \sum_{q_{31}=0}^{M_{31}} \sum_{k_{12}=0}^{L_{12}} \sum_{k_{23}=0}^{L_{23}} \sum_{k_{31}=0}^{L_{31}} \\ \times I_{\text{ang}}(\ell_1' m_1', \ell_2' m_2', \ell_3' m_3', \ell_1 m_1, \ell_2 m_2, \ell_3 m_3; q_{12}, q_{23}, q_{31}) \\ \times I_{\text{R}}(q_{12}, q_{23}, q_{31}, k_{12}, k_{23}, k_{31}; j_1, j_2, j_3, j_{12}, j_{23}, j_{31}; \bar{\alpha}, \bar{\beta}, \bar{\gamma}). \end{aligned} \tag{8.4}$$

For even values of j_{12}, $M_{12} = \frac{1}{2} j_{12}$ and $L_{12} = \frac{1}{2} j_{12} - q_{12}$. For odd values of j_{12}, $M_{12} = \infty$ and $L_{12} = \frac{1}{2}(j_{12}+1)$. The same type of upper limits apply to the j_{23} and j_{31} terms.

The angular part of I is given by

$$\begin{aligned} I_{\text{ang}}(\ell_1' m_1', \ell_2' m_2', \ell_3' m_3', \ell_1 m_1, \ell_2 m_2, \ell_3 m_3; q_{12}, q_{23}, q_{31}) \\ = (-1)^{m_1'+m_2'+m_3'+q_{12}+q_{23}+q_{31}} (\ell_1', \ell_2', \ell_3', \ell_1, \ell_2, \ell_3)^{1/2} \sum_{n_1 n_2 n_3} (n_1, n_2, n_3) \\ \times \begin{Bmatrix} n_1 & n_2 & n_3 \\ q_{23} & q_{31} & q_{12} \end{Bmatrix} \begin{pmatrix} n_1 & n_2 & n_3 \\ m_1' - m_1 & m_2' - m_2 & m_3' - m_3 \end{pmatrix} \\ \times \begin{pmatrix} \ell_1' & \ell_1 & n_1 \\ -m_1' & m_1 & m_1' - m_1 \end{pmatrix} \begin{pmatrix} \ell_2' & \ell_2 & n_2 \\ -m_2' & m_2 & m_2' - m_2 \end{pmatrix} \end{aligned}$$

$$\times \begin{pmatrix} \ell_1' & \ell_3 & n_3 \\ -m_1' & m_3 & m_3' - m_3 \end{pmatrix} \begin{pmatrix} \ell_1' & \ell_1 & n_1 \\ 0 & 0 & 0 \end{pmatrix} \begin{pmatrix} \ell_2' & \ell_2 & n_2 \\ 0 & 0 & 0 \end{pmatrix}$$
$$\times \begin{pmatrix} \ell_3' & \ell_3 & n_3 \\ 0 & 0 & 0 \end{pmatrix} \begin{pmatrix} q_{31} & q_{12} & n_1 \\ 0 & 0 & 0 \end{pmatrix} \begin{pmatrix} q_{12} & q_{23} & n_2 \\ 0 & 0 & 0 \end{pmatrix} \begin{pmatrix} q_{23} & q_{31} & n_3 \\ 0 & 0 & 0 \end{pmatrix}. \quad (8.5)$$

This expression includes summations over both the Wigner 3-j and 6-j coefficients [197, 198, 199], also known as the 3-j and 6-j symbols. The 3-j symbols are related to the Clebsch-Gordan coefficients by [197, p.46]

$$\begin{pmatrix} j_1 & j_2 & j_3 \\ m_1 & m_2 & m_3 \end{pmatrix} = (-1)^{j_1 - j_2 + m_3} (2j_3 + 1)^{-1/2} \langle j_1, j_2; m_1, m_2 \,|j_1, j_2; j_3, -m_3\rangle \,. \quad (8.6)$$

The advantage of the 3-j symbols over the Clebsch-Gordan coefficients is that they are a more symmetric representation of angular momentum. The factor $(2\ell + 1)$ appears often in these types of derivations, so we adopt their shorthand notation of $(l, m, n, \ldots) = (2l + 1)(2m + 1)(2n + 1) \cdots$.

The radial part of Equation (8.4) is

$$\begin{aligned} &I_{\mathrm{R}}(q_{12}, q_{23}, q_{31}, k_{12}, k_{23}, k_{31}; j_1, j_2, j_3, j_{12}, j_{23}, j_{31}; \bar{\alpha}, \bar{\beta}, \bar{\gamma}) \\ &\quad = C_{j_{12} q_{12} k_{12}} C_{j_{23} q_{23} k_{23}} C_{j_{31} q_{31} k_{31}} \\ &\qquad \times W_{\mathrm{R}}(q_{12}, q_{23}, q_{31}, k_{12}, k_{23}, k_{31}; j_1, j_2, j_3, j_{12}, j_{23}, j_{31}; \bar{\alpha}, \bar{\beta}, \bar{\gamma}). \end{aligned} \quad (8.7)$$

The C_{jqk} coefficients are the same as in Equation (4.3). The W_{R} function is built from the W functions in Equation (4.4) as

$$\begin{aligned} &W_{\mathrm{R}}(q_{12}, q_{23}, q_{31}, k_{12}, k_{23}, k_{31}; j_1, j_2, j_3, j_{12}, j_{23}, j_{31}; \bar{\alpha}, \bar{\beta}, \bar{\gamma}) \\ &= W(j_1 + 2 + s_{12} + s_{31}, j_2 + 2 + j_{12} - s_{12} + s_{23}, j_3 + 2 + j_{23} - s_{23} + j_{31} - s_{31}; \bar{\alpha}, \bar{\beta}, \bar{\gamma}) \\ &\quad + W(j_1 + 2 + s_{12} + s_{31}, j_3 + 2 + s_{23} + j_{31} - s_{31}, j_2 + 2 + j_{12} - s_{12} + j_{23} - s_{23}; \bar{\alpha}, \bar{\gamma}, \bar{\beta}) \\ &\quad + W(j_2 + 2 + s_{12} + s_{23}, j_1 + 2 + j_{12} - s_{12} + s_{31}, j_3 + 2 + j_{23} - s_{23} + j_{31} - s_{31}; \bar{\beta}, \bar{\alpha}, \bar{\gamma}) \\ &\quad + W(j_2 + 2 + s_{12} + s_{23}, j_3 + 2 + j_{23} - s_{23} + s_{31}, j_1 + 2 + j_{12} - s_{12} + j_{31} - s_{31}; \bar{\beta}, \bar{\gamma}, \bar{\alpha}) \\ &\quad + W(j_3 + 2 + s_{23} + s_{31}, j_1 + 2 + s_{12} + j_{31} - s_{31}, j_2 + 2 + j_{12} - s_{12} + j_{23} - s_{23}; \bar{\gamma}, \bar{\alpha}, \bar{\beta}) \\ &\quad + W(j_3 + 2 + s_{23} + s_{31}, j_2 + 2 + s_{12} + j_{23} - s_{23}, j_1 + 2 + j_{12} - s_{12} + j_{31} - s_{31}; \bar{\gamma}, \bar{\beta}, \bar{\alpha}), \end{aligned} \quad (8.8)$$

with $s_{ij} = q_{ij} + 2k_{ij}$. Note that there are similarities with Equation (4.2).

8.2.3 Spherical Harmonic Terms

The terms in Equation (8.2) involving the spherical harmonic operator $\hat{\nabla}_i^Y$ have to be handled differently than the other terms. In Ref. [60], they do different permutations for the three-electron problem, so for the p in their paper, we always use $p = 1$.

$$I^1(\hat{\boldsymbol{r}}_1 \cdot \hat{\nabla}_2^Y) = \sum_{q_{12}=0}^{M_{12}} \sum_{q_{23}=0}^{M_{23}} \sum_{q_{31}=0}^{M_{31}} \sum_{k_{12}=0}^{L_{12}} \sum_{k_{23}=0}^{L_{23}} \sum_{k_{31}=0}^{L_{31}} \sum_{T_1=|1-\ell_1|}^{1+\ell_1} \sum_{T_2=|1-\ell_2|}^{1+\ell_2} b(\ell_2; T_2) C^1(\hat{\boldsymbol{r}}_1 \cdot \hat{\boldsymbol{r}}_2)$$
$$\times I_R(q_{12}, q_{23}, q_{31}, k_{12}, k_{23}, k_{31}; j_1, j_2, j_3, j_{12}, j_{23}, j_{31}; \bar{\alpha}, \bar{\beta}, \bar{\gamma}) \tag{8.9}$$

The b function here is defined by

$$\begin{aligned} b(\ell; \ell - 1) &= \ell + 1 \\ b(\ell; \ell + 1) &= -\ell. \end{aligned} \tag{8.10}$$

For any other values of the arguments, b gives 0. C^1 is given by

$$C^1(\hat{\boldsymbol{r}}_1 \cdot \hat{\boldsymbol{r}}_2) = (\ell_1', \ell_2', \ell_3', \ell_1, \ell_2, \ell_3)^{1/2} (-1)^{q_{12}+q_{23}+q_{31}} \sum_{n_1 n_2 n_3} (n_1, n_2, n_3, T_1, T_2)$$
$$\times \begin{pmatrix} 1 & \ell_1 & T_1 \\ 0 & 0 & 0 \end{pmatrix} \begin{pmatrix} 1 & \ell_2 & T_1 \\ 0 & 0 & 0 \end{pmatrix} \begin{pmatrix} \ell_1' & T_1 & n_1 \\ 0 & 0 & 0 \end{pmatrix} \begin{pmatrix} \ell_2' & T_2 & n_2 \\ 0 & 0 & 0 \end{pmatrix} \begin{pmatrix} \ell_3' & \ell_3 & n_3 \\ 0 & 0 & 0 \end{pmatrix}$$
$$\times \begin{pmatrix} q_{31} & q_{12} & n_1 \\ 0 & 0 & 0 \end{pmatrix} \begin{pmatrix} q_{12} & q_{23} & n_2 \\ 0 & 0 & 0 \end{pmatrix} \begin{pmatrix} q_{23} & q_{31} & n_3 \\ 0 & 0 & 0 \end{pmatrix} \begin{Bmatrix} n_1 & n_2 & n_3 \\ q_{23} & q_{31} & q_{12} \end{Bmatrix} \tilde{C}^1(\hat{\boldsymbol{r}}_1 \cdot \hat{\boldsymbol{r}}_2), \tag{8.11}$$

with

$$\tilde{C}^1(\hat{\boldsymbol{r}}_1 \cdot \hat{\boldsymbol{r}}_2) = \sum_{\mu} (-1)^{\mu - m_3} \begin{pmatrix} 1 & \ell_1 & T_1 \\ \mu & m_1 & -\mu - m_1 \end{pmatrix} \begin{pmatrix} 1 & \ell_2 & T_2 \\ -\mu & m_2 & \mu - m_2 \end{pmatrix}$$
$$\times \begin{pmatrix} \ell_3' & \ell_3 & n_3 \\ -m_3' & m_3 & m_3' - m_3 \end{pmatrix} \begin{pmatrix} \ell_1' & T_1 & n_1 \\ -m_1' & \mu + m_1 & m_1' - \mu - m_1 \end{pmatrix}$$
$$\times \begin{pmatrix} \ell_2' & T_2 & n_2 \\ -m_2' & -\mu + m_2 & m_2' + \mu - m_2 \end{pmatrix} \begin{pmatrix} n_1 & n_2 & n_3 \\ m_1' - \mu - m_1 & m_2' + \mu - m_2 & m_3' - m_3 \end{pmatrix}. \tag{8.12}$$

The values that μ can take are -1, 0, and 1.

Considering the properties of the 3-j symbols in Equation (8.12), the limits for the T_1 summation in Equation (8.9) are $|1 - \ell_1|$ to $1 + \ell_1$. Similarly, for the T_2 summation, the limits are $|1 - \ell_2|$ to $1 + \ell_2$. However, considering that the b function in Equation (8.10) can give 0, not all T_2 in this range are used.

Unlike the previous section, the expressions here are not exactly the same as that in Yan and Drake [60], since as noted, their wavefunction for Li has an extra set of coefficients. This addition to their wavefunction is included in the $\tilde{C}^1(\hat{\boldsymbol{r}}_1 \cdot \hat{\boldsymbol{r}}_2)$ and allows them to reduce these using graphical methods as in Refs. [198, 200]. Unfortunately, such simplifications are not possible with the form of Equation (3.1).

We note that $C^1(\hat{\boldsymbol{r}}_1 \cdot \hat{\boldsymbol{r}}_2) = C^1(\hat{\boldsymbol{r}}_2 \cdot \hat{\boldsymbol{r}}_1)$, but $I^1(\hat{\boldsymbol{r}_1} \cdot \hat{\nabla}_2^Y) \neq I^1(\hat{\boldsymbol{r}_2} \cdot \hat{\nabla}_1^Y)$. Namely,

$$I^1(\hat{\boldsymbol{r}_2} \cdot \hat{\nabla}_1^Y) = \sum_{q_{12}=0}^{M_{12}} \sum_{q_{23}=0}^{M_{23}} \sum_{q_{31}=0}^{M_{31}} \sum_{k_{12}=0}^{L_{12}} \sum_{k_{23}=0}^{L_{23}} \sum_{k_{31}=0}^{L_{31}} \sum_{T_1 T_2} b(\ell_1; T_1) C^1(\hat{\boldsymbol{r}}_1 \cdot \hat{\boldsymbol{r}}_2) \times I_{\mathrm{R}}(q_{12}, q_{23}, q_{31}, k_{12}, k_{23}, k_{31}; j_1, j_2, j_3, j_{12}, j_{23}, j_{31}; \bar{\alpha}, \bar{\beta}, \bar{\gamma}). \tag{8.13}$$

More generally, these integrals can be written as

$$I^1(\hat{\boldsymbol{r}}_i \cdot \hat{\nabla}_j^Y) = \sum_{q_{12}=0}^{M_{12}} \sum_{q_{23}=0}^{M_{23}} \sum_{q_{31}=0}^{M_{31}} \sum_{k_{12}=0}^{L_{12}} \sum_{k_{23}=0}^{L_{23}} \sum_{k_{31}=0}^{L_{31}} \sum_{T_i T_j} b(\ell_j; T_j) C^1(\hat{\boldsymbol{r}}_i \cdot \hat{\boldsymbol{r}}_j) \times I_{\mathrm{R}}(q_{12}, q_{23}, q_{31}, k_{12}, k_{23}, k_{31}; j_1, j_2, j_3, j_{12}, j_{23}, j_{31}; \bar{\alpha}, \bar{\beta}, \bar{\gamma}), \tag{8.14}$$

and $C^1(\hat{\boldsymbol{r}}_i \cdot \hat{\boldsymbol{r}}_j) = C^1(\hat{\boldsymbol{r}}_j \cdot \hat{\boldsymbol{r}}_i)$. Using cyclic permutations,

$$\begin{aligned} C^1(\hat{\boldsymbol{r}}_2 \cdot \hat{\boldsymbol{r}}_3) = (\ell_1', \ell_2', \ell_3', \ell_1, \ell_2, \ell_3)^{1/2} (-1)^{q_{12}+q_{23}+q_{31}} \sum_{n_1 n_2 n_3} (n_1, n_2, n_3, T_2, T_3) \\ \times \begin{pmatrix} 1 & \ell_2 & T_2 \\ 0 & 0 & 0 \end{pmatrix} \begin{pmatrix} 1 & \ell_3 & T_3 \\ 0 & 0 & 0 \end{pmatrix} \begin{pmatrix} \ell_1' & \ell_1 & n_1 \\ 0 & 0 & 0 \end{pmatrix} \begin{pmatrix} \ell_2' & T_2 & n_2 \\ 0 & 0 & 0 \end{pmatrix} \begin{pmatrix} \ell_3' & T_3 & n_3 \\ 0 & 0 & 0 \end{pmatrix} \\ \times \begin{pmatrix} q_{31} & q_{12} & n_1 \\ 0 & 0 & 0 \end{pmatrix} \begin{pmatrix} q_{12} & q_{23} & n_2 \\ 0 & 0 & 0 \end{pmatrix} \begin{pmatrix} q_{23} & q_{31} & n_3 \\ 0 & 0 & 0 \end{pmatrix} \begin{Bmatrix} n_1 & n_2 & n_3 \\ q_{23} & q_{31} & q_{12} \end{Bmatrix} \tilde{C}^1(\hat{\boldsymbol{r}}_2 \cdot \hat{\boldsymbol{r}}_3) \end{aligned} \tag{8.15}$$

with

$$\begin{aligned} \tilde{C}^1(\hat{\boldsymbol{r}}_2 \cdot \hat{\boldsymbol{r}}_3) = \sum_{\mu} (-1)^{\mu - m_1} \begin{pmatrix} 1 & \ell_2 & T_2 \\ \mu & m_2 & -\mu - m_2 \end{pmatrix} \begin{pmatrix} 1 & \ell_3 & T_3 \\ -\mu & m_3 & \mu - m_3 \end{pmatrix} \\ \times \begin{pmatrix} \ell_1' & \ell_1 & n_1 \\ -m_1' & m_1 & m_1' - m_1 \end{pmatrix} \begin{pmatrix} \ell_2' & T_2 & n_2 \\ -m_2' & \mu + m_2 & m_2' - \mu - m_2 \end{pmatrix} \\ \times \begin{pmatrix} \ell_3' & T_3 & n_3 \\ -m_3' & -\mu + m_3 & m_3' + \mu - m_3 \end{pmatrix} \begin{pmatrix} n_1 & n_2 & n_3 \\ m_1' - m_1 & m_2' - \mu - m_2 & m_3' + \mu - m_3 \end{pmatrix}, \end{aligned} \tag{8.16}$$

and

$$\begin{aligned} C^1(\hat{\boldsymbol{r}}_3 \cdot \hat{\boldsymbol{r}}_1) = (\ell_1', \ell_2', \ell_3', \ell_1, \ell_2, \ell_3)^{1/2} (-1)^{q_{12}+q_{23}+q_{31}} \sum_{n_1 n_2 n_3} (n_1, n_2, n_3, T_3, T_1) \\ \times \begin{pmatrix} 1 & \ell_3 & T_3 \\ 0 & 0 & 0 \end{pmatrix} \begin{pmatrix} 1 & \ell_1 & T_1 \\ 0 & 0 & 0 \end{pmatrix} \begin{pmatrix} \ell_2' & \ell_2 & n_2 \\ 0 & 0 & 0 \end{pmatrix} \begin{pmatrix} \ell_3' & T_3 & n_3 \\ 0 & 0 & 0 \end{pmatrix} \begin{pmatrix} \ell_1' & T_1 & n_1 \\ 0 & 0 & 0 \end{pmatrix} \end{aligned}$$

$$\times \begin{pmatrix} q_{31} & q_{12} & n_1 \\ 0 & 0 & 0 \end{pmatrix} \begin{pmatrix} q_{12} & q_{23} & n_2 \\ 0 & 0 & 0 \end{pmatrix} \begin{pmatrix} q_{23} & q_{31} & n_3 \\ 0 & 0 & 0 \end{pmatrix} \begin{Bmatrix} n_1 & n_2 & n_3 \\ q_{23} & q_{31} & q_{12} \end{Bmatrix} \tilde{C}^1(\hat{\boldsymbol{r}}_3 \cdot \hat{\boldsymbol{r}}_1) \tag{8.17}$$

with

$$\begin{aligned} \tilde{C}^1(\hat{\boldsymbol{r}}_3 \cdot \hat{\boldsymbol{r}}_1) = \sum_{\mu} (-1)^{\mu - m_2} & \begin{pmatrix} 1 & \ell_3 & T_3 \\ \mu & m_3 & -\mu - m_3 \end{pmatrix} \begin{pmatrix} 1 & \ell_1 & T_1 \\ -\mu & m_1 & \mu - m_1 \end{pmatrix} \\ \times & \begin{pmatrix} \ell_2' & \ell_2 & n_2 \\ -m_2' & m_2 & m_2' - m_2 \end{pmatrix} \begin{pmatrix} \ell_3' & T_3 & n_3 \\ -m_3' & \mu + m_3 & m_3' - \mu - m_3 \end{pmatrix} \\ \times & \begin{pmatrix} \ell_1' & T_1 & n_1 \\ -m_1' & -\mu + m_1 & m_1' + \mu - m_1 \end{pmatrix} \begin{pmatrix} n_1 & n_2 & n_3 \\ m_1' + \mu - m_1 & m_2' - m_2 & m_3' - \mu - m_3 \end{pmatrix}. \end{aligned} \tag{8.18}$$

8.3 Programs

The general codes described in this chapter are available on GitHub [1].

The general short-short code implementing the equations described in Section 8.2 is at least an order of magnitude slower than the corresponding S-, P-, and D-wave short-short code developed separately for each of the first three partial waves. On the Talon 2 [201] cluster, an $\omega = 5$ run of the general short-short code takes approximately a full day running on a single node with 16 cores.

A rough analysis of the code shows that the bulk of the processing time is spent calculating the angular parts, i.e. the 3-j and 6-j symbols. Due to the symmetries inherent in the 3-j and 6-j symbols, different inputs can generate the same output. Also, many input values to these do not satisfy the selection rules for the 3-j and 6-j symbols [202, p.1054-1064] [197], giving a result of 0.

Multiple papers [203, 204, 205, 206] have detailed strategies to exploit the symmetries to speed up calculations of the 3-j and 6-j symbols. Storing a full lookup table with the full parameter space of the 6 input variables would be prohibitively memory-intensive. The most recent of these by Johansson and Forssén [206] provides a very promising algorithm with full code that could be used to speed up this general short-short code.

9 Higher Partial Waves

By the D-wave, the various cross sections in Chapter 10 have not fully converged, so we looked at the contributions from higher partial waves. This work includes partial waves through the H-wave ($\ell = 5$), but there is nothing preventing us from extending this to even higher partial waves now that we have determined general expressions for the external angular integrations in Appendix A.

9.1 Born-Oppenheimer Approximation

In an attempt to approximate the partial waves past the D-wave, we turned to the Born-Oppenheimer (BO) approximation [61, 207, 208, 209]. The BO approximation comes from using only the first term in Equations (3.10) and (3.11). Specifically, this is done with the Kohn variational method to get an estimate for the K-matrix, giving [43, p.720]

$$\tan\delta_\ell \approx -(\widetilde{S}_\ell, \mathcal{L}\widetilde{S}_\ell) = -(\bar{S}_\ell, \mathcal{L}\bar{S}_\ell) = \mp(S_\ell, \mathcal{L}S'_\ell)\,. \tag{9.1}$$

We have also performed Kohn variational method runs that only use the first two terms ($\widetilde{S}_\ell$ and $\widetilde{C}_\ell$) in Equations (3.10) and (3.11). This gives phase shifts that are very similar to the BO approximation and lines up nearly exactly with the BO on most partial waves, so we normally just use the BO approximation. We also note that the first Born approximation, $\tan\delta_\ell \approx -(S_\ell, \mathcal{L}S_\ell)$, cannot be used here due to Equation (3.112), since this gives 0.

These BO approximations were calculated for the first three partial waves but showed huge discrepancies, especially for the S-wave, as seen in Figures 9.1 to 9.3. The ^{1}S, ^{1}P, and ^{1}D partial waves have resonances before the Ps(n=2) threshold, which we would not expect to be represented by the BO approximation. The Ganas approximation described in Section 9.2 is also included in Figure 9.3. This approximation agrees with the ^{1}D phase shifts much better than the BO approximation.

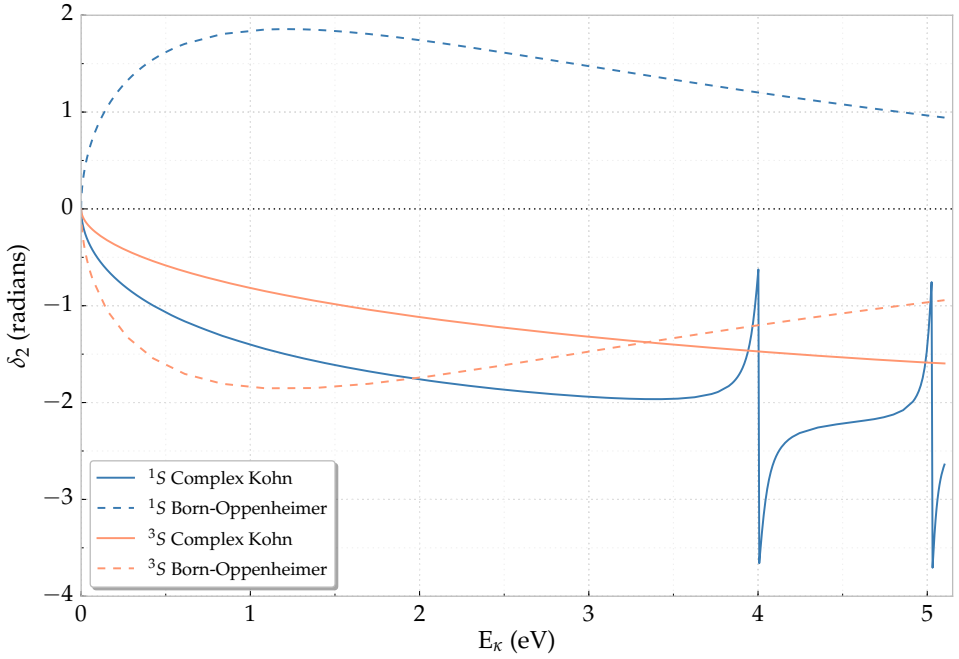

Figure 9.1: ^{1,3}S phase shift comparison between S-matrix complex Kohn and BO approximation

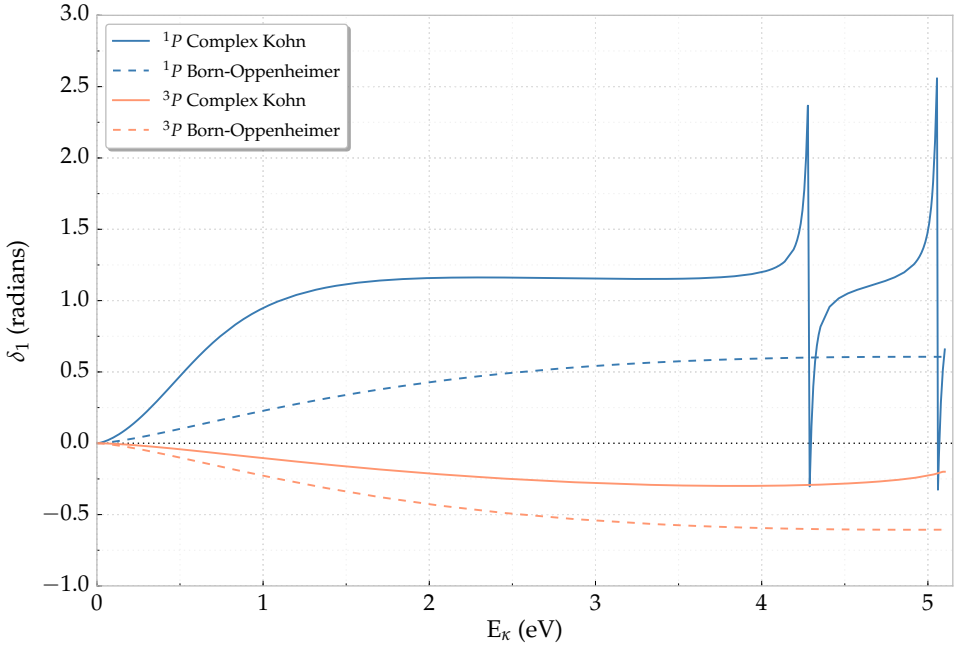

Figure 9.2: ^{1,3}P phase shift comparison between S-matrix complex Kohn and BO approximation

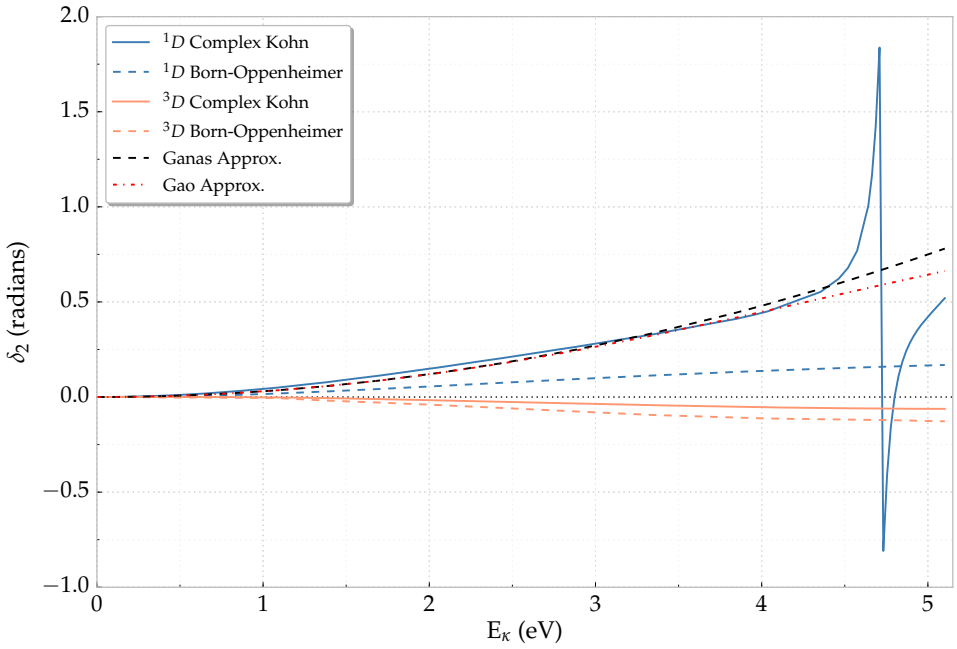

Figure 9.3: ^{1,3}D phase shift comparison between S-matrix complex Kohn, BO approximation, Ganas approximation and Gao approximation

For the ^{1}S, ^{1}P, ^{1}D, and ^{1}F partial waves, each has at least one resonance before or shortly after the Ps(n=2) threshold. The BO approximation does not capture resonance behavior, so we can really only look at this for partial waves that do not contain resonances in this region. As ℓ increases, the resonance positions (in Tables 5.3, 6.3, 7.2 and 9.1) increase, until they are past the threshold fully for the G-wave. Ho and Yan [210] calculate the G-wave resonance at 5.486 eV with a width of 0.0109 eV.

Due to the obvious discrepancies with even the D-wave, we decided to do full Kohn-type calculations for the F-wave to compare, again finding that the BO approximation does not match up as well as we would like for either ^{1}F or ^{3}F. We tried the same for the G-wave and H-wave, and the BO approximation does not match up with the complex Kohn phase shifts. The results of using the BO approximation for the higher partial waves are shown later in this chapter in Figures 9.4, 9.6 and 9.7. The BO approximation unfortunately does not represent any of the partial waves through the H-wave well for this system. Preliminary investigation shows that this pattern still holds

9.2 Ganas Approximation

Ganas [211] gives an expression to estimate phase shifts for $\ell \geq 2$ using a van der Waals ERT (see Section 11.1.3), which is given in a more convenient form by Refs. [42, 212, 213]

as

$$\delta_\ell(\kappa) \simeq \frac{6\pi m C_6 \kappa^4}{(2\ell+5)(2\ell+3)(2\ell+1)(2\ell-1)(2\ell-3)}. \tag{9.2}$$

For Ps scattering, $m = 2$. The van der Waals coefficient for Ps-H scattering is given in Section 11.1.3 as $C_6 = 34.78473$.

This approximation matches surprisingly well to the ^{1}D phase shifts in Figure 9.3. Figures 9.4, 9.6 and 9.7 show this approximation for the ^{1}F-, ^{1}G-, and ^{1}H-waves, and it normally gives a better approximation to the phase shifts than the BO approximation. For the H-wave, it matches relatively well but overestimates the phase shifts.

9.3 Gao Approximation

Gao [214] provides a QDT expansion for the van der Waals interaction, somewhat similar to those we used for the S-wave and P-wave in Section 11.1.3.4. For $\ell \geq 2$, the K_ℓ^0 and its derivatives do not come into play though. This expression is given in terms of $\tan\delta_\ell$:

$$\tan\delta_{\ell\geq 2} = (3\pi/32)\{(\ell+1/2)[(\ell+1/2)^2-4][(\ell+1/2)^2-1]\}^{-1}(\kappa\beta_6)^4, \tag{9.3}$$

where β_6 is given in Equation (11.18).

This approximation matches even better to the ^{1}D phase shifts than the Ganas approximation and matches the same as the Ganas approximation for $\ell \geq 3$. The behavior of all three of these approximations is shown in Figures 9.3, 9.4, 9.6 and 9.7.

9.4 F-Wave

Similar to the D-wave (see Appendix C.1.4), we investigated the dependence of the F-wave phase shifts on the nonlinear parameters. After multiple variations of α and β with a fixed γ, we settled on using the same set of nonlinear parameters that we used for the D-wave, as seen in Table C.13, but with the switchover between the two sets at $\kappa = 0.4$. We found that to keep $R'(5) < 1$ for ^{1,3}F, we had to use the restricted set described in Section 4.1.4 for $\kappa < 0.4$. We have calculated the F-wave phase shifts for $\omega = 5$ with these nonlinear parameters for the first two short-range symmetries using the general codes described in Sections 8.1 and 8.2.

9.4.1 Phase Shifts

Figure 9.4 shows the phase shifts for the F-wave. Similar to the D-wave (page 99), the triplet F-wave starts positive and becomes negative, though at a higher κ of about 0.7 (3.3 eV).

We can see that the phase shifts for the (modified) BO approximation do not agree very well with the full Kohn calculation, though they follow roughly the same shape.

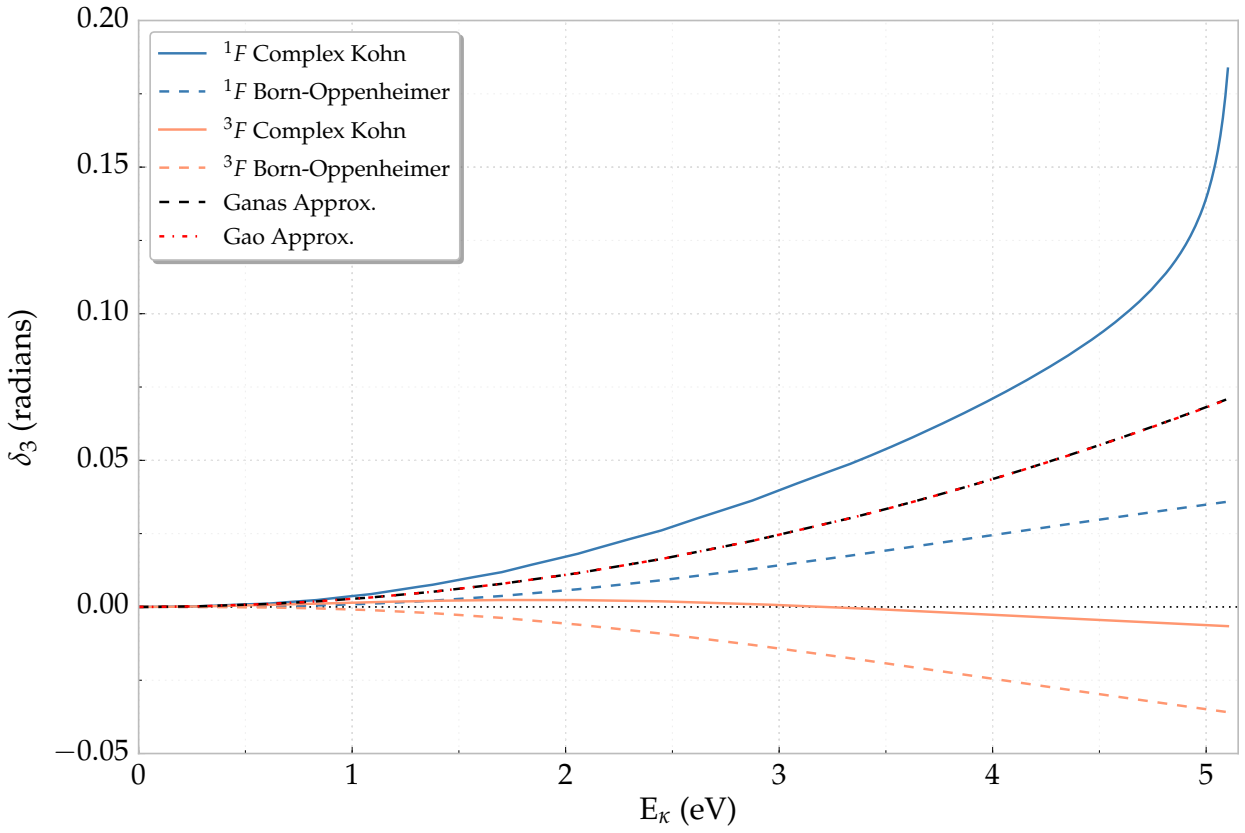

Figure 9.4: ^{1,3}F phase shifts

The triplet BO is fully negative, while the Kohn only goes negative past about $\kappa = 0.7$. The problem with the triplet gets even worse for the G-wave (Section 9.5) and H-Wave (Section 9.6). The Ganas Section 9.2 and Gao approximations Section 9.3, which do not distinguish between singlet and triplet states, match better with the singlet than the BO approximation but still disagrees near the resonance.

9.4.2 Resonance

There is the start of a resonance shortly before the threshold cutoff in Figure 9.4. Figure 9.5 gives a fuller plot past this resonance. As our code does not contain the open channels required to extend into the region that contains the full resonance, we likely cannot determine the resonance parameters as accurately. Table 9.1 give the resonance parameter fittings using a MATLAB script (Appendix C.5). The first two lines only use data before the Ps(n=2) threshold. The next two lines have the calculated values when we consider data on both sides of the resonance, in the range of $\kappa = 0.74 - 0.88$. These two sets agree well and would likely agree better if we considered the multichannel problem above the

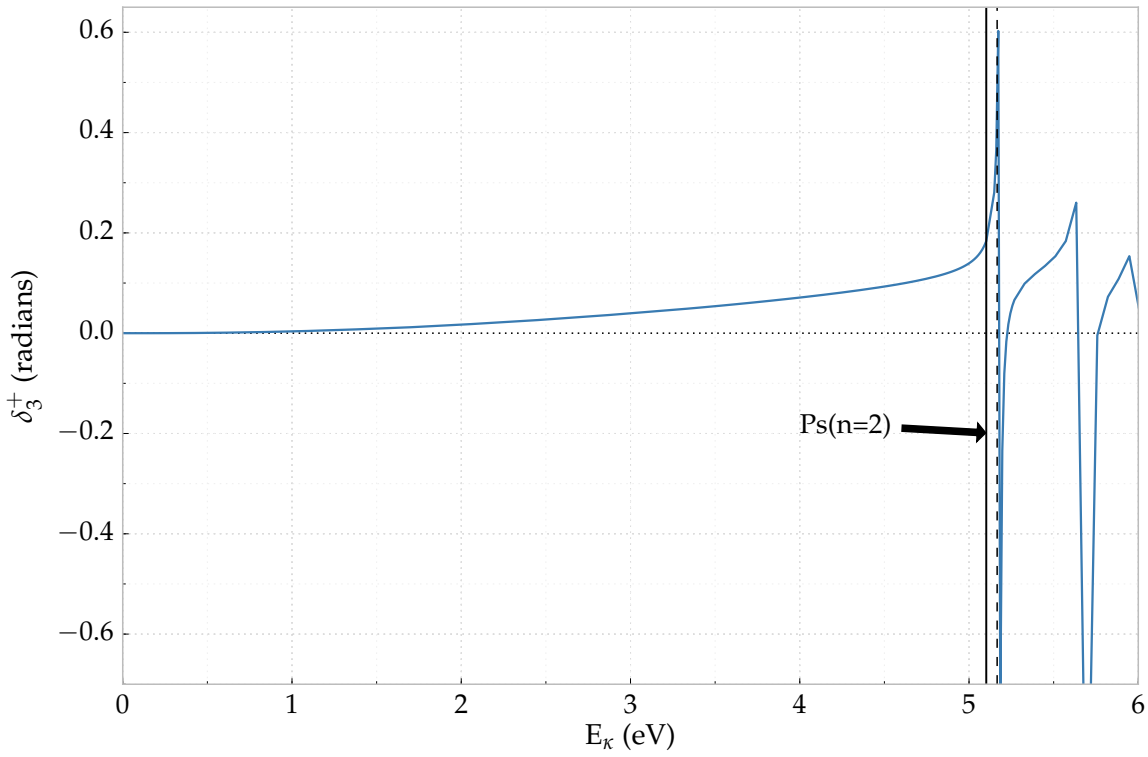

Figure 9.5: ^{1}F phase shifts showing full resonance past the inelastic threshold

Method	${}^1E_R$ (eV)	${}^1\Gamma$ (eV)
Current work[a]: Average $\pm$ standard deviation	5.1867 ± 0.0021	0.0125 ± 0.0003
Current work[a]: S-matrix complex Kohn	5.1863	0.0125
Current work[b]: Average $\pm$ standard deviation	5.1838 ± 0.0031	0.0114 ± 0.0015
Current work[b]: S-matrix complex Kohn	5.1857	0.0145
CC (9Ps9H + H^-) [72]	5.200	0.0095
CC (22Ps1H + H^-) [71]	5.151	0.010
Complex rotation [210]	5.1661 ± 0.0014	0.0174 ± 0.0027

Table 9.1: F-wave resonance parameters. [a] denotes that the data is only taken before the Ps(n=2) threshold. [b] indicates that data is used from both before and after the threshold, as described in the text.

Ps(n=2) threshold. As with the other partial waves, these resonance parameters compare reasonably well with the complex rotation [210], though there is more discrepancy with this partial wave, presumably because the resonance is past the inelastic threshold. The CC results of Ref. [72] agree relatively well, but their resonance position is higher than both the CC and complex Kohn results. Interestingly, their less accurate 22Ps1H + H^- calculation [71] has a resonance position closer to the complex rotation result.

9.5 G-Wave

In an effort to try to improve the convergence ratio, $R'(5)$, of the low energy phase shifts, we looked at the μ nonlinear parameter in the shielding function, given in Equation (3.7), along with the m_ℓ power in the same equation. Interestingly, the $\omega = 5$ phase shifts were very stable with the variation of μ from 0.5 to 0.8 (with a constant m_ℓ), agreeing to five significant figures. Keeping μ constant and increasing m_ℓ from 9 to 13 yielded the same phase shifts, again agreeing to five significant figures. The convergence ratios are greater than 1 for ^{1,3}G when $\kappa < 0.3$, but the phase shifts are very small in this range ($\lesssim 10^{-5}$). As for the F-wave, we also use the D-wave nonlinear parameters, but the switchover is at $\kappa = 0.45$.

Similar to the F-wave (section 9.4), the BO approximation does not work well for this partial wave. In fact, the G-wave triplet Kohn calculation is fully positive, yet the BO approximation is fully negative. The BO approximation gives a repulsive potential ($\delta_4^- < 0$), while the Kohn calculation gives an attractive potential ($\delta_4^- > 0$).

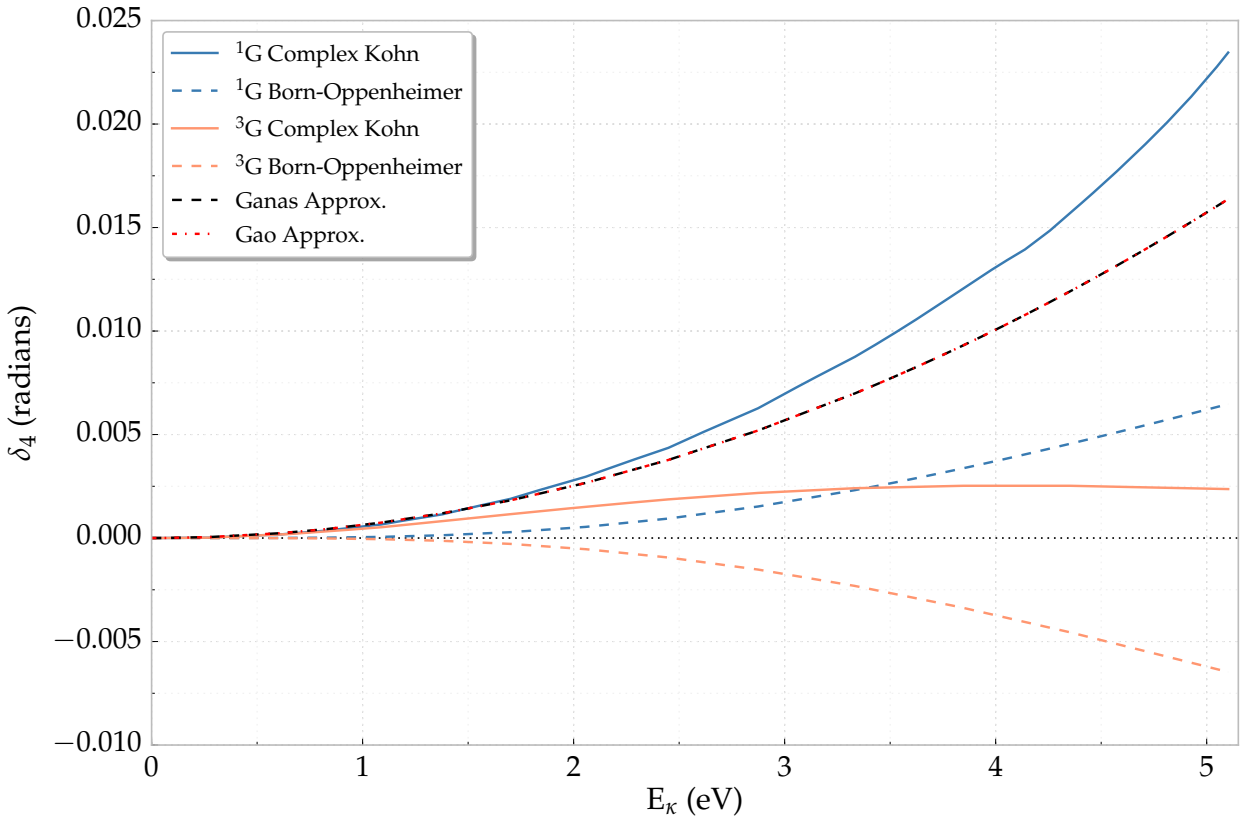

Figure 9.6: ^{1,3}G phase shifts

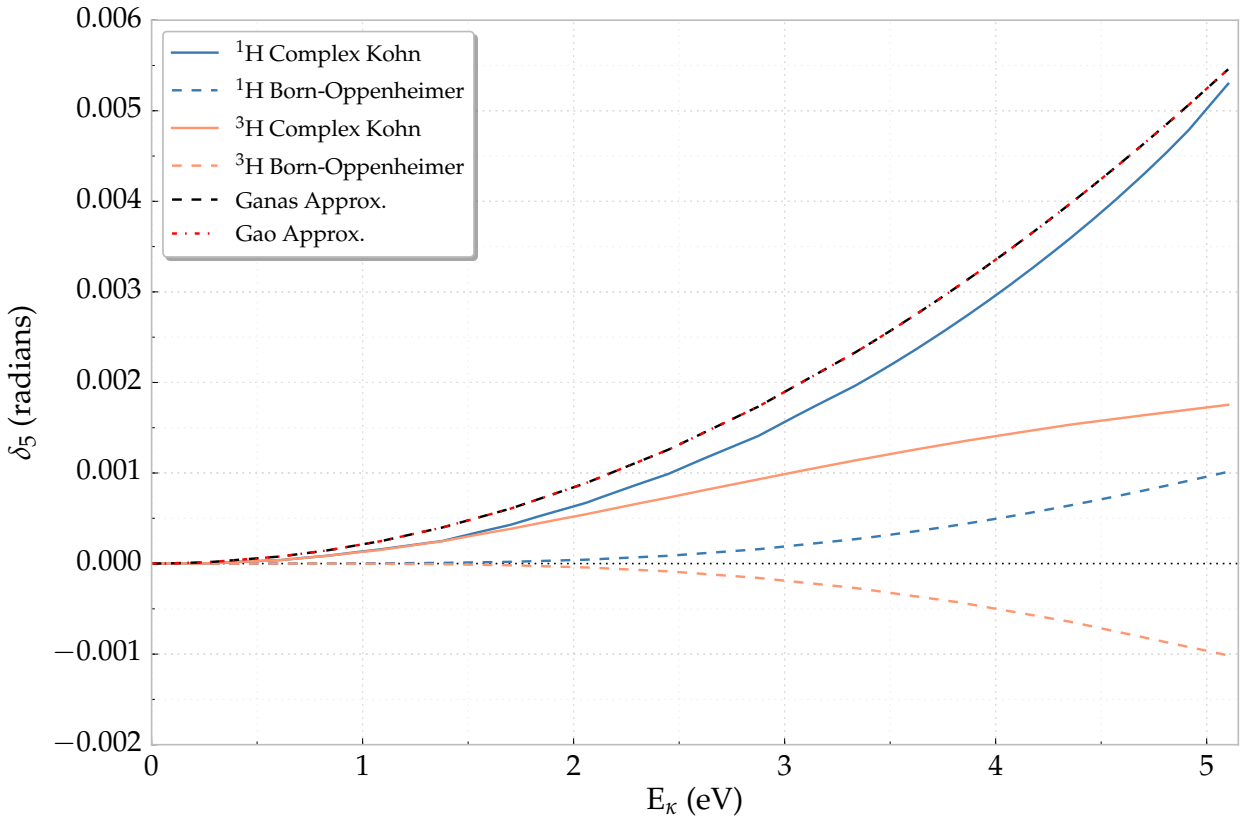

Figure 9.7: ^{1,3}H phase shifts

9.6 H-Wave

As for the F-wave and G-wave, we also use the D-wave nonlinear parameters, but the switchover is at a higher κ of 0.45. The convergence ratios are greater than 1 for ^{1,3}H when $\kappa < 0.4$, but the phase shifts are very small in this range ($\lesssim 10^{-5}$).

Figure 9.7 shows the ^{1,3}H phase shifts. The BO approximation also does not work well for the H-wave. Like the F-wave (section 9.4) and the G-wave (section 9.6), the triplet is particularly bad, giving the wrong type of potential. The Ganas approximation agrees relatively well with the ^{1}H curve. The phase shifts are small for this partial wave, so its contribution to the integrated cross section is essentially negligible, and its contribution to the differential cross section is small (see Chapter 10).

9.7 Singlet/Triplet Comparisons

Interestingly, there appears to be a pattern concerning the difference between the singlet and triplet phase shifts for Ps-H scattering as ℓ increases. From Figures 9.4, 9.6 and 9.7,

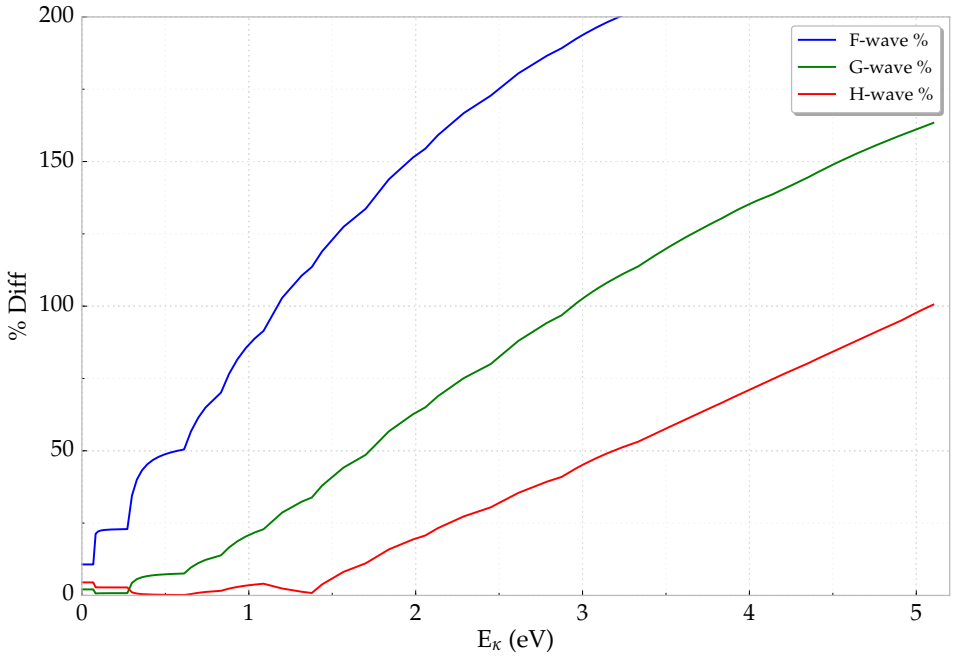

Figure 9.8: Percentage difference comparison between singlet and triplet higher partial waves

we see that at low energies, the singlet and triplet phase shifts are nearly the same. The energy at which the triplet curve diverges from the singlet becomes higher as ℓ increases. To this end, I calculated the percent difference between the singlet and triplet phase shifts for these three partial waves in Figure 9.8.

By 0.5 eV, the ^{1}F and ^{3}F phase shifts differ by more than 50%. The ^{1}G and ^{3}G differ by more than 50% at around 1.75 eV, and the ^{1}H and ^{3}H phase shifts differ to this degree at over 3 eV. In fact, the ^{1}H and ^{3}H phase shifts are approximately the same up to about 1.5 eV. This suggests that at a high enough value of ℓ and above, the singlet and triplet phase shifts are close to the same in the full energy range below the Ps(n=2) threshold.

It should be noted that for each of these, the singlet and triplet BO phase shifts are the opposite sign of each other, but the integrated elastic cross sections determined from the BO (Section 9.1) will be the same due to the $\sin^2\delta_\ell^\pm$ contribution. The Ganas approximation also does not differentiate between the singlet and triplet.

The similarity of the singlet and triplet phase shifts is also not without precedent. An analysis of two papers on e^--H scattering [215, 216] shows that the S-wave and P-wave singlet and triplet phase shifts do not agree, but the D-wave and F-wave singlet and triplet phase shifts agree well. It is also interesting that this occurs as low as $\ell = 2$, while for Ps-H scattering, these do not agree fully for even $\ell = 5$.

9.8 Summary

I was able to generalize the evaluation of the matrix elements for arbitrary ℓ (see Chapter 8), which enabled us to calculate phase shifts for the F-, G-, and H-waves. The phase shifts are not fully converged, but they are small and generally get smaller as ℓ increases. Including the mixed symmetry terms may allow us to get better converged phase shifts for these, but the very small phase shifts ($\lesssim 10^{-5}$) at low κ are not likely to improve without improved numerics as well. We are able to calculate the F-wave resonance parameters well, even though the resonance lies just past the Ps(n=2) threshold.

10 Cross Sections

We obtain the phase shifts directly from the Kohn-type variational methods, but a more relevant quantity for experiments is the cross section. Cross sections essentially give the strength of the interaction and are a quantity that can be measured experimentally.

If we have azimuthal symmetry, as we assume for Ps-H scattering, the results are independent of φ. The quantity that we are most interested in from this is the ratio $\frac{d\sigma}{d\Omega}$, which is is the differential cross section. The integrated cross section is related to the differential cross section by integrating over $d\Omega$:

$$\sigma = \int \frac{d\sigma}{d\Omega}\, d\Omega = \int_0^{2\pi} \int_0^{\pi} \frac{d\sigma}{d\Omega} \sin\theta \, d\theta \, d\varphi. \tag{10.1}$$

10.1 Integrated Cross Sections

The partial wave cross sections can be related to the phase shifts by [43, p.584]

$$\sigma^{\pm}_{el,\ell} = \frac{4}{\kappa^2}(2\ell+1)\sin^2\delta^{\pm}_{\ell}. \tag{10.2}$$

In addition to the relation of the integrated cross sections to the differential cross sections in Equation (10.1), using the partial wave expansion, the integrated cross sections can also be expressed as [43, p.584]

$$\sigma^{\pm}_{el} = \sum_{\ell=0}^{\infty} \sigma^{\pm}_{el,\ell} = \frac{4}{\kappa^2} \sum_{\ell=0}^{\infty} (2\ell+1)\sin^2\delta^{\pm}_{\ell}. \tag{10.3}$$

We consider that the H(1s) is unpolarized and the final spin states are not determined, giving spin-weighted cross sections where the singlet contributes $\frac{1}{4}$, and the triplet contributes $\frac{3}{4}$, i.e. [49, 70, 74, 137]

$$\sigma = \tfrac{1}{4}\sigma^{+} + \tfrac{3}{4}\sigma^{-}. \tag{10.4}$$

Figures 10.1 and 10.2 show the partial wave cross sections for the singlet and triplet, respectively. The "Summed" in each is the sum of each of the singlet or triplet partial waves through the H-wave.

The triplet cross section in Figure 10.2 is dominated almost completely by the ^{3}S-wave. The ^{3}P-wave contributes less, and the ^{3}D-wave barely registers on the graph. The higher partial waves contribute nearly negligible amounts. The summed cross section follows closely with ^{3}S, but the contribution from ^{3}P is evident.

The singlet cross sections in Figure 10.1 are more interesting due to their larger partial wave cross sections and the resonances from the first four partial waves. The "Summed" has peaks from each of the first three partial waves, giving it a more complicated structure than the summed from the triplet in Figure 10.2. As mentioned in Section 3.6, each of these resonances goes through a phase shift change of π. With the $(2\ell + 1)$ factor in Equation (10.3), higher partial wave resonances have a larger contribution to the summed cross sections, as long as the background does not change significantly. In Figure 10.1, the ^{1}D resonance clearly has the most significant contribution to the integrated elastic cross section out of the resonances for the first three partial waves. The ^{1}F resonance barely contributes, but this is because the resonance lies past the inelastic threshold.

The cross section at very low energy (less than 0.5 eV) is dominated by the S-wave, as we would expect. At zero energy, the S-wave is the only partial wave that has a non-zero cross section (for both ^{1}S and ^{3}S). Bransden and Joachain [43, p.589] point out that for $\ell \geq 1$, the partial cross sections vanish as $\kappa^{4\ell}$ as $\kappa \to 0$, so $\sigma_{el} = \sigma_0$ at this limit, and the scattering is isotropic. As can be seen in Figures 10.1 and 10.2, the D-wave falls off more quickly than the P-wave as $\kappa \to 0$, and the F-wave falls off even faster.

Also interesting is the minimum in the summed singlet cross section at approximately 0.25 eV and then the maximum at 0.74 eV. The dip here at low energy is due to the mixing of the ^{1}S and ^{1}P cross sections. The ^{1}S-wave cross section is decreasing rapidly while the ^{1}P-wave cross section is increasing, giving this feature. The maximum is due primarily to the ^{1}P-wave.

From Equation (10.3), for exact cross sections, we have to do an infinite summation. In practice, we add partial waves until the cross section no longer changes a significant amount. In Figure 10.3(a), we consider what the percentage contribution to the summed cross section for the singlet partial waves is at the 7 "standard" κ values. From this, we can see the trend that the ^{1}S-wave is by far the greatest contribution at small κ, but the ^{1}P-wave becomes the dominant contribution through most of the rest of the energy range. When $\kappa \geq 0.5$, the ^{1}D-wave is no longer a negligible contribution. The ^{1}F-wave barely contributes, even for $\kappa = 0.7$, and the ^{1}G- and ^{1}H-wave are not shown due to their insignificant contributions.

The corresponding bar chart for the triplet is in Figure 10.3(b). As qualitatively described earlier, the contribution to the elastic integrated cross section for the triplet is mainly due to the ^{3}S-wave. The ^{3}P-wave contributes about 20% at $\kappa = 0.7$, and the

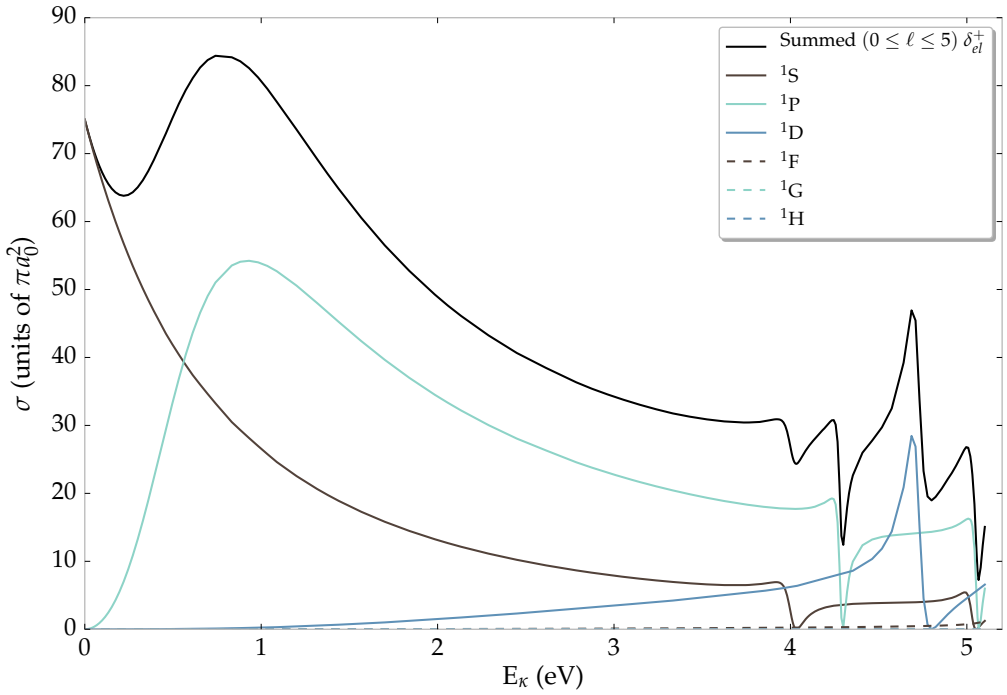

Figure 10.1: *S*-matrix complex Kohn singlet elastic partial wave cross sections and the sum through $\ell = 5$. An interactive version of this figure is available online [3] at `https://plot.ly/~Denton/95/singlet-partial-cross-sections-ps-h-scattering/`.

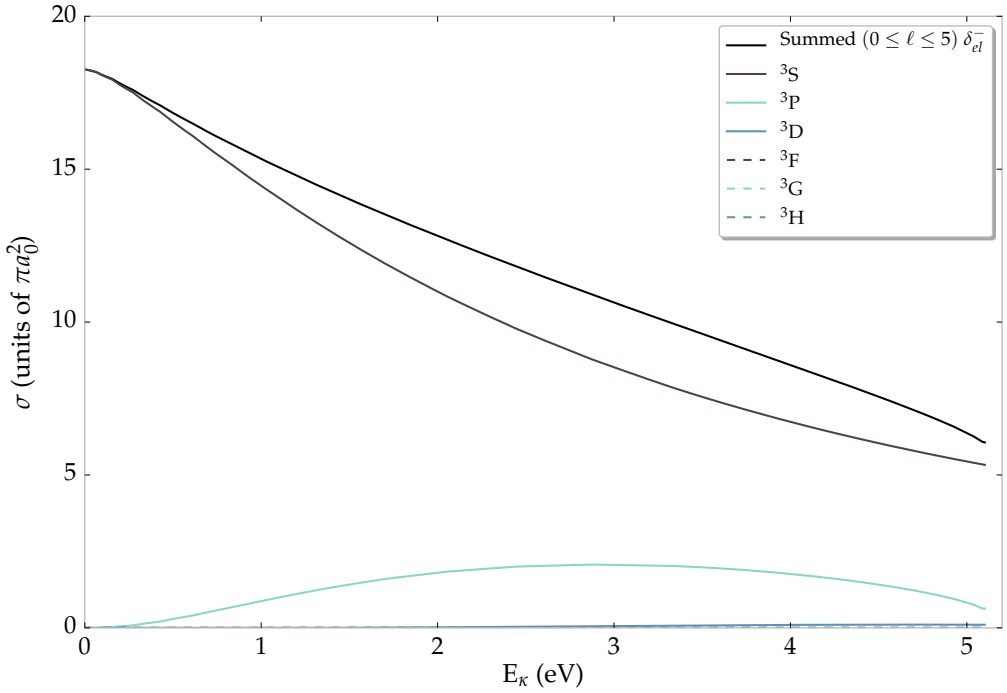

Figure 10.2: S-matrix complex Kohn triplet elastic partial wave cross sections and the sum through $\ell = 5$. An interactive version of this figure is available online [3] at `https://plot.ly/~Denton/138/triplet-partial-cross-sections-ps-h-scattering/`.

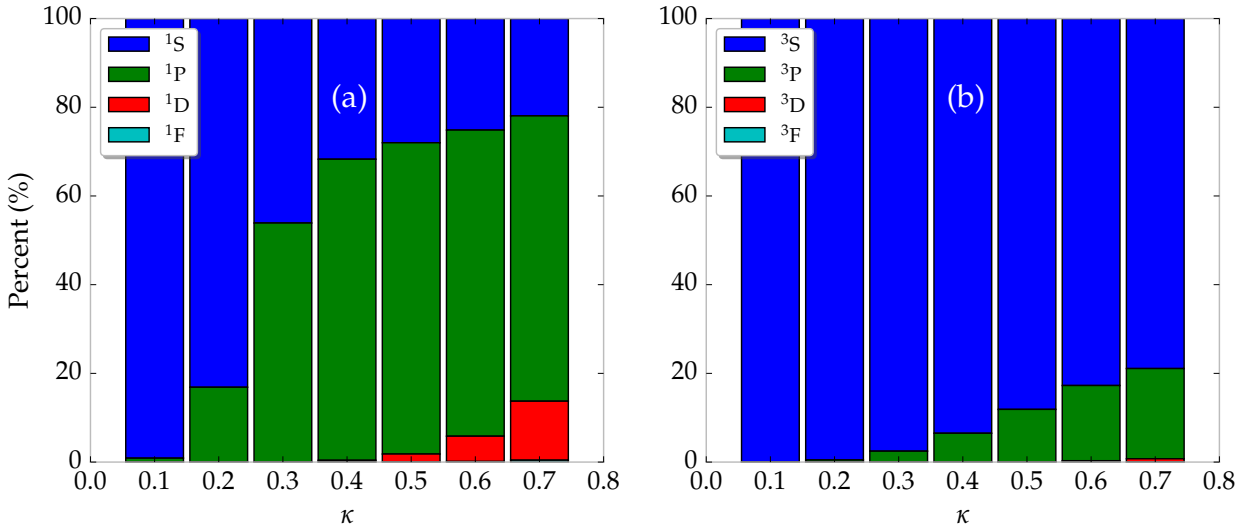

Figure 10.3: Percentage contribution to integrated elastic cross section from each partial wave with selected κ for the singlet (a) and triplet (b).

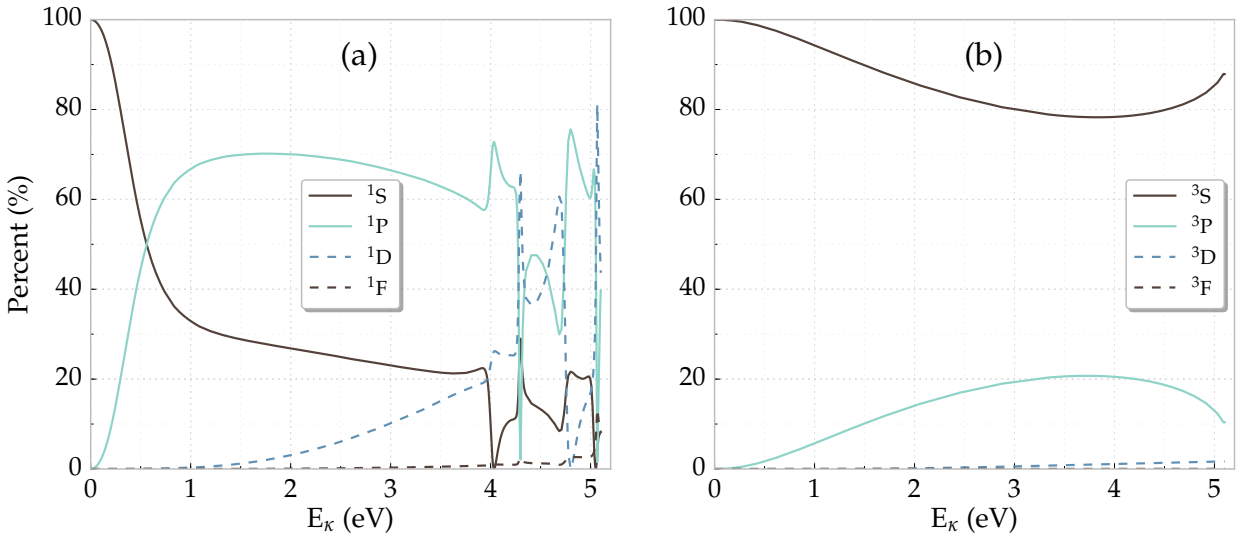

Figure 10.4: Percentage contribution to integrated elastic cross section from each partial wave for the singlet (a) and triplet (b).

^{3}D-wave contribution is nearly negligible.

Figure 10.4 also shows the percent contributions to the integrated elastic cross sections from each partial wave but shows this data for the entire energy range. The triplet graph in Figure 10.4(b) again shows that only the ^{3}S- and ^{3}P-waves give very significant contributions. The ^{3}D-wave gives a non-negligible but small contribution near the inelastic threshold

The corresponding singlet graph in Figure 10.4(a) is more difficult to interpret due to the resonances. The ^{1}S- and ^{1}P-wave dominate until about 3 eV, and the ^{1}P-wave is the largest contribution from approximately 0.5 eV to slightly over 4 eV. The ^{1}D-wave starts being a more dominant contribution past 4 eV, and it has spikes in the percentage when the ^{1}S and ^{1}P resonances go to their minima.

For a more quantitative approach, we calculate the percent contributions of the different partial waves to the spin-weighted integrated elastic cross section as presented in Table 10.1. The second and third columns give the contribution from the singlet and triplet combined for each partial wave. From this, it is noticeable that the F-wave should be included, though the average is less than 0.6%. The G-wave and H-wave barely contribute, with the H-wave contribution from both the singlet and triplet less than 0.002% on average.

For the last 4 columns of Table 10.1, we also compare each partial wave's contribution to the spin-weighted integrated elastic cross section, but we separate out the singlet and triplet. From columns 4 and 5 for the singlet, we see that the ^{1}F-wave is important, and it gives most of the combined ^{1,3}F-wave contribution to the elastic integrated cross section. The ^{3}F-wave contribution is 0.0011% on average, and the ^{3}D contribution is less than 0.41%

ℓ	Max. %	Avg. %	Max. ${}^1\ell$ %	Max. E_{κ}^{-} (eV)	Avg. $\%^{+}$	Max. $\%^{-}$	Max. E_{κ}^{+} (eV)	Avg. $\%^{-}$
S-wave	100.0%	60.61%	57.80%	2.721^{-7}	20.80%	20.86%	5.067	13.27%
P-wave	45.97%	30.21%	42.89%	1.200	24.36%	4.323%	4.300	1.947%
D-wave	42.07%	8.565%	41.61%	4.686	8.178%	0.401%	5.067	0.129%
F-wave	3.782%	0.596%	3.765%	5.078	0.593%	0.00606%	5.067	0.0011%
G-wave	0.103%	0.022%	0.0994%	5.067	0.0206%	0.00106%	5.067	0.00046%
H-wave	0.0083%	0.0019%	0.0062%	5.067	0.0013%	0.00070%	5.067	0.00021%

Table 10.1: Percent contribution to the elastic integrated cross section from each partial wave for both the maximum and average for the entire energy range. Superscripts give powers of 10.

through the entire energy range. We include all partial waves through the H-wave in the final results, but these would be relatively well converged if we stopped adding partial waves to Equation (10.3) at the F-wave. For comparison, the CC [72] cross section shown in Figure 10.5 uses partial waves through the G-wave, but their graph would likely not change if they included the H-wave.

Finally, combining the singlet and triplet integrated elastic cross sections using the spin-weighting in Equation (10.4) gives the result in Figure 10.5. We include the spin-weighted singlet and triplet cross sections for comparison with the combined integrated elastic cross section. The comparison to the CC [72] and SE [73] results is made possible by using the CurveSnap [217] program to extract the curves from the respective papers. The SE curve gives a decent approximation to the background without any resonances. We would not expect the SE to give resonance information. There is good agreement between the complex Kohn and CC cross sections, but the CC results have resonances shifted to higher energy. The complex Kohn resonances correspond better than the CC to the resonance positions that are given in the complex rotation results of Yan and Ho [92, 175, 182, 210], as seen in Tables 5.3, 6.3, 7.2 and 9.1.

For partial wave cross section data available from the CC papers [70, 71, 72], we compare the complex Kohn partial wave cross sections to these in Figures 10.6 and 10.7. The CC 9Ps9H + H^- cross sections are more accurate than the CC 22Ps1H + H^-, as pointed out in those papers. They also have CC data with the 9Ps9H approximation [70], but that gives less accurate results than the CC 22Ps1H + H^-.

Other than the shifted resonance positions, the CC results tend to match well with the complex Kohn results. However, there are some features that are worth noticing. For the ^{1}P cross section in Figure 10.6, the CC 9Ps9H + H^- maximum is lower than the complex Kohn maximum. The CC cross section 22Ps1H + H^- maximum is even lower, so we would expect that if more eigen- and pseudo-states are included, the CC maximum would

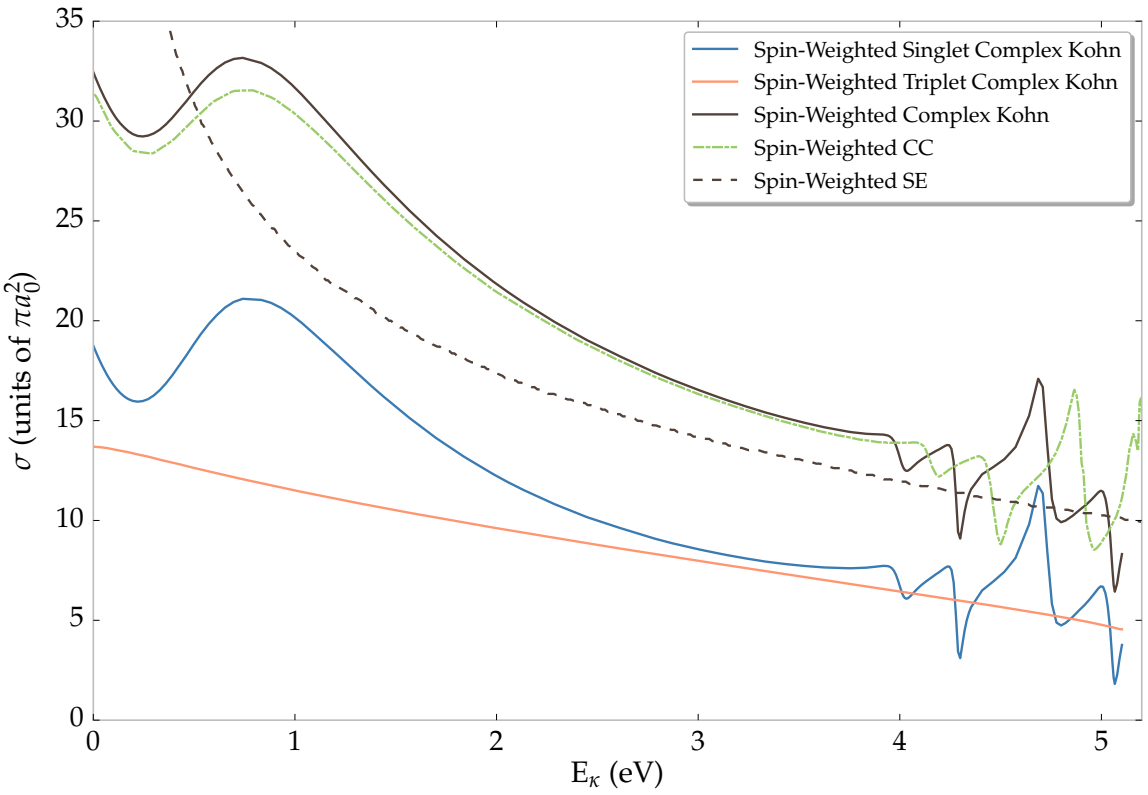

Figure 10.5: Elastic integrated cross sections. CC results are from Ref. [72], and SE results are from Ref. [73]. An interactive version of this figure is available online [3] at `https://plot.ly/~Denton/150/integrated-cross-sections-ps-h-scattering/`.

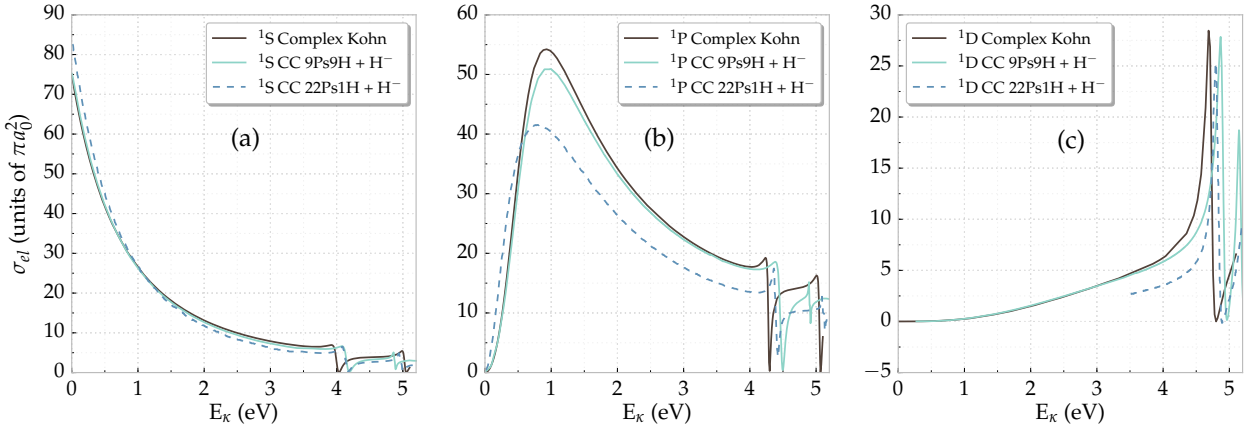

Figure 10.6: Comparisons of ^{1}S, ^{1}P, and ^{1}D elastic partial wave cross sections. CC 9Ps9H + H$^-$ results are from Ref. [72], and CC 22Ps1H + H$^-$ results are from Ref. [71].

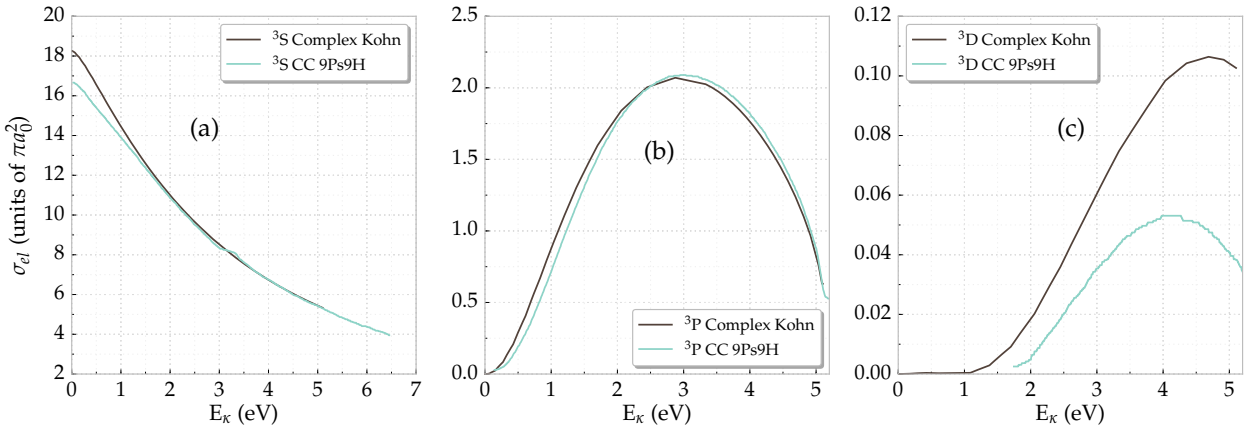

Figure 10.7: Comparisons of ^{3}S, ^{3}P, and ^{3}D elastic partial wave cross sections. CC results for ^{3}S and ^{3}P are from Ref. [72], and the CC results for ^{3}D are from Ref. [70].

likely match up with the complex Kohn. Also, the ^{3}D CC cross section is much smaller than the complex Kohn. This is a reflection of the fact that in Figure 7.1 and Table 7.1, the CC results are higher than the complex Kohn results, making them less negative and the corresponding cross sections smaller. Noting the magnitude of the ^{3}D cross section for both methods, the contribution to the full summed elastic integrated cross section is small. As a simple test, we tried replacing the complex Kohn $\kappa = 0.1 - 0.7$ ^{3}D phase shifts with those of the CC, and the change to the cross section is less than 0.084% for this range. Consequently, for the full summed cross section, the discrepancy between the complex Kohn and the CC results does not change things significantly.

In Figure 10.8, the BO approximation elastic partial wave cross sections do not match

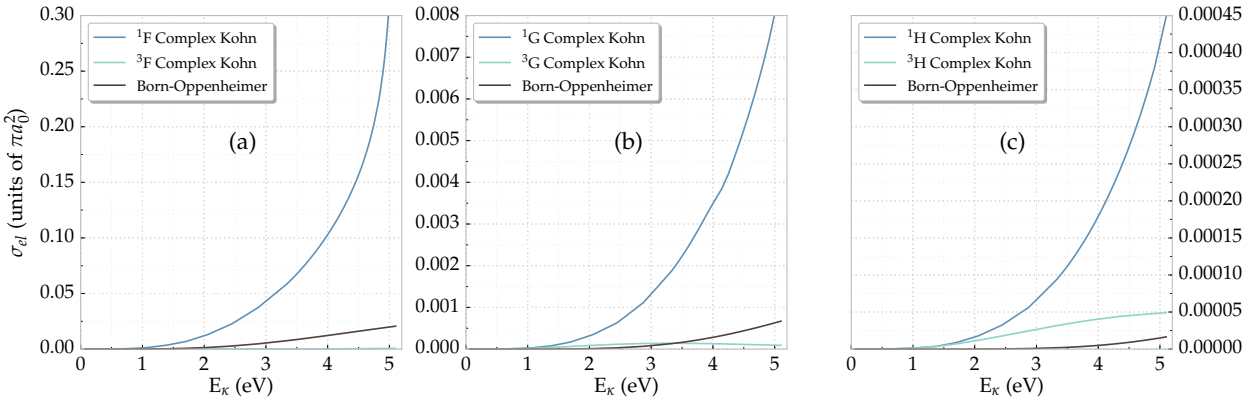

Figure 10.8: Comparisons of F-, G-, and H-wave elastic partial wave cross sections between complex Kohn and BO approximation

up with either the singlet or triplet for the F-, G-, or H-waves. Interestingly, we see that the plots for the singlet and the BO look approximately the same in (a), (b), and (c) but with a different vertical scale. Similar to what we noticed in Section 9.7, we also note that the singlet and triplet phase shifts match for higher κ as ℓ increases.

10.2 Differential Cross Sections

The differential cross section is important through Equation (10.1), but this also gives information about the angular dependence (θ) of the system. The differential cross sections can be calculated from the phase shifts by [43, p.584]

$$\frac{d\sigma_{el}^{\pm}}{d\Omega} = \frac{1}{\kappa^2}\sum_{\ell=0}^{\infty}\sum_{\ell'=0}^{\infty}(2\ell+1)(2\ell'+1)\exp\left\{\mathrm{i}\left[\delta_\ell(\kappa)-\delta_{\ell'}(\kappa)\right]\right\} \times \sin\delta_\ell^{\pm}(\kappa)\sin\delta_{\ell'}^{\pm}(\kappa)P_\ell(\cos\theta)P_{\ell'}(\cos\theta)\,. \tag{10.5}$$

This expression has the complex-valued exponential, for which we can use the well-known Euler formula of

$$\mathrm{e}^{\mathrm{i}x} = \cos x + \mathrm{i}\sin x \tag{10.6}$$

to split this into real-valued and imaginary-valued parts. As long as the finite truncation of the upper limits of the summations are the same, the imaginary part becomes 0 to within numerical accuracy. So we can use the approximation of

$$\frac{d\sigma_{el}^{\pm}}{d\Omega} \approx \frac{1}{\kappa^2}\sum_{\ell=0}^{\ell_{max}}\sum_{\ell'=0}^{\ell_{max}}(2\ell+1)(2\ell'+1)\cos\left[\delta_\ell(\kappa)-\delta_{\ell'}(\kappa)\right] \times \sin\delta_\ell^{\pm}(\kappa)\sin\delta_{\ell'}^{\pm}(\kappa)P_\ell(\cos\theta)P_{\ell'}(\cos\theta)\,. \tag{10.7}$$

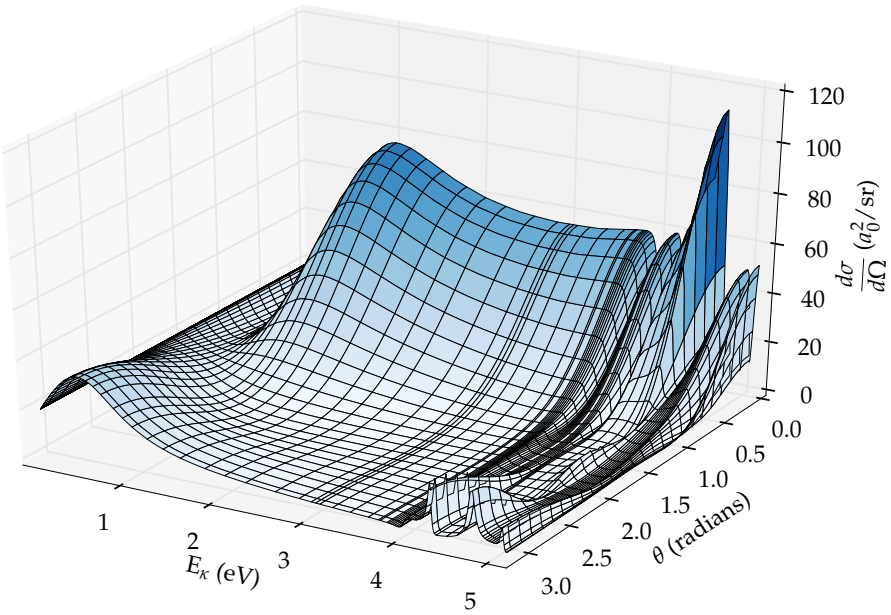

Figure 10.9: Singlet differential cross section

Graphs of the differential cross sections for the singlet and triplet are found in Figures 10.9 and 10.10, respectively. Note that the θ axis is plotting backwards so that the features are visible instead of being obscured by the higher value of the differential cross section in the front of the graph. The triplet $\frac{d\sigma_{el}^{-}}{d\Omega}$ is not particularly remarkable, being smooth and having a maximum at intermediate energies for the forward direction ($\theta = 0$). The triplet differential cross section in the forward direction is less than 7 a_0^2/sr for all energies considered. It is also of note that in the backward scattering direction ($\theta = \pi$), the triplet differential cross section quickly becomes very small.

In contrast, the singlet differential cross section, $\frac{d\sigma_{el}^{+}}{d\Omega}$, shown in Figure 10.9 has a much more complicated structure. The resonances are clearly visible in the plot, and the highest peak extending to 110.5 a_0^2/sr is due to the D-wave resonance, which is also the dominant resonance in the integrated cross section shown in Figures 10.1 and 10.5. The features in the integrated cross section graphs can easily be matched up to features in the differential cross section, including the rest of the resonances. The maximum and dip described in Section 10.1 for the integrated cross section can also be seen in Figure 10.9, especially in the forward direction.

Similar to the integrated cross section, we combine these using the same type of spin-weighting given in Equation (10.4). Due to the nearly featureless nature of the triplet in Figure 10.10, the combined differential cross section in Figure 10.11 looks very similar to Figure 10.9, but the 1/4 weighting of the singlet brings the vertical scale down. The

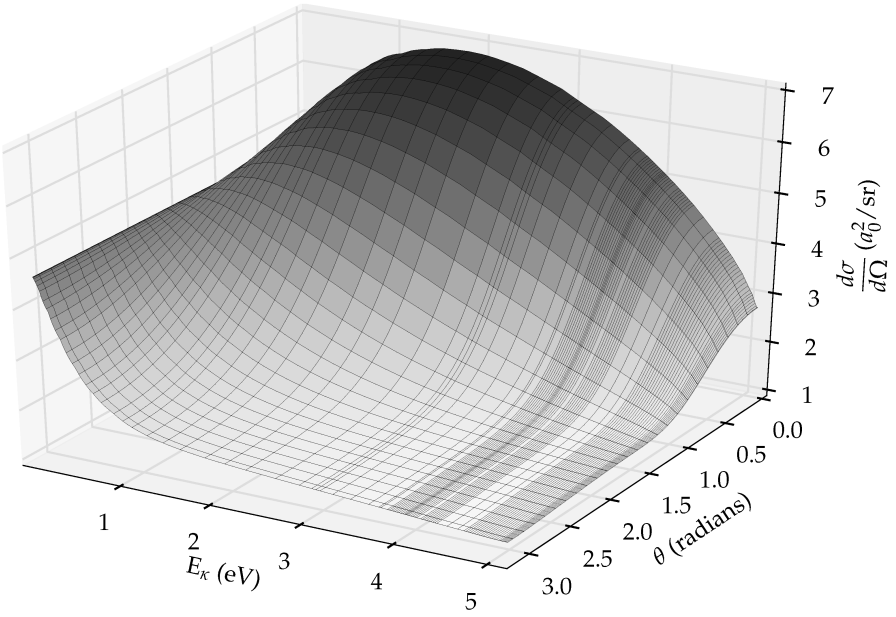

Figure 10.10: Triplet differential cross section

forward direction is enhanced slightly by the maximum in the triplet in Figure 10.10.

With the data in Figure 10.11, it is illustrative to plot 2-dimensional versions to see trends more clearly. In Figure 10.12, we restrict θ and vary $E_{\boldsymbol{\kappa}}$ to see the the energy-dependence for several θ values. From this figure, it is clear that scattering in the forward direction is dominant past approximately 0.46 eV. The maximum for forward scattering is due to the ^{1}D resonance. Particularly interesting is the contribution from backward scattering for low $E_{\boldsymbol{\kappa}}$ and the dip in the forward scattering direction, which corresponds to the dip in Figure 10.5. All angles give essentially the same value at very low energy, as we would expect. For nearly zero energy at $\kappa = 0.0001$ (6.8×10^{-8} eV), $\frac{d\sigma_{el}^{\pm}}{d\Omega}$ at 0°, 90°, and 180° is 8.112, 8.113, and 8.108 a_0^2/sr, showing that the differential cross section is essentially isotropic. At exactly 0 eV, it will be exactly isotropic. This is due to the S-wave having the only non-zero cross section at zero energy.

In Figure 10.13, we instead fix values of $E_{\boldsymbol{\kappa}}$ and plot with respect to θ. The legend gives the κ value instead, so it is clear what specific values we are plotting. At low κ (0.05 in the plot), the differential cross section is nearly isotropic, with a slight bias toward backward scattering. As κ is increased to 0.2, backward scattering is more prominent. Between $\kappa = 0.2$ and 0.3, there is an abrupt change in the differential cross section, where it becomes much more forward peaked, with a decreasing contribution to the backward direction, and a minimum at approximately 100°. As κ is increased further, the differential cross section becomes very strongly forward peaked, with even further decreases at larger

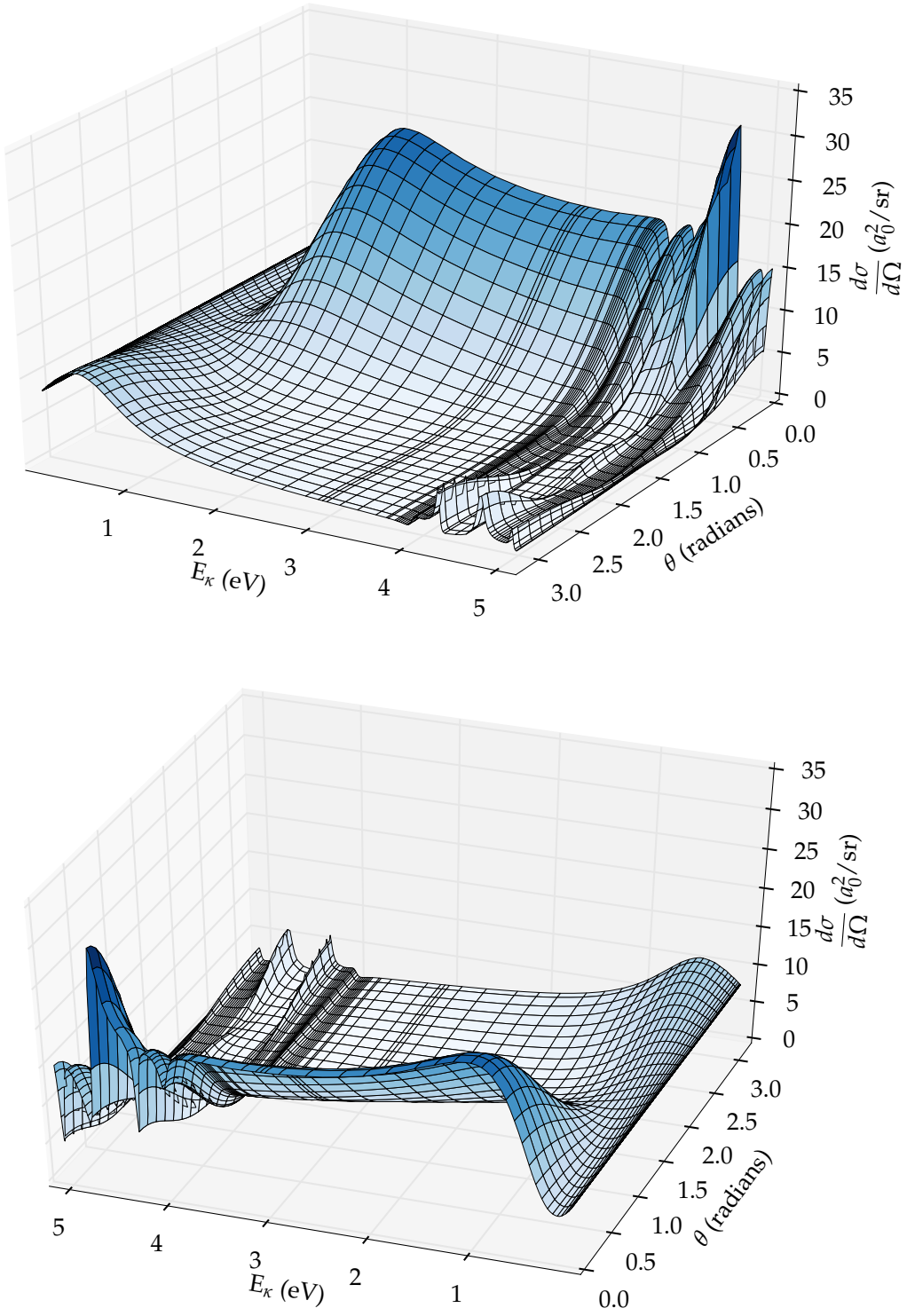

Figure 10.11: The combined spin-weighted elastic differential cross section for Ps-H scattering at two different viewing angles

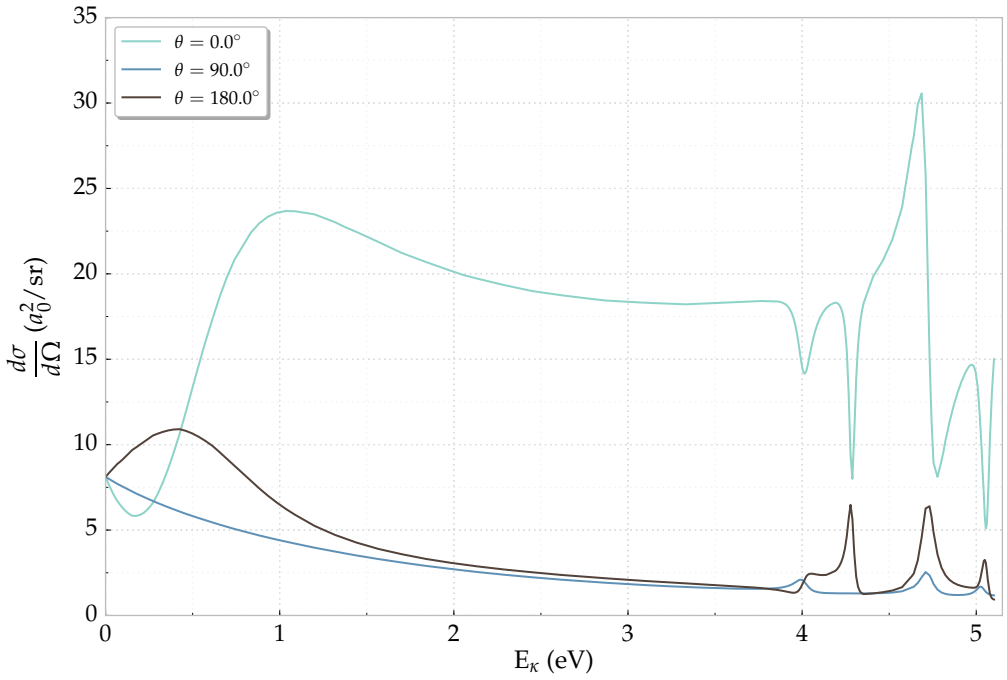

Figure 10.12: Differential cross section for selected θ

angles and a nearly constant value from about 100°. We see from Figure 10.11 that the majority of the scattering takes place between 0 and 1 radians.

We find that the elastic differential cross section converges slower with respect to ℓ than the elastic integrated cross section in Section 10.1. The convergence of the differential cross section is more difficult to quantitatively evaluate than that of the integrated cross section, since it has mixing between all of the included partial waves. We calculate $\frac{d\sigma_{el}}{d\Omega}$ for two subsequent values of ℓ_{max}, then find the percent difference between these.

Figures 10.14 and 10.15 shows this percentage difference for all angles and energies. These two figures look similar but have different vertical scales, as we would hope for if there was convergence. There are two important trends here. One is that the differential cross section is well converged at low energies, and the other is that it is less converged in the backward scattering direction than in the forward direction. In Figure 10.15, which includes all partial waves through the H-wave, the percentage differences are all below 4%, and most of the E_κ and θ range is much less than this. This indicates that the differential cross section is relatively well converged.

Figures 10.16 and 10.17 show the same data but for selected angles. We see here that $\theta = 90°$ is the best converged angle out of the three, and the backward scattering direction of $\theta = 180°$ is the worst converged. Again, as seen in Figure 10.17, the differential cross section is relatively well converged if we include the H-wave.

We would expect that as ℓ increases, $\theta = 180°$ will be the most sensitive to adding terms

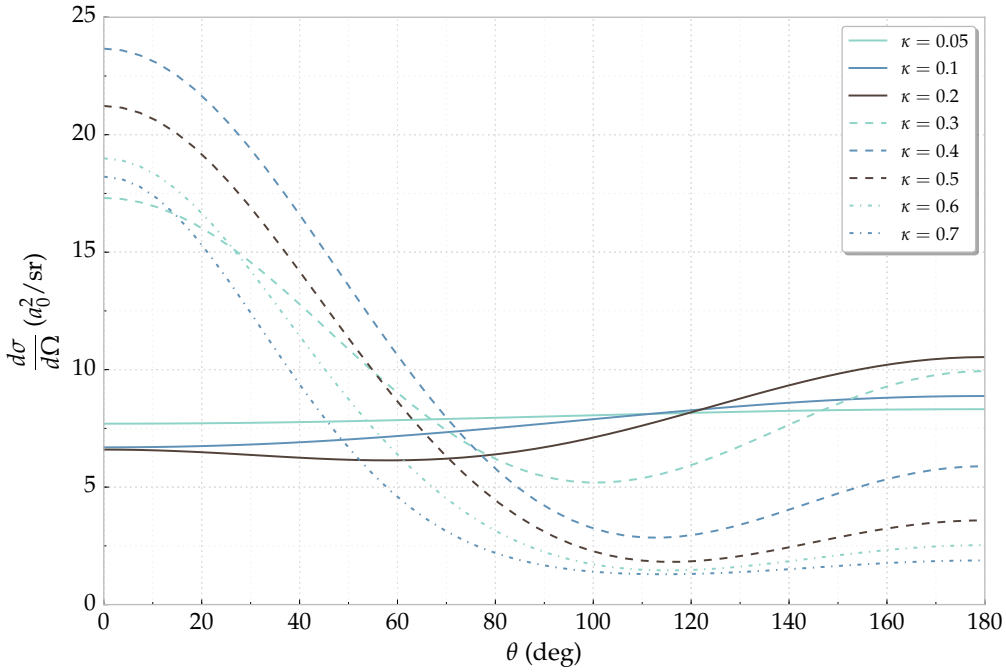

Figure 10.13: Differential cross section for selected κ

to the differential cross section. The partial wave expansion [43, p.583] has a $P_\ell(\cos\theta)$ for each term. If we set $\theta = 0°$, each of the Legendre polynomials equals 1, meaning that each term added is positive. If $\theta = 180°$, the Legendre polynomial alternates between 1 and -1, i.e. $(-1)^\ell$. This is then an alternating series, which we would expect to converge more slowly. The minimum for $\theta = 90°$ can be explained by every ℓ odd term equaling 0 from the Legendre polynomial.

Similar to Table 10.1, Table 10.2 gives the average and maximum percent differences for adding partial waves to the differential cross section (both the singlet and triplet). The average percent difference for adding the G-wave is less than 1% but has a fairly large maximum percent difference. Adding the H-wave is a much less significant contribution, and the differential cross section looks to be relatively well converged by the H-wave.

Table 10.3 separates the singlet and triplet contributions to the differential cross section. For this table, when the singlet contributions are analyzed, the triplet summations have $\ell_{max} = 5$. Likewise, when the singlet contributions are analyzed, $\ell_{max} = 5$ for the triplet. We see that with respect to ℓ, the triplet differential cross section converges much quicker for both the average and maximum. Columns 5 and 6 give the values of E_κ and θ where the maximum percent difference is located for the singlet, and columns 8 and 9 give the maximum percent difference location for the triplet. Unsurprisingly, for $\ell \geq 1$, the angles

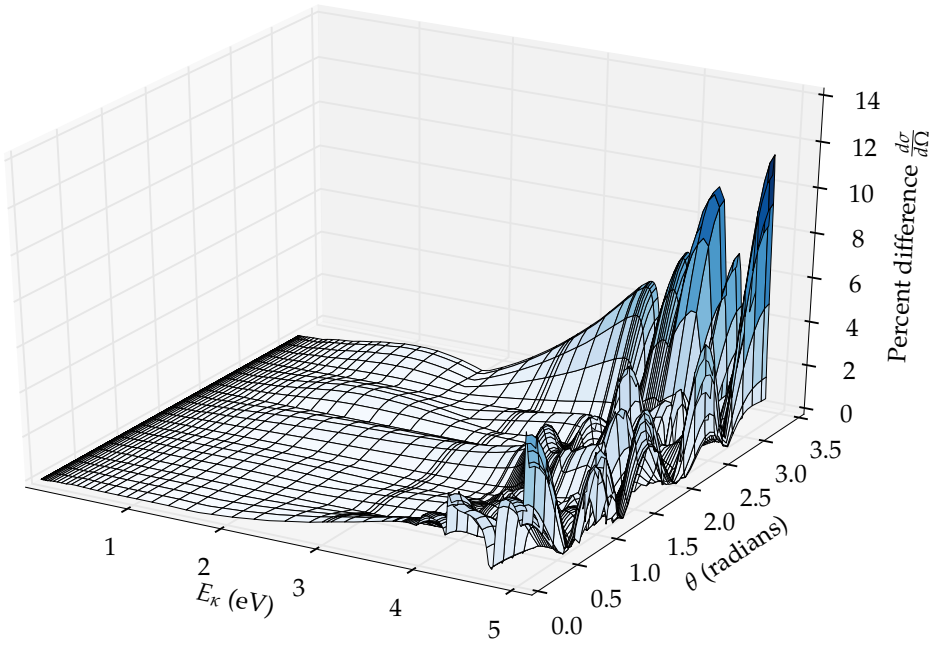

Figure 10.14: Percent difference of $\frac{d\sigma_{el}}{d\Omega}$ for upper limit of summations in Equation (10.5) as $\ell_{max} = 3$ versus $\ell_{max} = 4$ for all angles and energies

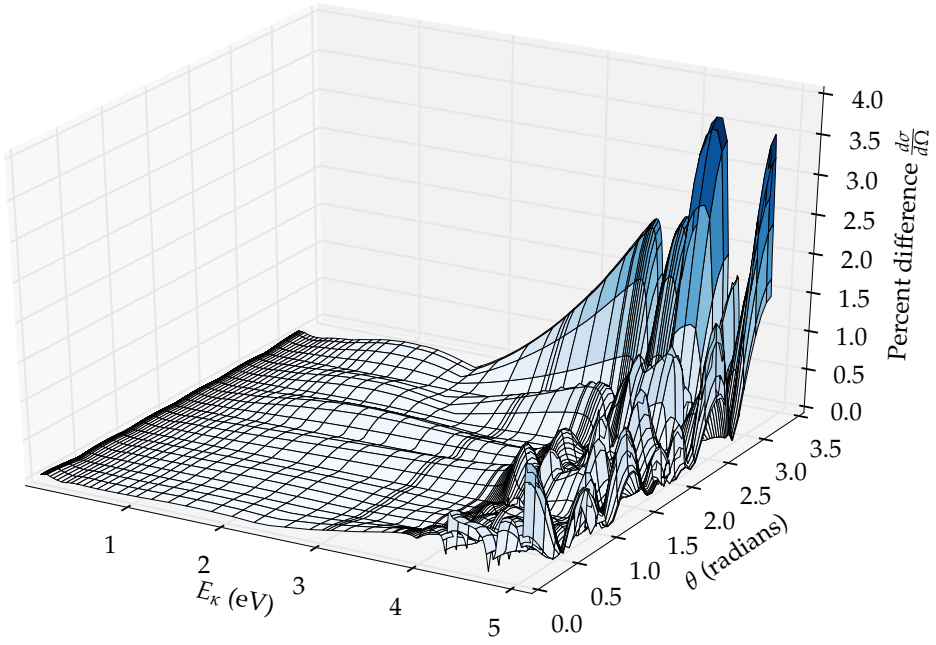

Figure 10.15: Percent difference of $\frac{d\sigma_{el}}{d\Omega}$ for upper limit of summations in Equation (10.5) as $\ell_{max} = 4$ versus $\ell_{max} = 5$ for all angles and energies

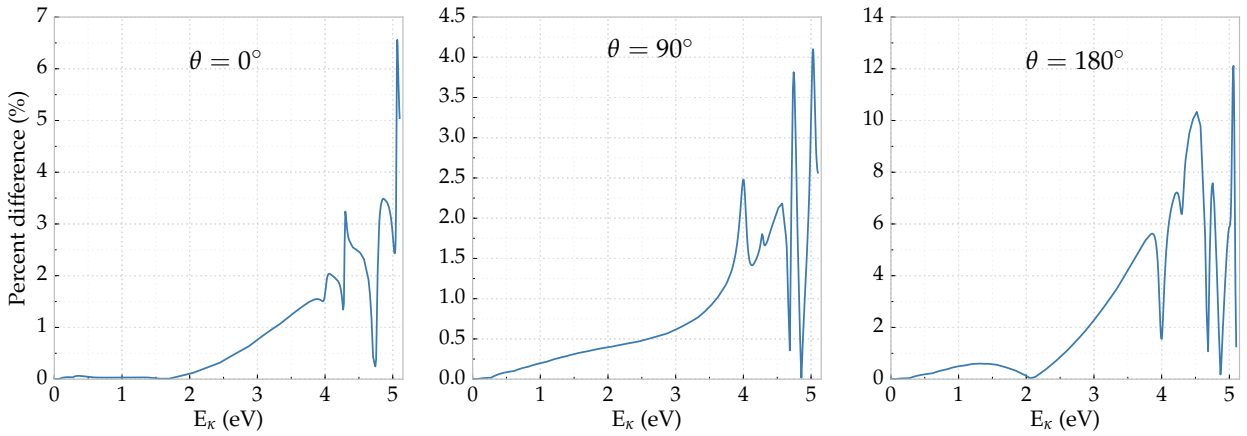

Figure 10.16: Percent difference of $\frac{d\sigma_{el}}{d\Omega}$ for upper limit of summations in Equation (10.5) as $\ell_{max} = 3$ versus $\ell_{max} = 4$ for selected angles

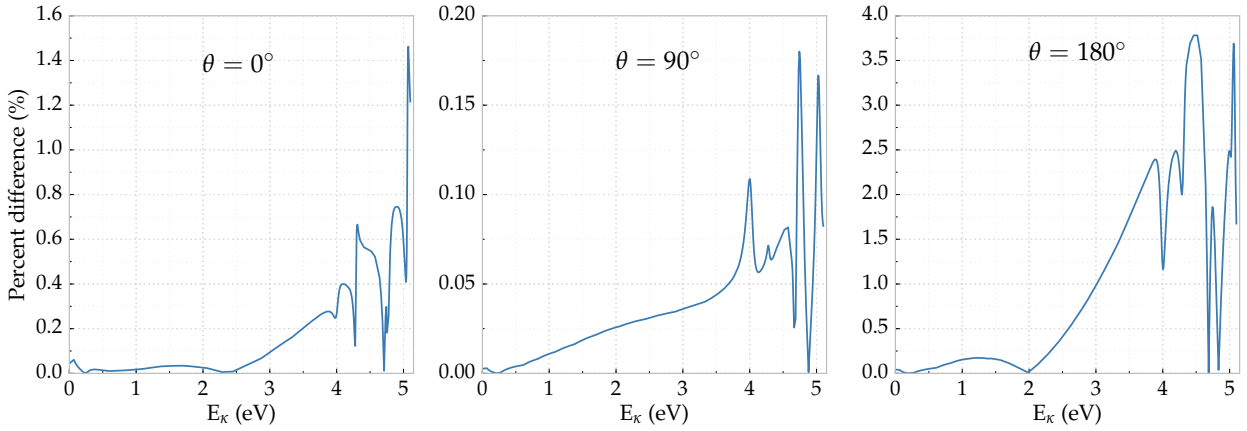

Figure 10.17: Percent difference of $\frac{d\sigma_{el}}{d\Omega}$ for upper limit of summations in Equation (10.5) as $\ell_{max} = 4$ versus $\ell_{max} = 5$ for selected angles

ℓ	Avg. % Diff.	Max. % Diff.
1	49.11%	140.8%
2	18.54%	122.6%
3	4.50%	58.1%
4	0.86%	12.1%
5	0.26%	3.8%

Table 10.2: Percent difference of the elastic differential cross section for each partial wave ℓ with respect to $\ell - 1$ for both the maximum and average for the entire $E_{\boldsymbol{\kappa}}$ and θ range

ℓ	Avg. $\%^+$ Diff.	Avg. $\%^-$ Diff.	Max. $\%^+$ Diff.	Max. $E_{\boldsymbol{\kappa}}^+$ (eV)	Max. θ^+ (rad)	Max. $\%^-$ Diff.	Max. $E_{\boldsymbol{\kappa}}^-$ (eV)	Max. θ^- (rad)
1	40.34%	9.84%	162.28%	4.686	0	50.11%	4.289	0.705
2	17.55%	3.31%	121.89%	4.686	0	24.72%	4.354	π
3	4.47%	0.39%	51.89%	5.072	π	3.31%	5.102	π
4	0.80%	0.20%	9.22%	5.067	0	1.48%	5.055	0
5	0.21%	0.15%	3.15%	5.061	π	1.64%	4.354	π

Table 10.3: Percent difference of the elastic differential cross section for each partial wave ℓ with respect to $\ell - 1$ for both the maximum and average for the entire $E_{\boldsymbol{\kappa}}$ and θ range. The values of $E_{\boldsymbol{\kappa}}^{\pm}$ and $\theta^{\pm}$ given are where $\frac{d\sigma_{el}^{\pm}}{d\Omega}$ is at its maximum value given in columns 4 and 7.

that are the most sensitive are 0 and π radians. The most sensitive energies are in the resonance region, and most of these are near the inelastic threshold of 5.102 eV.

10.3 Momentum Transfer Cross Section and Comparisons

Measurements of the momentum transfer cross section, σ_m, have been made for Ps scattering with atomic and molecular targets [35, 218, 219, 220], and calculations of Ps scattering by inert gases have been performed [221]. Calculations of momentum transfer cross sections for other systems have been made in Refs. [222, 223]. The momentum transfer cross section is similar to Equation (10.1) but with a weighting factor of $(1 - \cos\theta)$ [72]:

$$\sigma_m = \int (1 - \cos\theta) \frac{d\sigma_{el}}{d\Omega}\, d\Omega. \tag{10.8}$$

The momentum transfer cross sections can also be written in terms of the phase shifts as [43, p.589]

$$\sigma_m^{\pm} = \frac{4}{\kappa^2} \sum_{\ell=0}^{\infty} (\ell + 1) \sin^2(\delta_{\ell}^{\pm} - \delta_{\ell+1}^{\pm}). \tag{10.9}$$

This is the expression used in this work.

Figure 10.18 shows the momentum transfer cross section using the complex Kohn phase shifts. The spin-weighting is from Equation (10.4). The triplet is a nearly featureless curve that gives a nearly constant contribution to the spin-weighted momentum transfer cross section.

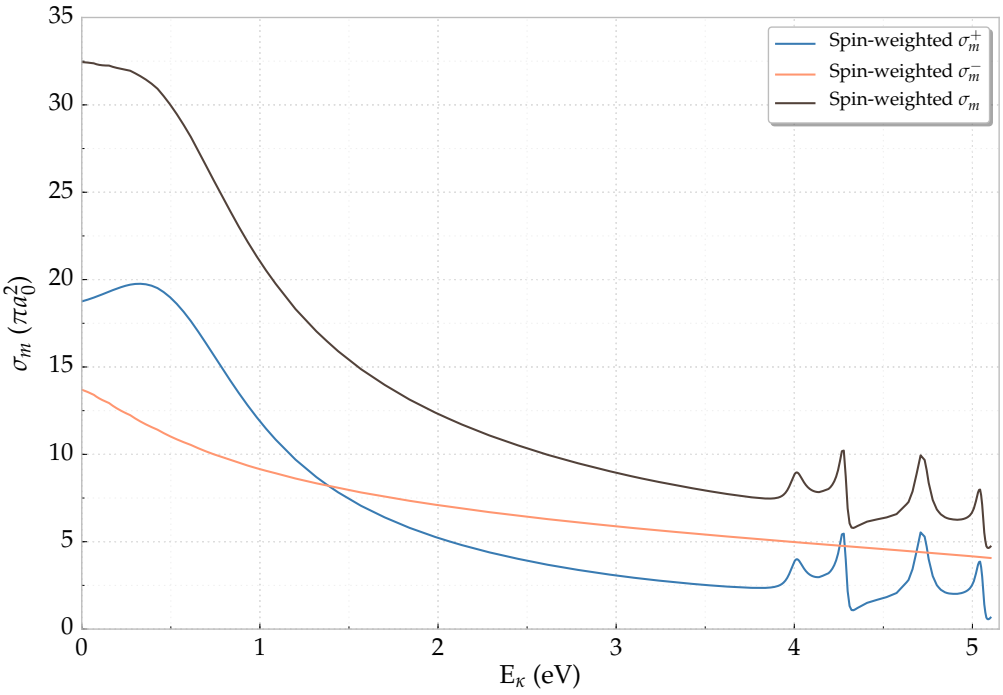

Figure 10.18: *S*-matrix complex Kohn momentum transfer cross sections

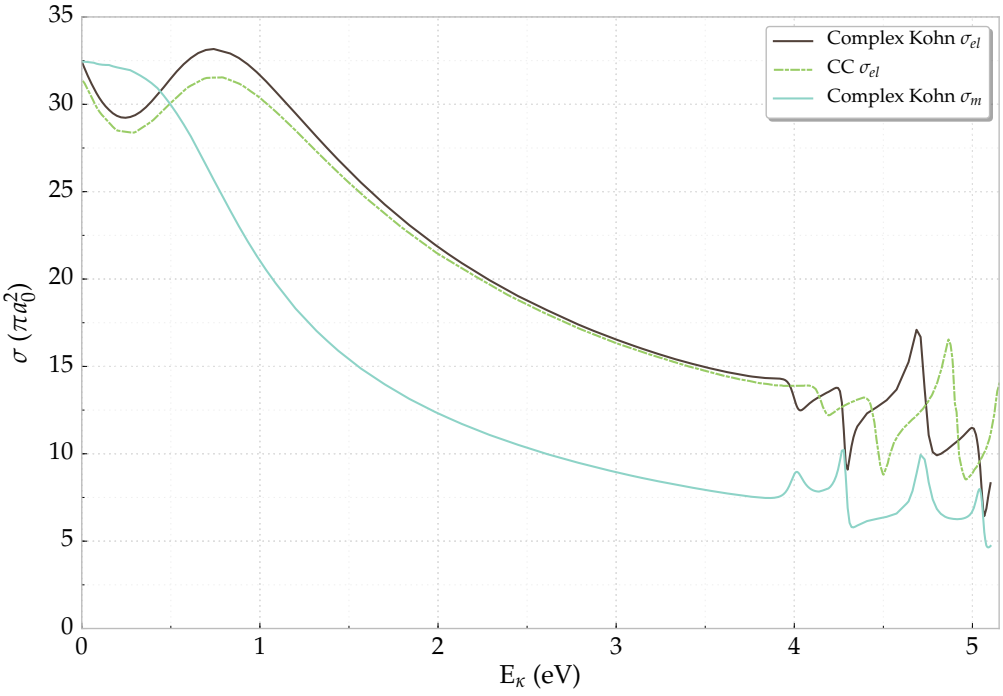

Figure 10.19: Comparison of cross sections. CC data is from Ref. [72].

Figure 10.19 shows the elastic integrated and momentum transfer cross sections. $\sigma_m \approx \sigma_{el}$ at very low energy. At zero energy, $\sigma_m = \sigma_{el}$ should hold, and for Ps-H, we find that $E_{\boldsymbol{\kappa}} < 10^{-6}$ eV, $\sigma_m = \sigma_{el} = 32.45\ \pi a_0^2$. As Blackwood et al. [221] note for Ps-Ne scattering, this is due to the differential cross section being essentially isotropic at low energy (and exactly isotropic at zero energy), as seen in Figures 10.11 and 10.13. If $\sigma_m < \sigma_{el}$, the scattering is mainly forward peaked, and if $\sigma_m > \sigma_{el}$, the scattering is mainly backward peaked [224]. Past zero energy, where $\sigma_m = \sigma_{el}$, we see that $\sigma_m > \sigma_{el}$ until approximately 0.46 eV or $\kappa = 0.26$. This is backward peaked (concentrated in the $\theta = \pi$ direction), which corresponds to the findings from the differential cross section in Section 10.2. Beyond 0.46 eV, $\sigma_m < \sigma_{el}$ for the rest of the energy range, indicating that the scattering is primarily forward peaked. The σ_m curve, as seen in Figure 10.19, gets close to the σ_{el} curve for the dips in some of the resonances at approximately 4.3 eV and 5.1 eV, showing that the scattering is concentrated nearly equally in the forward and backward directions at these energy values. This effect can slightly be seen in Figure 10.11, but it is most clearly shown in Figure 10.12.

10.4 Summary

Computing the phase shifts for the first three partial waves allowed us to calculate the elastic integrated cross section for for Ps-H scattering. This cross section compares well to the CC [72] but with some significant differences at both low and high κ (below the Ps(n=2) threshold). The $\ell = 3 - 5$ partial waves are used in this calculation but affect the integrated cross section little. An interesting feature is the dip and maximum under 1 eV, which is caused by the interference of the ^{1}S and ^{1}P partial wave cross sections.

The differential cross section converges more slowly than the integrated cross section with respect to ℓ. The differential cross section exhibits a complicated behavior, with the singlet resonances contributing greatly near the Ps(n=2) threshold. At very low energies, the differential cross section is slightly backward peaked and becomes strongly forward peaked as energy increases. The momentum transfer cross section is identical to the elastic integrated cross section at nearly zero energy but becomes larger as energy increases, up to approximately 0.46 eV, which corresponds with the differential cross section being backward peaked. Past this energy, the momentum transfer cross section is less than the elastic integrated cross section, indicating that scattering is more forward peaked.

11

Effective Range Theories

THE scattering length and effective range give information about very low energy scattering ($\kappa \to 0$). The Kohn-type variational methods can give an exact upper bound on the scattering length [137, 225], though we do not do a Kohn-type variation on the scattering length in this work. The scattering length can also give information about whether there is a bound state in the system.

11.1 S-Wave Scattering Length and Effective Range

There are multiple methods for calculating the scattering length and effective range. I describe the methods and results that we used in this section.

11.1.1 Scattering Length Definition

The scattering length [43, p.589] is defined as

$$a_\ell^\pm = -\lim_{\kappa\to 0} \frac{\tan\delta_\ell^\pm}{\kappa^{2\ell+1}}. \tag{11.1}$$

We approximate this with very small κ as

$$a_\ell^\pm \approx -\frac{\tan\delta_\ell^\pm}{\kappa^{2\ell+1}}. \tag{11.2}$$

To avoid confusion with the Bohr radius, a_0, we define $a = a_{\ell=0}$. If this definition is used for decreasing (but positive) values of κ, there is a clear convergence. Table 11.1 has the scattering length calculated for κ values of 0.001 and 0.0001. To the quoted accuracy, the values of the scattering length agree exactly for the two different values of κ for $\omega = 7$. This is the method used by Van Reeth and Humberston [57] for finding the scattering length (but for $\omega = 6$ only).

ω	$a^+(\kappa = 0.001)$	$a^+(\kappa = 0.0001)$	$a^-(\kappa = 0.001)$	$a^-(\kappa = 0.0001)$
6	4.3364	4.3364	2.1415	2.1415
7	4.3306	4.3306	2.1363	2.1363

Table 11.1: Scattering length from approximation to definition

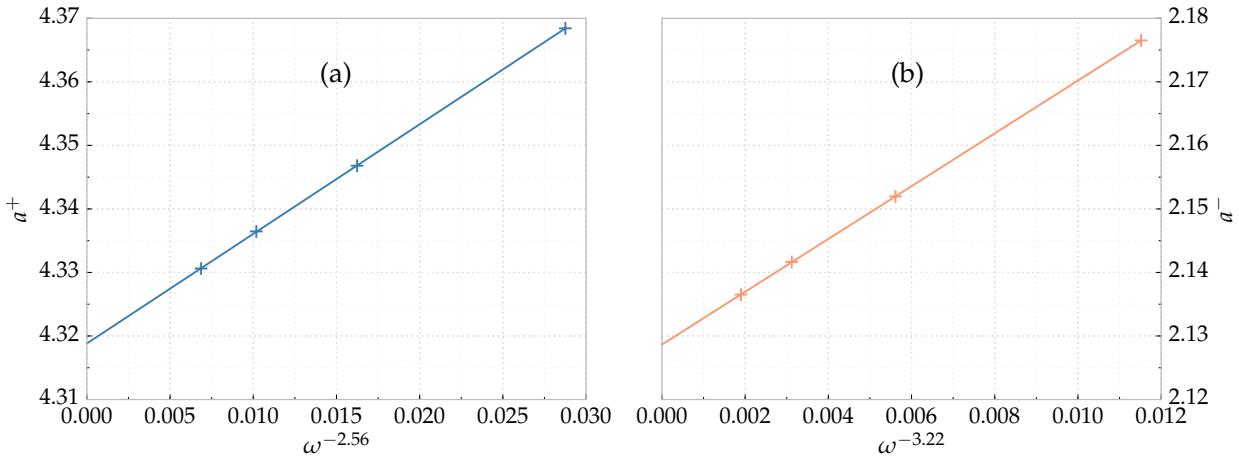

Figure 11.1: Convergence of (a) ^{1}S and (b) ^{3}S scattering lengths using Equation (11.3).

Van Reeth and Humberston [57] also extrapolate their scattering length to $\omega \to \infty$ using

$$a^{\pm}(\omega) = a^{\pm}(\omega \to \infty) + \frac{c}{\omega^p}, \tag{11.3}$$

where c and p depend on each extrapolation. Performing this extrapolation, we obtain the fits shown in Figure 11.1. The extrapolated ^{1}S and ^{3}S scattering lengths shown in Table 11.7 are 4.319 and 2.129, respectively.

At zero energy [226],

$$\sigma_m^{\pm} = \sigma_{el}^{\pm} = 4(a^{\pm})^2. \tag{11.4}$$

So we can compare the scattering lengths to the cross sections at zero energy (taken as $E_{\kappa} = 10^{-7}$ eV here) with (in units of πa_0^2)

$$\sigma_{el}^{+} = \sigma_m^{+} = 75.03 \approx 4(a^{+})^2 = 75.02 \tag{11.5a}$$

$$\sigma_{el}^{-} = \sigma_m^{-} = 18.27 \approx 4(a^{-})^2 = 18.26\,. \tag{11.5b}$$

Also at zero energy [43, p.590],

$$\frac{d\sigma_{el}}{d\Omega} = a^2 \tag{11.6}$$

κ Range	a^+	r_0^+	a^-	r_0^-
$0.1 - 0.5$	4.3080	2.2816	2.1623	1.3729
$0.01 - 0.09$	4.3306	2.2012	2.1367	1.9354
$0.001 - 0.009$	4.3306	2.1972	2.1365	2.0354

Table 11.2: Scattering length and effective range for short-range expansion

Using the values for a^+ and a^- for $\omega = 7$ from Table 11.1 and using the appropriate spin-weighting from Equation (10.4), this gives $(a^+)^2 \times 1/4 + (a^-)^2 \times 3/4 = 8.11$, and as seen on page 135, this is equal to the differential cross section at nearly zero energy.

11.1.2 Short-Range Interactions

For short-range interactions, the effective range is given by [227, 228, 229]

$$\kappa \cot \delta_0^{\pm} = -\frac{1}{a^{\pm}} + \frac{1}{2} r_0^{\pm} \kappa^2 + \mathcal{O}(\kappa^4). \tag{11.7}$$

This equation is referred to here as the short-range expansion. Phase shifts for low values of κ are fitted to this equation to determine the effective range and scattering length, and the results are shown in Table 11.2. This is a subset of Table 11.3. We used 10 equidistant values of κ for all κ ranges other than 0.1 - 0.5, where we used 5 equidistant points. This fitting is not carried out to κ higher than 0.5, due to the resonance structure described in Section 5.3.2.

This fitting works well enough for the singlet, but the triplet data does not fit exactly. This can be seen in Figure 11.2, which is similar to Figure 5 of Ref. [57]. Fraser [186] has also done a similar graph using the SE method but found a relatively straight line for both ^{1}S and ^{3}S.

For very small values of κ, the scattering length agrees with the definition in Equation (11.1). These values also agree well with the scattering length found by other recent calculations, shown in Table 11.7. The effective range for the $\kappa = 0.1 - 0.5$ entry for the short-range expansion also agrees relatively well with the results from other groups. As can easily be seen, when smaller κ values are used however, the value of $r_0^{\pm}$ changes drastically for the triplet and a much smaller amount for the singlet. Previous work using the Kohn / inverse Kohn variational methods found $r_0^- = 1.39$ [57], which is close to the value of $r_0^- = 1.3438$ using $\kappa = 0.1 - 0.5$.

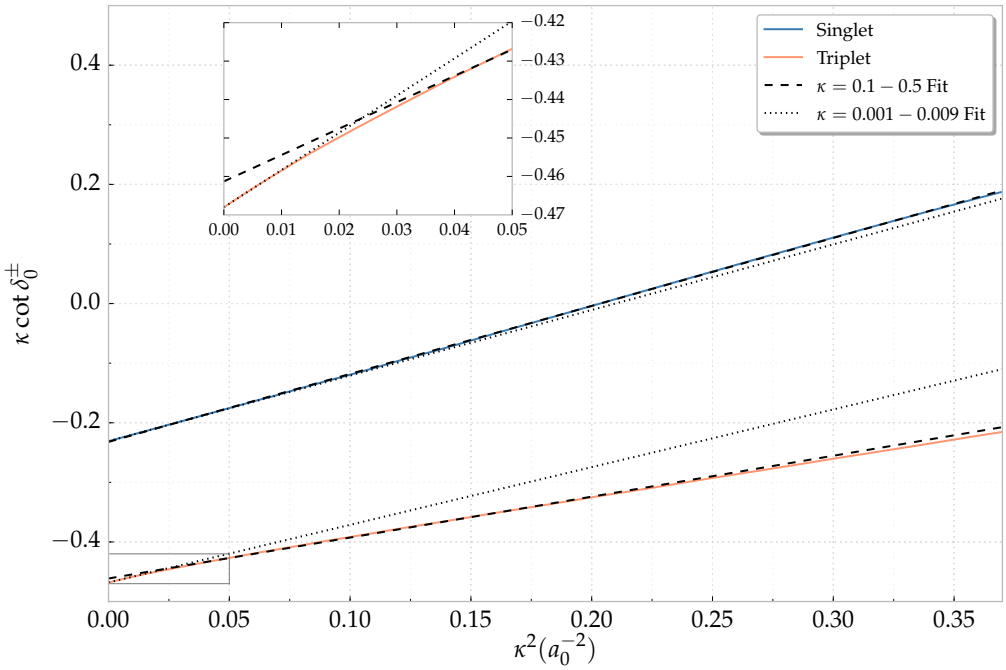

Figure 11.2: ^1S and ^3S phase shifts, plotted as $\kappa \cot \delta_0^{\pm}$ versus κ^2. The inset shows a magnified portion of the same data as denoted by the gray box in the lower left.

11.1.3 van der Waals Interaction

The dominant long-range interaction for Ps-H scattering is given by the van der Waals potential [42, 57, 230]. The van der Waals potential is given as

$$V(R) = -\frac{C_6}{R^6}. \tag{11.8}$$

For the Ps-H system, C_6 has been calculated in atomic units by Martin and Fraser to be 34.78473 [231]. Mitroy and Bromley [212] also calculate this to be 34.785 in a paper calculating C_6 for multiple Ps-atom problems. Ray [232] also investigates a modified static exchange model that explicitly includes the van der Waals interaction.

11.1.3.1 Flannery Expansion

When the van der Waals potential is taken into account, the effective range equation from Flannery [229, p.669] is (dropping the $\pm$ for brevity)

$$\kappa \cot \delta_0 = -\frac{1}{a} + \frac{1}{2} r_0 \kappa^2 - \frac{\pi}{15a^2} \left(\frac{2MC_6}{\hbar^2} \right) \kappa^3 - \frac{4}{15a} \left(\frac{2MC_6}{\hbar^2} \right) \kappa^4 \ln(\kappa a_0) + \mathcal{O}(\kappa^4). \tag{11.9}$$

Partial wave	κ Range	κ^2	κ^3	$\kappa^4 \ln$
^{1}S	$0.1 - 0.5$	4.3080/2.2816	3.9879/4.1474	3.1029/7.9026
	$0.01 - 0.09$	4.3306/2.2012	4.3288/2.4807	4.3297/2.3490
	$0.001 - 0.009$	4.3306/2.1972	4.3306/2.2251	4.3306/2.2207
^{3}S	$0.1 - 0.5$	2.1623/1.3729	1.9356/9.0125	1.7116/9.7221
	$0.01 - 0.09$	2.1367/1.9354	2.1350/3.0845	2.1359/2.6251
	$0.001 - 0.009$	2.1365/2.0354	2.1365/2.1502	2.1365/2.1394

Table 11.3: Scattering length and effective range using Equation (11.10). The column headings indicate which term this expansion is taken to. Entries are given as $a^{\pm}/r_0^{\pm}$.

In atomic units (see Section 1.7), $M = 2$ (mass of Ps), $\hbar = 1$ (Planck's constant) and $a_0 = 1$ (Bohr radius), simplifying this equation as

$$\kappa \cot \delta_0 = -\frac{1}{a} + \frac{1}{2} r_0 \kappa^2 - \frac{4\pi C_6}{15a^2}\kappa^3 - \frac{16C_6}{15a}\kappa^4 \ln(\kappa) + \mathcal{O}(\kappa^4). \tag{11.10}$$

In Table 11.3, the κ^2 column fits only to the first two terms of Equation (11.10), which makes this the same as the short-range expansion, Equation (11.7). The κ^3 column fits to the first three terms, and the $\kappa^4 \ln$ column fits to all four terms. Entries in these tables are given as $a^{\pm}/r_0^{\pm}$. The scattering length, $a^{\pm}$, is used as a fitting parameter, not a fixed value determined by Equation (11.1) in Table 11.1.

11.1.3.2 Hinckelmann-Spruch Expansion

Equation (11.9) is derived by starting with the expression given in Hinckelmann and Spruch [233], then inverting and performing an expansion. Hinckelmann and Spruch give this in terms of $\tan \delta_0$.

$$\tan \delta_0 = -a\kappa - \frac{1}{2} r_0 a^2 \kappa^3 + \frac{1}{15} C_6^4 \kappa^4 + \frac{4}{15} C_6^4 \kappa^5 \ln|2\kappa d| + \mathcal{O}(\kappa^5) \tag{11.11}$$

Table 11.4 has entries for the $\kappa^5 \ln$ term where the fitting cannot be used, since the fitting attempts to use a negative value of d, forcing the natural logarithm to return a complex value. The variable d is given in their paper as the distance $r > d$ at which the van der Waals potential is dominant. We have to fit to d in our problem, making this particular model not fit as well.

The scattering lengths for $\kappa = 0.001 - 0.009$ match well with the other methods, however. For the κ^3 and κ^4 terms in Equation (11.11) using this κ range, the effective range matches reasonably well with the previous methods, but the last term involving κ^5 does

Partial Wave	κ Range	κ^3	κ^4	$\kappa^5 \ln$
^{1}S	$0.1 - 0.5$	13.652/-0.7062	13.359/-0.6806	24.484/-484.65
	$0.01 - 0.09$	4.3286/2.3119	4.3276/2.3930	4.3306/34.834
	$0.001 - 0.009$	4.3306/2.1980	4.3306/2.2060	4.3306/34.622
^{3}S	$0.1 - 0.5$	1.7299/4.9923	1.4474/12.139	2.3287/-3.0949
	$0.01 - 0.09$	2.1369/1.9500	2.1359/2.2805	2.1364/2.1411
	$0.001 - 0.009$	2.1365/2.0382	2.1365/2.0711	2.1365/7.0068

Table 11.4: Scattering length and effective range using Equation (11.11). The column headings indicate which term this expansion is taken to. Entries are given as $a^{\pm}/r_0^{\pm}$.

ω	r_0^+	r_0^-
6	2.2809	2.1839
7	2.2796	2.1878

Table 11.5: Effective range from Arriola equation

not match for the effective range. The effective range is even negative when using the κ^5 term with $\kappa = 0.1 - 0.5$. The Flannery expansion, Equation (11.9), is a modified version of Equation (11.11) and is easier to fit to our type of problem.

11.1.3.3 Arriola Expression

Refs. [234, 235] give an analytic solution derived using a semiclassical approach for the effective range with a van der Waals potential of

$$\frac{r_0}{R} = 1.395 - 1.333\frac{R}{a_0} + 0.6373\frac{R^2}{a_0^2} \ , \tag{11.12}$$

where the van der Waals range, R, is

$$R = \left(\frac{MC_6}{\hbar^2}\right)^{\frac{1}{4}} . \tag{11.13}$$

Using the values from Table 11.1 for $a^{\pm}$, this equation produces the results in Table 11.5. Despite being derived using a semiclassical approach, it nonetheless returns values for the effective range similar to that returned from the other models.

11.1.3.4 Gao Model

Gao's [236] effective range theory treatment is the most complicated of the models tried. Gao solves the Schrödinger equation for an attractive r^{-6} potential to find an expression relating the phase shifts to a quantity he refers to as $K^0_\ell(E_{\boldsymbol{\kappa}})$:

$$\tan\delta_l = [Z_{ff} - K^0_\ell(E_{\boldsymbol{\kappa}})Z_{gf}]^{-1}[K^0_\ell(E_{\boldsymbol{\kappa}})Z_{gg} - Z_{fg}]. \tag{11.14}$$

The Z functions in this equation are complicated but described in his paper. The phase shifts are fitted to Equation (11.14) to determine $K^0_\ell(E_{\boldsymbol{\kappa}})$ for each κ value. $K^0_\ell(E_{\boldsymbol{\kappa}})$ can be expanded in a Taylor series as [214]

$$K^0_\ell(E_{\boldsymbol{\kappa}}) = K^0_\ell(0) + K^{0\prime}_\ell(0)E_{\boldsymbol{\kappa}} + \ldots. \tag{11.15}$$

We keep just the first two terms in this expression. From this, $K^0_l(0)$ and $K^{0\prime}_l(0)$ are determined. In another paper [214], Gao performs an expansion of this expression for low κ to generate expressions for a and r_0:

$$a_0 = \frac{2\pi}{[\Gamma(1/4)]^2}\frac{K^0_{l=0}(0) - 1}{K^0_{l=0}(0)}\beta_6 \tag{11.16}$$

and

$$r_0 = \frac{[\Gamma(1/4)]^2}{3\pi}\frac{[K^0_{l=0}(0)]^2 + 1}{[K^0_{l=0}(0) - 1]^2}\beta_6 + \frac{[\Gamma(1/4)]^2}{\pi}\frac{{K^0_{l=0}}'(0)^2(\hbar^2/2\mu)(1/\beta_6)^2}{[K^0_{l=0}(0) - 1]^2}\beta_6. \tag{11.17}$$

β_6 is related to C_6 by

$$\beta_6 = (2\mu C_6/\hbar^2)^{1/4}. \tag{11.18}$$

The results in Table 11.6 are computed by taking Equation (11.15) out to the second term, which includes the K^0_l derivative. Two values of κ are used to solve the equations for the unknowns $K^0_{\ell=0}(0)$ and ${K^0_{\ell=0}}'(0)$. These values are in the table and are used to determine a and r_0 via Equations (11.16) and (11.17).

The values for a are well-converged and compare well with the values in Table 11.1 from the definition in Equation (11.1). The values of r_0 are not so well-converged, but they normally compare well with the fittings in Section 11.1.3. In Ref. [56], we used the $\kappa = 0.002, 0.003$ values, as the smallest set of $\kappa = 0.001, 0.002$ is obviously unstable, with a much different effective range for ^{1}S.

We also attempted to carry the expansion in Equation (11.15) to the third term with the second derivative, but numerical inaccuracy proved to be a problem. This term is proportional to κ^4, which is vanishingly small for most κ values considered, making determining ${K^0_{\ell=0}}''$ impossible with the current phase shift precision.

The K^0_l is not particularly sensitive, but even the $K^{0\prime}_l$ can change drastically depending on the values of κ used. The $K^{0\prime}_l$ values for ^{3}S are also much larger than those of ^{1}S. While

	κ	K_l^0	$K_l^{0\prime}$	a	r_0
^1S	0.1, 0.2	-0.610967	-1.67672	4.3286	2.3380
	0.2, 0.3	-0.608704	-1.90301	4.3386	2.3128
	0.3, 0.4	—	—	—	—
^1S	0.001, 0.002	-0.61050	-13.8371	4.3307	0.9103
	0.002, 0.003	-0.61052	-2.76553	4.3306	2.2104
	0.003, 0.004	-0.61052	-0.46049	4.3306	2.4811
	0.004, 0.005	-0.61050	-4.51842	4.3307	2.0046
	0.005, 0.006	-0.61052	-2.67368	4.3306	2.2212
	0.006, 0.007	-0.61052	-2.66827	4.3306	2.2219
	0.007, 0.008	-0.61052	-2.63471	4.3306	2.2258
	0.008, 0.009	-0.61052	-2.59699	4.3306	2.2302
^3S	0.1, 0.2	-3.33674	-20.9648	2.1336	2.7510
	0.2, 0.3	-3.30159	-24.4797	2.1389	2.6778
	0.3, 0.4	—	—	—	—
^3S	0.001, 0.002	-3.31867	-62.3938	2.1363	2.0666
	0.002, 0.003	-3.31868	-57.2099	2.1363	2.1513
	0.003, 0.004	-3.31868	-57.6505	2.1363	2.1441
	0.004, 0.005	-3.31866	-62.0112	2.1363	2.0728
	0.005, 0.006	-3.31868	-58.7635	2.1363	2.1259
	0.006, 0.007	-3.31869	-57.7088	2.1363	2.1431
	0.007, 0.008	-3.31871	-55.5445	2.1363	2.1785
	0.008, 0.009	-3.31874	-54.1885	2.1363	2.2006

Table 11.6: Full Gao model scattering length and effective range

the Gao method gives results in line with the other ERTs presented thus far, it would likely be suited better for systems where phase shifts could be computed to more precision than we can do for Ps-H scattering.

Gao [214] also gives QDT expansions for the S-wave and P-wave in another paper. Equations (6) and (7) in [214] relate the phase shifts to K_ℓ^0. In Section 11.1.5, we also see that this QDT expansion does not do well for these two partial waves. Gao also gives an expansion for $\ell \geq 2$, which is discussed in Section 9.3.

11.1.4 Effective Range from Scattering Length and Binding Energy

We use an expression from Ref. [70] to get an estimate of the ^1S effective range, given by

$$r_0^+ = \frac{a^+\sqrt{4E_b} - 1}{2a^+E_b}. \tag{11.19}$$

This expression is also similar to one given by Page [76]. Using this with the complex Kohn a^+ and E_b at $\omega = 7$, we get $r_0^+ = 2.106$, which only agrees somewhat with the other results in Table 11.7. There is not an equivalent expression for r_0^-, as there is not a ^3S PsH bound state.

11.1.5 Comparison of Effective Range Theories

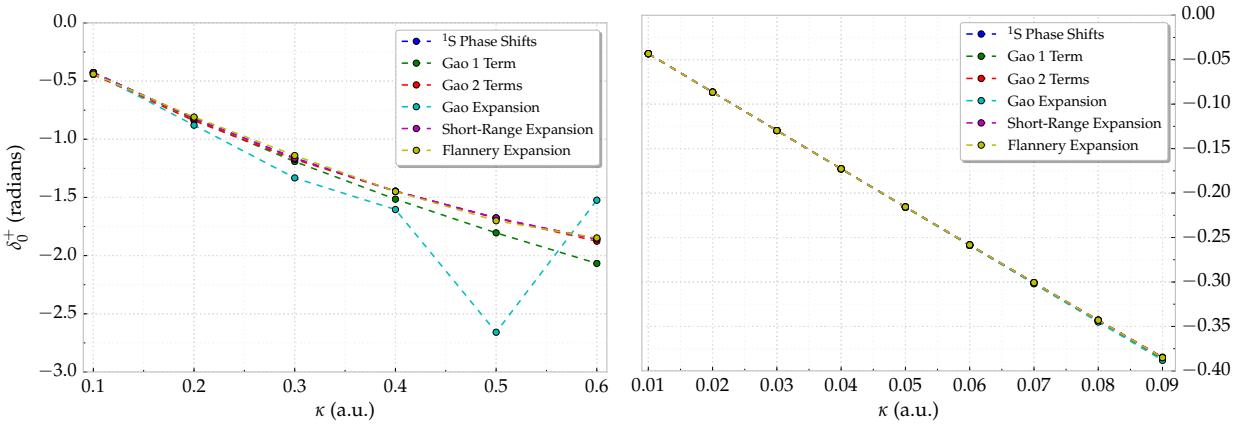

Figure 11.3: Comparison of results from effective range theories for ^1S Ps-H. Figure (a) shows a larger set of κ values, and (b) shows a range with small κ values. The Gao 1 and 2 term results use 1 and 2 terms from Equation (11.15), respectively. The Gao expansion uses the method in Ref. [214]. The short-range and Flannery expansions are given in Sections 11.1.2 and 11.1.3.1, respectively.

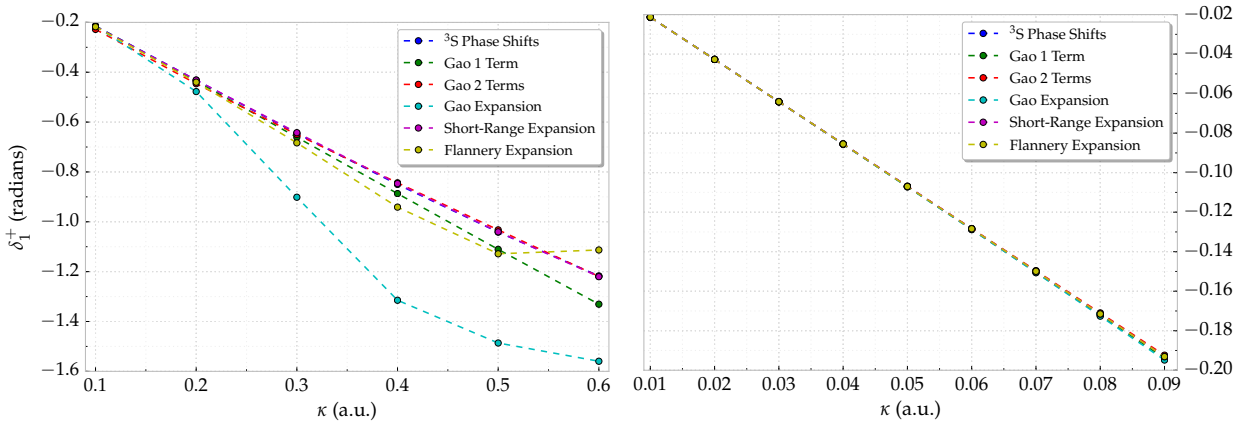

Figure 11.4: Comparison of results from effective range theories for ^3S Ps-H. Figure (a) shows a larger set of κ values, and (b) shows a range with small κ values. The Gao 1 and 2 term results use 1 and 2 terms from Equation (11.15), respectively. The Gao expansion uses the method in Ref. [214]. The short-range and Flannery expansions are given in Sections 11.1.2 and 11.1.3.1, respectively.

To obtain the plots in Figures 11.3 and 11.4, after obtaining fits for each of the models, we solved the respective equations for the phase shifts. This provides a reliable way to determine how well each model fits the phase shift data. When κ is small, the different models agree extremely well, as seen in Figures 11.3(b) and 11.4(b). Higher order terms in each of the model equations become negligible as κ gets smaller. Figures 11.3 and 11.4 do not include the Hinckelmann-Spruch results since, as seen in Table 11.4, this expression does not generate particularly good results due to the need to fit to the d parameter in Equation (11.11).

11.1.5.1 Comparisons with Other Groups' Results

The first eight entries of Table 11.7 show the scattering lengths and effective ranges we calculate with the various methods described in this chapter. Other than the ERT Short for $\kappa = 0.1 - 0.5$, the scattering lengths from the different methods are identical. There is much less agreement in the effective range. For the singlet, $r_0^+ \approx 2.2$, and for the triplet, $r_0^- \approx 2.0 - 2.1$. The effective range is much more sensitive to slight variations in the phase shifts. More agreement could likely be achieved if the wavefunction was fully optimized for this very low energy range. We also tried a smaller κ range of 0.0001 - 0.0009, but the phase shifts were less numerically stable in that region.

As noted earlier, there is good agreement between the scattering lengths and effective ranges for recent calculations from other groups and the results we obtain using the complex Kohn phase shifts. The older calculations tend to have higher values for $a^{\pm}$. The r_0^-

Method	κ	a^+	r_0^+	a^-	r_0^-
Approx. to def. - Eq. (11.2)	0.001	4.331 ± 0.012	—	2.137 ± 0.008	—
Extrapolated ($\omega = 4 \to 7$) - Eq. (11.1)	0.001	4.319	—	2.129	—
ERT Short - Eq. (11.7)	$0.001 - 0.009$	4.331 ± 0.012	2.197	2.137 ± 0.008	2.035
ERT Short - Eq. (11.7)	$0.1 - 0.5$	4.308 ± 0.003	2.275	2.162 ± 0.003	1.343
ERT vdW - Eq. (11.10)	$0.001 - 0.009$	4.331 ± 0.012	2.221	2.137 ± 0.008	2.137
QDT - Eqs. (11.14), (11.15)	$0.002, 0.003$	4.331 ± 0.012	2.210	2.136 ± 0.008	2.151
QDT expansion - Eq. (6) in Ref. [214]	0.001	4.331 ± 0.012	2.535	2.136 ± 0.008	3.086
Eq. (11.19)	—	—	2.106	—	—
CC 14Ps14H+H^- (Walters *et al* 2004) [70]	—	4.327	—	—	—
Kohn extrapolated (Van Reeth *et al* 2003) [57]	—	4.311	2.27	2.126	1.39
Kohn 721 terms (Van Reeth *et al* 2003) [57]	—	4.334	—	2.143	—
Kohn Eq. (11.7) [57]	up to 0.5	4.30	2.27	2.147	—
CC 14Ps14H (Blackwood *et al* 2002) [70]	—	4.41	2.19	2.06	1.47
SVM (Ivanov *et al* 2002) [65]	—	4.34	2.39	2.22	1.29
DMC (Chiesa *et al* 2002) [63]	—	4.375	2.228	2.246	1.425
T-matrix (Biswas *et al* 2002) [183]	—	3.89	—	—	—
SVM (Ivanov *et al* 2001) [64]	—	4.3	—	2.2	—
Variational basis-set (Adhikari *et al* 2001) [237]	—	3.49	—	2.46	—
6-state CC (Sinha *et al* 2000) [69]	—	5.90	2.73	2.32	1.29
5-state CC (Adhikari *et al* 1999) [68]	—	3.72	1.67	—	—
22-state CC (Campbell *et al* 1998) [67]	—	5.20	2.52	2.45	1.32
9-state CC (Campbell *et al* 1998) [67]	—	5.51	2.63	2.45	1.33
Stabilization (Drachman *et al* 1976) [184]	—	—	—	2.36	1.31
Stabilization (Drachman *et al* 1975) [185]	—	5.33	2.54	—	—
Kohn 35 terms (Page 1976) [76]	—	5.844	2.90	2.319	—
SE (Hara *et al* 1975) [73]	—	7.275	—	2.476	—

Table 11.7: ^{1,3}S-wave scattering lengths and effective ranges

Model	κ	a_1^+	a_1^-
Approx. to def. - Eq. (11.2)	0.01	-22.130 ± 0.173	1.4530 ± 0.1104
Extrap. approx. to def. ($\omega = 4 \to 7$) - Eq. (11.1)	0.01	-22.262	1.378
QDT - Eq. (11.14)	0.01, 0.02	-22.200 ± 0.173	1.4158 ± 0.1107
QDT expansion - Eq. (11.20)	0.01	-22.198 ± 0.172	1.4102 ± 0.1104
SVM [65]	—	-20.7	6.80

Table 11.8: ^{1,3}P scattering lengths summarized and compared

values from other groups lie close to our ERT Short values for $\kappa = 0.1 - 0.5$, but as seen in Figure 11.2 and Table 11.7, smaller κ values give a much larger effective range.

11.2 P-Wave Scattering Lengths

From Refs. [214, 238], the scattering length is only defined for a partial wave if $2\ell + 3 < n$, and the effective range is only defined if $2\ell + 5 < n$. For the van der Waals interaction, $n = 6$. Thus for Ps-H scattering, the P-wave has a scattering length but not an effective range. Ref. [65] calculates a P-wave effective range, but this does not appear to be physical.

To determine the scattering length, we can use Equation (11.2) with $\ell = 1$: This is the approximation to the definition shown as the first entry in Table 11.8. We also extrapolate the scattering lengths from this for $\omega = 4 - 7$ using Equation (11.3). Additionally, we use the QDT of Gao from Section 11.1.3.4 for the P-wave and the QDT expansion of Gao given by [214]

$$a_1 = -\frac{\pi}{18[\Gamma(3/4)]^2} \frac{K^0_{l=1}(0) + 1}{K^0_{l=1}(0)} \beta_6^3. \tag{11.20}$$

Each of these methods agree reasonably well for the ^{1}P and ^{3}P scattering lengths. The ^{1}P scattering length is negative and has a magnitude much larger than the ^{1,3}S scattering lengths, while the ^{3}P scattering length is positive and closer to the ^{1,3}S scattering lengths.

The only other calculation we have found of P-wave scattering lengths is the SVM calculation [65]. Their a_1^+ matches well with the complex Kohn value, but their a_1^- is much larger. They determine the scattering lengths with an effective range formula involving a $r_1^\pm$ term, but even if we fit the complex Kohn phase shifts to this form, the scattering lengths do not change much. The discrepancy in the a_1^- scattering lengths appears mainly to be due to the much smaller SVM phase shifts at low κ.

Despite there not being a P-wave effective range, spurred by the SVM [65] use of an ERT expression, we performed a similar plot to Figure 11.2, given in Figure 11.5. Similar to the S-wave, the ^{1}P gives a relatively straight line, while the ^{3}P curves downward at low κ. Negating and inverting the y-intercept gives another way to calculate the scattering

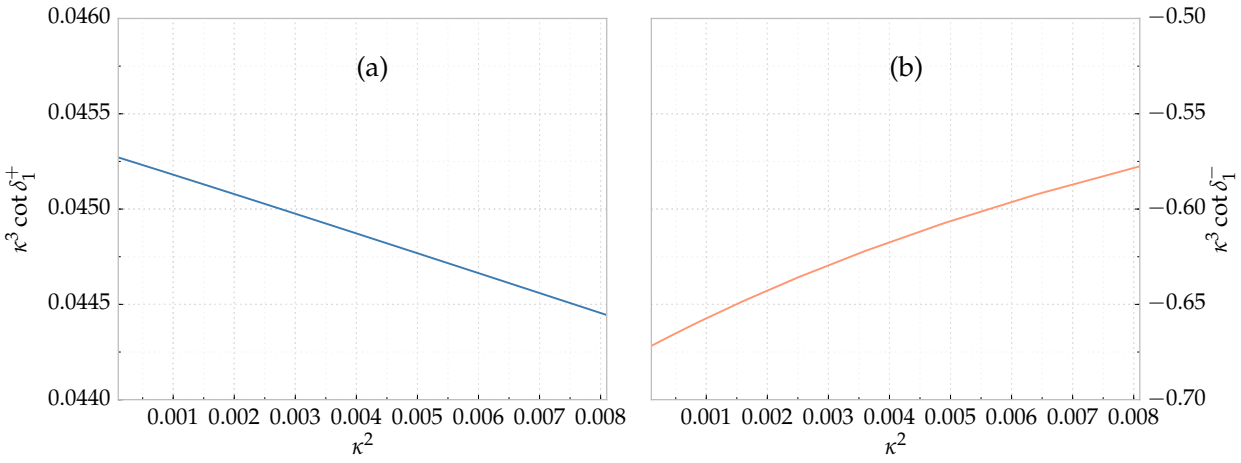

Figure 11.5: (a) ${}^1P$ and (b) ${}^3P$ phase shifts, plotted as $\kappa^3 \cot \delta_1^{\pm}$ versus κ^2.

length. Doing this, we get $a_1^+ = -22.101$ and $a_1^- = 1.474$. These match well with the other values we obtain in Table 11.8.

11.3 Summary

We calculated the ^{1,3}S-wave scattering lengths using the approximation to the definition, yielding similar results to the prior Kohn / inverse Kohn calculation [57]. In addition, we calculated the ^{1,3}S-wave scattering lengths and effective ranges using the short-range expansion, several models using the van der Waals interaction, and a QDT model incorporating the van der Waals interaction. These models yield nearly identical ^{1}S and ^{3}S scattering lengths when small κ values are used. The effective ranges vary more between the different models than the scattering lengths, but most models agree relatively well for several κ ranges for the ^{1}S-wave, with the exception of the QDT expansion, which gives less accurate results. Consequently, we do not report the QDT expansion results in Ref. [56].

We are able to reproduce approximately the ^{3}S effective range reported by other groups and the earlier Kohn / inverse Kohn calculations [57] by using $\kappa = 0.1 - 0.5$. As Van Reeth and Humberston [57] note, the graph of $\kappa \cot \delta^-$ versus κ^2 is not a straight line but curves down at low κ. Due to this, we also used a much smaller κ range of $0.001 - 0.009$, giving a more stable effective range that is higher than previously reported.

The P-wave does not have an effective range but does have a scattering length, which we calculated using the approximation to the definition and the QDT model. The scattering lengths between the different methods agreed relatively well, and the ^{1}P scattering length is similar to the SVM result [65]. However, the ^{3}P scattering length between our work and the SVM does not agree, with the SVM a_1^- being approximately 4.7 times as

large, which is likely due to the smaller SVM ^{3}P-wave phase shifts.

12

Conclusions

The Kohn variational method and variants of the method have been successful at treating Ps-H scattering in this work. We give a general formalism that can use any of the variants of the Kohn variational method, including the inverse Kohn, generalized Kohn, S-matrix complex Kohn, T-matrix complex Kohn, generalized S-matrix complex Kohn, and generalized T-matrix complex Kohn. We have also developed a general formalism and code that works for arbitrary ℓ, allowing us to calculate phase shifts for multiple partial waves. We have presented results for the first six partial waves through the H-wave using highly correlated Hylleraas-type short-range terms and an appropriate choice of long-range terms. The computational techniques that have enabled to do this work are also presented.

We used these short-range terms to calculate the binding energy for ^{1}S PsH, which compares very well to the accurate results of Refs. [80, 92]. This gave us confidence in using these terms for the Ps-H scattering problem. Despite there not being bound states for other partial waves, we also used these short-range terms to create stabilization plots to get rough estimates of the resonance positions for ^{1}P and ^{1}D.

The S-wave and P-wave phase shifts compare well to other accurate calculations, including the CC [70, 72]. The current complex Kohn phase shifts for these two partial waves are highly accurate. The resonance parameters we have computed for the singlet partial waves through the ^{1}F-wave generally compare better with the complex rotation [92, 175, 182, 210] than the CC [72].

The much larger differences come in with the lower κ phase shifts for the ^{1,3}D-wave. The complex Kohn ^{3}D phase shifts are consistently below the CC results [70], and the ^{1}D phase shifts are generally below but become slightly higher than the CC [72] near the resonance region. An analysis of the nonlinear parameters improved the phase shifts slightly, but we believe that some of this discrepancy with the CC can be explained by our omission of the mixed symmetry terms for the D-wave (and higher partial waves). These terms are very difficult to work with, and an analysis [194] of their contributions for e^+-H and e^--H scattering shows that they could be important for Ps-H scattering. The mixed symmetry terms for the three-body e^+-H and e^--H systems are much easier to use than for the four-body Ps-H system.

However, the multiple cross sections we calculate are not affected much by this discrepancy in the ^{1,3}D phase shifts. This is due to the D-wave mainly contributing only at higher κ values, while the S-wave and P-wave are dominant through much of the lower κ range. In this region, the complex Kohn phase shifts are better converged and match well with the CC phase shifts. The resonance parameters that we calculate for the ^{1}D resonance also match well with the complex rotation results. The ^{1,3}F, ^{1,3}G, and ^{1,3}H partial waves do not contribute significantly to the elastic integrated or momentum transfer cross sections, but they do contribute some to the elastic differential cross section. The differential cross section is relatively well converged by the H-wave, so we have presented all of these cross sections in this work. The differential cross section has interesting features, such as the contributions from the singlet ^{1}S through ^{1}F resonances. The differential cross section is nearly isotropic at very low energy and becomes slightly backward peaked at low energy, then becomes forward peaked at approximately 0.5 eV, continuing this way to the Ps(n=2) threshold.

Multiple effective range theories were used to analyze the effective ranges for ^{1,3}S and the scattering lengths for ^{1,3}S and ^{1,3}P, including several that incorporate the van der Waals interaction. We found that these all agreed relatively well at very low κ – even the short-range expansion. We find that the ^{3}S effective range changes significantly depending on the range of κ used. The r_0^- we obtain agrees with the values from other groups if $\kappa = 0.1 - 0.5$ but increases when we use the much smaller range of $\kappa = 0.001 - 0.009$. The other S-wave scattering lengths and effective ranges match up well with those calculated by other groups. The ^{1}P scattering length compares well with the SVM result [65], but the ^{3}P scattering length differs significantly.

A

External Angular Integrations

We perform rotations and then integrations over the 3 external angles to reduce the 9-dimensional integrations to 6 dimensions. The procedure described here is the same as in Van Reeth's thesis [95].

The integrals needed in Equations (2.11), (3.56), (4.1) and (8.3) have volume elements of

$$d\tau = d\mathbf{r}_1 d\mathbf{r}_2 d\mathbf{r}_3. \tag{A.1}$$

In spherical coordinates, this becomes

$$d\tau = r_1^2 dr_1 \sin\theta_1 d\theta_1 d\varphi_1 r_2^2 dr_2 \sin\theta_2 d\theta_2 d\varphi_2 r_3^2 dr_3 \sin\theta_3 d\theta_3 d\varphi_3. \tag{A.2}$$

These coordinates are given in an arbitrary coordinate system as in Figure A.1.

We can rotate the coordinate system multiple ways in order to integrate over the external angles. First consider rotating the coordinate system so that the z-axis is along $\mathbf{r}_1$. If we then choose to perform another rotation so that $\mathbf{r}_2$ is in the x′-z′ plane, from Figure A.2, the volume element becomes

$$d\tau = r_1^2 dr_1 \sin\theta_1 d\theta_1 d\varphi_1 r_2^2 dr_2 \sin\theta_{12} d\theta_{12} d\phi_2' r_3^2 dr_3 \sin\theta_{13} d\theta_{13} d\varphi_{23}. \tag{A.3}$$

The angles θ_{12}, θ_{13}, and φ_{23} are internal angles. The external angle ϕ_2' is measured from the x′-axis before the rotation into $\mathbf{r}_2$. The angles θ_1 and φ_1 are also external angles. As Peter Van Reeth points out in his thesis [95] on page 78, φ_{23} is the angle between the planes of the triangles (r_1, r_2, r_{12}) and (r_1, r_3, r_{13}). This angle can range between $\varphi_{23} = 0$ and $\varphi_{23} = 2\pi$.

For the PsH bound state and S-wave Ps-H scattering, integrating over the external angles gives

$$d\tau = 8\pi^2 r_1^2 dr_1 r_2^2 dr_2 \sin\theta_{12} d\theta_{12} r_3^2 dr_3 \sin\theta_{13} d\theta_{13} d\varphi_{23}. \tag{A.4}$$

We can transform this into integrations over r_{12} and r_{13} instead of $d\theta_{12}$ and $d\theta_{13}$ by differentiating the following expression from the law of cosines with respect to $\mathbf{r}_{kl}$:

$$r_{kl}^2 = r_k^2 + r_l^2 - 2 r_k r_l \cos\theta_{kl}. \tag{A.5}$$

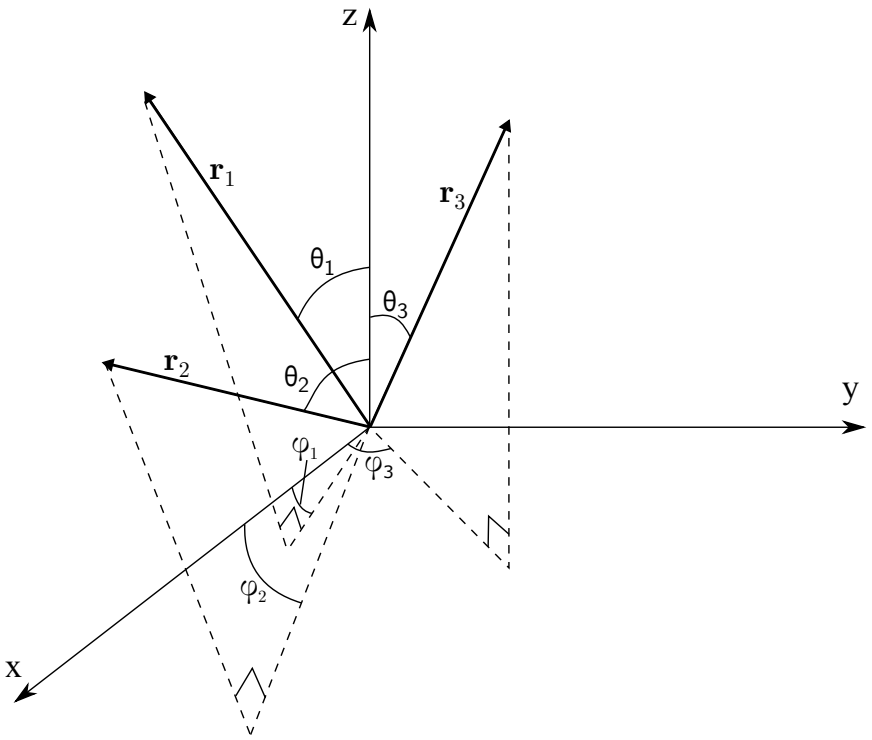

Figure A.1: Ps-H original coordinate system. This figure is the same as in Van Reeth [95].

When differentiated, this gives

$$dr_{kl}r_{kl} = r_k r_l \sin\theta_{kl} d\theta_{kl}. \tag{A.6}$$

Thus, we have

$$dr_{12}r_{12} = r_1 r_2 \sin\theta_{12} d\theta_{12} \tag{A.7a}$$
$$dr_{13}r_{13} = r_1 r_3 \sin\theta_{13} d\theta_{13}. \tag{A.7b}$$

Substituting these into Equation (A.4), we have

$$d\tau = 8\pi^2 dr_1 r_2 dr_2 r_3 dr_3 r_{12} dr_{12} r_{13} dr_{13} d\varphi_{23}. \tag{A.8}$$

This is the final form that we use in the short-range and long-range integrations, described in Sections 4.1 and 4.2.

If we do the rotations so that the z-axis is pointing in the direction of $\mathbf{r}_2$, then rotate so that $\mathbf{r}_1$ is in the x′-z′ plane, the volume element is instead

$$d\tau = 8\pi^2 r_1 dr_1 dr_2 r_3 dr_3 r_{12} dr_{12} r_{23} dr_{23} d\varphi_{13}. \tag{A.9}$$

We use this in the long-range integrations when there is an r_{23}^{-1} term, as in Sections 4.2.1 and 4.2.2.

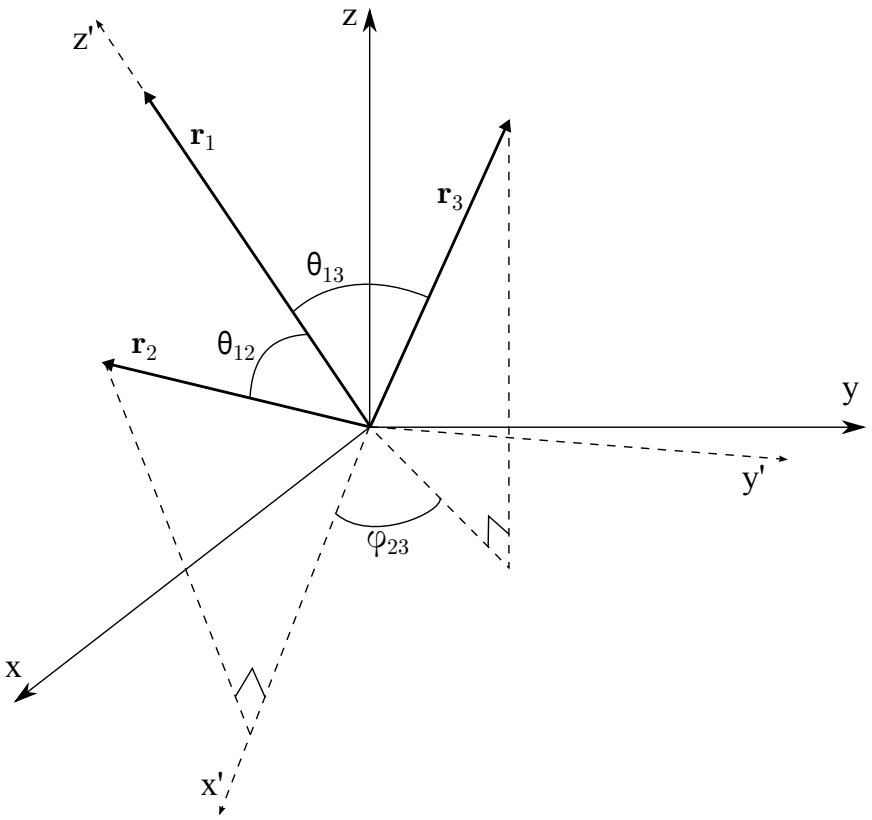

Figure A.2: Ps-H rotated coordinate system. This figure is the same as in Van Reeth [95].

There are 6 possible orderings to performing these rotations, but we only consider 3 and only use 2 in the final code. The last one rotates the z-axis into $\mathbf{r}_3$, then performs another rotation where the x′-z′ plane contains $\mathbf{r}_2$, giving a volume element of

$$d\tau = 8\pi^2 r_1 dr_1 r_2 dr_2 dr_3 r_{13} dr_{13} r_{23} dr_{23} d\varphi_{12}. \tag{A.10}$$

For the P-wave and higher, there is no spherical symmetry, but there is azimuthal symmetry for $m = 0$ of the spherical harmonics for all partial waves. The following sections show the results of performing these external angular integrations for general ℓ. These are shown in a *Mathematica* notebook entitled "General Angular Integrations.nb" [1].

A.1 Terms with Identical Spherical Harmonics

Since we are only investigating integrals over external angles in this Appendix, the orthogonality relations of the spherical harmonics do not hold. However, it can be seen that if we integrate over all external angles, $d\tau_{ext}$, any spherical harmonic with itself will give 2π, i.e.

$$\int_{\tau_{ext}} Y_\ell^0(\theta_i, \varphi_i) Y_\ell^0(\theta_i, \varphi_i)\, d\tau_{ext} = 2\pi, \tag{A.11}$$

where i = 1, 2, 3, ρ or ρ'.

A.2 Terms with $Y_\ell^0(\theta_i, \varphi_i) Y_\ell^0(\theta_j, \varphi_j)$

These terms are not completely necessary to generalize here, because they only appear in the short-short calculations. The derivations and code for the S-, P-, and D-wave short-short calculations use these. The general short-short derivations and code (Section 8.2) use a formalism from Drake and Yan [60] that does not do these external angular integrations. The general code is used for the F-, G-, and H-waves and can be used for arbitrary ℓ. Derivations for all of these can be seen in the *Mathematica* notebook "General Angular Integrations.nb" [1, 4]. Note that the result of 2π in Appendix A.1 is recovered if $i = j$. The general result is

$$\int_{\tau_{ext}} Y_\ell^0(\theta_i, \varphi_i) Y_\ell^0(\theta_j, \varphi_j)\, d\tau_{ext} = 2\pi P_\ell\big(\cos\theta_{ij}\big)\,. \tag{A.12}$$

where i = 1, 2, 3, ρ or ρ'. The results in the *Mathematica* notebook "General Angular Integrations.nb" are equivalent to this.

These integrations for the first three partial waves are given below:

$$\int_{\tau_{ext}} Y_0^0(\theta_i, \varphi_i) Y_0^0(\theta_j, \varphi_j)\, d\tau_{ext} = 2\pi \tag{A.13a}$$

$$\int_{\tau_{ext}} Y_1^0(\theta_i, \varphi_i) Y_1^0(\theta_j, \varphi_j)\, d\tau_{ext} = 2\pi \cos\theta_{ij} \tag{A.13b}$$

$$\int_{\tau_{ext}} Y_2^0(\theta_i, \varphi_i) Y_2^0(\theta_j, \varphi_j)\, d\tau_{ext} = 2\pi \left(3\cos^2\theta_{ij} - 1\right). \tag{A.13c}$$

When performing the external angular integrations instead of using the general short-range integrals in Section 8.2, the very specific form of the short-short integrals has to be that of the four-body integrals in Equation (4.1). From Equation (A.12), the results here have a $\cos\theta_{ij}$, which does not appear in the four-body integrals. To use these results, we have to use the law of cosines to replace any $\cos\theta_{ij}$ terms by

$$\cos\theta_{ij} = \frac{r_i^2 + r_j^2 - r_{ij}^2}{2 r_i r_j}. \tag{A.14}$$

This allows us to split these into multiple integrations with only polynomial r_i and r_{ij} terms with the decaying exponentials. Most of the other external angular integrations in this Appendix also end up with $\cos\theta_{ij}$, but those only apply to the long-range code, which does not have this restriction.

A.3 Terms with $Y_\ell^0(\theta_1, \varphi_1) Y_\ell^0(\theta_\rho, \varphi_\rho)$ and $Y_\ell^0(\theta_1, \varphi_1) Y_\ell^0(\theta_{\rho'}, \varphi_{\rho'})$

After doing these integrations by hand for the P-, D-, and F-wave (the S-wave is just 2π), I realized that it is possible to generalize these. This can be seen in the "Vector Gaussian Integration.cpp" file of the general long-range integration code (Appendix D). If we define

$$w_1 = \frac{r_1 + r_2\cos\theta_{12}}{2\rho}, \tag{A.15}$$

then

$$\int_{\tau_{ext}} Y_\ell^0(\theta_1, \varphi_1) Y_\ell^0(\theta_\rho, \varphi_\rho)\, d\tau_{ext} = 2\pi P_\ell(w_1), \tag{A.16}$$

where P_ℓ is the standard Legendre polynomial. This easily lets us calculate these terms in the C++ code. Likewise, for

$$w_1' = \frac{r_1 + r_3\cos\theta_{13}}{2\rho'}, \tag{A.17}$$

then

$$\int_{\tau_{ext}} Y_\ell^0(\theta_1, \varphi_1) Y_\ell^0(\theta_{\rho'}, \varphi_{\rho'})\, d\tau_{ext} = 2\pi P_\ell(w_1'). \tag{A.18}$$

A.4 Terms with $Y_\ell^0(\theta_2, \varphi_2) Y_\ell^0(\theta_\rho, \varphi_\rho)$ and $Y_\ell^0(\theta_3, \varphi_3) Y_\ell^0(\theta_{\rho'}, \varphi_{\rho'})$

Similar to Appendix A.3, these integrals are also generalizable and are used in the C++ file "Vector Gaussian Integration.cpp". Defining

$$w_2 = \frac{r_2 + r_1\cos\theta_{12}}{2\rho}, \tag{A.19}$$

then

$$\int_{\tau_{ext}} Y_\ell^0(\theta_2, \varphi_2) Y_\ell^0(\theta_\rho, \varphi_\rho)\, d\tau_{ext} = 2\pi P_\ell(w_2)\,. \tag{A.20}$$

Since ρ' is constructed from r_3, we can do the same method for the next set. We define

$$w_3 = \frac{r_3 + r_1 \cos\theta_{13}}{2\rho'}, \tag{A.21}$$

which gives

$$\int_{\tau_{ext}} Y_\ell^0(\theta_3, \varphi_3) Y_\ell^0(\theta_{\rho'}, \varphi_{\rho'})\, d\tau_{ext} = 2\pi P_\ell(w_3)\,. \tag{A.22}$$

A.5 Terms with $Y_\ell^0(\theta_2, \varphi_2) Y_\ell^0(\theta_{\rho'}, \varphi_{\rho'})$ and $Y_\ell^0(\theta_3, \varphi_3) Y_\ell^0(\theta_\rho, \varphi_\rho)$

This set is more complicated than those in Appendix A.4 but look similar. We first define

$$w_4 = \frac{r_1 \cos\theta_{12} + r_3 \cos\theta_{23}}{2\rho'}, \tag{A.23}$$

and then

$$\int_{\tau_{ext}} Y_\ell^0(\theta_2, \varphi_2) Y_\ell^0(\theta_{\rho'}, \varphi_{\rho'})\, d\tau_{ext} = 2\pi P_\ell(w_4)\,. \tag{A.24}$$

For the permuted version of this, we use

$$w_5 = \frac{r_1 \cos\theta_{13} + r_2 \cos\theta_{23}}{2\rho}, \tag{A.25}$$

giving

$$\int_{\tau_{ext}} Y_\ell^0(\theta_3, \varphi_3) Y_\ell^0(\theta_\rho, \varphi_\rho)\, d\tau_{ext} = 2\pi P_\ell(w_5)\,. \tag{A.26}$$

A.6 Terms with $Y_\ell^0(\theta_\rho, \varphi_\rho) Y_\ell^0(\theta_{\rho'}, \varphi_{\rho'})$

These are the most difficult angular integrations considered. After performing these integrations by hand through the D-wave, I came up with a way to compute them in *Mathematica*. These are derived in a *Mathematica* notebook entitled "General Angular Integrations.nb". Using this method, the H-wave integral ($\ell = 5$) took approximately 1 hour and 26 minutes to calculate in *Mathematica* using an Intel Q6600 processor-based desktop computer.

I discovered a way to generalize these integrals as well, but it was not until recently. Without realizing this relation, these integrals are very difficult to compute. Defining

$$y = \frac{4\left(\rho^2 + \rho'^2\right) - r_{23}^2}{8\rho\rho'}, \tag{A.27}$$

these integrals can be generalized to

$$\int_{\tau_{ext}} Y_\ell^0(\theta_\rho, \varphi_\rho) Y_\ell^0(\theta_{\rho'}, \varphi_{\rho'})\, d\tau_{ext} = 2\pi P_\ell(y)\,. \tag{A.28}$$

The results of these integrals for the first six partial waves follow.

$$\int_{\tau_{ext}} Y_0^0(\theta_\rho, \varphi_\rho) Y_0^0(\theta_{\rho'}, \varphi_{\rho'})\, d\tau_{ext} = 2\pi \tag{A.29}$$

$$\int_{\tau_{ext}} Y_1^0(\theta_\rho, \varphi_\rho) Y_1^0(\theta_{\rho'}, \varphi_{\rho'})\, d\tau_{ext} = \frac{\pi}{4\rho\rho'}\left[4\left(\rho^2 + \rho'^2\right) - r_{23}^2\right] \tag{A.30}$$

$$\begin{aligned}\int_{\tau_{ext}} Y_2^0(\theta_\rho, \varphi_\rho) Y_2^0(\theta_{\rho'}, \varphi_{\rho'})\, d\tau_{ext} = \frac{\pi}{64\rho^2\rho'^2}\Big[16\left(3\rho^4 + 2\rho^2\rho'^2 + 3\rho'^4\right) \\ +3r_{23}^4 - 24r_{23}^2\left(\rho^2 + \rho'^2\right)\Big]\end{aligned} \tag{A.31}$$

$$\begin{aligned}\int_{\tau_{ext}} Y_3^0(\theta_\rho, \varphi_\rho) Y_3^0(\theta_{\rho'}, \varphi_{\rho'})\, d\tau_{ext} = \frac{\pi}{512\rho^3\rho'^3}\Big[64\left(5\rho^6 + 3\rho^4\rho'^2 + 3\rho^2\rho'^4 + 5\rho'^6\right) \\ -5r_{23}^6 + 60r_{23}^4\left(\rho^2 + \rho'^2\right) - 48r_{23}^2\left(5\rho^4 + 6\rho^2\rho'^2 + 5\rho'^4\right)\Big]\end{aligned} \tag{A.32}$$

$$\begin{aligned}\int_{\tau_{ext}} Y_4^0(\theta_\rho, \varphi_\rho) Y_4^0(\theta_{\rho'}, \varphi_{\rho'})\, d\tau_{ext} = \frac{\pi}{16384\rho^4\rho'^4}\Big[8960\rho'^8 + 1280\rho'^6\left(4\rho^2 - 7r_{23}^2\right) \\ -80\rho'^2\left(r_{23}^2 - 4\rho^2\right)^2\left(7r_{23}^2 - 4\rho^2\right) + 35\left(r_{23}^2 - 4\rho^2\right)^4 \\ +96\rho'^4\left(48\rho^4 + 35r_{23}^4 - 120\rho^2 r_{23}^2\right)\Big]\end{aligned} \tag{A.33}$$

$$\begin{aligned}\int_{\tau_{ext}} Y_5^0(\theta_\rho, \varphi_\rho) Y_5^0(\theta_{\rho'}, \varphi_{\rho'})\, d\tau_{ext} = \frac{\pi}{131072\rho^5\rho'^5}\Big[64512\rho'^{10} - 8960\rho'^8\left(9r_{23}^2 - 4\rho^2\right) \\ +140\rho'^2\left(r_{23}^2 - 4\rho^2\right)^3\left(9r_{23}^2 - 4\rho^2\right) - 63\left(r_{23}^2 - 4\rho^2\right)^5 \\ +1920\rho'^6\left(16\rho^4 + 21r_{23}^4 - 56\rho^2 r_{23}^2\right) \\ -480\rho'^4(r_{23} - 2\rho)(2\rho + r_{23})\left(16\rho^4 + 21r_{23}^4 - 56\rho^2 r_{23}^2\right)\Big]\end{aligned} \tag{A.34}$$

B

Extra Derivations

THIS Appendix mainly contains short derivations and equations that are not critical to understanding the main results but are nonetheless needed for this work.

B.1 Spherical Functions

This section gives the spherical harmonics (Table B.1), spherical Bessel functions (Table B.2), and spherical Neumann functions (Table B.3) through $\ell = 5$ for easier reference. These were all obtained using the appropriate functions in *Mathematica* [239]. Most sources [135, 240] give these for $\ell \leq 2$.

B.2 ρ and ρ' Definitions

From equation 2.1 of Peter Van Reeth's thesis [95] and Armour and Humberston's paper [55],

$$\boldsymbol{\rho} = \frac{1}{2}\left(\boldsymbol{r}_1 + \boldsymbol{r}_2\right). \tag{B.1}$$

By switching coordinates 2 and 3, we have

$$\boldsymbol{\rho}' = \frac{1}{2}\left(\boldsymbol{r}_1 + \boldsymbol{r}_3\right). \tag{B.2}$$

In the original coordinate system (Figure A.1),

$$\begin{aligned} \boldsymbol{r}_1 &= \left(r_1 \sin\theta_1 \cos\varphi_1, r_1 \sin\theta_1 \sin\varphi_1, r_1 \cos\theta_1\right) \\ \boldsymbol{r}_3 &= \left(r_3 \sin\theta_3 \cos\varphi_3, r_3 \sin\theta_3 \sin\varphi_3, r_3 \cos\theta_3\right) \end{aligned} \tag{B.3}$$

Partial Wave	$Y_\ell^0(\theta,\phi)$
S-Wave	$\frac{1}{\sqrt{4\pi}}$
P-Wave	$\sqrt{\frac{3}{4\pi}}\cos\theta$
D-Wave	$\sqrt{\frac{5}{16\pi}}(3\cos^2\theta-1)$
F-Wave	$\sqrt{\frac{7}{16\pi}}\left(5\cos^3\theta-3\cos\theta\right)$
G-Wave	$\sqrt{\frac{9}{256\pi}}\left(35\cos^4\theta-30\cos^2\theta+3\right)$
H-Wave	$\sqrt{\frac{11}{256\pi}}\left(63\cos^5\theta-70\cos^3\theta+15\cos\theta\right)$

Table B.1: Spherical harmonics for partial waves $\ell = 0$ through 5

Partial Wave	$j_\ell(z)$
S-Wave	$\frac{\sin(\kappa\rho)}{\kappa\rho}$
P-Wave	$\frac{\sin z}{z^2}-\frac{\cos z}{z}$
D-Wave	$\left(\frac{3}{z^3}-\frac{1}{z}\right)\sin z-\frac{3}{z^2}\cos z$
F-Wave	$\frac{\left(z^2-15\right)\cos z}{z^3}-\frac{3\left(2z^2-5\right)\sin z}{z^4}$
G-Wave	$\frac{5\left(2z^2-21\right)\cos z}{z^4}+\frac{\left(z^4-45z^2+105\right)\sin z}{z^5}$
H-Wave	$\frac{15\left(z^4-28z^2+63\right)\sin z}{z^6}+\frac{\left(-z^4+105z^2-945\right)\cos z}{z^5}$

Table B.2: Spherical Bessel functions for partial waves $\ell = 0$ through 5

Partial Wave	$n_\ell(z)$
S-Wave	$-\frac{\cos z}{z}$
P-Wave	$-\frac{\cos z}{z^2} - \frac{\sin z}{z}$
D-Wave	$-\left(\frac{3}{z^3} - \frac{1}{z}\right)\cos z - \frac{3}{z^2}\sin z$
F-Wave	$\frac{3\left(2z^2-5\right)\cos z}{z^4} + \frac{\left(z^2-15\right)\sin z}{z^3}$
G-Wave	$\frac{5\left(2z^2-21\right)\sin z}{z^4} + \frac{\left(-z^4+45z^2-105\right)\cos z}{z^5}$
H-Wave	$\frac{\left(-z^4+105z^2-945\right)\sin z}{z^5} - \frac{15\left(z^4-28z^2+63\right)\cos z}{z^6}$

Table B.3: Spherical Neumann functions for partial waves $\ell = 0$ through 5

In the rotated coordinate system (Figure A.2),

$$\begin{aligned} \boldsymbol{r}_1 &= (0, 0, r_1) \\ \boldsymbol{r}_3 &= (r_3 \sin\theta_{13} \cos\varphi_{13}, r_3 \sin\theta_{13} \sin\varphi_{13}, r_3 \cos\theta_{13}) \end{aligned} \tag{B.4}$$

$$\begin{aligned} |r_1 + r_3|^2 &= r_3^2 \sin^2\theta_{13} \cos^2\varphi_{13} + r_3^2 \sin^2\theta_{13} \sin^2\varphi_{13} + (r_1 + r_3\cos\theta_{13})^2 \\ &= r_3^2 \sin^2\theta_{13} + r_1^2 + r_3^2 \cos^2\theta_{13} + 2r_1 r_3 \cos\theta_{13} \\ &= r_1^2 + r_3^2 + 2r_1 r_3 \cos\theta_{13}. \end{aligned} \tag{B.5}$$

Also, using the law of cosines,

$$r_{13}^2 = r_1^2 + r_3^2 - 2r_1 r_3 \cos\theta_{13} \tag{B.6}$$

Substituting Equation (B.6) into Equation (B.5) gives

$$|r_1 + r_3|^2 = 2\left(r_1^2 + r_3^2\right) - r_{13}^2. \tag{B.7}$$

From Equations (B.2) and (B.7),

$$\rho' = \frac{1}{2}\left[2\left(r_1^2 + r_3^2\right) - r_{13}^2\right]^{\frac{1}{2}}. \tag{B.8}$$

Similarly,

$$\rho = \frac{1}{2}\left[2\left(r_1^2 + r_2^2\right) - r_{12}^2\right]^{\frac{1}{2}}. \tag{B.9}$$

B.3 Perimetric Coordinates

Perimetric coordinates are used for the long-long integrations in the S-wave code. If perimetric coordinates are used for r_1, r_2 and r_{12}, then these are defined by [55]

$$\begin{aligned} x &= r_1 + r_2 - r_{12} \\ y &= r_2 + r_{12} - r_1 \\ z &= r_{12} + r_1 - r_2. \end{aligned} \tag{B.10}$$

These can alternately be written as

$$\begin{aligned} r_1 &= \frac{x+z}{2} \\ r_2 &= \frac{x+y}{2} \\ r_{12} &= \frac{y+z}{2}. \end{aligned} \tag{B.11}$$

From Equation (A.8), the volume element after integration over the external angles is

$$d\tau = 8\pi^2 dr_1 r_2 dr_2 r_3 dr_3 r_{12} dr_{12} r_{13} dr_{13} d\varphi_{23}. \tag{B.12}$$

We need to perform a change of variables to use perimetric coordinates for r_1, r_2 and r_{12}. The Jacobian is

$$J(x,y,z) = \begin{vmatrix} \frac{\partial r_1}{\partial x} & \frac{\partial r_1}{\partial y} & \frac{\partial r_1}{\partial z} \\ \frac{\partial r_2}{\partial x} & \frac{\partial r_2}{\partial y} & \frac{\partial r_2}{\partial z} \\ \frac{\partial r_{12}}{\partial x} & \frac{\partial r_{12}}{\partial y} & \frac{\partial r_{12}}{\partial z} \end{vmatrix} = \begin{vmatrix} \frac{1}{2} & 0 & \frac{1}{2} \\ \frac{1}{2} & \frac{1}{2} & 0 \\ 0 & \frac{1}{2} & \frac{1}{2} \end{vmatrix} = \frac{1}{4}. \tag{B.13}$$

This gives a transformed volume element of

$$d\tau = 2\pi^2 r_2 r_3 r_{12} r_{13} dx\, dy\, dz\, dr_3\, dr_{13}\, d\varphi_{23}. \tag{B.14}$$

The limits for each of the perimetric coordinates are 0 to ∞.

B.4 Spherical Bessel Derivatives

B.4.1 First Derivative

From Abramowitz and Stegun [240, p.437],

$$j_\ell(z) = z^{-1}\left[P(\ell+\tfrac{1}{2},z)\sin(z-\tfrac{1}{2}\ell\pi) + Q(\ell+\tfrac{1}{2},z)\cos(z-\tfrac{1}{2}\ell\pi)\right] \tag{B.15a}$$

$$n_\ell(z) = (-1)^{\ell+1} z^{-1}\left[P(\ell+\tfrac{1}{2},z)\cos(z+\tfrac{1}{2}\ell\pi) - Q(\ell+\tfrac{1}{2},z)\sin(z+\tfrac{1}{2}\ell\pi)\right]. \tag{B.15b}$$

where

$$P(\ell+\tfrac{1}{2},z) = 1 - \frac{\ell+2!}{2!\Gamma(\ell-1)}(2z)^{-2} + \dots \tag{B.16a}$$

$$Q(\ell+\tfrac{1}{2},z) = \frac{\ell+1!}{1!\Gamma(\ell)}(2z)^{-1} - \frac{n+3!}{3!\Gamma(\ell-2)}(2z)^{-3} + \dots \tag{B.16b}$$

Using *Mathematica* with these expansions, we get

$$j_\ell(z) = \frac{\sin(z-\frac{1}{2}\ell\pi)}{z} + \dots \tag{B.17a}$$

$$n_\ell(z) = \frac{(-1)^{\ell+1}\cos(z+\frac{1}{2}\ell\pi)}{z} + \dots \tag{B.17b}$$

and

$$j_\ell{}'(z) = \frac{\cos(z-\frac{1}{2}\ell\pi)}{z} + \dots \tag{B.18a}$$

$$n_\ell{}'(z) = \frac{(-1)^{\ell+2}\sin(z+\frac{1}{2}\ell\pi)}{z} + \dots \tag{B.18b}$$

In a more general format than that of Abramowitz and Stegun [240, p.73],

$$\cos\left(z-\frac{\ell\pi}{2}\right) = \begin{cases} (-1)^{\ell/2}\cos z & \text{if } \ell \text{ is even} \\ (-1)^{(\ell-1)/2}\sin z & \text{if } \ell \text{ is odd} \end{cases} \tag{B.19}$$

and

$$\sin\left(z-\frac{\ell\pi}{2}\right) = \begin{cases} (-1)^{\ell/2}\sin z & \text{if } \ell \text{ is even} \\ (-1)^{(\ell+1)/2}\cos z & \text{if } \ell \text{ is odd} \end{cases}. \tag{B.20}$$

Also,

$$\cos\left(z+\frac{\ell\pi}{2}\right) = \begin{cases} (-1)^{\ell/2}\cos z & \text{if } \ell \text{ is even} \\ (-1)^{(\ell+1)/2}\sin z & \text{if } \ell \text{ is odd} \end{cases} \tag{B.21}$$

and

$$\sin\left(z+\frac{\ell\pi}{2}\right) = \begin{cases} (-1)^{\ell/2}\sin z & \text{if } \ell \text{ is even} \\ (-1)^{(\ell-1)/2}\cos z & \text{if } \ell \text{ is odd} \end{cases}. \tag{B.22}$$

Using these with Equations (B.17a) and (B.18a), we see that to first order, there is a relationship between these functions and their derivatives given by

$$j_\ell{}'(z) \approx -n_\ell(z) \tag{B.23a}$$

$$n_\ell{}'(z) \approx j_\ell(z). \tag{B.23b}$$

This allows us to write the gradient of $\widetilde{S}_\ell$ and $\widetilde{C}_\ell$ for arbitrary ℓ to first order in Equation (3.34).

B.4.2 Second Derivative

The output we get from the *Mathematica* notebook "First Partial Waves LS General.nb" [1, 4] is

$$\frac{\nabla_\rho^2 \left[Y_\ell^0(\theta_\rho, \varphi_\rho)\, j_\ell(\kappa\rho) \right]}{Y_\ell^0(\theta_\rho, \varphi_\rho)\, j_\ell(\kappa\rho)} = \frac{(n + n^2 - \kappa^2\rho^2) P_\ell(\cos\theta) + 2\cot\theta\, P_\ell^1(\cos\theta) + P_\ell^2(\cos\theta)}{\rho^2 P_\ell(\cos\theta)}. \quad \text{(B.24)}$$

From Ref. [241], a recurrence relation for the associated Legendre polynomials is

$$P_\ell^{\mu+1}(z) - [\mu(\mu-1) - \ell(\ell+1)]\, P_\ell^{\mu-1}(z) + \frac{2\mu z}{\sqrt{1-z^2}} P_\ell^\mu(z) = 0. \quad \text{(B.25)}$$

Note that other books [240, 242] give slightly different forms of this recurrence relation. If we set $\mu = 1$ and $z = \cos\theta$, this becomes

$$P_\ell^2(\cos\theta) + \left(\ell^2 + \ell\right) P_\ell^0(z) + \frac{2\cos\theta}{\sin\theta} P_\ell^1(\cos\theta) = 0. \quad \text{(B.26)}$$

Using the definition of cot and solving for $\left(\ell^2 + \ell\right) P_\ell^0(z) = \left(\ell^2 + \ell\right) P_\ell(\cos\theta)$,

$$\left(\ell^2 + \ell\right) P_\ell(\cos\theta) = -P_\ell^2(\cos\theta) - 2\cot\theta\, P_\ell^1(\cos\theta)\,. \quad \text{(B.27)}$$

Substituting this back into Equation (B.24), we get cancellations with the associated Legendre polynomials and see that $Y_\ell^0(\theta_\rho, \varphi_\rho)\, j_\ell(\kappa\rho)$ is an eigenfunction of ∇_ρ^2 with eigenvalue $-\kappa^2$:

$$\nabla_\rho^2 \left[Y_\ell^0(\theta_\rho, \varphi_\rho)\, j_\ell(\kappa\rho) \right] = \frac{(-\kappa^2\rho^2) P_\ell(\cos\theta)}{\rho^2 P_\ell(\cos\theta)} = -\kappa^2\, Y_\ell^0(\theta_\rho, \varphi_\rho)\, j_\ell(\kappa\rho). \quad \text{(B.28)}$$

B.5 ${}_2F_1$ Recursion Relation

The backwards recursion relation for the hypergeometric function is used in the short-range code (Section 4.1). This is given in Refs. [59, 153] as

$${}_2F_1(1, a; c; z) = 1 + \left(\frac{a}{c}\right) z\ {}_2F_1(1, a+1; c+1; z)\,. \quad \text{(B.29)}$$

From Abramowitz and Stegun [240], the definition of the hypergeometric function is given by

$${}_2F_1(\alpha, \beta; \gamma; z) = 1 + \sum_{n=1}^{\infty} \frac{(\alpha)_n \cdot (\beta)_n}{(\gamma)_n} \frac{z^n}{n!}, \quad \text{(B.30)}$$

where $(x)_n$ is the Pochhammer symbol given by [240]

$$(x)_n \equiv \frac{\Gamma(x+n)}{\Gamma(x)} = x(x+1)\cdots(x+n-1) \quad \text{(B.31)}$$

with $(x)_0 = 1$. A special case is $(x)_1 = n!$, where $n!$ is the factorial.

Using the above definition of the Pochhammer symbol, we can easily see that

$$(x+1)_n = \frac{(x+n)}{(x)} \cdot (x)_n = \frac{(x)_{n+1}}{x}. \tag{B.32}$$

From Equations (B.30) and (B.32),

$$\begin{aligned} {}_2F_1(1, a+1; c+1; z) &= 1 + \sum_{n=1}^{\infty} \frac{(1)_n \cdot (a+1)_n}{(c+1)_n} \frac{z^n}{n!} = 1 + \sum_{n=1}^{\infty} \frac{(a+1)_n}{(c+1)_n} z^n \\ &= 1 + \left(\frac{c}{a}\right) \sum_{n=1}^{\infty} \frac{(a)_{n+1}}{(c)_{n+1}} z^n = 1 + \left(\frac{c}{a}\right) \sum_{n=2}^{\infty} \frac{(a)_n}{(c)_n} z^{n-1}. \end{aligned} \tag{B.33}$$

Multiplying by $\left(\frac{c}{a}\right) z$, we now have

$$\left(\frac{c}{a}\right) z \; {}_2F_1(1, a+1; c+1; z) = \left(\frac{c}{a}\right) z + \sum_{n=2}^{\infty} \frac{(a)_n}{(c)_n} z^n = \sum_{n=1}^{\infty} \frac{(a)_n}{(c)_n} z^n. \tag{B.34}$$

From the definition in Equation (B.30),

$${}_2F_1(1, a; c; z) = 1 + \sum_{n=1}^{\infty} \frac{(a)_n}{(c)_n} z^n, \tag{B.35}$$

which, when combined with Equation (B.34), gives the final result of

$${}_2F_1(1, a; c; z) = 1 + \left(\frac{a}{c}\right) z \; {}_2F_1(1, a+1; c+1; z). \tag{B.36}$$

B.6 Shielding Function

The spherical Neumann functions, $n_\ell(\kappa\rho)$, in C_ℓ go to $-\infty$ at the origin, and we remove this singularity with the shielding function. The shielding function given by Equation (3.7), $f_\ell(\rho) = \left[1 - \mathrm{e}^{-\mu\rho}\left(1 + \frac{\mu}{2}\rho\right)\right]^{m_\ell}$, is slightly different than earlier work [57, 58] on Ps-H scattering, which used $f(\rho) = (1 - \mathrm{e}^{-\lambda\rho})^3$.

This work is based on notes from Van Reeth [171] for the S-wave shielding function. We want to have C_ℓ behaving similar to S_ℓ at the origin. To accomplish this, we take a series expansion of both to see what the dominant terms are. To more easily see the behavior, we only take expansions of the spherical Bessel and Neumann functions for the S-wave. For S_0, the series expansion of j_0 is

$$j_0(\kappa\rho) \sim 1 - \frac{\kappa^2\rho^2}{6} + \frac{\kappa^4\rho^4}{120} + \mathcal{O}(\rho^5). \tag{B.37}$$

For C_0, the series expansion of n_0 is

$$n_0(\kappa\rho) \sim -\frac{1}{\kappa\rho} + \frac{\kappa\rho}{2} - \frac{\kappa^3\rho^3}{24} + \mathcal{O}(\rho^4). \tag{B.38}$$

The singular nature at the origin is easily seen by the first term. To have $C_0 \sim S_0$ at the origin, the shielding function needs to change the leading term to a constant. If we choose a shielding function of the form $[1 - \mathrm{e}^{-\mu\rho}(1 + a\rho)]$, the expansion at the origin of this multiplied by the spherical Neumann function is

$$n_0(\kappa\rho)\left[1 - \mathrm{e}^{-\mu\rho}(1 + a\rho)\right] \sim -\frac{\mu - a}{\kappa} - \frac{\left(a\mu - \frac{\mu^2}{2}\right)\rho}{\kappa} + \left(\frac{1}{2}\kappa(\mu - a) - \frac{\mu^2 - 3a\mu^2}{6\kappa}\right)\rho^2 + \dots \tag{B.39}$$

This is no longer singular, but it has a ρ term, so if we set $a = \frac{\mu}{2}$, the second term disappears, leaving us with

$$n_0(\kappa\rho)\left[1 - \mathrm{e}^{-\mu\rho}\left(1 + \frac{\mu}{2}\rho\right)\right] \sim -\frac{\mu}{2\kappa} + \left(\frac{\kappa\mu}{4} + \frac{\mu^3}{12\kappa}\right)\rho^2 + \dots . \tag{B.40}$$

This shows that with the choice of shielding function in Equation (3.7), we have C_0 behaving similar to S_0 at the origin.

The *Mathematica* notebook "Shielding Factor.nb" found on the GitHub page [1] shows these expansions and the expansions for the P-wave and D-wave. We normally choose $m_\ell = (2\ell + 1)$, but for the D-wave, we used $m_\ell = 7$ when we were trying to improve the convergence, which ultimately did not give improved results over $m_\ell = 5$. This notebook also shows the first and second derivatives of the shielding function given in Equations (3.107) and (3.108).

This notebook also has interactive graphs that show how the shielding function with and without the spherical Neumann function behaves with differing m_ℓ, μ, and ℓ values. Figure B.1 shows that as m_ℓ increases for fixed μ of 0.9, it takes a larger ρ before C_ℓ becomes significant. Figure B.2 keeps m_ℓ constant at 7 and varies μ. This figure shows that smaller μ values give a strong contribution for C_ℓ. Table C.13 shows the μ and m_ℓ values we use for each partial wave.

B.7 D-Wave Mixed Symmetry Terms

This derivation proves Equation (7.20). Using Equation (7.19) and substituting the appropriate spherical harmonics and Clebsch-Gordan coefficients,

$$\psi_{(1,1,2,0)} = \sum_{m=-1}^{+1} Y_{1,m}(\theta_1, \varphi_1) Y_{1,m}(\theta_2, \varphi_2) \langle 1, m; 1, -m, 0 | 2, 0 \rangle$$

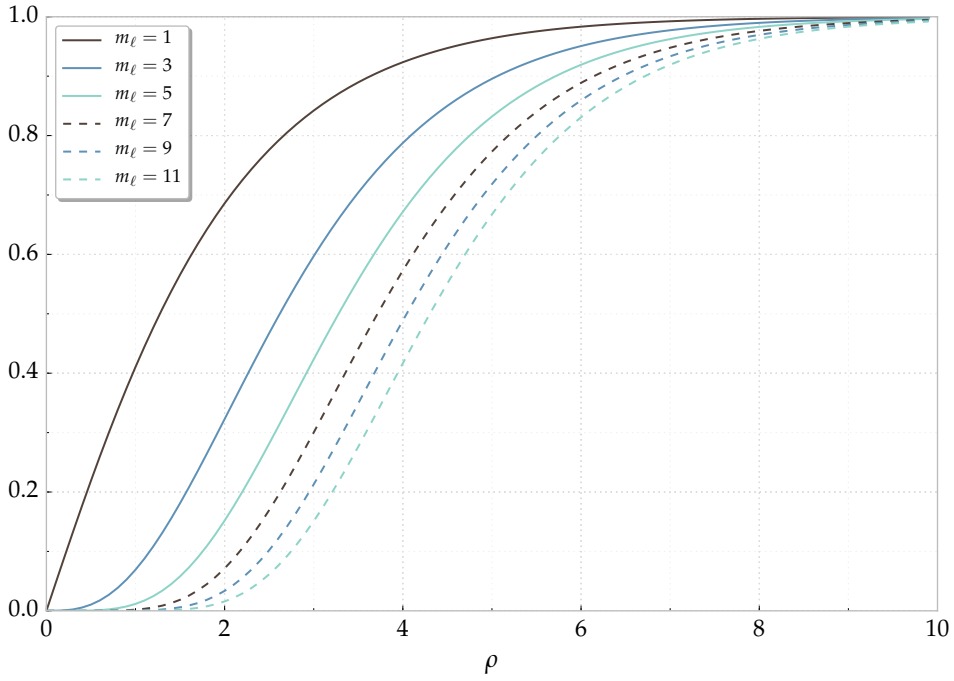

Figure B.1: Shielding function f_ℓ variation with respect to ρ for multiple values of m_ℓ with $\mu = 0.9$

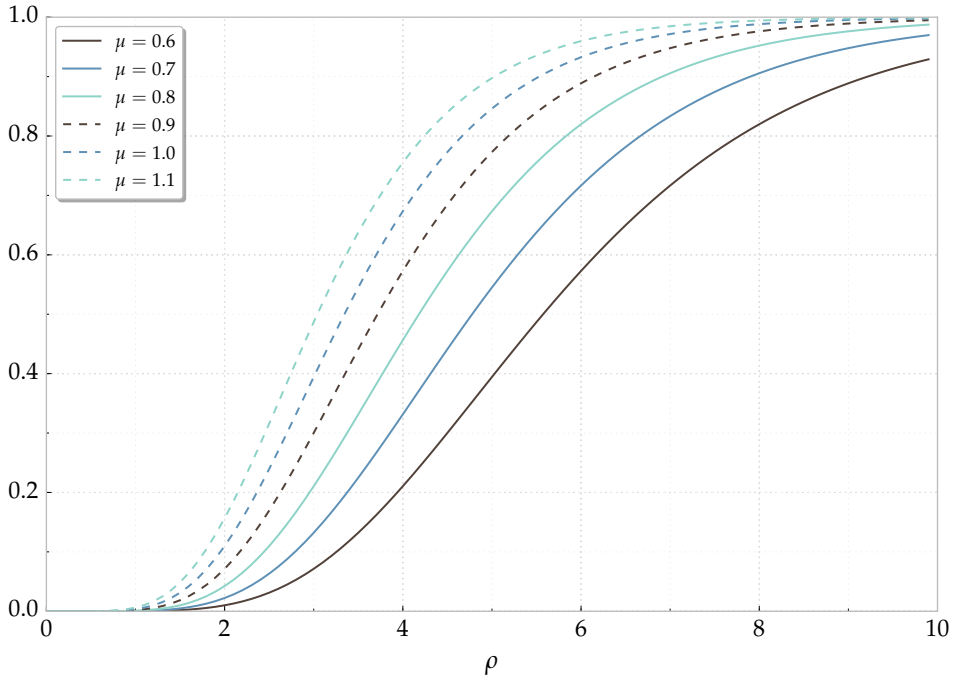

Figure B.2: Shielding function f_ℓ variation with respect to ρ for multiple values of μ with $m_\ell = 7$

$$
\begin{aligned}
&= -\sqrt{\frac{3}{8\pi}}\sin\theta_1\,\mathrm{e}^{-\mathrm{i}\varphi_1}\sqrt{\frac{3}{8\pi}}\sin\theta_2\,\mathrm{e}^{\mathrm{i}\varphi_1}\frac{1}{\sqrt{6}} \\
&\quad + \sqrt{\frac{3}{4\pi}}\cos\theta_1\sqrt{\frac{3}{4\pi}}\sin\theta_2\frac{2}{\sqrt{6}} \\
&\quad - \sqrt{\frac{3}{8\pi}}\sin\theta_1\,\mathrm{e}^{\mathrm{i}\varphi_1}\sqrt{\frac{3}{8\pi}}\sin\theta_2\,\mathrm{e}^{-\mathrm{i}\varphi_1}\frac{1}{\sqrt{6}}. \qquad \text{(B.41)}
\end{aligned}
$$

Using [95, p.192]

$$
\cos\theta_{12} = \sin\theta_1\sin\theta_2\cos(\varphi_1-\varphi_2) + \cos\theta_1\cos\theta_2 \qquad \text{(B.42)}
$$

in Equation (B.41), we obtain Equation (7.20):

$$
\begin{aligned}
\psi_{(1,1,2,0)} &= -\frac{3}{8\pi}\frac{1}{\sqrt{6}}\sin\theta_1\sin\theta_2\cdot 2\cos(\varphi_1-\varphi_2) + \frac{3}{4\pi}\frac{1}{\sqrt{6}}\cdot 2\cos\theta_1\cos\theta_2 \\
&= \frac{3}{4\pi}\frac{1}{\sqrt{6}}\left(3\cos\theta_1\cos\theta_2 - \cos\theta_{12}\right). \qquad \text{(B.43)}
\end{aligned}
$$

B.8 Miscellaneous

The cosine factors present in many of the matrix element equations are easily expressed in terms of r_i and r_{ij} by using the law of cosines [243, p.174]:

$$
\cos\theta_{12} = \frac{r_1^2+r_2^2-r_{12}^2}{2r_1r_2}, \quad \cos\theta_{13} = \frac{r_1^2+r_3^2-r_{13}^2}{2r_1r_3} \quad \text{and} \quad \cos\theta_{23} = \frac{r_2^2+r_3^2-r_{23}^2}{2r_2r_3}. \qquad \text{(B.44)}
$$

This allows us to express all short-short matrix elements in the form needed by the short-short methods described in Section 4.1.

C Extra Numerics

THIS Appendix gives more details than what is provided in Chapter 4 on computations.

C.1 Short-Range Code Nonlinear Parameter Optimization

A powerful property of the Rayleigh-Ritz variational method is the ability to systematically improve the wavefunction to lower the upper bound on the energy. By either adding terms to the expansion in Equation (2.1a) or changing the nonlinear parameters α, β and γ, the energy can be reduced and a possible minimum found. This is a three-dimensional optimization problem, and we tried multiple methods for the nonlinear parameter optimization.

C.1.1 Broyden's Method

We used Broyden's method [244], which can solve for all three nonlinear parameters simultaneously. This was more stable than the 1-D Newton method. The second Broyden's method, sometimes referred to as the "bad Broyden's method" was used here. As Kvaalen points out, this method is perfectly usable and can be faster than the first Broyden's method [245]. Tables C.1 and C.2 show the nonlinear parameters used for ^{3}S and ^{1}P. All other partial waves used the simplex method described in Appendix C.1.2. This is because I already had a number of results for ^{3}S and ^{1}P, so running everything again for simplex-optimized nonlinear parameters was unnecessary. For ^{3}S, we were able to use even more terms than we could use for ^{1}S Table C.13, and we were able to use the same number of terms for ^{1}P and ^{3}P.

ω	α	β	γ
1	0.264440	0.831645	0.498871
2	0.356175	0.452426	0.829591
3	0.347611	0.467298	0.814971
4	0.323300	0.333783	0.974653

Table C.1: Broyden optimized ^{3}S nonlinear parameters

ω	α	β	γ
1	0.47767	0.50273	0.97498
2	0.48253	0.49342	0.96874
3	0.42803	0.43099	0.98993
4	0.39740	0.37617	0.96205

Table C.2: Broyden optimized ^{1}P nonlinear parameters

ω	α	β	γ
0	0.30226	0.45479	1.07962
1	0.53592	0.59453	1.02206
2	0.57450	0.65222	0.98020
3	0.58966	0.63150	0.97397
4	0.58493	0.60995	0.98610
5	0.58691	0.58045	1.03321

Table C.3: Simplex optimized ^{1}S nonlinear parameters

Partial Wave	α	β	γ
^{3}P	0.310	0.311	0.995
^{1}D	0.359	0.368	0.976
^{3}D	0.356	0.365	0.976

Table C.4: Simplex optimized nonlinear parameters for the P-wave and D-wave

C.1.2 Simplex Method

Broyden's method was more stable than Newton's method for this work, but I also tried the `gsl_multimin_fminimizer_nmsimplex` routine from the GNU Scientific Library, which is an implementation of the simplex method [195, 246]. This was the most stable of the three methods tried to optimize α, β, and γ simultaneously. I normally stopped at $\omega = 5$ for the optimization, and the S-wave singlet runs are shown in Table C.3. Table C.4 has the optimized nonlinear parameters used for the P-wave and D-wave. Due to the slowness of the general short-range code (see Section 8.2), the F-wave through G-wave just use the parameters $\alpha = 0.5$, $\beta = 0.6$, and $\gamma = 1.1$.

With the work on the second formalism for the P-wave Appendix C.1.3, it was also possible to use the simplex method to optimize all 6 nonlinear parameters simultaneously instead of having to optimize each symmetry separately.

C.1.3 P-Wave Nonlinear Parameter Optimization

Using the simplex method described in Appendix C.1.2, we optimized the nonlinear parameters for both the first and second formalisms. Tables C.5 and C.6 show the results of these optimizations in the second and third columns. We also let each symmetry have its own set of nonlinear parameters for each symmetry in the fourth and fifth columns. This was inspired by the work of Yan and Ho [92], where they used 5 different sets of nonlinear parameters to calculate the PsH ground state energy.

From Tables C.5 and C.6, we see that lower energy eigenvalues are always obtained with the first formalism with 1 set versus the second formalism with 1 set. Likewise, the first formalism has lower energy eigenvalues than the second formalism when both have 2 sets. For $\omega \geq 2$, the first formalism with 1 set even has lower energy eigenvalues than the second symmetry with 2 sets. We had trouble obtaining phase shifts with two different sets of nonlinear parameters due to increased linear dependence, but for higher ω, we also see that the energy does not change much. Using more than one set of nonlinear parameters could be explored further in future work, and we have done preliminary investigation into this for the S-wave.

ω	1st formalism / 1 set	2nd formalism / 1 set	1st formalism / 2 sets	2nd formalism / 2 sets
			0.5341, 0.4536, 1.0139	0.5668, 0.4686, 0.9787
1	0.4776, 0.5027, 0.9749	0.4571, 0.5700, 0.9266	0.3792, 0.5455, 0.9816	0.6777, 0.8587, 0.4813
	-0.666819968640	**-0.663226610680**	**-0.670015702237**	**-0.665355147531**
			0.5270, 0.4394, 1.0036	0.4497, 0.5039, 0.9459
2	0.4825, 0.4934, 0.9687	0.4734, 0.5162, 0.9584	0.4087, 0.5213, 0.9704	0.3963, 1.0233, 0.4327
	-0.700681070987	**-0.699190666285**	**-0.701936448530**	**-0.700245066225**
			0.4632, 0.3918, 1.001	0.4653, 0.4512, 0.9905
3	0.4297, 0.4337, 0.9808	0.4317, 0.4564, 0.9621	0.3844, 0.4620, 0.9740	0.8745, 0.9796, 0.4957
	-0.718093418924	**-0.717282613790**	**-0.718548496648**	**-0.717931026880**
			0.3954, 0.3505, 0.9997	0.3744, 0.3746, 0.9537
4	0.3740, 0.3744, 0.9898	0.3803, 0.3951, 0.9648	0.3478, 0.39493, 0.9798	0.4078, 0.9010, 0.3351
	-0.727918723553	**-0.727281885394**	**-0.728067443345**	**-0.727981667586**
			0.3401, 0.3181, 0.9983	0.3373, 0.3390, 0.9635
5	0.3293, 0.3289, 0.9939	0.3371, 0.3468, 0.9680	0.3174, 0.3397, 0.9880	0.4299, 0.9452, 0.3023
	-0.734233160953	**-0.733680013812**	**-0.734264232997**	**-0.734219573964**

Table C.5: Simplex ^{1}P-Wave Short-Range Optimization

ω	1st formalism / 1 set	2nd formalism / 1 set	1st formalism / 2 sets	2nd formalism / 2 sets
			0.3832, 0.2911, 0.9894	0.3367, 0.3436, 0.9517
1	0.3316, 0.3535, 0.9956	0.3302, 0.3540, 0.9909	0.2854, 0.3959, 1.0112	0.7606, 0.6593, 0.2304
	-0.624190839847	**-0.622936676609**	**-0.629448013148**	**-0.626442778437**
			0.4056, 0.3294, 0.9799	0.3623, 0.3952, 0.9716
2	0.3664, 0.3750, 0.9900	0.3679, 0.3896, 0.9753	0.3226, 0.4097, 1.0078	0.1961, 0.7724, 0.7692
	-0.674819577647	**-0.672880514312**	**-0.676837948726**	**-0.673438894110**
			0.3874, 0.3314, 0.9823	0.3557, 0.3794, 0.9593
3	0.3585, 0.3613, 0.9911	0.3639, 0.3810, 0.9690	0.3257, 0.3881, 1.0036	0.2080, 0.5994, 0.7711
	-0.704764841366	**-0.703191879865**	**-0.705411707053**	**-0.703452729525**
			0.3539, 0.3192, 0.9879	0.3392, 0.3502, 0.9789
4	0.3357, 0.3366, 0.9936	0.3427, 0.3554, 0.9680	0.3162, 0.3539, 0.9989	0.1624, 0.6564, 0.9512
	-0.721696022987	**-0.720513417195**	**-0.721859567659**	**-0.720596381145**
			0.3184, 0.3038, 0.9935	0.3177, 0.3271, 0.9769
5	0.3106, 0.3109, 0.9953	0.3182, 0.3275, 0.9682	0.3025, 0.3186, 0.9966	0.1142, 0.4274, 1.1088
	-0.731463030326	**-0.730592482596**	**-0.731486455300**	**-0.730615490923**

Table C.6: Simplex ^{3}P Short-Range Optimization

C.1.4 D-Wave Nonlinear Parameter Optimization

The comparison to the CC results [70, 72] in Table 7.1 and Figure 7.1 for the ^{1}D-wave is reasonable, with the CC results below the complex Kohn results at $\kappa = 0.7$. For ^{3}D, the CC results are much higher, as can be seen in the inset in Figure 7.1. The ^{1}D phase shifts are small, so their overall contribution to the integrated cross section is small. This lead us to investigate whether the phase shifts could be improved by a better selection of the short-range nonlinear parameters. If the phase shifts were fully converged, varying the nonlinear parameters should have little effect on their values. Both Van Reeth [171] and I investigated this.

Using the simplex method described in Appendix C.1.2, we obtained a set of nonlinear parameters for ^{1}D and ^{3}D in Table C.4. We realized when calculating the phase shifts however that these were more sensitive to the values of the nonlinear parameters than the S-wave and P-wave, especially for ^{3}D. This is likely due to the short-range terms trying to make up for the missing mixed symmetry terms, and for higher partial waves, the interaction region is more extended. We performed some manual optimization of the nonlinear parameters for two κ values to try to improve the phase shifts.

For this investigation, we chose κ values in two different regions: one at lower κ and another at higher κ. After optimization with these, we also checked convergence ratios in the more sensitive resonance region. The $\kappa = 0.1$ choice was made, since this is the lowest value that we report. We chose $\kappa = 0.6$ for the higher κ region, as this gets closer to the Ps(n=2) threshold but is far enough away from the ^{1}D resonance to avoid sensitivity of the nonlinear parameters due to the resonance.

For these variations, we kept γ constant and used $\omega = 4$. From Table C.13, the value of γ was found to be near 1 using the simplex method (Appendix C.1.2) for every partial wave for both the singlet and triplet. An explanation is that the r_3 coordinate represents the electron in H, and $\gamma = 1$ gives the short-range terms multiplied by the H wavefunction given in Equation (1.1) [171]. We used the original nonlinear parameters found by the simplex method and given in Table C.4 as a starting set. For ^{1}D, these are $\alpha = 0.359$, $\beta = 0.368$, and $\gamma = 0.976$. For ^{3}D, these are $\alpha = 0.356$, $\beta = 0.365$, and $\gamma = 0.976$.

For the first variation, we investigated the α nonlinear parameter at $\kappa = 0.1$. We varied α to see its effect on the phase shifts. Figure C.1 shows the results of this variation. There is a maximum in the phase shift in Figure C.1(a) and a large difference between the phase shifts at low and high α. If we decrease α from its value of 0.359, however, from Figure C.1(b), the convergence ratio $R'(4)$, given by Equation (4.23), increases drastically. From this analysis, we had hoped for higher phase shifts, but we have a trade-off between this and reasonable convergence ratios. Due to this, we have kept the nonlinear parameter α at 0.359, which seems to be a reasonable compromise between higher phase shifts and better convergence ratios. This is likely an indication of the amount of numerical instability we have with small phase shifts.

At the higher κ of 0.6, the variation looks very different, as seen in Figure C.2. The maximum is at about $\alpha = 0.6$, and $R'(4)$ is much less than 1. Interestingly, $R'(4)$ decreases

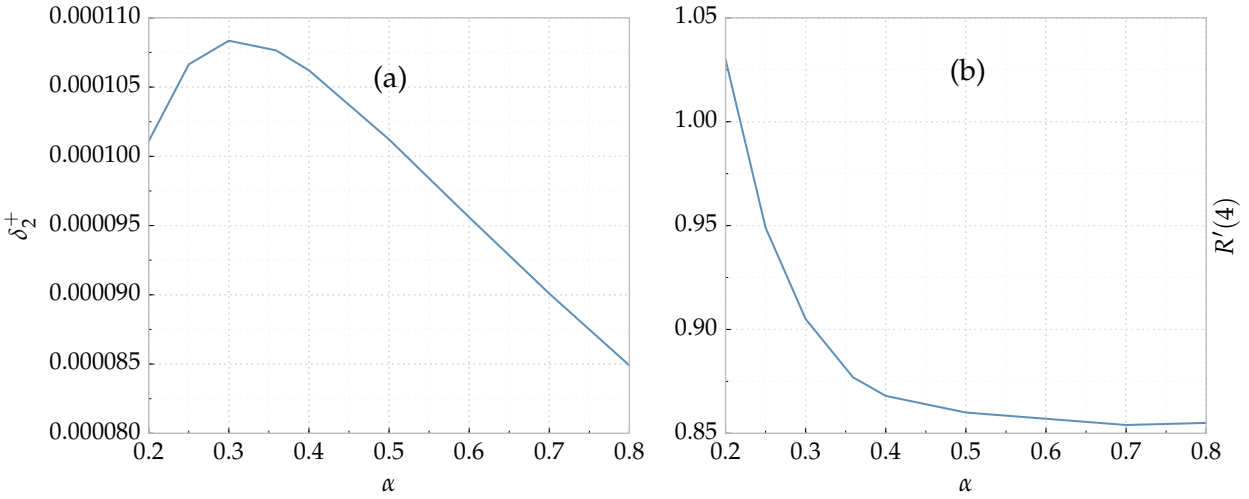

Figure C.1: Phase shifts (a) and convergence ratios (b) for variation of the nonlinear parameter α for ^{1}D at $\kappa = 0.1$

monotonically as α is increased. For $\kappa = 0.6$, it is clear that choosing $\alpha = 0.6$ is much better than the original 0.359.

Starting from the original nonlinear parameters, we also varied β. The β variation looks very similar to the α derivation, but there is a surprising breakdown of the phase shifts when $\beta > 0.6$. At $\beta = 0.7$, δ_2^+ increases significantly, and $R'(4) > 5$. For $\beta = 0.8$, $\delta_2^+ = -2.0694^{-3}$, and $R'(4) = -128.3$, so the phase shifts for large β are obviously not reliable. When β is smaller, we see very similar behavior to that of the α variation in Figure C.1. The convergence ratio increases as β gets too low, and the maximum is around $\beta = 0.3$. Similar to the α variation, we kept the original $\beta = 0.368$ value.

For $\kappa = 0.6$, we see a breakdown when β is large as well. The plot in Figure C.4 shows that we have not hit the maximum δ_2^+ before the phase shifts exhibit breakdown. The α variation appears to be more stable than the β variation from these runs.

The variations for ^{3}D look similar to that of ^{1}D. There are less points in Figure C.5, but we can see that as α is lowered, $R'(4)$ increases, and there is a maximum around $\alpha = 0.3$. Again, we kept the original α of 0.356.

Due to the problems we had with the β variation for ^{1}D and the original α, we did not pursue this for ^{3}D. With these new choices of ^{1,3}D nonlinear parameters for higher κ that use a higher α of 0.6, we also investigated varying β, as shown in Figure C.7 for ^{1}D. Again, the phase shifts are unreliable as β is increased much. The equivalent plots for ^{3}D are in

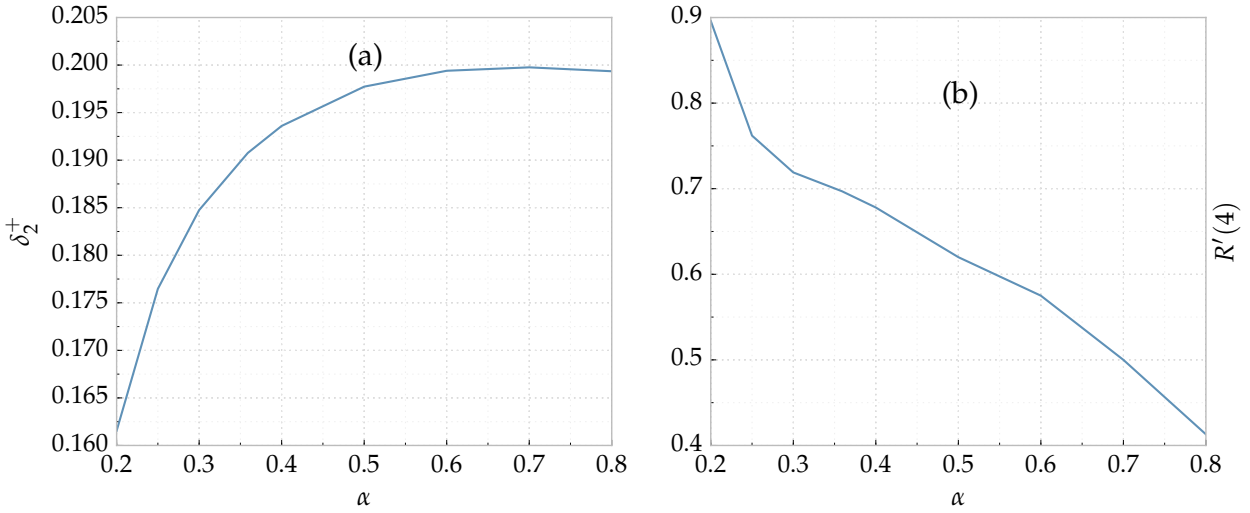

Figure C.2: Phase shifts (a) and convergence ratios (b) for variation of the nonlinear parameter α for ^{1}D at $\kappa = 0.6$

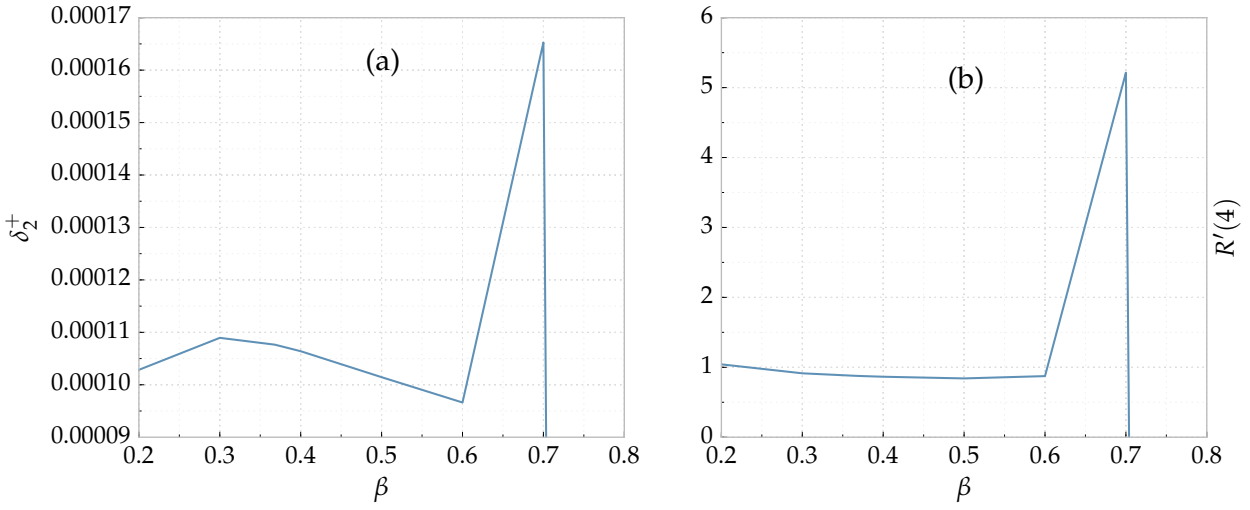

Figure C.3: Phase shifts (a) and convergence ratios (b) for variation of the nonlinear parameter β for ^{1}D at $\kappa = 0.1$

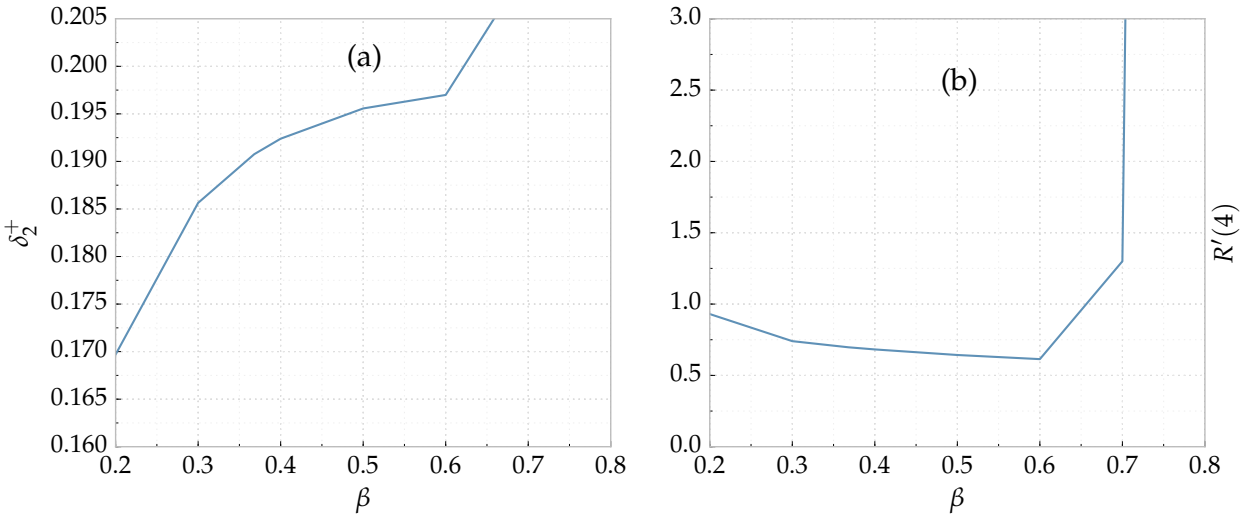

Figure C.4: Phase shifts (a) and convergence ratios (b) for variation of the nonlinear parameter β for ^{1}D at $\kappa = 0.6$

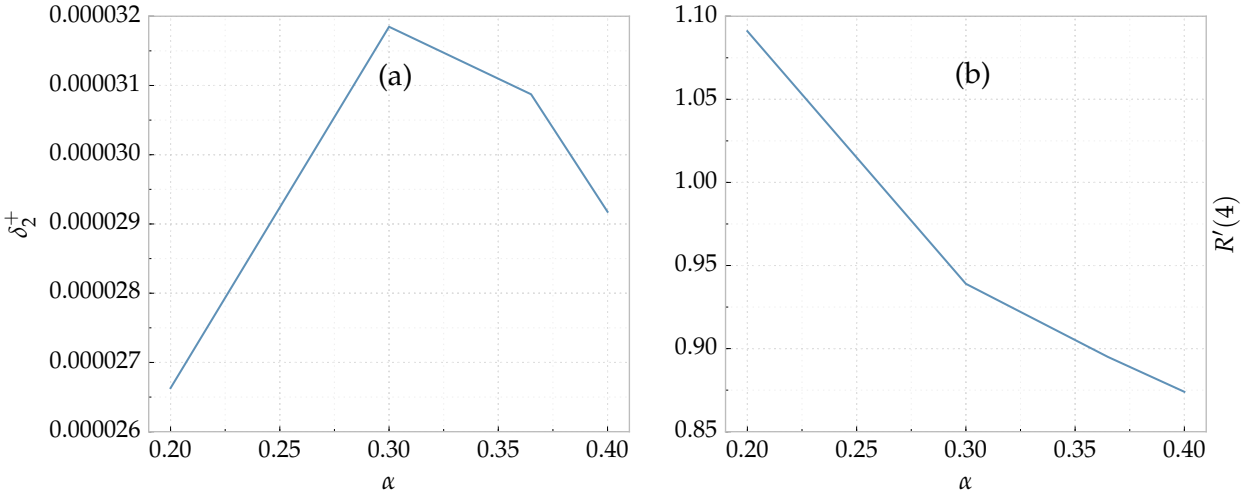

Figure C.5: Phase shifts (a) and convergence ratios (b) for variation of the nonlinear parameter α for ^{3}D at $\kappa = 0.1$

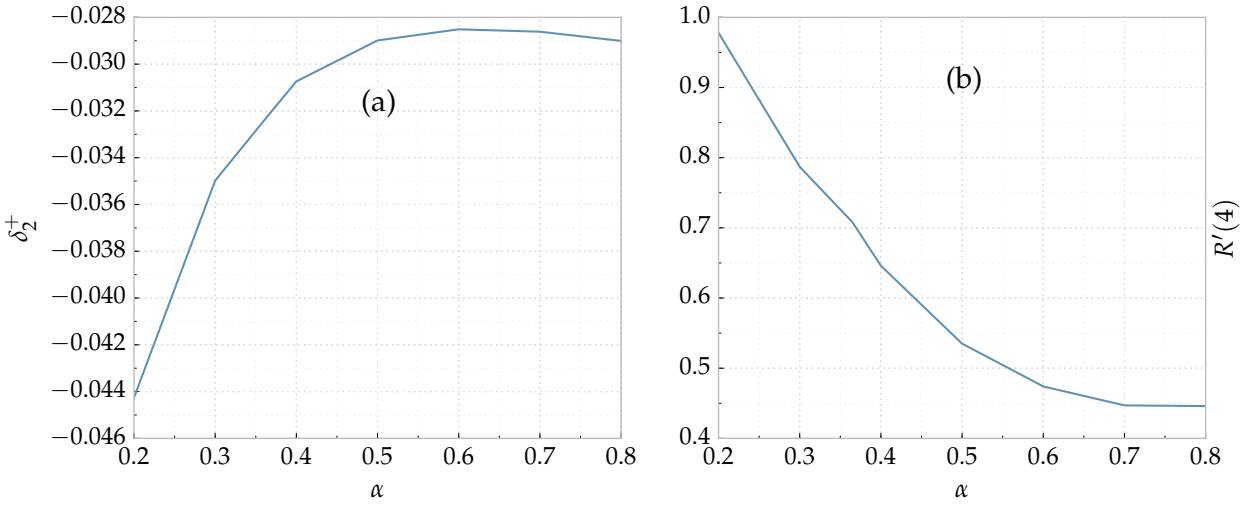

Figure C.6: Phase shifts (a) and convergence ratios (b) for variation of the nonlinear parameter α for ^{3}D at $\kappa = 0.6$

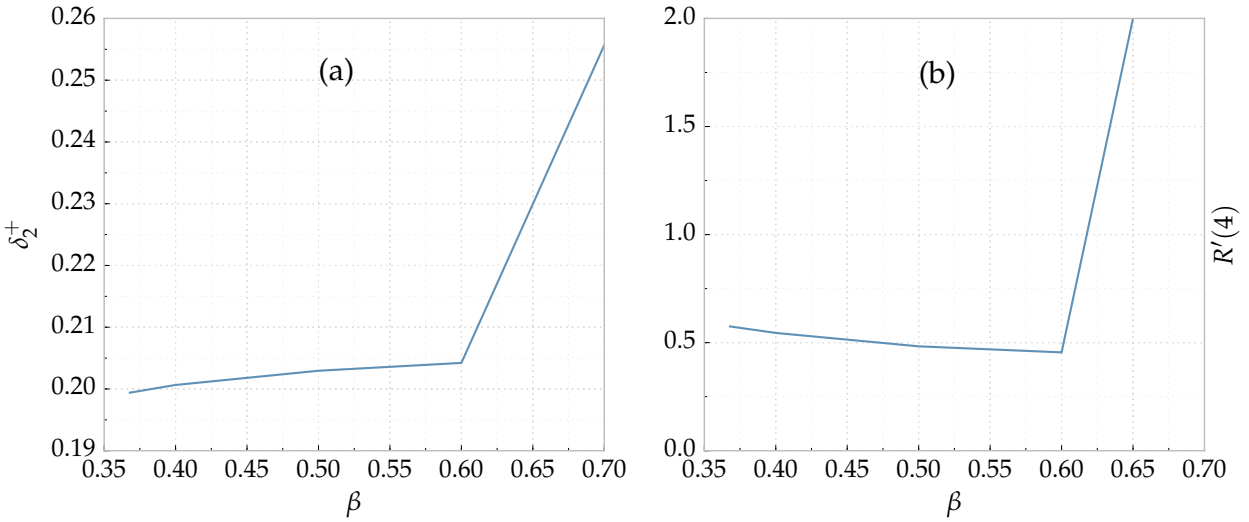

Figure C.7: Phase shifts (a) and convergence ratios (b) for variation of the nonlinear parameter β for ^{1}D at $\kappa = 0.1$ and $\alpha = 0.6$

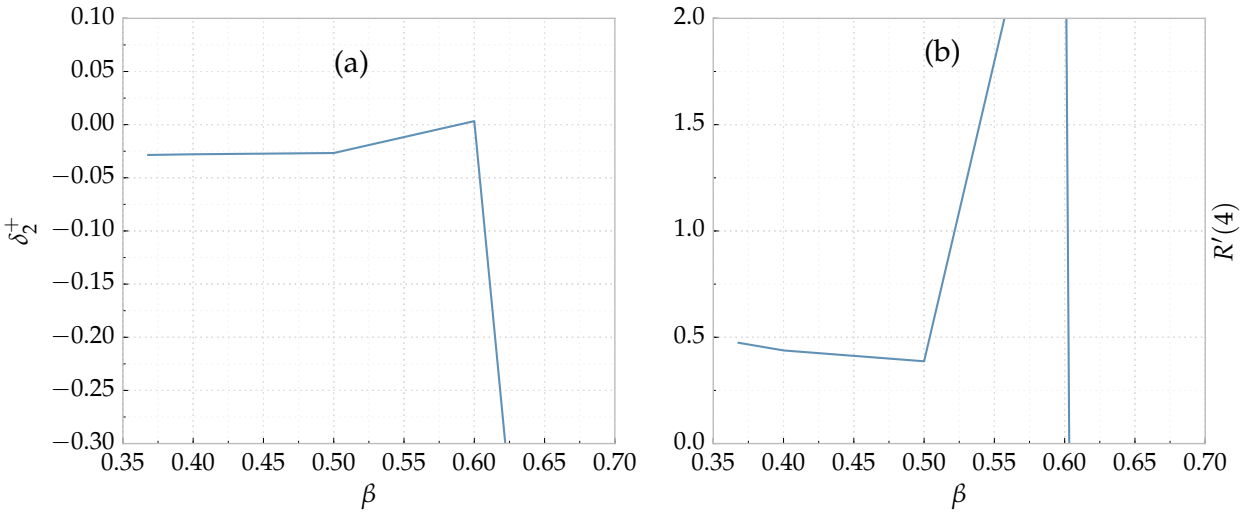

Figure C.8: Phase shifts (a) and convergence ratios (b) for variation of the nonlinear parameter β for ^{3}D at $\kappa = 0.1$ and $\alpha = 0.6$

Figure C.8. For this, the phase shifts break down even earlier, starting after $\beta = 0.5$.

We had previously noticed for multiple partial waves that if α and β are equal, linear dependence becomes a large issue. Based on this and the graphs in Figures C.7 and C.8, we tried the set of nonlinear parameters $\alpha = 0.6$, $\beta = 0.5$, and $\gamma = 0.976$ for ^{1,3}D for a full run of $\omega = 6$. Using the Todd procedure in Section 4.1.3, this ^{1}D set only uses 844 terms, and the ^{3}D set uses 854 terms.

Table C.7 compares the sets with $\beta = 0.368$ and 0.5 (using $\alpha = 0.6$ and $\gamma = 0.976$). We do not use the restricted set described in Section 4.1.4 for our final calculations, but a comparison with it can give an idea of how stable the phase shifts are. Comparing the full and restricted sets for $\beta = 0.368$, the phase shifts do not change much, even though we are reducing the basis set from 913 to 720 terms. However, comparison of the full and restricted sets for $\beta = 0.5$ shows a much larger change in the phase shifts, despite only changing from 844 to 720 terms. This seems to indicate that the set with $\beta = 0.5$ is not as stable and could potentially suffer from linear dependence.

To see whether the $\beta = 0.5$ set has linear dependence issues, we compared the convergence ratios. From Table C.8, we see that the convergence ratios are less than 0.5 for $\omega = 6$, which indicates good convergence. Table C.9 however shows a problem with linear dependence for the $\beta = 0.5$ set. Based on this analysis, we have chosen the set $\alpha = 0.359$, $\beta = 0.368$, and $\gamma = 0.976$ for higher κ for ^{1}D.

We also looked at the convergence ratios for ^{3}D, as given in Tables C.11 and C.12. Again, the set of nonlinear parameters with $\beta = 0.5$ is problematic, giving $R'(6) > 1$ for

κ	δ_2^- full $\beta = 0.368$	δ_2^- restricted $\beta = 0.368$	δ_2^- full $\beta = 0.5$	δ_2^- restricted $\beta = 0.5$
0.3	1.599^{-2}	1.595^{-2}	1.693^{-2}	1.600^{-2}
0.4	4.978^{-2}	4.965^{-2}	5.176^{-2}	4.987^{-2}
0.5	1.126^{-1}	1.124^{-1}	1.152^{-1}	1.130^{-1}
0.6	2.058^{-1}	2.053^{-1}	2.083^{-1}	2.066^{-1}
0.7	3.275^{-1}	3.269^{-1}	3.302^{-1}	3.293^{-1}

Table C.7: ^{1}D phase shifts for sets of nonlinear parameters with $\alpha = 0.6$ and $\gamma = 0.976$. The full set for $\beta = 0.368$ has 913 terms, and the full set for $\beta = 0.5$ has 844 terms. The restricted sets have 720 terms.

κ	$R'(2)$	$R'(3)$	$R'(4)$	$R'(5)$	$R'(6)$
0.3	1.523	0.795	0.572	0.491	0.377
0.4	1.286	0.680	0.475	0.412	0.429
0.5	1.048	0.603	0.464	0.442	0.466
0.6	0.826	0.534	0.575	0.435	0.481
0.7	0.471	0.874	0.472	0.521	0.465

Table C.8: Convergence ratios for ^1D at multiple ω values for the full $\beta = 0.368$ set

most κ values. From this analysis, we decided on the ^{3}D nonlinear parameters of $\alpha = 0.356$, $\beta = 0.365$, and $\gamma = 0.976$.

C.2 Nonlinear Parameters and Terms Used in the Scattering Wavefunction

Table C.13 gives the nonlinear parameters and total short-range terms used for each partial wave. This table is the same as that in our Ref. [56].

C.3 S-Wave Maximum μ

For the first three partial waves, we truncated the short-range basis set of size $N(\omega)$ using the method in Section 4.3. For ^{1}S however, we found that we could more easily determine

κ	$R'(2)$	$R'(3)$	$R'(4)$	$R'(5)$	$R'(6)$
0.3	2.475	0.352	1.611	0.316	1.628
0.4	2.157	0.291	1.372	0.209	1.902
0.5	1.835	0.254	1.133	0.225	1.343
0.6	1.539	0.237	0.979	0.299	0.667
0.7	1.206	0.306	0.696	0.360	0.441

Table C.9: Convergence ratios for ${}^1D$ at multiple ω values for the full $\beta = 0.5$ set

κ	δ_2^- full $\beta = 0.368$	δ_2^- restricted $\beta = 0.368$	δ_2^- full $\beta = 0.5$	δ_2^- restricted $\beta = 0.5$
0.3	1.100^{-3}	1.058^{-3}	1.977^{-3}	1.079^{-3}
0.4	-1.796^{-3}	-1.898^{-3}	8.016^{-6}	-1.751^{-3}
0.5	-1.070^{-2}	-1.087^{-2}	-8.432^{-3}	-1.052^{-2}
0.6	-2.544^{-2}	-2.568^{-2}	-2.331^{-2}	-2.501^{-2}
0.7	-4.281^{-2}	-4.314^{-2}	-4.085^{-2}	-4.191^{-2}

Table C.10: ^{3}D phase shifts for sets of nonlinear parameters with $\alpha = 0.6$ and $\gamma = 0.976$. The full set for $\beta = 0.365$ has 913 terms, and the full set for $\beta = 0.5$ has 854 terms. The restricted sets have 720 terms.

κ	$R'(2)$	$R'(3)$	$R'(4)$	$R'(5)$	$R'(6)$
0.3	3.950	0.932	0.564	0.512	0.432
0.4	3.399	0.811	0.446	0.404	0.469
0.5	2.812	0.740	0.417	0.411	0.519
0.6	2.261	0.730	0.466	0.400	0.527
0.7	1.714	0.860	0.490	0.433	0.484

Table C.11: Convergence ratios for ${}^3D$ at multiple ω values for the full $\beta = 0.365$ set

κ	$R'(2)$	$R'(3)$	$R'(4)$	$R'(5)$	$R'(6)$
0.3	7.392	3.424	0.505	0.426	1.768
0.4	6.978	3.035	0.390	0.265	2.421
0.5	6.435	2.625	0.345	0.229	2.235
0.6	5.739	2.241	0.393	0.242	1.251
0.7	5.082	2.063	0.504	0.244	0.723

Table C.12: Convergence ratios for ^3D at multiple ω values for the full $\beta = 0.5$ set

Partial wave	ω	$N'(\omega)$	α	β	γ	μ	m_ℓ
^{1}S	7	1505	0.568	0.580	1.093	0.9	1
^{3}S	7	1633	0.323	0.334	0.975	0.9	1
^{1}P	7	1000	0.397	0.376	0.962	0.9	3
^{3}P	7	1000	0.310	0.311	0.995	0.9	3
^{1}D ($\kappa < 0.3$)	6	916	0.359	0.368	0.976	0.7	7
^{1}D ($\kappa \geq 0.3$)	6	913	0.600	0.368	0.976	0.7	7
^{3}D ($\kappa < 0.3$)	6	919	0.356	0.365	0.976	0.7	7
^{3}D ($\kappa \geq 0.3$)	6	913	0.600	0.365	0.976	0.7	7
^{1}F ($\kappa < 0.4$)	5	385*	0.359	0.368	0.976	0.7	7
^{1}F ($\kappa \geq 0.4$)	5	462	0.500	0.600	1.100	0.7	7
^{3}F ($\kappa < 0.4$)	5	385*	0.356	0.365	0.976	0.7	7
^{3}F ($\kappa \geq 0.4$)	5	462	0.600	0.365	0.976	0.7	7
^{1}G ($\kappa < 0.45$)	5	462	0.359	0.368	0.976	0.7	9
^{1}G ($\kappa \geq 0.45$)	5	462	0.500	0.600	1.100	0.7	9
^{3}G ($\kappa < 0.45$)	5	462	0.356	0.365	0.976	0.7	9
^{3}G ($\kappa \geq 0.45$)	5	462	0.600	0.365	0.976	0.7	9
^{1}H ($\kappa < 0.5$)	5	462	0.359	0.368	0.976	0.7	11
^{1}H ($\kappa \geq 0.5$)	5	462	0.500	0.600	1.100	0.7	11
^{3}H ($\kappa < 0.45$)	5	462	0.356	0.365	0.976	0.7	11
^{3}H ($\kappa \geq 0.45$)	5	462	0.600	0.365	0.976	0.7	11

Table C.13: Nonlinear parameters α, β, γ, μ, integer power m_ℓ in the shielding function, ω, and the number of terms $N'(\omega)$ of each symmetry in the wavefunction for each partial wave. Numbers marked with a star indicate the restriction in the r_3 power described in Section 4.1.4.

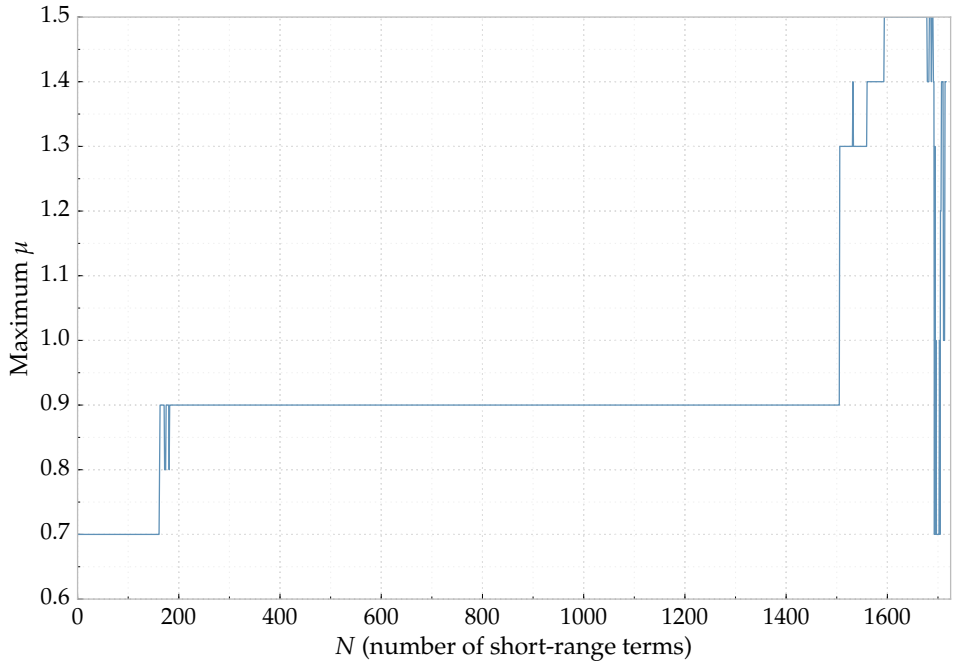

Figure C.9: Value of μ in the shielding function, Equation (3.7), that gives the largest phase shift versus the number of terms for the ^{1}S-wave with $\kappa = 0.1$

the cutoff by performing phase shift runs for multiple μ values and various κ to see what the optimal value of μ was that gave the highest phase shift. As shown in Figure C.9, this value of μ was fairly stable through most of the N range, but it suddenly spikes up after 1505 terms and fluctuates greatly. For some κ values, we also saw that when this happened, the value of μ that gave the highest phase shift was sometimes unbounded, definitely indicating linear dependence. Interestingly, this behavior was not noticed for the ^{3}S-wave. We did not try this for other partial waves, but it gave a good cutoff point for the ^{1}S-wave.

C.4 Gaussian Quadratures

Gaussian quadratures are used to integrate many classes of integrals. In their most general form, these quadratures are given by [240, p.887]

$$\int_a^b W(x)f(x)dx \approx \sum_{i=1}^{n} w_i f(x_i). \tag{C.1}$$

Gaussian quadratures are particularly attractive, since they give exact results for polynomials up to degree $2n-1$. The weight function $W(x)$ can be chosen for certain classes of integrals. Three main types of weight functions are used in this work. For a discussion on the number of quadrature points used, refer to Appendix C.4.4.

For most integrals over finite intervals, we use the Gauss-Legendre quadrature. The exception is when we integrate over an interior angle (φ_{ij}), where we use the Chebyshev-Gauss quadrature. For semi-infinite integrations, we use Gauss-Laguerre quadratures. Each of these can be seen in Ref. [240, p.887-890].

The Gauss-Laguerre quadrature is typically over the range $(-1, 1)$ but can be modified to arbitrary finite intervals using a standard formula given in Ref. [240, p.887]. Discussion over adapting the Gauss-Laguerre quadrature to use an arbitrary lower limit and an extra constant multiplying the variable in the exponential is found in Appendix C.4.1. Discussion over adapting the Chebyshev-Gauss quadrature to the φ_{ij} innermost integrations is given in Appendix C.4.2.

C.4.1 Gauss-Laguerre Quadrature

The Gauss-Legendre quadrature cannot be used on semi-infinite intervals, so we use the Gauss-Laguerre quadrature in these cases. The orthogonal polynomials in this case are the Laguerre polynomials, $L_n(x)$, and the weight function is $W(x) = e^{-x}$. The specific form of Equation (C.1) is

$$\int_0^\infty e^{-x} f(x) dx \approx \sum_{i=1}^{n} w_i f(x_i). \tag{C.2}$$

When the integration is over the interval (a, ∞) instead, Equation (C.2) is transformed by

$$\int_a^\infty e^{-x} f(x) dx = \int_0^\infty e^{-(x+a)} f(x+a) dx = e^{-a} \int_0^\infty e^{-x} f(x+a) dx \approx e^{-a} \sum_{i=1}^{n} w_i f(x_i + a). \tag{C.3}$$

A more general form of this is obtained by using a coefficient in the exponential, i.e.

$$\int_a^\infty e^{-mx} f(x) dx = \frac{1}{m} \int_a^\infty e^{-y} f\left(\frac{y}{m}\right) dy, \tag{C.4}$$

where we have defined $y = mx$. This allows for Equation (C.3) to be generalized to

$$\begin{aligned} \int_a^\infty e^{-mx} f(x) dx &= \frac{1}{m} \int_{ma}^\infty e^{-y} f\left(\frac{y}{m}\right) dy = \frac{1}{m} \int_0^\infty e^{-(y+ma)} f\left(\frac{y}{m} + a\right) dy \\ &= \frac{e^{-ma}}{m} \int_0^\infty e^{-y} f\left(\frac{y}{m} + a\right) dy \approx \frac{e^{-ma}}{m} \sum_{i=1}^{n} w_i f\left(\frac{y_i}{m} + a\right). \end{aligned} \tag{C.5}$$

The y_i abscissas and w_i weights are the same as the standard Gauss-Laguerre quadrature. This more general form quadrature is what we use for semi-infinite integrations.

C.4.2 Chebyshev-Gauss Quadrature

To integrate over the φ_{ij} variable, we can use [95, p.79]

$$\int_0^{2\pi} D(\cos\varphi_{23})\, d\varphi_{23} \approx \frac{2\pi}{n} \sum_{i=1}^{n} D\left[\cos\left(\frac{2i-1}{2n}\pi\right)\right]. \tag{C.6}$$

To prove this, we start with

$$\int_0^{\pi} D(\cos\varphi_{23})\, d\varphi_{23} \approx \frac{\pi}{n}\sum_{i=1}^{n} D\left[\cos\left(\frac{2i-1}{2n}\pi\right)\right]. \tag{C.7}$$

Both of these equations are variations on Gaussian quadratures. The Chebyshev-Gauss quadrature is given by [240, 247]

$$\int_{-1}^{1} \frac{f(x)}{\sqrt{1-x^2}}\, dx \approx \sum_{i=1}^{n} w_i f(x_i), \tag{C.8}$$

with $w_i = \frac{\pi}{n}$ and $x_i = \cos\left(\frac{2i-1}{2n}\pi\right)$.

Starting from the left side of Equation (C.7), we have

$$\int_0^{\pi} D(\cos\varphi)\ d\varphi = \int_0^{\pi} \frac{1}{\sqrt{1-\cos^2\varphi}}\sqrt{1-\cos^2\varphi}\, D(\cos\varphi)\ d\varphi \tag{C.9}$$

$$= \int_0^{\pi} \frac{1}{\sqrt{1-\cos^2\varphi}} D(\cos\varphi)\sin\varphi\ d\varphi. \tag{C.10}$$

Using the substitution $x = \cos\varphi$ and $dx = -\sin\varphi\, d\varphi$ changes the limits to $x_{min} = \cos 0 = 1$ and $x_{max} = \cos\pi = -1$. Equation (C.10) becomes

$$\int_0^{\pi} D(\cos\varphi)\, \mathrm{d}\varphi = -\int_1^{-1} \frac{1}{\sqrt{1-x^2}} D(x)\, \mathrm{d}x = \int_{-1}^{1} \frac{1}{\sqrt{1-x^2}} D(x)\, \mathrm{d}x. \tag{C.11}$$

This is the exact form needed for Gauss-Chebyshev quadrature (with f = D):

$$\int_0^{\pi} D(\cos\varphi)\, \mathrm{d}\varphi \approx \frac{\pi}{n}\sum_{i=1}^{n} D\left[\cos\left(\frac{2i-1}{2n}\pi\right)\right] \tag{C.12}$$

This proves only form Equation (C.7). To prove Equation (C.6), we split up the integration into two parts:

$$\int_0^{2\pi} D(\cos\varphi_{23})\, \mathrm{d}\varphi_{23} = \int_0^{\pi} D(\cos\varphi_{23})\, \mathrm{d}\varphi_{23} + \int_{\pi}^{2\pi} D(\cos\varphi_{23})\, \mathrm{d}\varphi_{23}. \tag{C.13}$$

The first integration is just Equation (C.7). The only difference between the first and second integration is the limits. Defining $y = \varphi - \pi$ gives

$$\int_{\pi}^{2\pi} D(\cos\varphi)\, \mathrm{d}\varphi = \int_0^{\pi} D[\cos(\varphi)]\, dy = \int_0^{\pi} D[\cos(y+\pi)]\, dy. \tag{C.14}$$

If we also define $z = \cos\varphi = \cos(y+\pi)$ and $dz = \sin y\, dy$, we get an expression the same as Equation (C.11):

$$\int_0^{\pi} D(\cos\varphi)\, dy = \int_0^{\pi} \frac{1}{\sqrt{1-z^2}} D(z)\, sin\varphi\, dy = \int_{-1}^{1} \frac{1}{\sqrt{1-z^2}} D(z) dz \tag{C.15}$$

Since this is the same as Equation (C.11), we just combine this with Equations (C.12) and (C.13) to get Equation (C.6), proving the first form.

C.4.3 Selection of Quadrature Points

The number of quadrature points for each coordinate in the 6-dimensional integrations is critical to have fully converged results. In our testing, the r_1 coordinate (the coordinate of e^+) required more integration points than any other. The r_2 and r_3 coordinates required less points, and the interparticle terms (r_{12}, r_{13} and r_{23}) required the least. These results only apply to the long-long and long-short terms, as the short- short terms are integrated using the asymptotic expansion method (see Section 3.4.3).

To determine this, we held the number of integration points fixed, except for one coordinate, which we increased in steps. The difference in the output between steps was used to analyze how important each coordinate was. Also, some terms are more sensitive to the number of integration points than other. For instance, the $(\bar{S}_\ell, \mathcal{L}\bar{S}_\ell)$ term converges relatively quickly, while the $(\bar{C}_\ell, \mathcal{L}\bar{C}_\ell)$ term requires more integration points.

We also used a sample input file from Van Reeth [171] for the number of quadrature points he used in his code as a starting point. This is shown in Table C.16. Using a comparison program with the Developer's Image Library [248], we determined a set of quadrature points that yielded good convergence of the matrix elements with a reasonable runtime. The final set of quadrature points that we use for all partial waves is shown in Table C.17. This set yielded good convergence for partial waves through the H-wave.

C.4.4 Quadrature Points

Describing the number of points used in integrating the different coordinates in Sections 4.2.1 and 4.2.2 can be confusing, so we have taken to grouping the sets of points as in Tables C.14 and C.15. Each column of these tables is referred to as an "effective coordinate", as the r_2 and r_3 integrations are split into two parts, as described in Section 4.2.3. The "Lag" entries use the Gauss-Laguerre quadrature, "Leg" uses the Gauss-Legendre quadrature, and "Che" uses Chebyshev-Gauss quadrature. Note that the only difference between Tables C.14 and C.15 is that the S-wave long-long matrix elements are integrated using perimetric coordinates when the r_{23}^{-1} is not present, while the other partial waves use the same coordinates as the long-short terms.

Table C.16 shows the set of integration points used by Van Reeth [171]. This was the starting point for trying to obtain better convergence of the matrix element integrations, as described in Appendix C.4.3. Using a comparison program to investigate this convergence, we determined a more extensive set of integration points given in Table C.17 that we use for all partial waves.

Integral	Coord 1	Coord 2	Coord 3	Coord 4	Coord 5	Coord 6	Coord 7	Coord 8
Long-long, no r_{23}^{-1}	x Lag	y Lag	z Lag	r_3 Leg	r_3 Leg	r_{13} Leg		
Long-long, r_{23}^{-1}	r_1 Lag	r_2 Leg	r_2 Lag	r_3 Leg	r_3 Lag	φ_{12} Che	r_{13} Leg	r_{23} Leg
Long-short $q_i = 0$, no r_{23}^{-1}	r_1 Lag	r_2 Leg	r_2 Lag	r_3 Leg	r_3 Lag	r_{12} Leg	r_{13} Leg	
Long-short $q_i = 0$, r_{23}^{-1}	r_1 Lag	r_2 Leg	r_2 Lag	r_3 Leg	r_3 Lag	r_{12} Leg	φ_{13} Che	r_{23} Leg
Long-short $q_i > 0$	r_1 Lag	r_2 Leg	r_2 Lag	r_3 Leg	r_3 Lag	r_{12} Leg	r_{13} Leg	φ_{23} Che

Table C.14: Description of the values in Tables C.16 and C.17 for the S-wave. Refer to the text for explanation of this table.

Integral	Coord 1	Coord 2	Coord 3	Coord 4	Coord 5	Coord 6	Coord 7	Coord 8
Long-long, no r_{23}^{-1}	r_1 Lag	r_2 Leg	r_2 Lag	r_3 Leg	r_3 Lag	r_{12} Leg	r_{13} Leg	
Long-long, r_{23}^{-1}	r_1 Lag	r_2 Leg	r_2 Lag	r_3 Leg	r_3 Lag	φ_{12} Che	r_{13} Leg	r_{23} Leg
Long-short $q_i = 0$, no r_{23}^{-1}	r_1 Lag	r_2 Leg	r_2 Lag	r_3 Leg	r_3 Lag	r_{12} Leg	r_{13} Leg	
Long-short $q_i = 0$, r_{23}^{-1}	r_1 Lag	r_2 Leg	r_2 Lag	r_3 Leg	r_3 Lag	r_{12} Leg	φ_{13} Che	r_{23} Leg
Long-short $q_i > 0$	r_1 Lag	r_2 Leg	r_2 Lag	r_3 Leg	r_3 Lag	r_{12} Leg	r_{13} Leg	φ_{23} Che

Table C.15: Description of the values in Tables C.16 and C.17 for $\ell > 0$. Refer to the text for explanation of this table.

Integral	Coord 1	Coord 2	Coord 3	Coord 4	Coord 5	Coord 6	Coord 7	Coord 8
Long-long, no r_{23}^{-1}	45	35	35	35	28	15		
Long-long, r_{23}^{-1}	65	35	28	35	28	12	15	15
Long-short $q_i = 0$, no r_{23}^{-1}	90	57	34	57	34	30	30	
Long-short $q_i = 0$, r_{23}^{-1}	90	58	30	55	35	33	33	33
Long-short $q_i > 0$	90	57	34	57	34	30	30	30

Table C.16: Base set of effective coordinates for integrations from Van Reeth [171]

Integral	Coord 1	Coord 2	Coord 3	Coord 4	Coord 5	Coord 6	Coord 7	Coord 8
Long-long, no r_{23}^{-1}	75	40	40	40	40	25		
Long-long, r_{23}^{-1}	75	40	40	40	40	25	25	25
Long-short $q_i = 0$, no r_{23}^{-1}	100	65	45	65	45	45	45	
Long-short $q_i = 0$, r_{23}^{-1}	115	65	45	65	45	45	45	45
Long-short $q_i > 0$	100	65	45	65	45	45	45	45

Table C.17: Final set of effective coordinates for integrations

C.5 Resonance Fitting

To find the resonance parameters (positions and widths), the phase shifts for multiple energy values are fitted to Equation (3.121). There have been multiple programs described in the literature [144, 145, 249] to do these fittings. Some of the difficulty with this type of fitting is choosing appropriate guesses for the resonance parameters. Ref. [249] describes methods that some groups use to try to identify resonance parameters.

With the help of Bosca [250], I wrote a MATLAB® [251] script that uses the `nlinfit` routine of MATLAB. `nlinfit` is specifically designed for fitting to nonlinear functions, and its robust option allows for a variety of weighting functions to be used. This script does the fitting for all eight of the possible weightings: Bisquare, Andrews, Cauchy, Fair, Huber, Logistic, Talwar and Welsch. This fitting routine is also not as sensitive to the initial guesses as the Mathematica and SciPy routines.

Later on, I adapted this resonance fitting code to be called from IPython [252] using the mlabwrap [253] Python to MATLAB wrapper. This allows fits and graphs of the fittings to be in the same IPython notebook, including the flexibility of querying a MySQL database for the phase shift data for any partial wave at any number of terms and for any Kohn-type variational method. The mlabwrap package is difficult to install properly, requiring a compilation against MATLAB. The mlabwrap-purepy package [254] has been created to simplify this, but I have not tried it yet.

The results of fitting the phase shifts from the S matrix are shown in Figures C.10 and C.11 for each of the weighting functions, and the resonance parameters are given in each subfigure. There is good agreement between the fits performed with each of the weighting functions, and the Fair is the furthest from the others. In our testing, the Cauchy is consistently one of the best choices for fitting. In addition, Figure C.12 has plots of the residuals (the absolute value of the difference between the fitted curve and the actual phase shifts). Each graph also has the residual sum of squares (RSS) calculated. The RSS gives an easy way to compare the performance of the weightings with each other. The

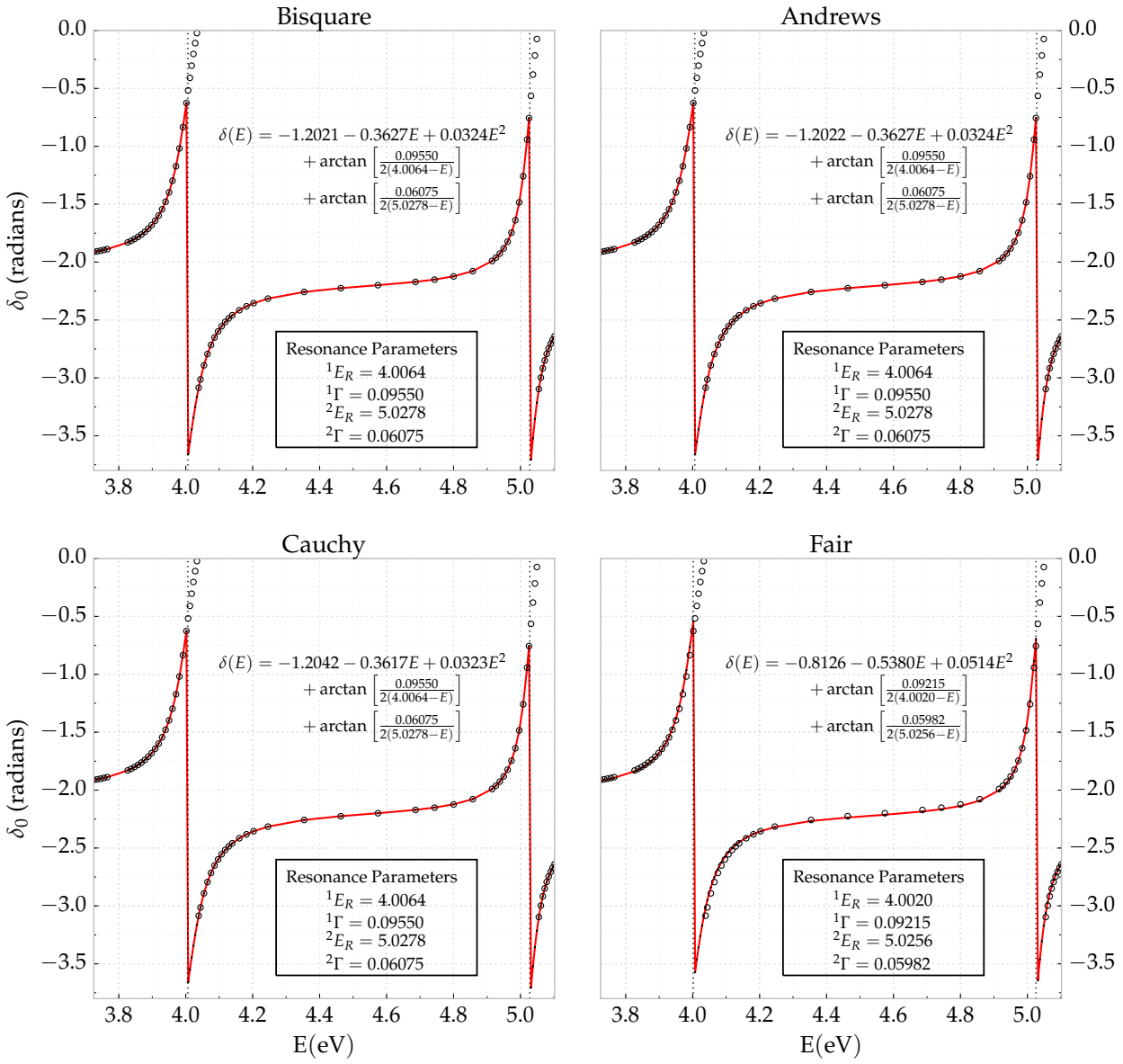

Figure C.10: First set of uncorrected resonance fitting graphs for ^{1}S at $\omega = 7$

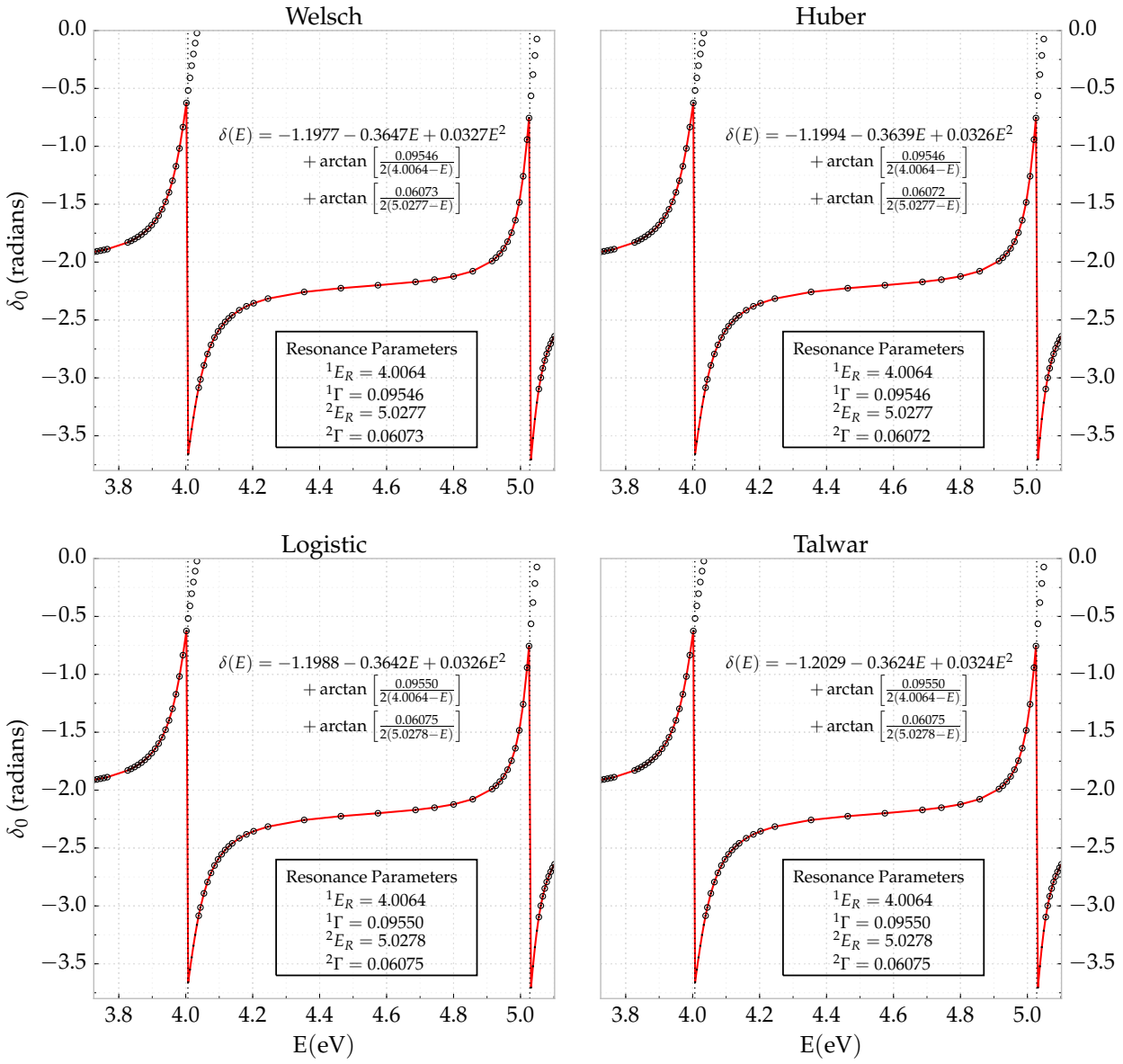

Figure C.11: Second set of uncorrected resonance fitting graphs for ^{1}S at $\omega = 7$

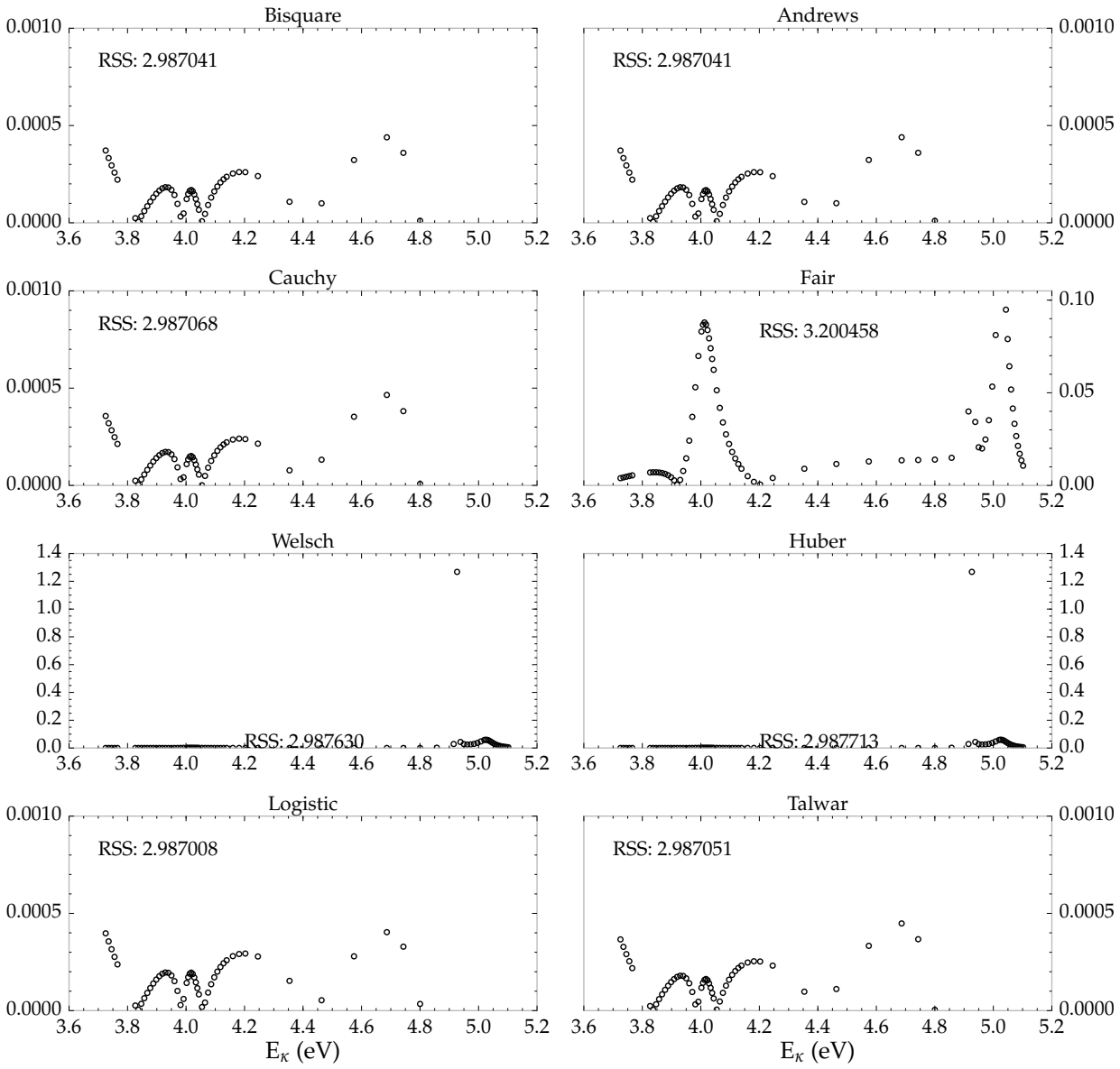

Figure C.12: Residuals for uncorrected resonance fitting graphs for ^{1}S at $\omega = 7$

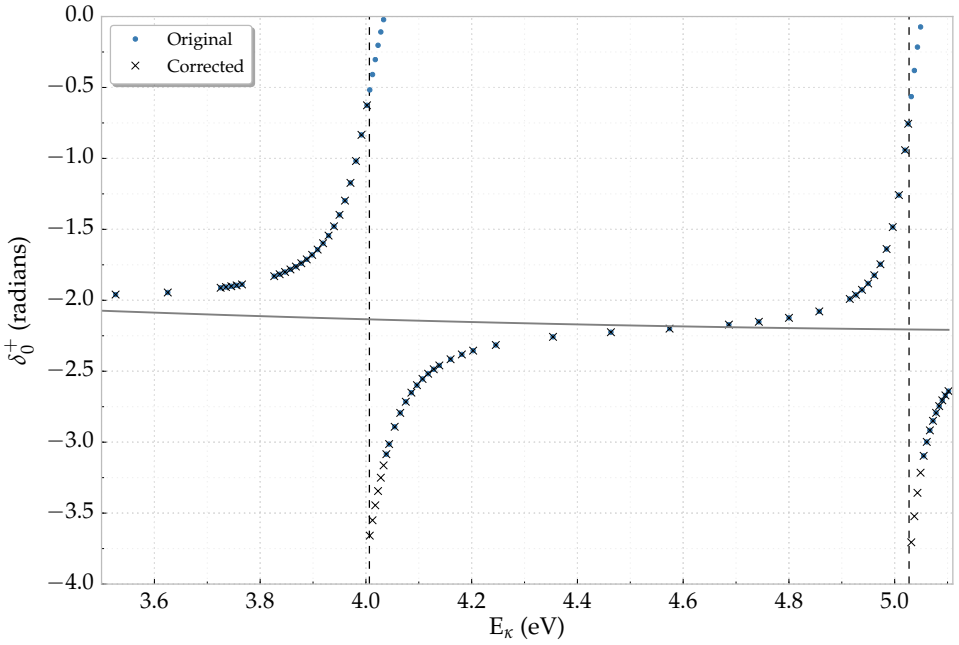

Figure C.13: ^{1}S resonance data showing raw data from *S*-matrix complex Kohn and the corrected version. The solid gray line shows the polynomial background, and the vertical dashed lines give the calculated resonance positions.

Fair has a notably larger RSS than all of the other fittings.

One important thing to notice with the fits in Figures C.10 and C.11 is that the *S*-matrix complex Kohn phase shifts extend above the fitted curve at the resonances before matching up again on the right side of the resonance below -3.0. The red curves still fit to the data well, but the fits can be improved by correcting for these.

In Equation (3.121), the first three polynomial terms form the background, and the two arctan terms represent the resonances. The range of arctan is $(-\frac{\pi}{2}, \frac{\pi}{2})$, so the arctan parts of this model cannot bring the phase shift from the background (near 2.0) all the way to 0.0, as it can only add up to $\frac{\pi}{2}$ to the background. It is important to realize that the Kohn-type variational methods will only return phase shifts in a certain range. From Equation (3.67), we are not finding the phase shifts directly but are rather calculating $\tan \delta_\ell$. The phase shifts found this way sometimes have to have π added or subtracted if they are outside this range.

Figure C.13 shows the results of subtracting π from phase shifts that are more than $\frac{\pi}{2}$ above the background. The original and the corrected data are both shown on this plot, and the background is given as a gray line. Note that the slope of the original data changes when crossing over the vertical dashed lines, which gives the resonance positions. When corrected, these upper points are moved down to their appropriate place, shown as x's on the graph. These match up better with the fitting curve. This fitting is an iterative

process, because the background polynomial has to be determined with Equation (3.121) before we can do this correction. Then the phase shifts are fitted again after performing the correction.

Finally, this corrected and re-fitted data is shown in Figures C.14 and C.15. The different weighting methods agree extremely well now, with the only notable differences being in the ${}^2\Gamma$ width of the second resonance for the Bisquare, Andrews, and Talwar fits. This is still a very small difference, and the other resonance parameters are almost all identical. Figure C.16 gives the residuals and RSS for the corrected phase shifts, similar to Figure C.12. The Bisquare, Andrews, and Talwar weightings have larger RSS values than the other weightings, indicating that their fits are not quite as accurate, but they are still relatively accurate.

The differences between the different weighting methods gives us one way to determine errors for the resonance parameters. Additionally, comparing the different Kohn-type variational methods methods gives us an idea of the error. The real-valued generalized Kohn variational methods give more disagreement, so we compute the resonance parameters for each of these. We also have to take into account Schwartz singularities. In Figure 3.2(a) on 46, the second resonance parameters are not as accurate. The fitting routine described here chooses fitting parameters of ${}^2E_R = 5.0295\,\text{eV}$ and ${}^2\Gamma = 0.060\,11\,\text{eV}$. In Figure 3.2(b), where there are no Schwartz singularities, ${}^2E_R = 5.0278\,\text{eV}$ and ${}^2\Gamma = 0.060\,75\,\text{eV}$. This highlights the importance of using multiple Kohn-type variational methods and trying to detect Schwartz singularities. After removing obvious Schwartz singularities, the mean value of the different Kohn-type variational methods for all weightings is taken for each resonance parameter, and these are the results listed for each of the partial waves in Sections 5.3.2, 6.4.2, 7.6.2 and 9.4.2. The errors given in these tables are simply the standard deviation with all generalized Kohn variational methods and weightings used for each resonance parameter. For this, we do not use the generalized S-matrix or T-matrix complex Kohn methods, because using these would decrease the error, as they agree to a significant precision.

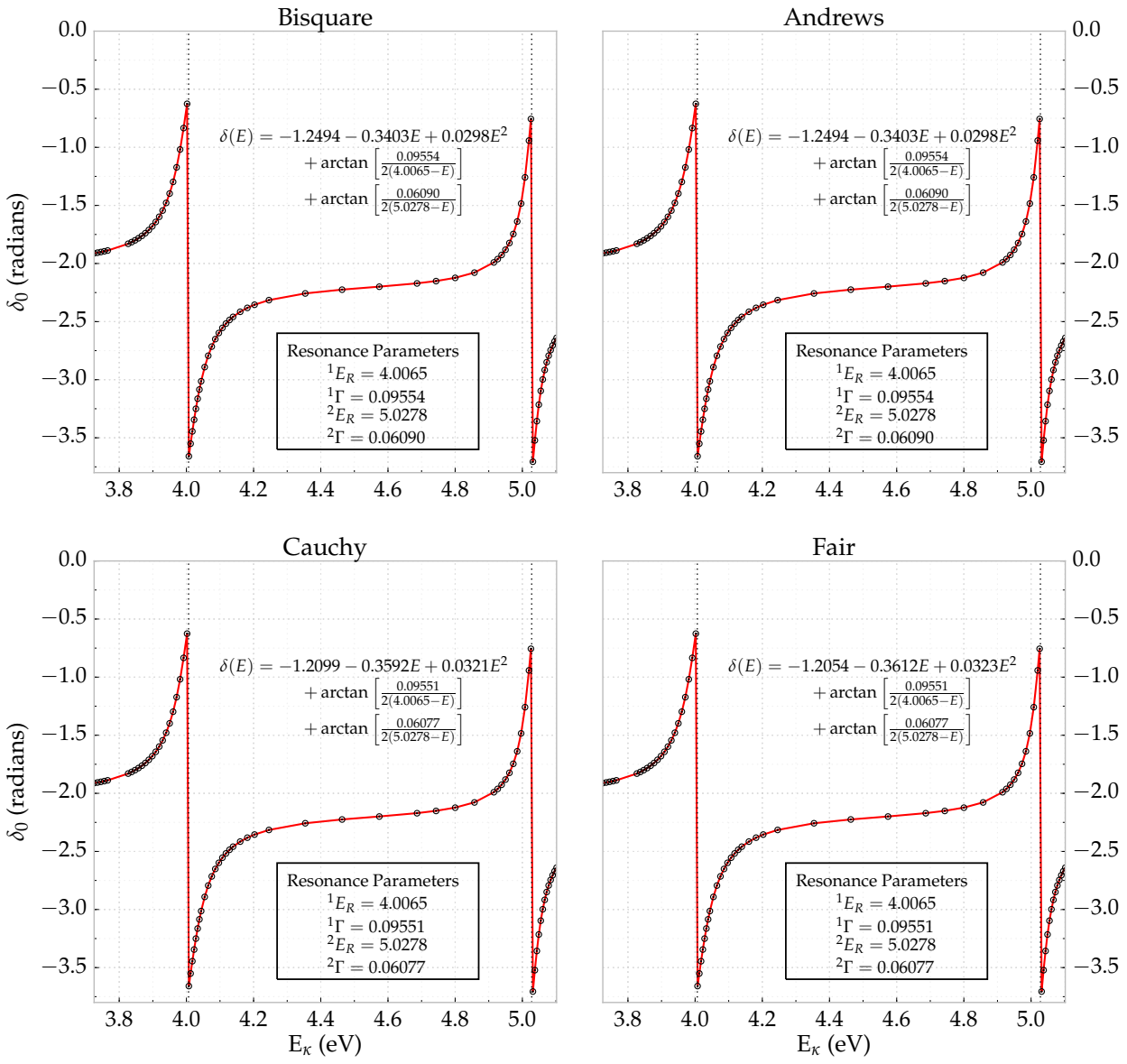

Figure C.14: First set of corrected resonance fitting graphs for ^{1}S at $\omega = 7$

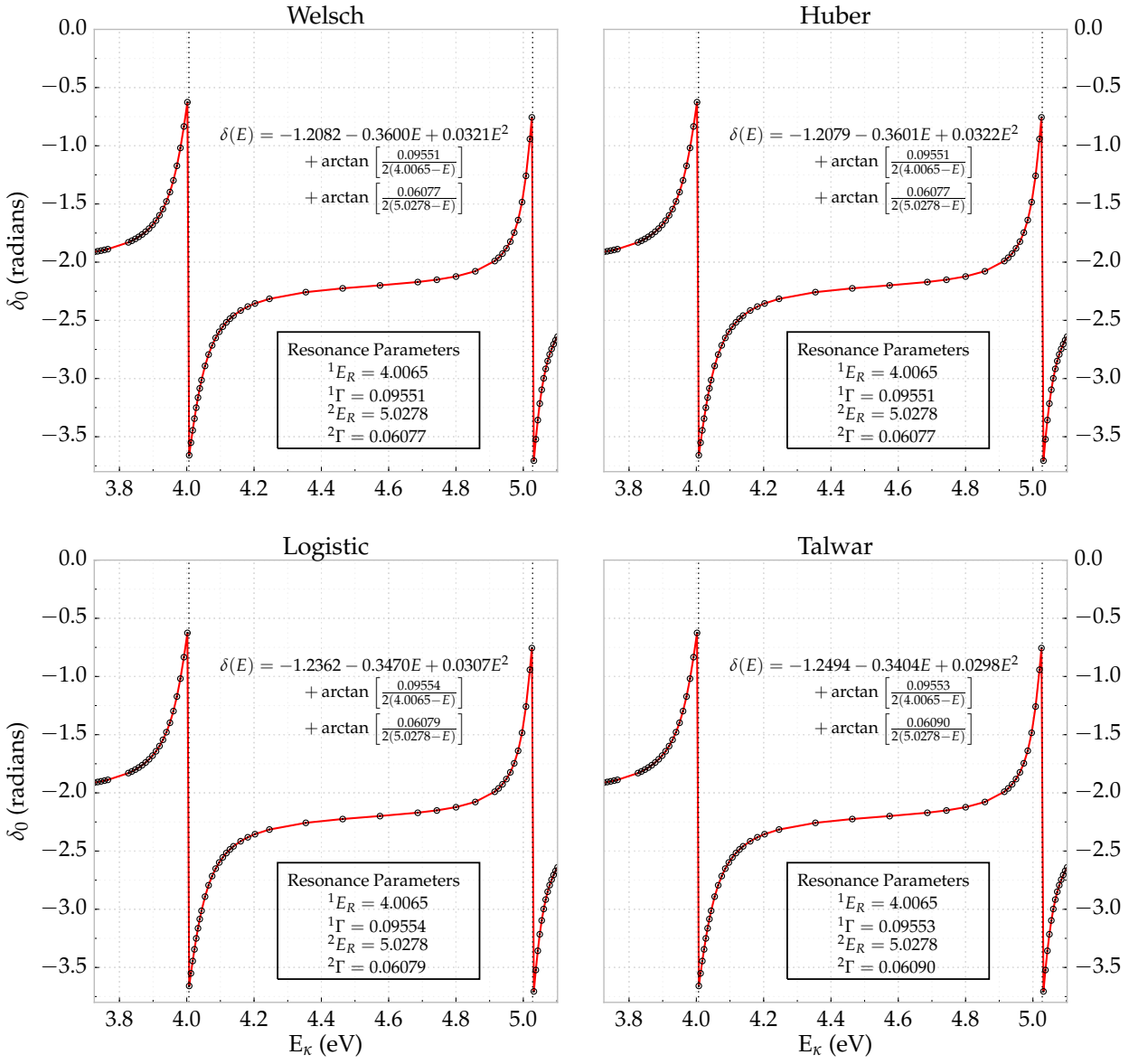

Figure C.15: Second set of corrected resonance fitting graphs for ^{1}S at $\omega = 7$

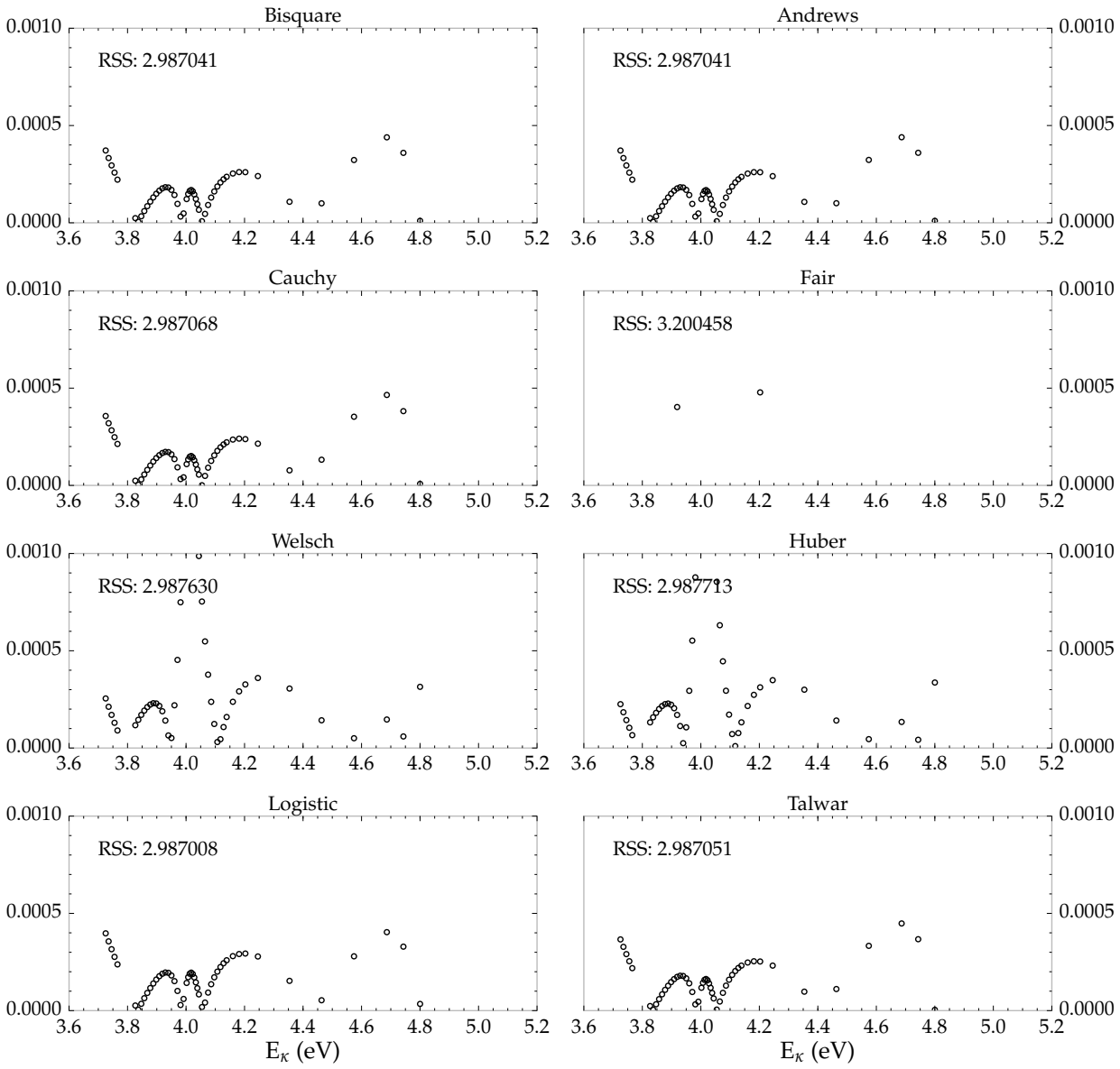

Figure C.16: Residuals for corrected resonance fitting graphs for ^{1}S at $\omega = 7$

D

Program Descriptions

DOING this work required writing multiple codes, and I have made my codes available on GitHub at `https://github.com/DentonW/Ps-H-Scattering` [1]. Much of the codes are what is described in Chapter 4. A flowchart of the steps required to calculate phase shifts and any additional quantities, such as cross sections, is given by Figure D.1.

The short-range program typically only needs to be run once for a partial wave, and those short-range matrix elements are used for all κ runs. For $\ell \geq 2$, we have a low and high κ set of nonlinear parameters, so there are two runs of the short-range program that have to be done. The long-range program is run for every κ value for each partial wave, and if needed, we restrict the short-range terms using Todd's method from Section 4.1.3. Then the phase shift program uses these inputs to run many Kohn-type variational methods and generate phase shifts. These phase shifts can then be further analyzed with several scripts.

As the codes are freely available on GitHub, it is worthwhile to show the directory structure when this package is downloaded with git or as a zip. Figure D.2 shows this directory tree. The S-wave, P-wave, and D-wave codes only work for their respective partial wave, and the code in "General Code" works for arbitrary ℓ, as described in Chapters 3 and 8.

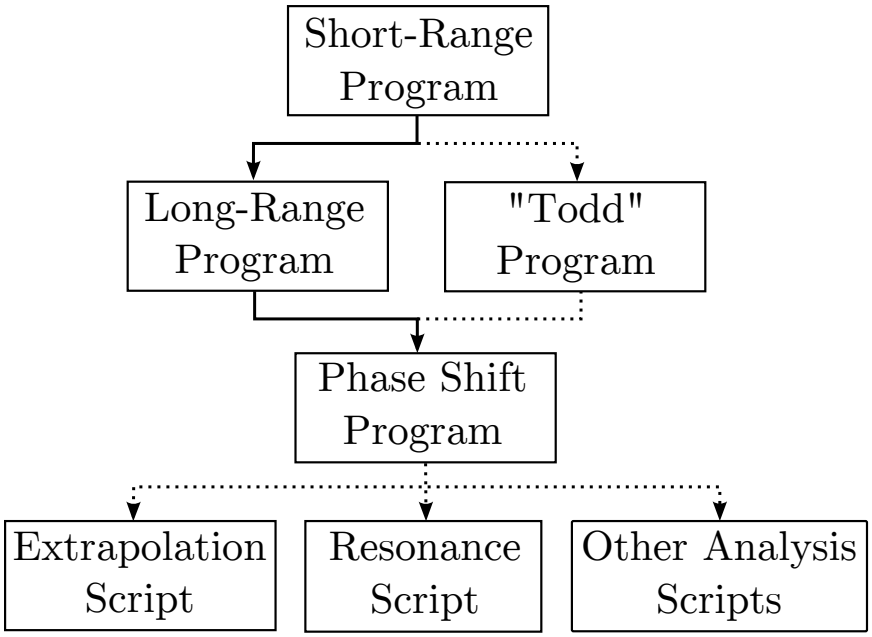

Figure D.1: Flowchart for programs and scripts

```
/
├── S-Wave
│   ├── Long
│   └── Short
├── P-Wave
│   ├── Long
│   └── Short
├── D-Wave
│   ├── Long
│   └── Short
├── General Code
│   ├── Comparison
│   ├── Long-Range
│   ├── Phase Shift
│   ├── Python Scripts
│   ├── Short-Range
│   └── Todd Method
└── Derivations and Tests
```

Figure D.2: Directory tree of code on GitHub [1]

S-, P-, and D-wave Codes

The S-, P-, and D-wave folders each have a Short subfolder (short-short code) and a Long subfolder (short-long and long-long code). As shown in the flowchart in Figure D.1, the Short code is run first, and then Long code is run for all κ values of interest. To obtain phase shifts, use the "Phase Shift" code in the "General Code" folder. Extrapolations, etc. are also in the "General Code" folder.

General Short and Long

The general Short and Long codes act similarly to the S-, P-, and D-wave codes but for arbitrary ℓ. It should be noted that because these codes are general, they are much slower than running the corresponding code specific to a partial wave if $\ell \leq 2$.

Phase Shifts

The phase shift code, located in "General Code/Phase Shift", uses the outputs of the Short and Long codes from the S-Wave, P-Wave, D-wave or "General Code" folders to calculate the phase shifts. An optional file describing which short-range terms to use (such as that generated by the "Todd Code"), can also be used as an input. The output is an XML file showing phase shifts calculated for every N value for each of the 109 total Kohn-type methods used.

Extrapolation Program

I wrote a Python [255] script, located in "General Code/Python Scripts", to extrapolate the phase shifts for a run for all Kohn-type methods used, including the 35 values of τ used in each of the generalized Kohn, generalized S-matrix Kohn, and generalized T-matrix Kohn. The extrapolation is performed with a least-squares fitting using the `polyfit` function of the SciPy package [256] to the form of Equation (4.24). This program can do the extrapolation over any interval of ω values requested. The extrapolations from the 109 total Kohn-type methods are compared to see if there is any large discrepancy between them, indicating numerical instability. The phase shifts can have a singularity in the real-valued Kohn-type variational methods as seen in Figure 3.2, so care must be taken to ensure extrapolations are not taken around this interval.

Derivations and Tests

The "General Code/Derivations and Tests" folder has files referenced throughout this document that are usually *Mathematica* notebooks. Examples are the "Shielding Factor.nb" notebook that is referenced in Appendix B.6 and notebooks to generate the powers and coefficients needed for the short-short integrations for each partial wave.

Bibliography

[1] Codes for this dissertation work are publicly available on GitHub at https://github.com/DentonW/Ps-H-Scattering, and my profile page is at https://github.com/DentonW. (Cited on pages 42, 43, 110, 162, 163, 171, 174, 205, and 206)

[2] Many of the notes for full derivations are available at my figshare profile at http://figshare.com/authors/Denton_Woods/581638. Old posters and other relevant materials will also be available here. (Cited on pages 78, 83, 92, 95, and 105)

[3] Some figures have interactive online versions at https://plot.ly/~Denton. The data used in these is also easily viewable on that page. (Cited on pages 71, 87, 100, 124, 125, and 129)

[4] The research Wiki is currently hosted at http://129.120.30.66/wiki/index.php, but this could change. My personal website at http://www.dentonwoods.com will have a permanent link to it. The page is currently behind a login/password, but that may also change in the future. For access, contact me directly at denton.woods@unt.edu. (Cited on pages 7, 11, 40, 42, 43, 78, 92, 95, 105, 163, and 171)

[5] D. Woods, P. Van Reeth, and S. J. Ward, http://meetings.aps.org/link/BAPS.2014.DAMOP.Q1.55, http://meetings.aps.org/link/BAPS.2014.MAR.W26.3. (Cited on page 4)

[6] D. Woods, S. J. Ward, and P. Van Reeth, http://meetings.aps.org/link/BAPS.2013.DAMOP.Q1.122, http://meetings.aps.org/link/BAPS.2013.MAR.J25.8, http://meetings.aps.org/link/BAPS.2012.DAMOP.U3.4, http://meetings.aps.org/link/BAPS.2011.DAMOP.Q1.88, http://meetings.aps.org/link/BAPS.2010.DAMOP.T1.165. (Cited on page 4)

[7] S. J. Ward, D. Woods, and P. Van Reeth, http://meetings.aps.org/Meeting/DAMOP15/Session/Q1.113. (Cited on page 4)

[8] D. Woods, P. Van Reeth, and S. J. Ward, *Elaborate Calculations of low-energy Ps-H collisions*, Book of Abstracts, XVIII International Workshop on Low-Energy Positron and Postronium Physics & XIX International Symposium Electron-Molecule Collisions and Swarms, 17-20 July 2015, Lisbon, Portugal, POSMOL 2015; ISBN 978-989-20-5845-0 (Paulo Limão-Vieira, Filipino Ferrero da Silva, Guilherme Mendes, and Emanuele Langworthy, and Tiago Cunha; P. 44, ed.), p. 67. (Cited on page 4)

[9] P. Van Reeth, J. W. Humberston, D. Woods, and S. J. Ward, *A comparison of positron, electron and positronium low-energy scattering from hydrogen*, Book of Abstracts, XVIII International Workshop on Low-Energy Positron and Postronium Physics & XIX International Symposium Electron-Molecule Collisions and Swarms, 17-20 July 2015, Lisbon, Portugal, POSMOL 2015; ISBN 978-989-20-5845-0 (Paulo Limão-Vieira, Filipino Ferrero da Silva, Guilherme Mendes, and Emanuele Langworthy, and Tiago Cunha; P. 41, ed.), p. 64. (Cited on page 4)

[10] St. Mohorovičić, *Möglichkeit neuer elemente und ihre bedeutung für die astrophysik*, Astronomische Nachrichten **253** (1934), no. 4, 93. (Cited on page 1)

[11] Martin Deutsch, *Evidence for the Formation of Positronium in Gases*, Physical Review **82** (1951), no. 3, 455. (Cited on page 1)

[12] M. Charlton and J. W. Humberston, *Positron Physics*, Cambridge University Press, Cambridge, England, UK, 2001. (Cited on page 1)

[13] Andrzej Czarnecki, Kirill Melnikov, and Alexander Yelkhovsky, α^2 *Corrections to Parapositronium Decay*, Physical Review Letters **83** (1999), no. 6, 1135. (Cited on page 1)

[14] R. S. Vallery, P. W. Zitzewitz, and D. W. Gidley, *Resolution of the Orthopositronium-Lifetime Puzzle*, Physical Review Letters **90** (2003), no. 20, 203402. (Cited on page 1)

[15] R.L. Kinzer, W.R. Purcell, W.N. Johnson, J.D. Kurfess, G. Jung, and J. Skibo, *OSSE observations of positron annihilation in the Galactic plane*, Astronomy and Astrophysics Supplement **120** (1996), 317. (Cited on page 2)

[16] Carol Jo Crannel, Glenn Joyce, Reuven Ramaty, and Carl Werntz, *Formation of the 0.511 MeV line in solar flares*, ApJ **210** (1976), 582–592. (Cited on page 2)

[17] G. Laricchia and H.R.J. Walters, *Positronium collision physics*, Rivista del Nuovo Cimento **35** (2012), no. 6, 305. (Cited on page 2)

[18] H. R. J. Walters, *Antimatter Atomic Physics*, Science **330** (2010), no. 6005, 762–763. (Cited on page 2)

[19] ALPHA Collaboration, G. B. Andresen, M. D. Ashkezari, M. Baquero-Ruiz, W. Bertsche, E. Butler, C. L. Cesar, A. Deller, S. Eriksson, J. Fajans, T. Friesen, M. C.

Fujiwara, D. R. Gill, A. Gutierrez, J. S. Hangst, W. N. Hardy, R. S. Hayano, M. E. Hayden, A. J. Humphries, R. Hydomako, S. Jonsell, S. Kemp, L. Kurchaninov, N. Madsen, S. Menary, P. Nolan, K. Olchanski, A. Olin, P. Pusa, C. Ø. Rasmussen, F. Robicheaux, E. Sarid, D. M. Silveira, C. So, J. W. Storey, R. I. Thompson, D. P. van der Werf, J. S. Wurtele, and Y. Yamazaki, *Confinement of antihydrogen for 1,000 seconds*, Nature Physics **7** (2011), 558–564. (Cited on page 2)

[20] A. S. Kadyrov, A. V. Lugovskoy, R. Utamuratov, and I. Bray, *Benchmark calculation of hydrogen (antihydrogen) formation at rest in positronium-proton (-antiproton) scattering*, Physical Review A - Atomic, Molecular, and Optical Physics **87** (2013), no. 6, 1–3. (Cited on page 2)

[21] S. A. Elkilany, *Formation of antihydrogen in antiproton positronium inelastic scattering*, Indian Journal of Physics **88** (2014), no. 1, 19–24. (Cited on page 2)

[22] A. S. Kadyrov, C. M. Rawlins, A. T. Stelbovics, I. Bray, and M. Charlton, *Antihydrogen Formation via Antiproton Scattering with Excited Positronium*, Physical Review Letters **114** (2015), no. 18, 183201. (Cited on page 2)

[23] Lisa Zyga, *Physicists find ways to increase antihydrogen production* [online], 2015, `http://phys.org/news/2015-05-physicists-ways-antihydrogen-production.html`. (Cited on page 2)

[24] Jason Engbrecht, *Positron Research Group* [online], 2013, `https://web.archive.org/web/20130202180954/http://www.stolaf.edu/academics/positron/`. (Cited on page 2)

[25] University College London, *The UCL Positron Group* [online], 2015, `http://www.ucl.ac.uk/positron-physics/title.html`. (Cited on page 2)

[26] B. L. Brown, *Creation of Monoenergetic Positronium (Ps) in a Gas*, Bull. Am. Phys. Soc. **30** (1985), 614. (Cited on page 2)

[27] G. Laricchia, M. Charlton, S. A. Davies, C. D. Beling and T. C. Griffith, *The production of collimated beams of o-Ps atoms using charge exchange in positron-gas collisions*, Journal of Physics B: Atomic and Molecular Physics **20** (1987), no. 3, L99. (Cited on page 2)

[28] N. Zafar, G. Laricchia, M. Charlton, and A. Garner, *Positronium-Argon Scattering*, Physical Review Letters **76** (1996), no. 10, 1595. (Cited on page 2)

[29] A. J. Garner, G. Laricchia, and A. Özen, *Ps beam production and scattering from gaseous targets*, Journal of Physics B: Atomic and Molecular Physics **29** (1996), no. 23, 5961. (Cited on page 2)

[30] G. Laricchia, S. Armitage, Á. Kövér, and D.J. Murtagh, *Ionizing collisions by positrons and positronium impact on the inert atoms*, Advances In Atomic, Molecular, and Optical Physics, Elsevier BV, 2008, p. 1. (Cited on page 2)

[31] A. J. Garner, A. Özen, and G. Laricchia, *The effect of forward-angle scattering on positronium-gas total cross sections*, Journal of Physics B: Atomic and Molecular Physics **33** (2000), no. 6, 1149. (Cited on page 2)

[32] S. Armitage, D. E. Leslie, A. J. Garner, and G. Laricchia, *Fragmentation of Positronium in Collision with He Atoms*, Physical Review Letters **89** (2002), no. 17, 173402. (Cited on page 2)

[33] G. Laricchia, S. Armitage, and D.E. Leslie, *Positronium induced collisions*, Nuclear Instruments and Methods in Physics Research Section B: Beam Interactions with Materials and Atoms **221** (2004), 60. (Cited on page 2)

[34] S. Armitage, D.E. Leslie, J. Beale, and G. Laricchia, *Collisions involving positronium*, Nuclear Instruments and Methods in Physics Research Section B: Beam Interactions with Materials and Atoms **247** (2006), no. 1, 98. (Cited on page 2)

[35] J. J. Engbrecht, M. J. Erickson, C. P. Johnson, A. J. Kolan, A. E. Legard, S. P. Lund, M. J. Nyflot, and J. D. Paulsen, *Energy-dependent Ps-He momentum-transfer cross section at low energies*, Physical Review A **77** (2008), no. 1, 012711. (Cited on pages 2 and 140)

[36] S. J. Brawley, S. Armitage, J. Beale, D. E. Leslie, A. I. Williams, and G. Laricchia, *Electron-Like Scattering of Positronium*, Science **330** (2010), no. 6005, 789. (Cited on pages 2 and 3)

[37] A. J. Garner, A. Özen, and G. Laricchia, *Positronium beam scattering from atoms and molecules*, Nuclear Instruments and Methods in Physics Research Section B: Beam Interactions with Materials and Atoms **143** (1998), no. 1-2, 155. (Cited on page 2)

[38] J. Beale, S. Armitage, and G. Laricchia, *Positronium- and positron-H_2O total cross sections*, Journal of Physics B: Atomic and Molecular Physics **39** (2006), no. 6, 1337. (Cited on page 2)

[39] S. J. Brawley, A. I. Williams, M. Shipman, and G. Laricchia, *Resonant Scattering of Positronium in Collision with CO_2*, Physical Review Letters **105** (2010), no. 26, 263401. (Cited on page 2)

[40] New Scientist, *Cloaking effect in atoms baffles scientists* [online], 2015, `http://www.newscientist.com/article/dn19682-cloaking-effect-in-atoms-baffles-scientists.html`. (Cited on page 2)

[41] I. I. Fabrikant and G. F. Gribakin, *Similarity between Positronium-Atom and Electron-Atom Scattering*, Physical Review Letters **112** (2014), no. 24, 243201. (Cited on page 2)

[42] I. I. Fabrikant and G. F. Gribakin, *Positronium-atom scattering at low energies*, Physical Review A **90** (2014), no. 5, 052717. (Cited on pages 2, 114, and 146)

[43] B. H. Bransden and C. J. Joachain, *Physics of Atoms and Molecules*, Pearson Education Limited, Harlow, England, 2003. (Cited on pages 3, 10, 37, 47, 111, 122, 123, 131, 136, 140, 143, and 144)

[44] W. Kohn, *Variational methods in nuclear collision problems*, Physical Review **74** (1948), no. 12, 1763. (Cited on page 3)

[45] Charles Schwartz, *Electron scattering from hydrogen*, Physical Review **124** (1961), no. 5, 1468. (Cited on pages 3 and 45)

[46] C. William McCurdy and Thomas N. Rescigno, *Collisions of electrons with polyatomic molecules: Electron-methane scattering by the complex Kohn variational method*, Physical Review A **39** (1989), no. 9, 4487. (Cited on pages 3 and 4)

[47] E. A. G. Armour and C. W. Chamberlain, *Calculation of cross sections for very low-energy hydrogen antihydrogen scattering using the Kohn variational method*, Journal of Physics B: Atomic, Molecular and Optical Physics **35** (2002), no. 22, L489–L494. (Cited on page 3)

[48] J. N. Cooper, E. A. G. Armour, and M. Plummer, *The importance of an accurate target wavefunction in variational calculations for (e^+-H_2) scattering*, Journal of Physics B: Atomic, Molecular and Optical Physics **41** (2008), no. 24, 245201. (Cited on page 3)

[49] S. J. Ward, J. W. Humberston, and M. R. C. McDowell, *Elastic scattering of electrons (or positrons) from positronium and the photodetachment of the positronium negative ion*, Journal of Physics B: Atomic and Molecular Physics **20** (1987), no. 1, 127. (Cited on pages 3 and 122)

[50] P. Van Reeth and J. W. Humberston, *A partial-wave analysis of positronium formation in positron-helium scattering*, Journal of Physics B: Atomic and Molecular Physics **30** (1997), no. 3, L95. (Cited on pages 3 and 96)

[51] Lauro Tomio, Carlos F. de Araujo, and Sadhan K. Adhikari, *Complex Kohn variational principle for two-nucleon bound-state and scattering*, AIP Conference Proceedings, vol. 334, AIP, May 1995, pp. 829–832. (Cited on page 3)

[52] A. Kievsky, *The complex Kohn variational method applied to N-d scattering*, Nuclear Physics A **624** (1997), no. 2, 125–139. (Cited on page 3)

[53] Robert R. Lucchese, *Anomalous singularities in the complex Kohn variational principle of quantum scattering theory*, Physical Review A **40** (1989), no. 12, 6879. (Cited on pages 4, 27, 29, 36, 37, 45, and 46)

[54] J. N. Cooper, M. Plummer, and E. A. G. Armour, *Equivalence of the generalized and complex Kohn variational methods*, J. Phys. A **43** (2010), no. 17, 175302. (Cited on pages 4, 27, 29, 36, 37, 45, and 46)

[55] E. A. G. Armour and J. W. Humberston, *Methods and programs in collisions of positrons with atoms and molecules*, Phys. Rep. **204** (1991), no. 2, 165. (Cited on pages 4, 9, 11, 59, 168, and 169)

[56] Denton Woods, S. J. Ward, and P. Van Reeth, *Detailed Investigation of Low-Energy Positronium-Hydrogen Scattering*, Phys. Rev. A (in press). (Cited on pages 4, 5, 7, 26, 96, 98, 99, 150, 155, and 190)

[57] P. Van Reeth and J. W. Humberston, *Variational calculations of s-wave positronium-hydrogen scattering*, Journal of Physics B: Atomic and Molecular Physics **36** (2003), no. 10, 1923. (Cited on pages 4, 5, 9, 15, 16, 27, 56, 61, 64, 66, 70, 71, 72, 73, 74, 88, 91, 101, 143, 144, 145, 146, 153, 155, and 173)

[58] P. Van Reeth and J. W. Humberston, *Low energy positronium-hydrogen scattering*, Nuclear Instruments and Methods in Physics Research Section B: Beam Interactions with Materials and Atoms **221** (2004), 140. (Cited on pages 4, 5, 18, 19, 47, 61, 74, 82, 86, 89, 91, and 173)

[59] G. W. F. Drake and Zong-Chao Yan, *Asymptotic-expansion method for the evaluation of correlated three-electron integrals*, Physical Review A **52** (1995), no. 5, 3681. (Cited on pages 4, 49, 50, 51, 52, 54, and 172)

[60] Zong-Chao Yan and G. W. F. Drake, *Computational methods for three-electron atomic systems in Hylleraas coordinates*, Journal of Physics B: Atomic and Molecular Physics **30** (1997), no. 21, 4723. (Cited on pages 4, 11, 50, 51, 105, 106, 107, 108, and 162)

[61] H. S. W. Massey and C. B. O. Mohr, *Gaseous Reactions involving Positronium*, Proceedings of the Physical Society: Section A **67** (1954), no. 8, 695. (Cited on pages 5 and 111)

[62] Mary T. McAlinden, F. G. R. S. MacDonald, and H.R.J. Walters, *Positronium-atom scattering*, Canadian Journal of Physics **74** (1996), no. 7-8, 434. (Cited on page 5)

[63] Simone Chiesa, Massimo Mella, and Gabriele Morosi, *Orthopositronium scattering off H and He*, Physical Review A **66** (2002), no. 4, 042502. (Cited on pages 5, 72, 73, and 153)

[64] I. A. Ivanov, J. Mitroy, and K. Varga, *Elastic Positronium-Atom Scattering Using the Stochastic Variational Method*, Physical Review Letters **87** (2001), no. 6, 063201. (Cited on pages 5, 72, and 153)

[65] I. A. Ivanov, J. Mitroy, and K. Varga, *Positronium-hydrogen scattering using the stochastic variational method*, Physical Review A **65** (2002), no. 3, 032703. (Cited on pages 5, 72, 73, 88, 89, 153, 154, 155, and 158)

[66] Prabal K. Sinha, Puspitapallab Chaudhury and A. S. Ghosh, *Ps-H scattering using the three-state positronium close-coupling approximation*, Journal of Physics B: Atomic and Molecular Physics **30** (1997), no. 20, 4643. (Cited on pages 5, 72, 73, 86, 88, 89, 98, and 101)

[67] C. P. Campbell, Mary T. McAlinden, F. G. R. S. MacDonald, and H. R. J. Walters, *Scattering of Positronium by Atomic Hydrogen*, Physical Review Letters **80** (1998), no. 23, 5097. (Cited on pages 5, 16, 72, 74, 75, 89, 102, and 153)

[68] Sadhan K. Adhikari and P. K. Biswas, *Positronium–hydrogen-atom scattering in a five-state model*, Physical Review A **59** (1999), no. 3, 2058. (Cited on pages 5, 15, 72, 73, 86, 88, 89, 98, 101, and 153)

[69] Prabal K. Sinha, Arindam Basu, and A. S. Ghosh, *Low-energy positronium-hydrogen elastic scattering using the six-state close coupling approximation*, Journal of Physics B: Atomic and Molecular Physics **33** (2000), no. 13, 2579. (Cited on pages 5, 72, 88, 101, and 153)

[70] Jennifer E. Blackwood, Mary T. McAlinden, and H. R. J. Walters, *Positronium scattering by atomic hydrogen with inclusion of target excitation channels*, Physical Review A **65** (2002), no. 3, 032517. (Cited on pages 5, 16, 47, 70, 71, 72, 73, 74, 76, 86, 87, 88, 89, 98, 99, 100, 101, 102, 122, 129, 130, 151, 153, 157, and 181)

[71] Jennifer E. Blackwood, Mary T. McAlinden, and H. R. J. Walters, *Importance of the H^- channel in Ps-H scattering*, Physical Review A **65** (2002), no. 3, 030502. (Cited on pages 5, 16, 47, 74, 89, 102, 116, 117, 129, and 130)

[72] H. R. J. Walters, A. C. H. Yu, S. Sahoo, and Sharon Gilmore, *Positronium-atom collisions*, Nuclear Instruments and Methods in Physics Research Section B: Beam Interactions with Materials and Atoms **221** (2004), 149. (Cited on pages 5, 16, 47, 70, 71, 72, 73, 74, 75, 76, 86, 87, 88, 89, 98, 99, 100, 101, 102, 116, 117, 127, 128, 129, 130, 140, 141, 142, 157, and 181)

[73] S. Hara and P. A. Fraser, *Low-energy ortho-positronium scattering by hydrogen atoms*, Journal of Physics B: Atomic and Molecular Physics **8** (1975), no. 18, L472. (Cited on pages 5, 72, 73, 86, 88, 89, 98, 101, 128, 129, and 153)

[74] H. Ray and A. S. Ghosh, *Positronium - hydrogen atom scattering using the static exchange model*, J. Phys. B **29** (1996), no. 22, 5505. (Cited on pages 5 and 122)

[75] H. Ray and A. S. Ghosh, *Positronium - hydrogen-atom scattering using the static exchange model*, Journal of Physics B: Atomic and Molecular Physics **30** (1997), 3745. (Cited on pages 5, 72, 73, 86, 88, 89, 98, and 101)

[76] B. A. P. Page, *Positronium-hydrogen scattering lengths*, Journal of Physics B: Atomic and Molecular Physics **9** (1976), no. 7, 1111. (Cited on pages 5, 151, and 153)

[77] John Archibald Wheeler, *Polyelectrons*, Annals of the New York Academy of Sciences **48** (1946), no. 3, 219. (Cited on page 5)

[78] Aadne Ore, *The Existence of Wheeler-Compounds*, Physical Review **83** (1951), no. 3, 665. (Cited on pages 5 and 16)

[79] D. M. Schrader, Finn M. Jacobsen, Niels-Peter Frandsen, and Ulrik Mikkelsen, *Formation of Positronium Hydride*, Physical Review Letters **69** (1992), no. 1, 57. (Cited on pages 5 and 16)

[80] Sergiy Bubin and Ludwik Adamowicz, *Nonrelativistic variational calculations of the positronium molecule and the positronium hydride*, Physical Review A **74** (2006), no. 5, 052502. (Cited on pages 6, 15, 16, 17, and 157)

[81] Dario Bressanini and Gabriele Morosi, *Compact boundary-condition-determined wave function for positronium hydride (PsH)*, Journal of Chemical Physics **119** (2003), no. 14, 7037. (Cited on pages 6 and 15)

[82] Alexei M. Frolov and Vedene H. Smith, Jr., *Positronium hydrides and the Ps_2 molecule: Bound-state properties, positron annihilation rates, and hyperfine structure*, Physical Review A **55** (1997), no. 4, 2662. (Cited on pages 6 and 15)

[83] Shiro L. Saito, *Is positronium hydride atom or molecule?*, Nuclear Instruments and Methods in Physics Research Section B: Beam Interactions with Materials and Atoms **171** (2000), no. 1-2, 60. (Cited on pages 6 and 15)

[84] Y. K. Ho, *Positron annihilation in positronium hydrides*, Physical Review A **34** (1986), no. 1, 609. (Cited on pages 6 and 16)

[85] M. W. J. Bromley and J. Mitroy, *Configuration-interaction calculations of PsH and e+Be*, Physical Review A **65** (2001), 012505. (Cited on pages 6 and 15)

[86] P. K. Biswas and J. W. Darewych, *Positronium scattering from 2s and 3s excited states of hydrogen*, Nuclear Instruments and Methods in Physics Research Section B: Beam Interactions with Materials and Atoms **192** (2002), no. 1-2, 138. (Cited on pages 6 and 74)

[87] Raji Heyrovska, *Atomic and molecular structures of positronium, dipositronium and positronium hydride*, Nature Precedings (2011), 1. (Cited on page 6)

[88] D. R. Hartree, *The Wave Mechanics of an Atom with a Non-Coulomb Central Field. Part I. Theory*, Mathematical Proceedings of the Cambridge Philosophical Society **24** (1928), no. 1, 89. (Cited on page 6)

[89] Peter J. Mohr, Barry N. Taylor, and David B. Newell, *CODATA recommended values of the fundamental physical constants: 2010*, Rev. Mod. Phys. **84** (2012), no. 4, 1527. (Cited on page 6)

[90] NIST Conversions, *NIST Conversions* [online], 2014, `http://physics.nist.gov/cuu/Constants/energy.html`. (Cited on page 6)

[91] E. A. G. Armour, J.-M. Richard, and K. Varga, *Stability of few-charge systems in quantum mechanics*, Physics Reports **413** (2005), no. 1, 1–90. (Cited on page 8)

[92] Zong-Chao Yan and Y. K. Ho, *Ground state and S-wave autodissociating resonant states of positronium hydride*, Physical Review A **59** (1999), no. 4, 2697. (Cited on pages 9, 15, 16, 17, 54, 64, 71, 74, 87, 89, 128, 157, and 179)

[93] Tosio Kato, *On the eigenfunctions of many-particle systems in quantum mechanics*, Communications on Pure and Applied Mathematics **10** (1957), no. 2, 151. (Cited on pages 9 and 16)

[94] Knowino, *Rayleigh-Ritz method*, `http://www.webcitation.org/6VhFOV4O8`, 2014. (Cited on page 10)

[95] P. Van Reeth, *Theoretical Studies of Positronium Formation in Low Energy Positron-Helium Collisions*, Ph.D. thesis, University College London, unpublished, 1996. (Cited on pages 11, 27, 28, 38, 56, 59, 68, 96, 159, 160, 161, 168, 175, and 193)

[96] B. A. P. Page and P. A. Fraser, *The ground state of positronium hydride*, Journal of Physics B: Atomic and Molecular Physics **7** (1974), no. 13, L389. (Cited on pages 12 and 16)

[97] Alexei M. Frolov, *Semi-exponential basis for highly accurate computations of three-electron atomic systems*, Physics Letters A **374** (2010), no. 23, 2361. (Cited on pages 15 and 17)

[98] J. Mitroy, *Energy and expectation values of the PsH system*, Physical Review A **73** (2006), no. 5, 054502. (Cited on pages 15, 16, and 17)

[99] Simone Chiesa, Massimo Mella, and Gabriele Morosi, *Quantum Monte Carlo estimators for the positron-electron annihilation rate in bound and low-energy scattering states*, Physical Review A **69** (2004), 022701. (Cited on page 15)

[100] Sergiy Bubin and Ludwik Adamowicz, *Non-BornOppenheimer study of positronic molecular systems: e^+LiH*, The Journal of Chemical Physics **120** (2004), no. 13, 6051. (Cited on pages 15 and 16)

[101] Shiro L. Saito, *Multireference configuration interaction calculations of some low-lying states of positronium hydride*, Journal of Chemical Physics **118** (2003), no. 4, 1714. (Cited on pages 15 and 16)

[102] M. W. J. Bromley, J. Mitroy, and G. G. Ryzhikh, *Configuration interaction calculations of positronic atoms and ions*, Nuclear Instruments and Methods in Physics Research, Section B: Beam Interactions with Materials and Atoms **171** (2000), 47. (Cited on page 15)

[103] Zong-Chao Yan and Y. K. Ho, *Relativistic effects in positronium hydride*, Physical Review A **60** (1999), no. 6, 5098–5100. (Cited on page 15)

[104] G. G. Ryzhikh and J. Mitroy, *Positron annihilation profiles for HPs and $He(^3S^e)e^+$*, Journal of Physics B: Atomic, Molecular and Optical Physics **32** (1999), 4051. (Cited on page 15)

[105] Massimo Mella, Gabriele Morosi, and Dario Bressanini, *Positron and positronium chemistry by quantum Monte Carlo. IV. Can this method accurately compute observables beyond energy?*, Journal of Chemical Physics **111** (1999), no. 1, 108. (Cited on page 15)

[106] G. G. Ryzhikh, J. Mitroy, and K. Varga, *The structure of exotic atoms containing positrons and positronium*, Journal of Physics B: Atomic, Molecular and Optical Physics **31** (1998), 3965. (Cited on page 15)

[107] K. Strasburger and H. Chojnacki, *Quantum chemical study of simple positronic systems using explicitly correlated Gaussian functions PsH and $PsLi^+$*, The Journal of Chemical Physics **108** (1998), no. 8, 3218. (Cited on page 15)

[108] Dario Bressanini, Massimo Mella, and Gabriele Morosi, *Stability and positron annihilation of positronium hydride L=0,1,2 states: A quantum Monte Carlo study*, Physical Review A **57** (1998), no. 3, 1678. (Cited on page 15)

[109] Nan Jiang and D. M. Schrader, *Diffusion quantum Monte Carlo calculation of the binding energy and annihilation rate of positronium hydride, PsH*, J. Chem. Phys. **109** (1998), no. 21, 9430. (Cited on page 15)

[110] C. Le Sech and B. Silvi, *Study of positronium hydride with a simple wavefunction: Application to the Stark effect of PsH*, Chemical Physics **236** (1998), 77. (Cited on page 15)

[111] J. Usukura, K. Varga, and Y. Suzuki, *Signature of the existence of the positronium molecule*, Physical Review A **58** (1998), no. 3, 1918. (Cited on page 15)

[112] Alexei M. Frolov and Vedene H. Smith, Jr., *Ground state of positronium hydride*, Physical Review A **56** (1997), no. 3, 2417. (Cited on page 15)

[113] G. G. Ryzhikh and J. Mitroy, *Positronic lithium, an electronically stable Li-e^+ ground state*, Physical Review Letters **79** (1997), no. 21, 4124. (Cited on page 15)

[114] Takashi Yoshida and Gensho Miyako, *Diffusion quantum Monte Carlo calculations of positronium hydride and positron lithium*, Physical Review A **54** (1996), no. 5, 4571. (Cited on page 15)

[115] Shiro L. Saito and Fukashi Sasaki, *Application of pair correlation theory to positronium compounds*, The Journal of Chemical Physics **102** (1995), no. 20, 8040. (Cited on page 16)

[116] Shiro L. Saito, *Calculation of positronium compounds, PsLi, PsF, and PsCl, by second-order variational perturbation method*, Chemical Physics Letters **245** (1995), no. 1, 54. (Cited on page 16)

[117] K. Strasburger and H. Chojnacki, *On the reliability of the SCF and CI wavefunctions for systems containing positrons*, Chemical Physics Letters **241** (1995), no. August, 485. (Cited on page 16)

[118] M. Maruyama, Ph.D. thesis, The University of Electro-Communications, 1985. (Cited on page 16)

[119] Y. K. Ho, *A resonant state and the ground state of positronium hydride*, Physical Review A **17** (1978), no. 5, 1675. (Cited on pages 16 and 74)

[120] David C. Clary, *Configuration-interaction-Hylleraas calculations on one-positron atomic systems*, Journal of Physics B: Atomic and Molecular Physics **9** (1976), no. 17, 3115. (Cited on page 16)

[121] Peter B. Navin, D. M. Schrader, and C. F. Lebeda, *An improved wave function for positronium hydride: Preliminary report*, Physical Review A **3** (1974), no. 2, 159. (Cited on page 16)

[122] S. K. Houston and Richard J. Drachman, *Comment on the Ground State of Positronium Hydride*, Physical Review A **7** (1973), no. 2, 819. (Cited on page 16)

[123] C. F. Lebeda and D. M. Schrader, *Towards an Accurate Wave Function for Positronium Hydride*, Physical Review **178** (1969), no. 1, 24. (Cited on page 16)

[124] Oliver G. Ludwig and Robert G. Parr, *Configuration interaction wavefunction for positronium hydride*, Theoretica Chimica Acta **5** (1966), no. 5, 440. (Cited on page 16)

[125] V. I. Goldanskii, A. V. Ivanova, and E. P. Prokopev, Zh. eksp. Teor. Fiz. **47** (1964), 659. (Cited on page 16)

[126] S. M. Neamtan, G. Darewych, and G. Oczkowski, *Annihilation of Positrons from the H^-e^+ Ground State*, Physical Review **126** (1962), no. 1, 192. (Cited on page 16)

[127] Jim Mitroy, Sergiy Bubin, Wataru Horiuchi, Yasuyuki Suzuki, Ludwik Adamowicz, Wojciech Cencek, Krzysztof Szalewicz, Jacek Komasa, D. Blume, and Kálmán Varga, *Theory and application of explicitly correlated Gaussians*, Reviews of Modern Physics **85** (2013), no. 2, 693. (Cited on page 16)

[128] J. Mitroy and M. W. J. Bromley, *Second Bound State of PsH*, Physical Review Letters **98** (2007), no. 6, 063401. (Cited on page 17)

[129] Andrew U. Hazi and Howard S. Taylor, *Stabilization Method of Calculating Resonance Energies: Model Problem*, Physical Review A **1** (1970), no. 4, 1109–1120. (Cited on pages 18, 48, 74, and 75)

[130] Z.-C. Yan and Y. K. Ho, *Determination of resonance energies and widths in Ps-H scattering using the stabilization method*, Journal of Physics B: Atomic and Molecular Physics **36** (2003), no. 22, 4417. (Cited on pages 19, 74, 89, and 102)

[131] C. J. Brown, *The Interactions of Low Energy Positrons with Atomic Hydrogen*, Ph.D. thesis, University College London, 1986. (Cited on pages 27 and 96)

[132] Charles Schwartz, *Lamb Shift in the Helium Atom*, Phys. Rev. **123** (1961), no. 5, 1700. (Cited on pages 27 and 96)

[133] Sadhan Adhikari, *Variational Principles and the Numerical Solution of Scattering Problems*, Wiley, New York, 1998. (Cited on page 28)

[134] John Z. H. Zhang, Shih-I. Chu, and William H. Miller, *Quantum scattering via the S-matrix version of the Kohn variational principle*, Chemical Physics Letters **88** (1988), no. 10, 6233–6239. (Cited on page 29)

[135] George B. Arfken and Hans Weber, *Mathematical methods for physicists*, 6^{th} ed., Elsevier, Boston, 2005. (Cited on pages 32, 33, and 167)

[136] Tosio Kato, *Upper and Lower Bounds of Scattering Phases*, Progress of Theoretical Physics **6** (1951), no. 3, 394. (Cited on page 33)

[137] C. J. Joachain, *Quantum Collision Theory*, North-Holland, Amsterdam Oxford, 1979. (Cited on pages 33, 122, and 143)

[138] J. N. Cooper, E. A. G. Armour, and M. Plummer, *Anomaly-free singularities in the generalized Kohn variational method*, J. Phys. A **42** (2009), no. 9, 095207. (Cited on page 36)

[139] B. H. Bransden, *Atomic Collision Theory*, W. A. Benjamin, Inc., New York, 1970. (Cited on page 37)

[140] R. K. Nesbet, *Analysis of the Harris variational method in scattering theory*, Physical Review **175** (1968), no. 1, 134–142. (Cited on page 45)

[141] R. K. Nesbet, *Anomaly-Free Variational Method for Inelastic Scattering*, Physical Review **179** (1969), no. 1, 60–70. (Cited on page 45)

[142] William H. Miller and Bernadette M. D. D. Jansen op de Haar, *A new basis set method for quantum scattering calculations*, J. Chem. Phys. **86** (1987), no. 11, 6213. (Cited on page 46)

[143] C. William McCurdy, Thomas N. Rescigno, and Barry I. Schneider, *Interrelation between variational principles for scattering amplitudes and generalized R-matrix theory*, Physical Review A **36** (1987), no. 5, 2061. (Cited on page 46)

[144] Jonathan Tennyson and Cliff J. Noble, *RESON - A program for the detection and fitting of Breit-Wigner resonances*, Computer Physics Communications **33** (1984), no. 4, 421. (Cited on pages 47 and 196)

[145] Darian T. Stibbe and Jonathan Tennyson, *TIMEDEL: A program for the detection and parameterization of resonances using the time-delay matrix*, Computer Physics Communications **114** (1998), no. 1-3, 236. (Cited on pages 47 and 196)

[146] U. Fano, *Effects of Configuration Interaction on Intensities and Phase Shifts*, Phys. Rev. **124** (1961), no. 6, 1866. (Cited on page 47)

[147] Joseph Macek, *Behavior of Eigenphases near a Resonance*, Physical Review A **2** (1970), no. 3, 1101. (Cited on page 47)

[148] A. U. Hazi, *Behavior of the eigenphase sum near a resonance*, Physical Review A **19** (1979), no. 2, 920. (Cited on page 47)

[149] Richard J. Drachman, *Autodissociating Rydberg states of positronium hydride*, Physical Review A **19** (1979), no. 5, 1900. (Cited on page 47)

[150] P.K. Biswas, *Effect of H^- ion formation on positronium-hydrogen elastic scattering*, Journal of Physics B: Atomic, Molecular and Optical Physics **34** (2001), no. 23, 4831. (Cited on pages 47, 72, and 73)

[151] Joseph Di Rienzi and Richard J. Drachman, *Resonances in positronium hydride*, Physical Review A **65** (2002), no. 3, 032721. (Cited on pages 48, 74, and 89)

[152] Joseph DiRienzi and Richard J. Drachman, *D-wave resonances in positronium hydride*, Physical Review A **66** (2002), no. 5, 054702. (Cited on pages 48 and 102)

[153] Alexei M. Frolov and David H. Bailey, *Highly accurate evaluation of the few-body auxiliary functions and four-body integrals*, Journal of Physics B: Atomic, Molecular and Optical Physics **36** (2003), no. 9, 1857. (Cited on pages 49, 51, and 172)

[154] Paul J. Pelzl and Frederick W. King, *Convergence accelerator approach for the high-precision evaluation of three-electron correlated integrals*, Physical Review E **57** (1998), no. 6, 7268. (Cited on pages 49 and 51)

[155] María Belén Ruiz, *Evaluation of Hylleraas-CI atomic integrals by integration over the coordinates of one electron. II. Four-electron integrals*, Journal of Mathematical Chemistry **46** (2009), no. 4, 1322–1355. (Cited on page 49)

[156] Krzysztof Pachucki, Mariusz Puchalski, and Ettore Remiddi, *Recursion relations for the generic Hylleraas three-electron integral*, Physical Review A **70** (2004), no. 3, 032502. (Cited on pages 49, 50, 51, 52, and 53)

[157] Zong-Chao Yan, *Computational methods for three-electron atomic systems in Hylleraas coordinates: II. QED terms* $\left\langle r_{ij}^{-3} \right\rangle$ *and* $\left\langle r_{i}^{-3} \right\rangle$, Journal of Physics B: Atomic, Molecular and Optical Physics **33** (2000), no. 13, 2437. (Cited on page 50)

[158] Krzysztof Pachucki and Mariusz Puchalski, *Extended Hylleraas three-electron integral*, Physical Review A **71** (2005), no. 3, 032514. (Cited on pages 50 and 53)

[159] Krzysztof Pachucki and Mariusz Puchalski, *Singular Hylleraas three-electron integrals*, Physical Review A **77** (2008), no. 3, 032511. (Cited on page 50)

[160] Zong-Chao Yan and G. W. F. Drake, *Lithium Fine Structure in the* $1s^2\ 2p\ {}^2P_J$ *States*, Physical Review Letters **79** (1997), no. 9, 1646. (Cited on pages 50 and 54)

[161] Mariusz Puchalski and Krzysztof Pachucki, *Applications of four-body exponentially correlated functions*, Physical Review A **81** (2010), no. 5, 052505. (Cited on page 50)

[162] Yngve Öhrn and Jan Nordling, *On the Calculation of Some Atomic Integrals Containing Functions of* r_{12}, r_{13}, *and* r_{23}, Journal of Chemical Physics **39** (1963), 1864. (Cited on page 50)

[163] J. F. Perkins, *Atomic Integrals Containing* $r_{23}^{\lambda}\ r_{31}^{\mu}\ r_{12}^{\nu}$, The Journal of Chemical Physics **48** (1968), no. 5, 1985. (Cited on page 50)

[164] R. A. Sack, *Generalization of Laplace's Expansion to Arbitrary Powers and Functions of the Distance between Two Points*, Journal of Mathematical Physics **5** (1964), no. 2, 245. (Cited on page 50)

[165] I. Porras and Frederick W. King, *Evaluation of some integrals for the atomic three-electron problem using convergence accelerators*, Physical Review A **49** (1994), no. 3, 1637. (Cited on page 50)

[166] David Meloy Fromm and Robert Nyden Hill, *Analytic evaluation of three-electron integrals*, Physical Review A **36** (1987), no. 3, 1013. (Cited on pages 51 and 52)

[167] Frank E. Harris, *Recurrence formulas for fully exponentially correlated four-body wave functions*, Physical Review A **79** (2009), no. 3, 032517. (Cited on page 51)

[168] Frederick W. King, *Analysis of some integrals arising in the atomic four-electron problem*, The Journal of Chemical Physics **99** (1993), no. 5, 3622. (Cited on page 51)

[169] Paul J. Pelzl, Gregory J. Smethells, and Frederick W. King, *Improvements on the application of convergence accelerators for the evaluation of some three-electron atomic integrals*, Physical Review E **65** (2002), no. 3, 036707. (Cited on page 51)

[170] Mariusz Puchalski and Krzysztof Pachucki, *Ground-state wave function and energy of the lithium atom*, Physical Review A **73** (2006), no. 2, 022503. (Cited on page 52)

[171] P. Van Reeth, Private communication, 2008-2015. (Cited on pages 54, 56, 61, 66, 77, 80, 86, 91, 173, 181, 182, 194, and 195)

[172] LAPACK dsygv, *LAPACK dsygv* [online], 2011, `http://www.netlib.org/lapack/double/dsygv.f`. (Cited on page 54)

[173] Arne Lüchow and Heinz Kleindienst, *Stable and efficient algorithm for selected eigenvalues and eigenvectors of the general symmetric eigenproblem*, Computers & Chemistry **17** (1993), no. 1, 61. (Cited on page 54)

[174] Zong-Chao Yan, M. Tambasco, and G. W. F. Drake, *Energies and oscillator strengths for lithiumlike ions*, Physical Review A **57** (1998), no. 3, 1652. (Cited on page 54)

[175] Zong-Chao Yan and Y. K. Ho, *P-wave autodissociating resonant states of positronium hydride*, Physical Review A **57** (1998), no. 4, R2270. (Cited on pages 54, 71, 128, and 157)

[176] A. C. Todd, *Helium-Antihydrogen Interactions*, Ph.D. thesis, The University of Nottingham, 2007. (Cited on page 55)

[177] E.A.G. Armour, A.C. Todd, S. Jonsell, Y. Liu, M. R. Gregory, and M. Plummer, *The interaction of antihydrogen with simple atoms and molecules*, Nuclear Instruments and Methods in Physics Research Section B: Beam Interactions with Materials and Atoms **266** (2008), no. 3, 363–368. (Cited on page 55)

[178] Arne Lüchow and Heinz Kleindienst, *An efficient basis selection procedure for the reduction of the dimension in large Hylleraas-CI calculations*, Chem. Phys. Lett. **197** (1992), no. 1-2, 105. (Cited on page 55)

[179] OpenMP Architecture Review Board, *OpenMP application program interface version 3.0*, May 2008. (Cited on page 56)

[180] MPI Forum, *MPI: A Message-Passing Interface Standard. Version 2.2*, September 4th 2009, available at: `http://www.mpi-forum.org` (Dec. 2009). (Cited on page 56)

[181] J.-Y. Zhang, Z.-C. Yan, and U. Schwingenschlögl, *Elastic scattering of positronium: Application of the confined variational method*, Europhysics Letters **99** (2012), no. 4, 43001. (Cited on pages 70, 71, 73, 74, 76, and 99)

[182] Y. K. Ho and Zong-Chao Yan, *A D-wave resonance in positronium-hydrogen scattering*, Journal of Physics B: Atomic and Molecular Physics **31** (1998), no. 20, L877. (Cited on pages 71, 100, 102, 128, and 157)

[183] P. K. Biswas, T. Frederico, and J. S. E. Germano, *Zero- and negative-energy solutions of the coupled T-matrix equations: Application to positronium-hydrogen singlet scattering*, Physical Review A **66** (2002), 054701. (Cited on pages 72, 73, 74, and 153)

[184] Richard J. Drachman and S. K. Houston, *Positronium-hydrogen elastic scattering: The electronic S=1 state*, Physical Review A **14** (1976), no. 2, 894. (Cited on pages 72 and 153)

[185] Richard J. Drachman and S. K. Houston, *Positronium-hydrogen elastic scattering*, Physical Review A **12** (1975), no. 3, 885. (Cited on pages 72, 74, and 153)

[186] P. A. Fraser, *The Scattering of Low-energy Ortho-positronium by Hydrogen Atoms*, Proc. Phys. Soc. **78** (1961), no. 3, 329. (Cited on pages 72 and 145)

[187] Sadhan K. Adhikari, *Differential cross sections for elastic and inelastic positronium–hydrogen-atom scattering*, Physical Review A **63** (2001), no. 5, 054502. (Cited on pages 74 and 89)

[188] Hasi Ray, *Findings in Ps-H scattering*, Physical Review A **73** (2006), no. 6, 064501. (Cited on page 75)

[189] C. J. Brown and J. W. Humberston, *Positronium formation in positron-hydrogen scattering*, J. Phys. B **18** (1985), no. 12, L401–L406. (Cited on page 96)

[190] Martin Stephen Thomas Watts, *Theoretical Studies of Positronium Formation in Positron Collisions with Lithium and Hydrogen Atoms*, Ph.D. thesis, University College London, unpublished, 1994. (Cited on page 96)

[191] J. W. Humberston, P. Van Reeth, M. S. T. Watts, and W. E. Meyerhof, *Positron-hydrogen scattering in the vicinity of the positronium formation threshold*, J. Phys. B **30** (1997), 2477. (Cited on page 96)

[192] J. T. Dunn, P. Van Reeth, J. W. Humberston, and G. Peach, *Positron scattering by equivalent one-electron models of helium*, J. Phys. B **33** (2000), 2589. (Cited on page 96)

[193] Joel T. Dunn, *Helium-Antihydrogen Interactions*, Ph.D. thesis, The University of London, 2002. (Cited on page 96)

[194] P. Van Reeth and J. W. Humberston, unpublished, 2015. (Cited on pages 96, 97, and 157)

[195] Mark Galassi, *GNU Scientific Library Reference Manual (3rd. Ed.)*, 3rd ed., Network Theory Ltd., Bristol, 2009. (Cited on pages 104 and 178)

[196] Frank E. Harris, *Angular Symmetry and Hylleraas Coordinates in Four-Body Problems*, Advances in Quantum Chemistry **50** (2005), 61. (Cited on page 105)

[197] A. R. Edmonds, *Angular Momentum in Quantum Mechanics*, Princeton University Press, Princeton, N.J, 1996. (Cited on pages 107 and 110)

[198] D. M. Brink and G. R. Satchler, *Angular Momentum*, Oxford University Press, Oxford New York, 1993. (Cited on pages 107 and 108)

[199] Morris Rose, *Elementary Theory of Angular Momentum*, Dover, New York, 1995. (Cited on page 107)

[200] I. Lindgren and J. Morrison, *Atomic Many-Body Theory*, Springer, 2012. (Cited on page 108)

[201] University of North Texas High Performance Computing, *Talon 2.0 (archived by WebCite©)* [online], 2015, `http://hpc.unt.edu/compute-nodes`. (Cited on page 110)

[202] Albert Messiah, *Quantum Mechanics*, Dover Publications, Inc., Mineola, N.Y, 1999. (Cited on page 110)

[203] James H. Luscombe and Marshall Luban, *Simplified recursive algorithm for Wigner 3j and 6j symbols*, Physical Review E **57** (1998), no. 6, 7274. (Cited on page 110)

[204] Liqiang Wei, *New formula for 9-j symbols and their direct calculation*, Computers in Physics **12** (1998), no. 6, 632. (Cited on page 110)

[205] J. Rasch and A. C. H. Yu, *Efficient Storage Scheme for Precalculated Wigner 3j, 6j and Gaunt Coefficients*, SIAM Journal on Scientific Computing **25** (2003), no. 4, 1416–1428. (Cited on page 110)

[206] H. T. Johansson and C. Forssén, *Fast and accurate evaluation of Wigner 3j, 6j, and 9j symbols using prime factorisation and multi-word integer arithmetic*, 1–7. (Cited on page 110)

[207] J. R. Oppenheimer, *On the Quantum Theory of Electronic Impacts*, Phys. Rev. **32** (1928), 361. (Cited on page 111)

[208] Sydney Geltman, *Topics in Atomic Collision Theory*, Academic Press, New York and London, 1969. (Cited on page 111)

[209] N. F. Mott and H. S. W. Massey, *The Theory of Atomic Collisions*, 3^{rd} ed., Clarendon Press, Oxford, 1965. (Cited on page 111)

[210] Y. K. Ho and Zong-Chao Yan, *F- and G-wave resonances in positronium-hydrogen scattering*, Physical Review A **62** (2000), no. 5, 052503. (Cited on pages 113, 116, 117, 128, and 157)

[211] P. S. Ganas, *Effective-range theory for van der Waals scattering*, Physical Review A **5** (1972), no. 4, 1684. (Cited on page 114)

[212] J. Mitroy and M. W. J. Bromley, *van der Waals coefficients for positronium-atom interactions*, Physical Review A **68** (2003), no. 3, 035201. (Cited on pages 114 and 146)

[213] A. R. Swann, J. A. Ludlow, and G. F. Gribakin, *van der Waals coefficients for positronium interactions with closed-shell atoms*, (2015), 1–6. (Cited on page 114)

[214] Bo Gao, *Quantum-defect theory of atomic collisions and molecular vibration spectra*, Physical Review A **58** (1998), no. 5, 4222. (Cited on pages 114, 149, 151, 152, 153, and 154)

[215] J. Shertzer and J. Botero, *Finite-element analysis of electron-hydrogen scattering*, Physical Review A **49** (1994), no. 5, 3673–3679. (Cited on page 120)

[216] Ming-Keh Chen, C. D. Lin, and J. Z. Tang, *Hyperspherical close-coupling calculation of electron-hydrogen scattering cross sections*, Physical Review A **56** (1997), no. 3, 2435. (Cited on page 120)

[217] xoofee, *CurveSnap* [online], 2014, `https://github.com/xoofee/CurveSnap`. (Cited on page 128)

[218] Y. Nagashima, T. Hyodo, K. Fujiwara, and A. Ichimura, *Momentum-transfer cross section for slow positronium-He scattering*, Journal of Physics B: Atomic and Molecular Physics **31** (1998), no. 2, 329. (Cited on page 140)

[219] F. Saito, Y. Nagashima, and T. Hyodo, *Momentum-transfer cross sections for slow positroniumgas collisions*, Journal of Physics B: Atomic and Molecular Physics **36** (2003), no. 20, 4191. (Cited on page 140)

[220] M. Skalsey, J. J. Engbrecht, R. K. Bithell, R. S. Vallery, and D. W. Gidley, *Thermalization of positronium in gases*, Phys. Rev. Lett. **80** (1998), 3727. (Cited on page 140)

[221] Jennifer E. Blackwood, Mary T. McAlinden, and H. R. J. Walters, *Positronium scattering by Ne, Ar, Kr and Xe in the frozen target approximation*, Journal of Physics B: Atomic and Molecular Physics **35** (2002), no. 12, 2661. (Cited on pages 140 and 142)

[222] Yang Wang, Oleg Zatsarinny, and Klaus Bartschat, *B-spline R-matrix-with-pseudostates calculations for electron-impact excitation and ionization of nitrogen*, Physical Review A **89** (2014), no. 6, 062714. (Cited on page 140)

[223] R.P. McEachran and A. D. Stauffer, *Momentum transfer cross sections for the heavy noble gases*, The European Physical Journal D **68** (2014), no. 6, 153. (Cited on page 140)

[224] U. Thumm and D. W. Norcross, *Angle-differential and momentum-transfer cross sections for low-energy electron-Cs scattering*, Physical Review A **47** (1993), no. 1, 305–316. (Cited on page 142)

[225] Larry Spruch and Leonard Rosenberg, *Upper Bounds on Scattering Lengths for Static Potentials*, Physical Review **116** (1959), no. 4, 1034–1040. (Cited on page 143)

[226] Stephen J. Buckman and Jim Mitroy, *Analysis of low-energy electron scattering cross sections via effective-range theory*, Journal of Physics B: Atomic and Molecular Physics **22** (1989), no. 9, 1365. (Cited on page 144)

[227] H. A. Bethe, *Theory of the Effective Range in Nuclear Scattering*, Physical Review **76** (1949), no. 1, 38. (Cited on page 145)

[228] John M. Blatt and J. David Jackson, *On the Interpretation of Neutron-Proton Scattering Data by the Schwinger Variational Method*, Phys. Rev. **26** (1949), no. 1, 18. (Cited on page 145)

[229] M. Raymond Flannery, *Springer Handbook of Atomic, Molecular, and Optical Physics*, 2nd ed., Springer, New York, NY, 2006. (Cited on pages 145 and 147)

[230] C. K. Au and Richard J. Drachman, *Van der Waals force between positronium and hydrogenic atoms: Finite-mass corrections*, Physical Review Letters **56** (1986), 324. (Cited on page 146)

[231] D. W. Martin and P. A. Fraser, *The van der Waals force between positronium and light atoms*, Journal of Physics B: Atomic and Molecular Physics **13** (1980), no. 17, 3383. (Cited on page 146)

[232] Hasi Ray, Anuradha De, and Deparpita Ray, *The Effect of van der Waals interaction in Elastic Collision between Ps(1s) and H(1s)*, no. 03. (Cited on page 146)

[233] Otto Hinckelmann and Larry Spruch, *Low-Energy Scattering by Long-Range Potentials*, Physical Review A **3** (1971), no. 2, 642. (Cited on page 147)

[234] A. Calle Cordón and E. Ruiz Arriola, *Low-energy universality and scaling of van der Waals forces*, Physical Review A **81** (2010), 044701. (Cited on page 148)

[235] E. Ruiz Arriola, *Van der Waals forces and Photon-less Effective Field Theories*, 2010. (Cited on page 148)

[236] Bo Gao, *Solutions of the Schrödinger equation for an attractive $1/r^6$ potential*, Physical Review A **58** (1998), no. 3, 1728. (Cited on page 149)

[237] Sadhan K. Adhikari and Puspajit Mandal, *Convergent variational calculation of positronium-hydrogen-atom scattering lengths*, Journal of Physics B: Atomic and Molecular Physics **34** (2001), L187. (Cited on page 153)

[238] Bertram R. Levy and Joseph B. Keller, *Low-Energy Expansion of Scattering Phase Shifts for Long-Range Potentials*, J. Math. Phys. **4** (1963), no. 1, 54. (Cited on page 154)

[239] Mathematica, *Mathematica, version 8.0*, 2010. (Cited on page 167)

[240] Milton Abramowitz and Irene A. Stegun, *Handbook of Mathematical Functions with Formulas, Graphs, and Mathematical Tables*, Dover, 1965. (Cited on pages 167, 170, 171, 172, 191, 192, and 193)

[241] Wolfram Research, *Associated Legendre Polynomials: Identities* [online], 2015, `http://functions.wolfram.com/05.07.17.0003.01`. (Cited on page 171)

[242] Daniel Zwillinger, *CRC Standard Mathematical Tables and Formulae*, 31^{st} ed., Chapman & Hall/CRC, Boca Raton, 2003. (Cited on page 172)

[243] William H. Beyer, *CRC Standard Mathematical Tables*, 25^{th} ed., CRC Press, Inc., Boca Raton, FL, 1978. (Cited on page 176)

[244] Timothy Sauer, *Numerical Analysis*, Pearson Addison Wesley, Boston, 2006. (Cited on page 177)

[245] Eric Kvaalen, *A Faster Broyden Method*, BIT Numerical Mathematics **31** (1991), no. 2, 369. (Cited on page 177)

[246] GNU Scientific Library, *Multidimensional Minimization* [online], 2012, `https://www.gnu.org/software/gsl/manual/html_node/Multidimensional-Minimization.html`. (Cited on page 178)

[247] Eric W. Weisstein, *Chebyshev-Gauss Quadrature. From MathWorld—A Wolfram Web Resource* [online], 2011, `http://mathworld.wolfram.com/Chebyshev-GaussQuadrature.html`. (Cited on page 193)

[248] Denton Woods, Nicolas Weber, Meloni Dario, and Mat**e**j Tý**c**, *Developer's Image Library*, `http://openil.sourceforge.net`, 2009. (Cited on page 194)

[249] Taha Sochi and P. J. Storey, *Methods for analyzing resonances in atomic scattering*, The European Physical Journal Plus **128** (2013), no. 8, 82. (Cited on page 196)

[250] Ryan Bosca, Private communication, 2008-2015. (Cited on page 196)

[251] MATLAB, *version 8.3.0 (r2014a)*, The MathWorks Inc., Natick, Massachusetts, 2014. (Cited on page 196)

[252] Fernando Pérez and Brian E. Granger, *IPython: A System for Interactive Scientific Computing*, Computing in Science and Engineering **9** (2007), no. 3, 21–29. (Cited on page 196)

[253] Alexander Schmolck and Vivek Rathod, *mlabwrap* [online], 2014, `http://mlabwrap.sourceforge.net`. (Cited on page 196)

[254] Charl Botha, *mlabwrap-purepy* [online], 2015, `https://github.com/cpbotha/mlabwrap-purepy`. (Cited on page 196)

[255] Python, *Python* [online], 2011, `http://www.python.org`. (Cited on page 207)

[256] SciPy, *Scipy* [online], 2011, `http://www.scipy.org`. (Cited on page 207)